DOCTORAL THESIS

Improving the effectiveness of oncolytic virotherapy: insights from mathematical modelling

Author:
David MORSELLI

Supervisors:
Marcello Edoardo DELITALA
Federico FRASCOLI

Politecnico di Torino
Department of Mathematical Sciences "G. L. Lagrange"

Swinburne University of Technology
Department of Mathematics,
School of Science, Computing and Engineering Technologies

Università di Torino
Department of Mathematics "G. Peano"

October 23, 2024

Declaration of Authorship

I, David MORSELLI, declare that this thesis titled, "Improving the effectiveness of oncolytic virotherapy: insights from mathematical modelling", submitted in fulfilment of the requirements for the Degree of Doctor of Philosophy in the Faculty of Science, Engineering and Technology of Swinburne University of Technology and in the Graduate School of Politecnico di Torino (ScuDo), and the work presented in it are my own. I confirm that:

- This work was done wholly while in candidature for a research degree at these Universities.
- No part of this thesis has previously been submitted for a degree or any other qualification at these Universities or any other institution.
- Where I have consulted the published work of others, this is always clearly attributed.
- Where I have quoted from the work of others, the source is always given. With the exception of such quotations, this thesis is entirely my own work.
- I warrant that I have obtained, where necessary, permission from the copyright owners to use any third party copyright material reproduced in the thesis (such as artwork, images, unpublished documents), or to use any of my own published work (such as journal articles) in which the copyright is held by another party (such as publisher, co-author).
- I have acknowledged all main sources of help.
- Where the thesis is based on work done by myself jointly with others, I have made clear exactly what was done by others and what I have contributed myself.

Signed: **David Morselli**

Date: October 23, 2024

Abstract

Oncolytic viruses are viral particles that specifically infect cancer cells, while mostly preserving healthy tissues. Their use as cancer treatment has received considerable attention in recent years, but their clinical use still faces many challenges. Some of the main obstacles to the propagation of oncolytic viruses inside a tumour include clearance by the immune system, physical obstacles (such as the extracellular matrix) and inhibition of the infection in hypoxic areas. Furthermore, stochastic events may play a central role in blocking viral infection. All these dynamics are still poorly understood from the biological point of view and the use of mathematical models could help to reach a more comprehensive understanding. The main aim of this thesis is to develop mathematical models to study spatial dynamics of infections by oncolytic viruses and obstacles to its diffusion, with a special emphasis on the role of stochastic events.

Furthermore, in the last Chapter, we describe a hybrid mathematical framework whose application is not exclusive to oncolytic virotherapy. This framework adopts either a pointwise or a density-based description for the cells, according to their phenotype: transitions between the two descriptions are assumed to happen stochastically and are affected by environmental conditions and gene expression; thus, the model is hybrid, but not necessarily multiscale. This modelling framework could help reproduce phenomena such as epithelial-to-mesenchymal transitions, metastasis and, in the future, evaluate the effect of an oncolytic viral infection on these phenomena.

Publications from this Thesis

1. G. Chiari, M. E. Delitala, **D. Morselli**, M. Scianna (2022). "A hybrid modeling environment to describe aggregates of cells heterogeneous for genotype and behavior with possible phenotypic transitions." In: *International Journal of Non-Linear Mechanics* 144, p. 104063. DOI: 10.1016/j.ijnonlinmec.2022.104063.

2. **D. Morselli**, M. E. Delitala, F. Frascoli (2023). "Agent-based and continuum models for spatial dynamics of infection by oncolytic viruses." In: *Bulletin of Mathematical Biology* 85.92. DOI: 10.1007/s11538-023-01192-x.

3. **D. Morselli**, M. E. Delitala, A. L. Jenner, F. Frascoli (2024). "A hybrid discrete-continuum modelling approach for the interactions of the immune system with oncolytic viral infections." Preprint. DOI: 10.48550/arXiv.2404.06459.

4. **D. Morselli**, G. Chiari, M. E. Delitala, F. Frascoli (2024). "A phenotype-structured mathematical model for the influence of hypoxia on oncolytic virotherapy". Preprint. DOI: 10.48550/arXiv.2411.02413.

Contents

List of Figures

List of Tables

List of Abbreviations

BiTE	**Bi**specific **T**-cell **E**ngager
CAR-T	**C**himeric **A**ntigen **R**eceptor **T**-cells
DNA	**D**eoxyribo**n**ucleic **A**cid
ECM	Extra**c**ellular **M**atrix
EMT	Epithelial-to-**M**esenchymal **T**ransition
GoG	**G**o **o**r **G**row
HGF	**H**epatocyte **G**rowth **F**actor
HIF	**H**ypoxia-**I**nducible **F**actor **1**
ICI	**I**mmune **C**heckpoint **I**nhibitors
TME	**T**umour **M**icro**e**nvironment
ODE	**O**rdinary **D**ifferential **E**quation
OV	**O**ncolytic **V**iruses
PD-1	**P**rogrammed cell **D**eath **1**
PDE	**P**artial **D**ifferential **E**quation
PIDE	**P**artial **I**ntegro-**D**ifferential **E**quation
PD-L1	**P**rogrammed cell **D**eath **L**igand **1**
VEGF	**V**ascular **E**ndothelial **G**rowth **F**actor

1 Introduction

The healthy life of multicellular beings is based on the cooperation among a very large number of cells. When this cooperation is disrupted, cells proliferate uncontrolled and uncoordinated; this may lead to the invasion of adjacent tissues and, eventually, to the death of the whole organism. This disease is known as cancer.

Cancer develops as the result of an accumulation of several mutations, which can be seen as an evolutionary process: random genetic mutations may occasionally lead to the creation of a fitter variant, which then originates the new predominant population as a result of its selective advantage (Nowell, 1976). Different kinds of cancers are clearly characterised by different sets of mutations and it would be very difficult to understand within a unitary framework the wide variety of molecular processes affected. Despite this huge complexity, it is believed that a few common hallmarks characterise every kind of cancer growth, irrespective of the specific underlying biological processes (Hanahan and Weinberg, 2000; Hanahan and Weinberg, 2011; Hanahan, 2022). Indeed, some traits allow cancer cells to overcome the body's natural defences against unregulated proliferation and must, therefore, be acquired in some way by all tumours.

In this view, some of the primary tumour dynamics appear understandable in terms of a small number of underlying principles, which are easier to include in mathematical models than detailed molecular processes (although the specific level of detail that should be included in the model varies significantly in relation to the phenomenon under investigation). In the last decades, it has become clear that often experimental results cannot distinguish between reasonable hypotheses about the dynamics underlying the development of tumours and a mathematical mechanistic model could allow to gain deeper insights (Araujo and McElwain, 2004; Byrne et al., 2006; Byrne, 2010). Indeed, the translation of a verbal hypothesis in mathematical terms and the theoretical analysis of its consequences can act as a *proof of concept*: logical verbal chains may hide critical assumptions and some counter-intuitive predictions may be hard to guess without the use of the mathematical formalism (Servedio et al., 2014).

Mathematical models can also be used to suggest optimal cancer therapies before their clinical application, taking into account toxic side effects and the emergence of drug resistance (Kuznetsov et al., 2021). In recent years, it has become increasingly important to use targeted therapies that attack cancer cells while mostly sparing healthy tissues (such as small molecule inhibitors, immunotherapy and oncolytic virotherapy); mathematical models could be particularly beneficial in this promising field to optimise the combination of different therapies and limit the therapeutical protocols that should undergo clinical tests (we refer to Engeland et al., 2022 for a review of the current situation in relation to immunovirotherapy). It is essential to observe that, in mathematical oncology, a good quantitative description of the phenomena under investigation may not always be the ideal goal: indeed, a correct outcome classification that serves as a base for decision-making is often more important (Enderling and Wolkenhauer, 2021).

This Chapter is organised as follows. In Section 1.1, we briefly review some fundamental aspects of cancer biology and its most common therapies, with a particular focus on oncolytic viruses (OV); this provides the background for the rest of the thesis. In

Section 1.2, we recall some general approaches to mathematical modelling in biology. In Section 1.3, we review the mathematical literature related to oncolytic virotherapy. In Section 1.4, we briefly mention some mathematical models of interactions between cancer and the immune system; we then explain how these approaches can be extended to include oncolytic viruses. In Section 1.5, we review the mathematical literature related to hypoxia and its influence on cancer therapies. Finally, in Section 1.6, we describe the organisation of the rest of the thesis and highlight the main contributions of the thesis. Throughout the Chapter, some text boxes explain how the ideas presented relate to other parts of the thesis.

1.1 Some remarks on the biological background

The vast majority of PhD theses in mathematical biology begin by quoting the World Health Organisation about statistics on cancer incidence. We refrain from that and assume that the reader is already familiar with the concept that "cancer is bad and should be cured". Instead, we restrict our attention to the biological aspects that are more relevant to the models developed in the rest of the thesis. Here, we give a general overview without the aim of being comprehensive; additional details will be provided in relation to specific mathematical models. We first describe the main cancer features, focusing on the well-known *hallmarks* and therapies. We then introduce oncolytic virotherapy and explain the main obstacles this targeted therapy faces. Finally, we give an overview of cancer-immune interactions and the ways to enhance immune response through immunotherapy.

1.1.1 Cancer development

The above-mentioned theses usually continue by explaining the *hallmarks of cancer* introduced in Hanahan and Weinberg, 2000, later expanded in Hanahan and Weinberg, 2011 and then further increased in Hanahan, 2022. Although the reader is probably also familiar with them, it is still worth recalling some of these concepts, as they justify the phenomenological modelling of cancer with relatively simple mathematical equations that neglect specific molecular pathways; furthermore, this serves as a background to the rest of the biological introduction. Fig. 1.1 therefore lists the *hallmarks* that, according to Hanahan and Weinberg, most (if not all) human tumours share in common. We now review the more relevant ones to our interests, focusing also on some collateral aspects that are not directly incorporated in the hallmarks.

Evolutionary aspects: genome instability and mutation As previously mentioned, the development of cancer requires the sequential accumulation over time of several mutations, which confer some growth advantage with respect to healthy cells (Nowell, 1976): in this respect, it can be seen as an evolutionary process driven by Darwinian natural selection, with multiple clonal expansions triggered by the acquisition of a fitter genotype. Healthy cells have several mechanisms to keep the spontaneous mutation rate low; hence, in cancer cells, the evolution is facilitated by a breakdown in the genomic maintenance machinery, which increases the rate of mutations.

The genomic instability also causes a certain degree of intratumoral genetic heterogeneity. However, it is important to keep in mind that tumour heterogeneity is not restricted to genetic mutations: it has been shown that malignant cells within the same mass exhibit different behaviour despite carrying the same genetic alterations (Marusyk et al., 2012).

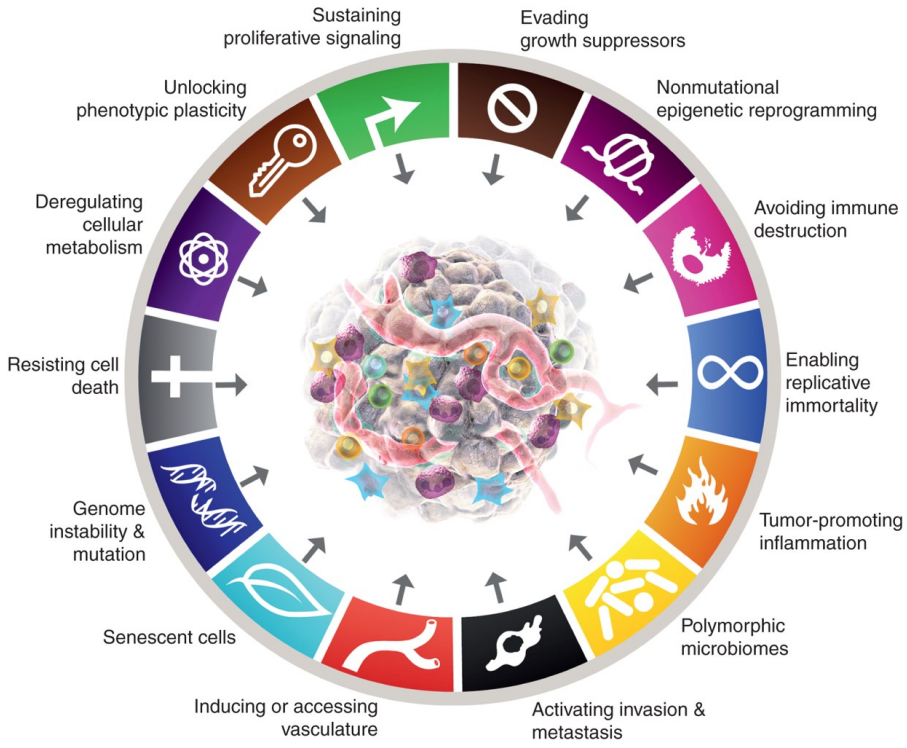

FIGURE 1.1: Schematic representation of the full list of *hallmarks of cancer*. Reprinted from Hanahan, 2022 by permission from the American Association for Cancer Research (license number: 5803560059863).

Ecological aspects: inducing or accessing vasculature The tumour microenvironment (TME) plays a central role in determining cellular behaviour (Palumbo et al., 2015; Sonugür and Akbulut, 2019). It can be seen as an ecosystem containing both evolving cancer cell populations and multiple host components, including immune cells, blood and lymphatic vessels, and extracellular matrices. Furthermore, nutrients such as oxygen and glucose are fundamental for cell function and survival. The physiological vasculature is clearly unable to sustain uncontrolled cell proliferation, hence most tumours are characterised by *hypoxia* (i.e., lack of oxygen); this condition is also involved in the acquisition of several other hallmarks by cancer cells (Ruan et al., 2009). The growth of a large tumour mass requires the formation of new blood vessels that enable nutrient delivery (a process known as *angiogenesis*). The spatially heterogeneous distribution of intratumoral blood vessels contributes to the development of different phenotypes in different areas: its role has been compared to the one of rivers in deserts, in which a riparian habitat establishes close to the river, in sharp contrast with the surrounding habitat. Microenvironmental conditions are modified by the tumour in several other ways (e.g., pH reduction and degradation of the extracellular matrix) in a way that resembles niche construction in ecology (Laland et al., 2016).

Phenotypic heterogeneity: nonmutational epigenetic reprogramming, deregulating cellular metabolism, unlocking phenotypic plasticity Cells exhibiting different sequences of genes and/or phenotypic determinants have been found in several types of tumours, including breast cancer (Al-Hajj et al., 2003), colorectal cancer (O'Brien et al., 2007), brain cancer (Singh et al., 2004), and prostate cancer (Collins et al., 2005). In the just-described ecological view, this is partially due to the fact that the development of cancer cells is affected by the surrounding molecular landscape, which is, in turn, actively influenced by those cells in a feedback/feedforward fashion. The adaptation

to the microenvironmental conditions is only minimally caused by genetic mutations and mostly follows other pathways such as phenotypic plasticity and nonmutational epigenetic reprogramming.

Phenotypic plasticity allows some cancer cells to evade the state of terminal differentiation and either go back to a progenitor-like cell state or switch to an entirely different developmental programme (Hanahan, 2022). The switch between alternative phenotypic states may occur spontaneously or in response to ecological inputs. For example, nutrient-deprived malignant individuals activate downstream pathways that result in a shift towards more aggressive behaviour. These cells lose epithelial characteristics, such as high adhesiveness and high duplication capacity, and acquire mesenchymal features, such as enhanced motility, which allow them to invade surrounding tissue more effectively. This phenomenon, denoted as *epithelial-to-mesenchimal transition* (EMT), is also involved in physiological scenarios, such as morphogenesis and organogenesis. The inverse process may also occur: tumour cells with mesenchymal determinants can lose their migratory freedom and re-acquire epithelial hallmarks, including expression of junctional proteins, when experiencing a sufficient level of environmental substrates (Nieto et al., 2016).

> The modelling of EMT is the main focus of Chapter 6.

The word *epimutation* refers to heritable modifications in gene expressions not associated with changes in the deoxyribonucleic acid (DNA) sequences (Oey and Whitelaw, 2014). Its role in embryonic development, differentiation and organogenesis is well-established; recent evidence suggests that it also contributes to the acquisition of cancer hallmarks, especially in the context of metabolic reprogramming in adaptation to hypoxia and EMT transition (Hanahan, 2022).

A common feature in the eco-evolutionary is the need for individuals to perform multiple tasks; the limited amount of resources available implies that not all of them can be optimised simultaneously. This leads to *trade-offs* between the different abilities, in the sense that the increase of a specific ability corresponds to the decrease of a distinct trait; consequently, the fittest population depends on the particular situation that is modelled. Trade-offs are well-documented in the context of cancer (Aktipis et al., 2013; Boddy et al., 2018; Hausser and Alon, 2020; Jacqueline et al., 2017). Specific examples will be introduced later, in the context of the modelling of infections (Section 1.3.3) and hypoxia (Section 1.5).

We remark that it is not trivial to understand all these features just from experimental evidence; hence, the use of mathematical models could allow for deeper insights.

Activating invasion and metastasis Some tumour cells often acquire the ability to invade adjacent tissues in search of new areas of the body with more nutrients and fewer space restrictions; this colonisation may result in the formation of a *metastasis*, a distant cancer settlement with properties similar to the primary tumour. Invasion and metastasis are closely allied processes which utilise similar operational strategies (Hanahan and Weinberg, 2000): in this respect, they somehow resemble the previously described EMT. Although metastases are not explicitly modelled in the rest of the thesis, it is still worth mentioning them due to their central role in human cancer deaths.

Avoiding immune destruction and tumour-promoting inflammation The immune system constantly monitors tissues to eradicate malignant mutations; therefore, a tumour can develop only if it finds some way to evade immune destruction (Hanahan and Weinberg, 2011). Due to its relevance in the rest of the thesis, we will describe

cancer-immune interactions in more detail in Section 1.1.3. We here limit our attention to the fact that tumour-associated inflammatory response may have the paradoxical effect of enhancing tumour progression by facilitating the acquisition of other hallmark capabilities (Hanahan and Weinberg, 2011).

Therapies Some classical cancer therapies include (Abbas and Rehman, 2018):

- *surgical removal* of the tumour;
- *radiotherapy*, which uses radiation to damage the DNA of cancer cells to stop their replication;
- *chemotherapy*, which consists of the injection of toxic chemical agents able to target a specific phase of the cell cycle to induce cell death;
- *hormone therapy*, which relies on the fact that several tumours need hormonal stimuli to develop.

All those therapies are not specifically targeted against cancer cells; hence, they cause relevant side effects. As a consequence, in recent years, the attention has been shifting to therapies that do not harm healthy tissues significantly: two notable examples are *anti-angiogenic therapy* (which aims at cutting off the blood supply to the tumour cells) and *small-molecules inhibitors* (which target specific molecular defects of cancer cells).

In this thesis, we focus on two other targeted therapies, namely *oncolytic virotherapy* and *immunotherapy*.

Therapies may vary their effectiveness on different tumour subpopulations: for example, the adaptation to hypoxia is often associated with an increased resistance to therapies (see also Section 1.5). Furthermore, therapeutic agents substantially modify the fitness landscape and favour the emergence of resistant clones. Therefore, a good comprehension of the phenotypic composition of a tumour is a critical factor for the optimisation of the therapy in a patient-specific approach; evolutionarily informed strategies could keep the resistant population under control by allowing the survival of a significant population of sensitive cells, with the aim to control the tumour rather than eradicate it (Gatenby and Brown, 2020). The use of mathematical models could be beneficial for the development of such strategies.

1.1.2 Oncolytic virotherapy

As anticipated, the main focus of the thesis is oncolytic virotherapy. Oncolytic viruses constitute a targeted cancer therapy, which uses viral particles preferentially infecting tumour cells while mostly sparing healthy tissues (Blanchette and Teodoro, 2023; Fountzilas et al., 2017; Kelly and Russell, 2007; Lawler et al., 2017; Russell and Peng, 2018). The two main delivery routes for the virus are intratumoral injection and intravenous administration (Jin et al., 2021). Viral particles are genetically modified to infect cells through receptors highly expressed in tumours (Lawler et al., 2017); virus-infected cells then burst due to lysis and release a high number of new viral particles, which can infect neighbouring cells. The infection can often stimulate an antitumour immune response, contributing to the treatment or, in some cases, hindering an efficient viral diffusion. The potential of this therapy has been recognised for a long time and in recent years the clinical use of some oncolytic viruses has been approved, with several clinical trials still ongoing (Blanchette and Teodoro, 2023). In 2005, the Chinese State Food and Drug

Administration approved for the first time in the word the clinical use of an oncolytic virus to treat head and neck cancers (Garber, 2006). A different oncolytic virus was approved by the United States of America Food and Drug Administration in patients with accessible and unresectable melanomas; this therapy was later also approved in Europe, Australia and Israel (Shalhout et al., 2023). Nevertheless, there are still many challenges that prevent the systematic use of this treatment. The difficulties in creating a set of rules and practises that make this therapy reliable, reproducible and clinically mainstream may also be associated with "stochastic", hard-to-predict events, which affect consistency in viral delivery, tumour invasion, viral replication and diffusion. Here, we review the basic biological facts about oncolytic viruses and the main problems that prevent the success of virotherapy, which will be analysed in the thesis using suitable mathematical models.

Dynamics of viral infections As we already mentioned, the therapy's key aspect is that the viral infection occurs through receptors highly expressed on cancer cells (Lawler et al., 2017). However, the exact mechanisms of the infection are not entirely understood. In general, viruses enter target cells with a combination of dynamics, whose effectiveness depends on several factors (Kalia and Jameel, 2011). In recent years, it has also become clear that some viruses (such as human immunodeficiency virus type 1 and hepatitis C virus) may infect both through direct cell-to-cell transmission and cell-free transmission mediated by diffusing *virions* (i.e., free viral particles outside cells); the actual combination of the two processes is hard to establish in full detail (see Graw and Perelson, 2016 and the references therein). There are also newly investigated mechanisms that allow cell-to-cell transmission: for example, some viruses, such as the influenza virus, might exploit tunnelling nanotubes between cells (Kumar et al., 2017).

In the specific case of oncolytic viruses, there are several obstacles to viral diffusion in the tumour microenvironment, as we explain in the following paragraphs: it is therefore likely that most of the time, the infection is mainly driven by cell-to-cell contact and close-range free virions. Effective ways to enhance viral delivery and improve their circulation are currently under study (Hill and Carlisle, 2019).

Interactions with the tumour microenvironment: extracellular matrix, immune system and hypoxia As previously highlighted, the tumour microenvironment is crucial in shaping cancer evolution. It is now clear that it also influences viral infections in several ways.

First, physical obstacles, such as the extracellular matrix (ECM), inhibit viral diffusion due to the increased pressure, the interlocked meshwork of secreted proteins and cellular tight junctions (Jin et al., 2021; Wojton and Kaur, 2010). Indeed, the administration of ECM-degrading enzymes improves viral diffusion in the tumour, but it is essential to consider that the destruction of cellular junctions poses some concerns regarding an increased likelihood for cells to metastasise.

> One of the models studied in Chapter 2 implicitly considers these obstacles in viral intratumoral diffusion.

Secondly, the interplay between oncolytic viruses and immune cells is among the most complex aspects that involve the microenvironment. Its influence on the therapeutic outcome is twofold: oncolytic viruses can stimulate immune cells, not only against viral particles but also against tumour cells; on the other hand, an immune response that targets the oncolytic virus may prevent an effective infection in the whole tumour, making virotherapy inefficient (Filley and Dey, 2017; Shi et al., 2020). A complete shutdown of

the immune response is clearly unfeasible in any realistic scenario; even if possible, it would not be amenable to stop the antitumour action of the immune system stimulated by the virus. This suggests that the strength of the immune response should be adapted and regulated as much as possible in order to optimise the outcome and immunotherapy is a natural tool for this goal. This concept will be further elucidated in the following subsection after a brief review of the interactions between cancer and the immune system in a general context.

Another interesting interaction involves the neovasculature that the tumour originates through angiogenesis: most oncolytic viruses disrupt it by targeting tumour-associated vascular endothelial cells (Jin et al., 2021; Wojton and Kaur, 2010). On the one hand, the decrease in nutrient inflow contributes to slowing down cancer growth and, in this respect, oncolytic virotherapy could act in the same way as antiangiogenic therapy. On the other hand, blood vessels also play a vital role in the arrival of viral particles and immune cells. It is also important to take into account the role of hypoxia, which is twofold: in general, hypoxic cells have a slower metabolic activity, which results in a slower infection; nonetheless, some particular oncolytic viruses are able to specifically target receptors that are upregulated in case of the lack of oxygen (Sadri et al., 2023; Sheng Guo, 2011). The best strategy appears to be the vasculature's normalisation so that viral particles and immune cells can regularly penetrate the tumour, the risk of severe hypoxia and acidosis is decreased and, at the same time, anomalous vessels are reverted towards more physiological phenotypes (Santry et al., 2020).

The role of hypoxia on oncolytic viral infections is studied in Chapter 5.

Combination with other therapies For all the reasons we just explained, virotherapy cannot eradicate a tumour alone in most cases. Consequently, most current efforts are devoted toward its combination with other therapies (Martin and Bell, 2018; Ottolino-Perry et al., 2010). One of the most promising of such combinations is with immunotherapies (Engeland et al., 2022), as already mentioned and further explained shortly. We remark that OV may also be combined with chemotherapy (Binz and Lauer, 2015) and radiotherapy (Touchefeu et al., 2012), with viruses often used to deliver molecules that enhance the other therapy; furthermore, the fact that the two therapies are mediated by different pathways allows them to act synergistically. In light of the difficulties of standard therapies to be effective in hypoxic tumours, the combination with viruses that specifically target those cells could be particularly beneficial (Sheng Guo, 2011).

1.1.3 Immunotherapy and immunovirotherapy

From the previous discussion, it is clear that the study of oncolytic virotherapy cannot ignore the immune component. We first review some elementary aspects of the immune system, its response against cancer cells and how tumours avoid immune destruction. We then explain how the most common immunotherapies enhance the immune response and the role that oncolytic viruses may play in this context through the so-called immunovirotherapy.

Overview of the immune system and antitumour immune response The functioning of the immune system is highly complex and the models presented in this thesis rely just on very elementary assumptions. Hence, we here restrict our attention to a few essential features. Broadly speaking, there are two types of immune systems: the *innate immune system*, involving cells such as natural killers, macrophages and dendritic cells, is the first

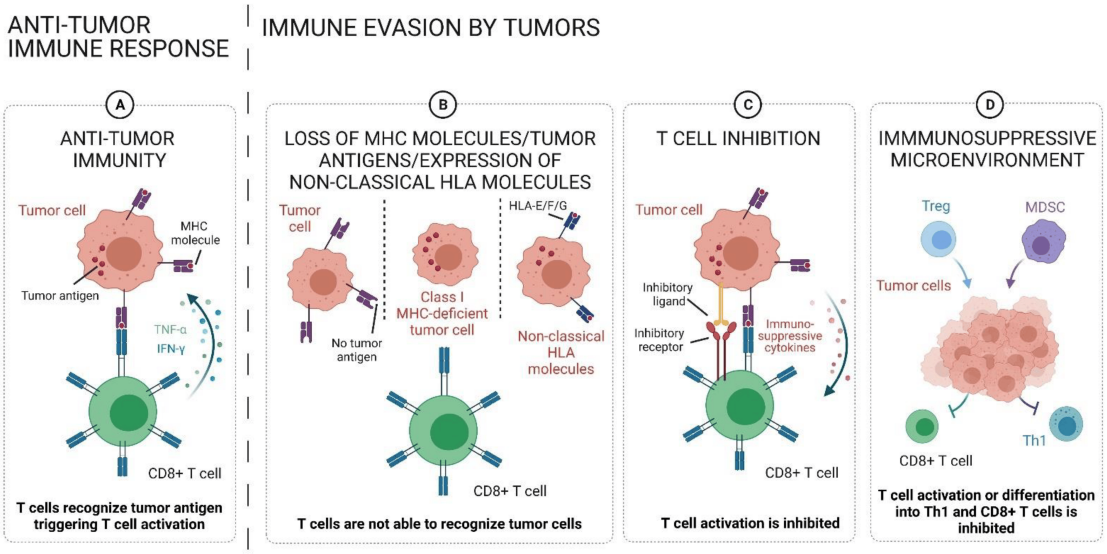

FIGURE 1.2: Schematic representation of the immune response against cancer and immunoevasion in the context of $CD8^+$ T-cells. (a) The $CD8^+$ T-cells recognise the *major histocompatibility complex* (MHC) molecules of a cancer cell and bind through the *T cell receptor*. (b) Some cancer cells may lose their tumour antigen or downregulate the expression of MHC, hence avoiding immune recognition. (c) The expression of an inhibitory ligand or the presence of immunosuppressive cytokines stops immune killing. (d) $CD8^+$ T-cells are suppressed by *regulatory T-cells* (T-reg) or *myeloid-derived suppressor cells* (MDCSs). Reprinted from Pansy et al., 2021 by permission from MDPI (CC BY license).

line of defence and does not require any specific activation; the *adaptive immune system*, involving B-cells and T-cells (also called *lymphocytes*), needs to be specifically activated to target a specific *antigen* (i.e., a molecule or a protein that characterises the substance that needs to be eliminated) and its ability to recognise that antigen is maintained as time passes (Chaplin, 2010). The activation of adaptive immune cells is mediated by *antigen presenting cells*, a role that can be played by both innate immune cells (macrophages and dendritic cells) and adaptive immune cells ($CD4^+$ helper T-cells). In the context of tumour-immune interactions, the most relevant cells are $CD8^+$ killer T-cells, which use their *T-cell receptor* to bind with the *major histocompatibility complex* molecules of a cancer cell and kill it, as depicted in Fig. 1.2a (Pansy et al., 2021). The movement of T-cells is guided by small proteins called *chemokines*; because of their role, we refer to them with the generic term *chemoattractant*. We also mention the existence of a third class of T-cells, namely *regulatory T-cells* (T-reg): their role is to down-modulate the immune response when needed.

Immunoediting As we already mentioned, the appearance of dangerous mutations in cells is usually recognised by immune cells, which kill the mutants and prevent their overproliferation. As a consequence, a malignant tumour cannot develop unless it manages to avoid the immune action: this process is known as *immunoediting* and it involves the three stages of elimination, equilibrium and escape (Dunn et al., 2002). Figs. 1.2b-d summarise the main mechanisms that a tumour uses to achieve immune escape: loss of major histocompatibility complex molecules or antigens; expression of inhibitory ligands; presence of immunosuppressive cells in the tumour microenvironment (Pansy et al., 2021). These last two mechanisms are fundamental for cell tolerance in physiological situations and allow all healthy tissues to avoid immune killing.

These strategies can be combined in several ways and result in different degrees of immune infiltration. In Galon and Bruni, 2019, starting from these considerations, the

authors proposed the classification of tumours in four categories:

hot: the tumour is infiltrated by a large number of T-cells and the immunosuppression is mostly due to immune checkpoints;

altered-immunosuppressed: the tumour is poorly infiltrated (although some T-cells are present) due to an immunosuppressive environment rich in T-reg and MDSC, and tumour cells express immune checkpoints;

altered-excluded: T-cells accumulate at the tumour border without being able to infiltrate due to poor vascularisation (and, consequently, hypoxia), physical barriers and lack of T-cell recruiting chemokines;

cold: absence of T-cells in the tumour microenvironment and its surroundings due to low mutational burden and poor tumour antigen presentation.

Immunotherapies Immunotherapy aims to overcome the tumour's evasion strategies and enhance the immune response. A first way to do so is a direct increase of the quantity of $CD8^+$ T-cells that can target the tumour. In this respect, *adoptive T-cell transfer* consists in culturing the patient's immune cells that target specific tumour antigens and then reinjecting them at the tumour site: while the use of the patient's own immune cells minimises side effects, the isolation of the right kind of T-cells poses some challenges; furthermore, transferred T-cells may lack sufficient specificity or be too few to completely reject a tumour (Fesnak et al., 2016). An alternative approach requires genetic manipulation of T-cells to enhance antigen recognition: the most common approach involves the *chimeric antigen receptor* (CAR), which combines antigen-binding and T-cell activation in a single receptor (Wang and Rivière, 2016). Both strategies pose the concern of overactivation of the immune system, which may harm healthy cells (Gross and Eshhar, 2016).

Alternatively, other immunotherapies enhance the cytotoxic action. For example, *immune checkpoint inhibitors* (ICI) bind to receptors that suppress the immune response, such as programmed cell death 1 (PD-1) on cancer cells and the programmed cell death ligand 1 (PD-L1) on immune cells; in this way, co-inhibitory signalling pathways are interrupted and immune-mediated elimination of tumour cells is promoted (Darvin et al., 2018). The proliferation and activation of immune cells can also be enhanced using bispecific T-cell engagers (BiTEs), bispecific proteins with two linked *single-chain variable fragments*, which target respectively immune and cancer cells (Slaney et al., 2018).

Despite some relevant successes, immunotherapies still fail to show substantial benefits in many situations. It appears that the mechanisms of resistance to immunotherapy are analogous to the ones employed in the starting stage of a tumour to achieve evasion from the physiological immune response (O'Donnell et al., 2018). As a consequence, the most effective type of immunotherapy highly depends on the degree of immune infiltration in a given tumour; the choice of the best therapeutic approach should, therefore, be based on the knowledge of immune-related features (such as the ones involved in the previously described characterisation) and could involve the combination of different strategies.

Immunovirotherapy Oncolytic viruses could be seen as a specific case of immunotherapy because of their ability to activate the immune system. It is, therefore, natural to explore how to best combine the viral infection with other kinds of immunotherapies. A first strategy involves using oncolytic viruses as adjuvants of other therapies: indeed, the lysis of infected cells increases the release of tumour antigens, helping to turn a

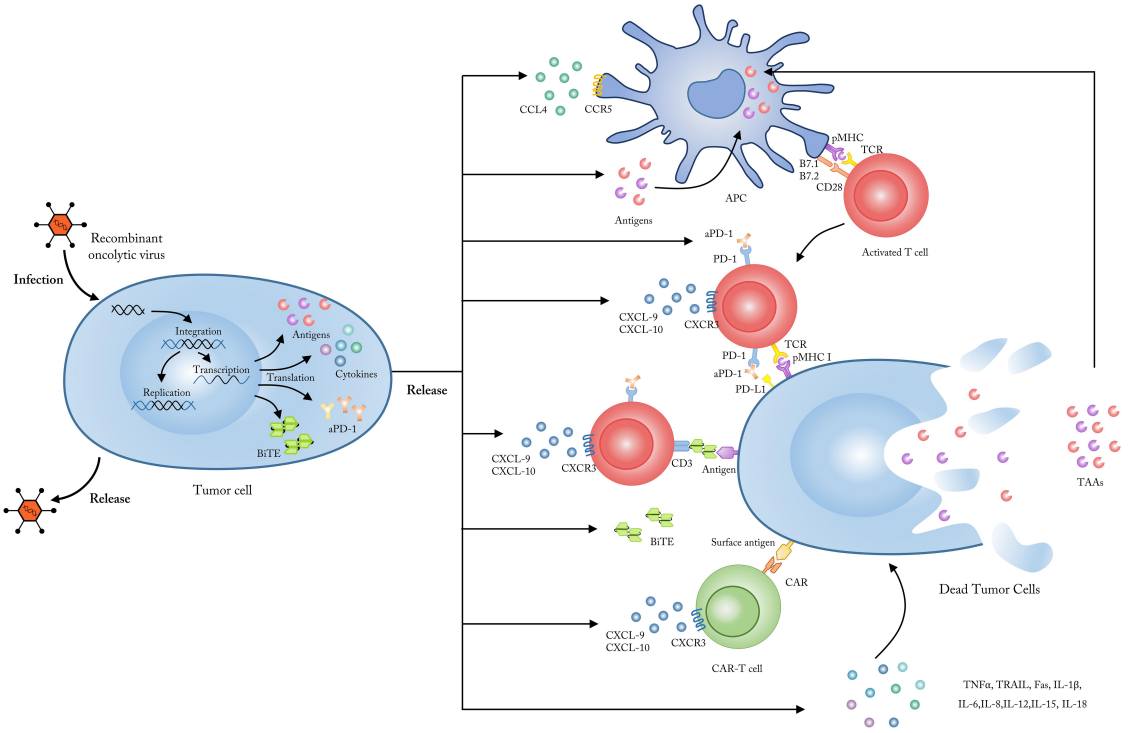

FIGURE 1.3: Schematic representation of different ways in which oncolytic viruses can be used as genetic vectors to enhance immune response. Reprinted from Shi et al., 2020 by permission from Frontiers (CC BY license).

cold tumour into a hot one (Shi et al., 2020). A less intuitive contribution of oncolytic virotherapy involves the genetic modification of the virus to make infected cells produce and secret specific molecules (such as, but not limited to, antigens, checkpoint inhibitors and BiTEs). Some examples of this process are depicted in Fig. 1.3. Again, we remark that the appropriate type of combination therapy is highly dependent on the features of the target tumour.

> In Chapter 3, we analyse the influence of virotherapy on the immune response and suggest some strategies of immune enhancement that could be beneficial for tumour eradication.

1.2 Some general remarks about mathematical modelling in biology

1.2.1 Discrete and continuous approaches

An important starting point of any model is the choice of the most suitable mathematical tools, depending on the spatiotemporal scale of the phenomenon under investigation and on whether stochasticity plays an any role. The main distinction is between discrete, continuum or hybrid models: although this division applies to all mathematical models, for the sake of simplicity, we focus on the modelling approaches for cells.

In a discrete setting, every cell is an individual agent and its evolution is described by some rules, which may be either deterministic or stochastic. In lattice-based models, individuals are constrained to move on the points of a given discrete lattice; conversely, in lattice-free models, individuals do not have such a constraint and can occupy any point in space.

In a continuum setting, cells are not modelled at the individual level because larger volume fractions are considered. The most basic continuous models involve ordinary differential equations (ODEs), which allow the description of a discrete set of homogeneous cell populations. On the other hand, partial differential equations (PDEs) consider a population's heterogeneity using continuous *structuring variables*, which may represent space, size, age or phenotype.

Discrete individual-based models allow to include randomness in the processes easily, but are also associated with higher computational costs and do not allow to easily obtain analytical results. On the other hand, continuum models are amenable both to numerical simulations and analytical results but cannot easily include stochastic events; furthermore, the phenomenological assumptions commonly used in this approach may also hinder the biological interpretation of the mathematical assumptions. For these reasons, in recent years, the derivation of continuum macroscopic models from underlying discrete stochastic models has attracted the attention of an increasing number of researchers (see, for example, Champagnat and Méléard, 2007; Johnston et al., 2015; Lorenzi et al., 2020; Macfarlane et al., 2022; Penington et al., 2011; we refer to the introduction of Chaplain et al., 2020 for a more comprehensive literature review). Some standard techniques include mean-field limits (Carrillo et al., 2010), heuristic laws of large numbers (Capasso and Morale, 2009), or coarse-graining procedures (Drasdo, 2005); macroscopic formulations have also been derived by selected lattice-gas cellular automata (LGCA) in Bottger et al., 2012. The comparison between a discrete model and its continuous counterpart allows us to understand clearly the modelling assumptions for a continuum model, gain some theoretical intuition on the behaviour of an individual-based model and, as a consequence, reach a more comprehensive understanding of the biological system under study.

This approach is used in Chapters 2, 3 and 4.

Finally, some models combine discrete and continuum descriptions and are thus defined as hybrid models. In most cases, the "discrete vs. continuous" dichotomy refers to the spatial scale at which the system is modelled: for example, cells are described as discrete individuals, while chemical elements such as oxygen and nutrients are described as continuous functions of time and space. An alternative approach relates the mathematical description to cells' behaviours, as described below.

1.2.2 Mathematical models of heterogeneous cell populations and phenotypic switch

As a first approximation, cells are usually modelled as indistinguishable individuals that evolve according to a unique set of rules. However, in many situations, it is important to take into account heterogeneous behaviours due to differences at the genetic, epigenetic and/or phenotypic levels and even allow for transitions among different classes. In the context of cancer, cell plasticity has been extensively studied (Weerasinghe et al., 2019). We now briefly recall some classical approaches relevant to this thesis' models; we here present them in a general framework: the application in specific settings will be presented in the following (both in other sections of the current chapter and in Chapters 4, 5 and 6).

Discrete compartments The most elementary approach to modelling heterogeneous populations is to structure them in discrete compartments, which evolve according to different rules. For instance, in individual-based/cellular automata models, each single

cell is allowed to vary a label indicating its actual phenotype, as in the case of the well-celebrated Cellular Potts Model (see Scianna and Preziosi, 2012 and the references therein). Furthermore, models based on a continuous cell description (also in the framework of the Theory of Mixtures) instead typically associate to each subpopulation a distinct density function (as in Giverso et al., 2022): phenotypic conversions are then implemented by mass exchanging terms included in the evolution equations for cell dynamics, as done for instance in Wise et al., 2008. Finally, we note that hybrid approaches (in which the discrete setting is used for all cell dynamics while the continuous description is adopted for microenvironmental dynamics) allow the description of different phenotypes with different discrete populations, as done in Anderson et al., 2006.

A less common approach consists of choosing the most suitable mathematical representation for cells in different compartments based on their phenotypes, as first proposed in Colombi et al., 2017; Scianna and Colombi, 2017. In this context, cells are described either as discrete agents or through a continuous density function depending on their behaviour. Consequently, the "discrete vs. continuous" dichotomy does not refer to the spatial scale at which the system is modelled. Indeed, a pointwise description is, in fact, more appropriate for *specialised/activated/highly metabolic* cells or for cells with *mesenchymal* determinants, i.e., with the ability to undergo individual directional movement in response to environmental cues; on the other hand, a density-based representation, characterised by a lower level of individual detail, is more suitable for *non-specialised/quiescent/poorly metabolic* cell ensembles or for cells with *epithelial* determinants, i.e., which undergo collective dynamics mainly guided by intercellular communication. Furthermore, in principles, both mathematical descriptions may be associated with multiple compartments. It is also possible to model transitions between the two descriptive instances by the definition of a bubble function that represents a plausible spatial distribution of the mass of a single individual (Colombi et al., 2017; Scianna and Colombi, 2017).

> In Chapter 6, we present an extension of this modelling framework that considers phenotypic conversions triggered by environmental signals, dependent on cell genetic traits and affected by randomness.

Continuous trait variable A common alternative approach involves a population $u(t,y)$ structured on a continuous trait variable $y \in Y$, which may be referred to either genotype or behavioural determinants (we here restrict to a scalar variable, although the generalisation to higher dimensions is straight-forward). Its evolution is usually described by a partial integro-differential equation (PIDE) of the form

$$\partial_t u(t,y) = D_y \partial^2_{yy} u(t,y) + R\Big(y, \int_Y u(t,y)\,\mathrm{d}y\Big) u(t,y) \tag{1.1}$$

where the diffusion term on the trait domain models random changes in the trait and the dependence on the total density $\rho(t) := \int_Y u(t,y)\,\mathrm{d}y$ represents the competition for limited resources; the growth rate R can be interpreted as the fitness landscape. The growth rate typically takes the form

$$R(y,\rho) := r(y) - \kappa\rho \tag{1.2}$$

where $r(y)$ is the trait-dependent proliferation rate and $-\kappa\rho$ models the interspecific competition. A common alternative is

$$R(y,\rho) := p(y)\Big(1 - \frac{\rho}{K}\Big) - \eta(y-\varphi)^2 \tag{1.3}$$

where the interspecific competition is included in the logistic growth term (with carrying capacity K) and the selection of the fittest phenotype φ is modelled through a quadratic term, with η defining the time scale at which the process takes place.

This class of models has been widely studied from the mathematical point of view; we refer to Lorenzi et al., 2024a for a review. Most of the results rely on a Hamilton–Jacobi approach (Diekmann et al., 2005; Lorz et al., 2011; Perthame, 2006; Perthame and Barles, 2008). The typical behaviour is the concentration of u on the points that maximise R as the diffusion coefficient vanishes and the time goes to infinity (Perthame, 2006). A similar result holds for $D_y = 0$, although the limit clearly depends also on the initial condition (Lorenzi and Pouchol, 2020). It is also possible to add a spatial variable and consider spatial heterogeneity, resulting in the selection of fittest traits that vary in time and space (Alfaro et al., 2013; Mirrahimi and Perthame, 2015). The spatial context allows us to account for heterogeneous cell motilities, which is particularly useful in the study of the *proliferation-migration trade-off*, also known as *Go or Growth* (GoG) (Fiandaca et al., 2022; Lorenzi et al., 2021a).

In Chapters 4, 5 we use equations analogous to Eq. (1.1): we follow the approach of Eq. (1.2) in Chapter 4 and the approach of Eq. (1.3) in Chapter 5.

The most common way to model random phenotypic transitions in this context is through a diffusion term on the trait domain, as in Eq. (1.1). We observe that some models also include a mutation drift that represents the active adaptation of an individual to the environment (Chisholm et al., 2016); however, we do not adopt this approach in this thesis.

1.3 Models of oncolytic virotherapy in the absence of immune response

1.3.1 Models without explicit viral dynamics

The most basic approach consists in modelling only uninfected cancer cells, denoted by u, and infected cancer cells, denoted by i; in this way, viral dynamics are neglected for simplicity. This mathematical formulation closely resembles models widely used in epidemiology and ecology, as explained below; consequently, it is sometimes possible to partially rely on previous analytical results on the subject.

ODE models A generic model can be written in the form

$$\begin{cases} \dfrac{\mathrm{d}u}{\mathrm{d}t} = uF(u+i) - \beta G(u,i)i \\ \dfrac{\mathrm{d}i}{\mathrm{d}t} = \beta G(u,i)i - qi \end{cases} \tag{1.4}$$

The function $F(\rho)$ with $\rho = u + i$ models cancer growth. Its most common expressions are:

- *exponential* growth: $F(\rho) = p$ (independent of ρ)
- *logistic* growth: $F(\rho) = p\left(1 - \dfrac{\rho}{K}\right)$
- *Gompertz* growth: $F(\rho) = p \ln\left(\dfrac{K}{\rho}\right)$

In all these functions, there is a parameter $p > 0$, which corresponds to the maximal proliferation rate. In the last two functions, $K > 0$ is the *carrying capacity*, with the property that $F(K) = 0$ and so the growth stops when it reaches this value. We refer to Benzekry et al., 2014; Jarrett et al., 2018; Vaghi et al., 2020 for additional examples and comparisons with experimental data.

The function G models viral infection: the most common choices are *density-dependent* infection and *frequency-dependent* infection, as we explain in the following paragraphs.

Finally, the term $-qi$ models the death of infected cells due to lysis. It is assumed that infected cancer cells do not proliferate: this may be justified by the fact that the viral infection disrupts the cellular machinery and does not allow a cell to duplicate.

The simplest form is the basic susceptible-infected (SI) epidemic model, with $F = 0$ (no growth of susceptibles) and $G(u, i) = u$ (*mass-action* or *density-dependent* infection); this corresponds to the most elementary case presented in Kermack and McKendrick, 1927. Another common form of this equation is the Lotka–Volterra model (Lotka, 1926; Volterra, 1937), which was developed in the ecological settings to model interactions between predators (in our notation i) and prey (u); the only difference with respect to the SI model is the inclusion of exponential growth of prey. A similar model considers logistic growth (see Eq. (2.14)). The behaviour of these two systems and their differences will be discussed in Section 2.3.1. We remark that, when the law of mass-action is used to model the infection, it is often convenient to scale the infection rate β by the carrying capacity K for dimensional reasons.

The other common choice for the infection term is a *frequency-dependent* function (sometimes also referred to as *ratio-dependent* function), i.e.

$$G(u, i) = \frac{u}{u + i + \delta} \tag{1.5}$$

with either $\delta = 0$ or $\delta > 0$; the latter choice allows the equation to be properly defined also when both populations vanish. This infection term models a situation in which the virus remains mostly localised, with the infection rate depending on the frequency of uninfected cells rather than their numbers; such an approach is not uncommon in the general modelling of infections (Dobson and Meagher, 1996; Holt and Roy, 2007; Roy and Holt, 2008; McCallum et al., 2001). In Berezovskaya et al., 2007; Novozhilov et al., 2006, it is shown that, if G takes this form with $\delta = 0$ and both populations experience logistic growth, then the singular equilibrium $(0, 0)$ has a non-empty basin of attraction, consisting of heteroclinic orbits. When infected cells are not allowed to proliferate, the system exhibits stable limit cycles for $\delta \geq 0$.

These models always admit $(0, 0)$ as an equilibrium, although it is often unstable. If the tumour growth saturates at carrying capacity K, then there is also an infection-free equilibrium $(K, 0)$, which may be stable or unstable depending on the forms of F and G, as well as on parameter values. In most cases there exists also a coexistence equilibrium (u^*, i^*) and in some cases stable limit cycles or homoclinic orbits may appear in some parameter ranges.

The previous discussion highlights the wide variety of behaviours that may be obtained by varying the functional form of the terms in Eq. (1.4). To overcome the strong dependence of the outcome to the specific mathematical choices, Eq. (1.4) is studied under very general assumptions in Komarova and Wodarz, 2010. Two categories of models are identified based on the infection term: *fast spread* models, with G such as in Eq. (1.5), and *slow spread* models, with G such as

$$G(u, i) = \frac{u}{(u + \delta_1)(i + \delta_2)}$$

In the former case, it is always possible to eradicate the tumour if the infection rate β is high enough, while in the latter case this may not be true. The situation $G(u,i) = i$ does not fall in this framework; this infection is faster than the one considered for fast spread. This analysis is only based on the study of the equilibria, since the authors remark that in the nonspatial settings the extinction of the tumour due to wide population oscillations is always associated with the possibility that different initial conditions lead to treatment failure.

We conclude this discussion by observing that the functional choice

$$G(u,i) = \frac{(1+\varepsilon)\beta u}{u+\varepsilon}$$

is able to correctly model HIV infection (Wodarz et al., 2014). This expression can be derived from an underlying agent-based model.

PDE models A simple way to include spatial dynamics is to consider the reaction-diffusion equation

$$\begin{cases} \partial_t u = D_u \Delta u + uF(u,i) - \beta G(u,i) i \\ \partial_t i = D_i \Delta i + \beta G(u,i) i - qi \end{cases} \tag{1.6}$$

(see, for example, Eq. (2.7)). This class of model typically admits travelling wave solutions. In the context of spatial models, the absence of the viral population models a virus that faces some challenges in propagating in the tumour microenvironment (Wojton and Kaur, 2010), so that the infection is mainly driven by cell-to-cell contact and close-range free virions, as explained in Section 1.1.2. The resulting systems fall in the category of classical spatial Lotka–Volterra models for prey and predators, which have been widely studied (Dunbar, 1984; Li, 2015; Morozov et al., 2006; Petrovskii et al., 2005; Petrovskii et al., 2002). Although from the mathematical point of view the diffusion coefficients may assume any value, in the context of oncolytic virotherapy it is usually assumed $D_u = D_i$, as a priori we have no reason to assume that the infection affects cell movement. However, we remark that, in some situations, higher motility of infected cells could be interpreted as a phenomenological way to incorporate some additional viral diffusion indirectly; we refer to Section 2.4.4 for further discussions.

An interesting variation of Eq. (1.6) is obtained by replacing the standard diffusion with pressure-driven movement, leading to the equation

$$\begin{cases} \partial_t u = D_u \nabla \cdot (u \nabla (u+i)) + uF(u,i) - \beta G(u,i) i \\ \partial_t i = D_i \nabla \cdot (i \nabla (u+i)) + \beta G(u,i) i - qi \end{cases} \tag{1.7}$$

(see also Eq. (2.10)). This kind of equation was first proposed in Byrne and Drasdo, 2009. Since we consider two cell populations, the movement term becomes a cross-diffusion and poses several mathematical challenges (see Bubba et al., 2020b; Carrillo et al., 2018; Gwiazda et al., 2019; Lorenzi et al., 2017 for similar models, although to our knowledge the case of our interest is not present in the literature). The two models may show significantly different phenomena: a central localised infection can always spread in the whole domain in the presence of spatial diffusion, but remains localised if pressure-driven movement is considered.

In Chapter 2, we derive both Eqs. (1.6) and (1.7) from microscopic considerations. We then describe their behaviour and compare them to the corresponding agent-based counterpart, with the aim of improving our understanding of oncolytic viral

infection in the context of spatial constraints and a particular focus on the effects of stochasticity.

Agent-based models The most elementary approach requires defining rules for the proliferation of uninfected cells, death of uninfected cells, infection and movement; viral particles are assumed to be unable to move far away from infected cells. In Wodarz et al., 2012, such a model is developed and compared to experiments *in vitro*; some additional insights are obtained from a related continuous model. In Chapter 2, we develop a similar model and formally derive the corresponding continuum PDE. The main difference with respect to Wodarz et al., 2012 is that we allow several cells to occupy the same lattice point: this makes it possible to analyse more complex rules for the movement, which significantly affect the behaviour of the system.

It is helpful to remark once again that the mathematical formulation is analogous to SI and predator-prey agent-based models due to the absence of a viral population.

In ecological settings, the comparison between discrete and continuum models of this form has been widely studied, with an approach somehow similar to the one adopted in Chapter 2 (for example, in Aronson, 1980; Keeling et al., 2002; Wilson et al., 1993). On the other hand, with the exception of Wodarz et al., 2012, we are not aware of any other work comparing agent-based and continuous models about oncolytic viruses; this motivates the model developed in Chapter 2.

1.3.2 Inclusion of viral dynamics

Let us now add viral dynamics to the previous modelling approach. We denote viral particles by v. As we explain below, we can often recover the formulation without the virus by making appropriate quasi-steady assumptions.

ODE models We consider a generic system of the form

$$\begin{cases} \dfrac{\mathrm{d}u}{\mathrm{d}t} = uF(u,i) - \tilde{\beta}\tilde{G}(u,i,v)v \\ \dfrac{\mathrm{d}i}{\mathrm{d}t} = \tilde{\beta}\tilde{G}(u,i,v)v - qi \\ \dfrac{\mathrm{d}v}{\mathrm{d}t} = \alpha q i - q_v v \end{cases} \tag{1.8}$$

The equation for the virus models the viral release caused by the lysis of infected cells (α viral particles released for each cell) and viral decay; it does not take into account the uptake of free virions by cancer cells: a few models include this process (Bajzer et al., 2008; Pooladvand et al., 2021), but most of the time it is assumed to be negligible. Eq. (1.4) can be seen as an approximation of (1.8) under the quasi-steady assumption $\frac{\mathrm{d}v}{\mathrm{d}t} = 0$, which is justified by the fact that viral dynamics are much faster than cells' dynamics. This assumption implies that $v = \frac{\alpha q}{q_v} i$ and we recover Eq. (1.4) by setting

$$\beta = \frac{\tilde{\beta}\alpha q}{q_v}, \qquad G(u,i) = \tilde{G}\Big(u, i, \frac{\alpha q}{q_v} i\Big) \tag{1.9}$$

The addition of the third equation allows for stable limit cycles even in the most elementary case of exponential growth and mass-action infection (Jenner et al., 2018b);

this remains true in the case of logistic growth (Baabdulla and Hillen, 2024; Pooladvand et al., 2021). The case of G as in (1.5) with δ and logistic growth, i.e.

$$F(u) = p \ln\left(\frac{K}{u}\right), \qquad \tilde{G}(u,i,v) = \frac{u}{u+i}$$

exhibits several interesting behaviours, such as stable limit cycles and stability of the extinction singular equilibrium (Jenner et al., 2019). This same model is also employed in Jenner et al., 2018c to analyse the effectiveness of treatment protocols involving several viral injections.

PDE models The inclusion of spatial diffusion in Eq. 1.8 yields the reaction-diffusion system

$$\begin{cases} \partial_t u = D_u \Delta u + uF(u,i) - \tilde{\beta}\tilde{G}(u,i,v)v \\ \partial_t i = D_i \Delta i + \tilde{\beta}\tilde{G}(u,i,v)v - qi \\ \partial_t v = D_v \Delta v + \alpha q i - q_v v \end{cases} \tag{1.10}$$

The case of logistic growth and density-dependent infection (as in Eq. (4.2)) exhibits either travelling waves or persistent oscillations (Baabdulla and Hillen, 2024; Pooladvand et al., 2021).

> In this formulation, the virus is assumed to diffuse in the full domain perfectly; as a consequence, the laws that regulate cells' movement do not significantly affect the spatial spread of the infection. In Chapter 4 we will further analyse this situation.

Spatial constraints should, therefore, be added in the last equation: for example, in Pooladvand and Kim, 2022, the viral concentration evolves according to the equation

$$\partial_t v = D_v \nabla \cdot [(1-c^n)\nabla v - v\nabla(1-c^n)] + \alpha q i - q_v v$$

where $c(t,x)$ is the normalised collagen concentration.

A common alternative formulation is a free-boundary problem (Friedman and Tao, 2003; Friedman et al., 2006; Wu et al., 2001); this formulation allows us to take into account ECM and its degradation due to the viral infection (Kim et al., 2014). We also mention the approach of Alzahrani et al., 2019, in which a macroscopic model that takes into account the ECM is derived from the microscopic dynamics of the urokinase plasminogen activator system. These models differ significantly from the mathematical formulations of the thesis, therefore we do not provide further details.

Agent-based and hybrid discrete-continuous models The first way to include the viral population into an agent-based model is to consider a discrete viral population (Jenner et al., 2020). As we already pointed out, viral dynamics occur at a spatio-temporal scale that is very different from cell processes. This often leads to models that let viral density evolve according to a deterministic balance equation, as done in Paiva et al., 2009. This approach is widely used to model the evolution of several chemical elements, such as oxygen (Anderson et al., 2006) or chemoattractant (Almeida et al., 2022; Bubba et al., 2020a; Charteris and Khain, 2014; Cooper and Kim, 2014). Observe that the continuous description of viral density makes the model hybrid and multiscale.

> In Chapter 4, we add viral dynamics to the models of Chapter 2 and analyse the impact of such a modification. The derivation of the corresponding macroscopic continuous model follows the same techniques explained in Chapter 3 and presents

no additional challenges.

1.3.3 Modelling heterogeneity and delay

We now present models that take into account some kind of heterogeneity related either to cancer cells, viral particles or both at the same time. We remark that the most basic kind of heterogeneity is spatial, which has already been extensively mentioned in previous sections. We now focus on other heterogeneities, keeping in mind that adding the spatial structure is always possible.

Temporal heterogeneity of infected cells In epidemiological settings, the infectivity of an individual depends strongly on how much time has passed from infection. Including the time from the infection as a structuring variable for the infected individuals dates back to the first modern SI model (Kermack and McKendrick, 1927); an extension of the model taking into account spatial heterogeneity was later studied in Diekmann, 1978.

Analogous considerations hold in the case of oncolytic virotherapy, since it takes some time for a newly infected cell to start the viral production at the most efficient rate. Indeed, the age-structured approach was adopted in Ding et al., 2022; Gao et al., 2022. An alternative approach to model the phenomenon, which is more widely used, is through delay differential equations (Crivelli et al., 2012; Rioja et al., 2016; Najm et al., 2023; Rajalakshmi and Ghosh, 2022; Wang et al., 2013; Wang et al., 2019), in which there is a sharp transition between newly infected cells and "mature" infected cells that produce viral particles; this approximation is justified by the fact that the period of transition is relatively short with respect to other processes; hence its exact dynamics may be neglected. These second kinds of models differ significantly from the mathematical formulations of the thesis, therefore we do not elaborate further.

Other heterogeneous traits Discrete heterogeneous compartments are commonly employed in general epidemic models. In the context of oncolytic virotherapy, the model developed in Crivelli et al., 2012 takes into account the fact that vesicular stomatitis viruses are unable to replicate in T-lymphocytes in the resting phase. Consequently, uninfected cells are divided into a quiescent population, which cannot be infected, and a susceptible population: as time passes, cells move between the two states. Discrete compartments may also be used in agent-based models, as it is done in Bhatt et al., 2022 in relation to the resistance of uninfected cancer cells to viral infection. An analogous approach may also be used to model heterogeneity involving the virus, either genetically (Jenner et al., 2018a) or as a coating level that prevents immune recognition (Lee et al., 2020).

Another possible approach is to consider a continuous trait variable and describe the system's evolution via PDEs, similar to age-structured infections. Several examples can be found in the epidemiological settings (Almeida et al., 2021; Barbarossa and Röst, 2015; Bernardi et al., 2022; Lorenzi et al., 2021b; Lorenzi et al., 2024b; Novozhilov, 2008; Veliov and Widder, 2016), as well as in the ecological settings (de Araujo et al., 2024; Delitala and Lorenzi, 2013a); in the context of oncolytic virotherapy, this approach was used in Karev et al., 2006 to model several kinds of heterogeneity (susceptibility to infections, death rates, virulence).

A common characteristic of continuous structured models is the possibility to easily model *trade-offs* between different features, in the sense described in Section 1.1. In the context of infections, one may consider a trade-off involving the susceptible compartment between proliferation rate and resistance to the infection (Lorenzi et al., 2021b); in the

context of oncolytic viral infections, this is a way to model the fact that less proliferative cells have a slower metabolic activity, resulting in a slower infection. In the absence of infection, the fittest trait is clearly the more proliferative one, whereas infection does modify the fitness landscape, making the situation less clear.

To our knowledge, there is no extension of the model presented in Lorenzi et al., 2021b that takes into account spatial heterogeneity in addition to phenotypic heterogeneity. This motivates the model developed in Chapter 4, which we derive from the underlying stochastic counterpart. In Chapter 5, we consider a similar model that takes into account oxygen dynamics and hypoxia-driven heterogeneity.

1.4 Models of the interactions between cancer, immune system and oncolytic viruses

All the models presented so far do not include explicit interactions with the immune system, although its effects are somewhat implicitly taken into account in some parameter values: for example, the death rate of infected cells q and the decay rate of the virus q_v in Eq. (1.8) may easily be increased to consider immune clearance. However, the influence of the immune system is much more complicated than that.

Immune interactions with a tumour involve several different types of immune cells, which are stimulated and inhibited by a large number of molecules. For notational simplicity, in this section, we denote by z any kind of immune cell interacting with the tumour (e.g., T-cells or macrophages), keeping in mind that models often combine more than one immune population.

1.4.1 Cancer and immune system without oncolytic viruses

Interactions between cancer and the immune system have been widely studied. We give a quick review of some common modelling approaches, which serve as a base for including oncolytic viruses in the framework. We also provide some insights on how to include therapeutic interventions.

ODE models The most elementary models take into account only two equations of predator–prey type, in which the interactions are not dissimilar from the ones described in Eq. (1.4) (d'Onofrio, 2005). A general model can be written in the form

$$\begin{cases} \dfrac{\mathrm{d}u}{\mathrm{d}t} = uF(u) - H_u(u,z)u \\ \dfrac{\mathrm{d}z}{\mathrm{d}t} = S(u,z)z - H_z(u,z)z - q_z(z)z + S_0(t) \end{cases} \tag{1.11}$$

where F is the cancer growth rate, as explained in Section 1.3. The term $H_u(u,z)u$ plays a role analogous to the infection term $\beta G(u,i)i$ and similar functional forms are often used. Immune cells are assumed to be recruited by the interactions with the tumour (described by the function S) and to die due to autoregulation ($q_z(z)z$) and inhibition by the tumour ($H_z(u,z)z$); this last term usually represents the actions of other immune cell types or chemical signals, which are not modelled explicitly. The term S_0 models an external source of immune cells independent of the tumour and the immune cell concentration, which may vary in time; this allows us to model the effect of generic immunotherapy on the number of immune cells (d'Onofrio, 2005). We remark that immunotherapy may

also be implicitly taken into account by modifying some parameters (e.g., an increase in the immune killing rate may be interpreted as the consequence of enhanced immune response due to targeted therapeutic interventions).

The basic framework we just described can be modified to include several other dynamics, such as different kinds of immune cells or signalling proteins (i.e., chemokines and cytokines). We refer to Eftimie et al., 2011a for a review of models of increasing complexity. Some of those models give rise to persistent oscillations. In the context of complex models, additional equations may be used to directly incorporate immunotherapies (e.g., the concentration of an immune checkpoint inhibitor may be taken into account).

PDE models Spatial heterogeneity can be easily incorporated in Eq. (1.11) by adding a diffusion term (Singh and Banerjee, 2020), although such models are not so commonly used. From the application point of view, it makes more sense to consider a chemotactic movement of immune cells towards the tumour: we, therefore, assume that cancer cells secrete a chemoattractant ϕ, whose evolution is described by a reaction-diffusion equation; immune cell concentration is then described by the equation

$$\partial_t z = \nabla \cdot (D_z \nabla z - \chi z \nabla \phi) + S(u,z)z - H_z(u,z)z - q_z(z)z + S_0(t)$$

The spatial term models two contributions: diffusion with coefficient D_z and directed movement towards the gradient of the chemoattractant with coefficient χ. The chemotactic movement has been widely studied from the mathematical point of view (Hillen and Painter, 2009) and it is commonly used to model self-organisation in several different settings (Painter, 2019). In the context of the interactions between cancer and the immune system, it is used, for example, in Knútsdóttir et al., 2014; Matzavinos et al., 2004; Owen and Sherratt, 1997. Some variations of this equation allow us to take into account the difficulties of T-cells' infiltration in the tumour microenvironment (Almeida et al., 2022).

Other kinds of PDEs arise when an alternative structuring variable is considered. For example, in Atsou et al., 2020 tumour cells are structured in size and space. Another important modelling approach, which applies specifically to tumour-immune interactions, is the one introduced in Delitala and Lorenzi, 2013b; Lorenzi et al., 2015: it takes into account target-antigenic expressions of T cells and the antigenic expressions of tumour target cells, which are represented by continuous variables; immune cells then may only interact with cancer cells whose antigen expression is not too different from their target. This kind of models can mimic the recognition, learning and memory aspects of the immune response. This approach allows us to consider immunotherapies that enhance antigen-driven expansion of immune cells, which increases the number of immune cells compatible with the existing tumour population (Lorenzi et al., 2015).

Agent-based models Individual-based models allow the inclusion of stochasticity in modelling the two kinds of heterogeneity that we just discussed in relation to PDE, namely: the spatial distribution and the aspects related to the movement (Macfarlane et al., 2018) and the infiltration of immune cells in the tumour microenvironment (Almeida et al., 2022; Kather et al., 2017); the antigens presented by tumour cells and the aspects related to immunoevasion and immunoediting (Almeida et al., 2023; Christophe et al., 2015; Leschiera et al., 2022; Macfarlane et al., 2019). Several models use a hybrid approach, describing immune and cancer cells at the individual level and chemical components (e.g., nutrients or chemoattractant) as a continuous density (Cooper and Kim, 2014; Mallet and De Pillis, 2006).

The vast complexity of the biological phenomena related to the immune response makes individual-based approaches particularly suitable in this context. Some simple

models are also amenable to be compared with their continuous counterparts (Almeida et al., 2022; Almeida et al., 2023), as described in Section 1.2.1.

1.4.2 Oncolytic virotherapy with immune response

We now combine all the previous considerations to describe models of cancer, oncolytic virus and immune system, with some remarks related to additional immunotherapies leading towards immunovirotherapies. While some of the immune cells stimulated by the virus specifically target viral particles and infected cells, others can kill every cancer cell; this distinction clearly has important consequences on the therapy outcome.

ODE models A generic ODE model is obtained by combining Eqs. (1.4) and (1.11) (see also Eq. (3.11)):

$$\begin{cases} \dfrac{\mathrm{d}u}{\mathrm{d}t} = uF(u,i) - \beta G(u,i)i - H_u(u,z)z \\ \dfrac{\mathrm{d}i}{\mathrm{d}t} = \beta G(u,i)i - qi - H_i(i,z)z \\ \dfrac{\mathrm{d}z}{\mathrm{d}t} = S(u,i,z)z - H_z(u,i,z)z - q_z(z)z + S_0(t) \end{cases} \tag{1.12}$$

An additional equation is sometimes added to model viral dynamics: in this case, the immune response also affects the virus. Other equations may also be included to model the effect of immunotherapies (see Storey et al., 2020 for the case of immune checkpoint inhibitors and Mahasa et al., 2022 for the case of CAR-T cells in the absence of innate immune response).

As anticipated, the outcome strongly depends on the type of cancer cells targeted by the immune response. For example, in Wodarz, 2001, it was observed that virus-specific T-cells (modelled by setting $H_u = 0$) are always detrimental to the patient, as they increase the total number of tumour cells at the equilibrium; on the other hand, tumour specific T-cells (modelled by setting $H_u = H_i$) are not. In this setting, the best therapeutical strategy based on equilibrium values would be to avoid any immune response (although it appears unattainable in any realistic situation). The conclusion that an immunosuppressive microenvironment may hinder viral therapy efficacy is also reached in Vithanage et al., 2023. On the other hand, the presence of immune response appears beneficial in some situations in which different kinds of macrophages are considered (Almuallem et al., 2021; Eftimie and Eftimie, 2018). We also remark that the study of the equilibrium of the equation may not be enough to fully characterise the dynamics, as sometimes stable limit cycles or chaotic behaviours arise for some parameter values (Eftimie et al., 2016). Indeed, when two viral populations are considered and the immune response is taken into account, it is possible to observe complex phenomena such as multi-stability and multi-instability (Eftimie et al., 2011b); in some situations, the latter is associated with tumour eradication.

While it is true that the immune response, in general, decreases the efficacy of oncolytic virotherapy, the emergence of oscillations may be associated with tumour eradication in some situations. In Chapter 3, we analyse one of such situations in the ODE settings, observing the presence of a Hopf bifurcation; we then study the implications on the corresponding spatial continuous and agent-based models. We also assume that the killing rate of cancer cells by immune cells may be modulated through immunotherapy (e.g., by inhibition of the binding between PD-1 and PD-L1

checkpoints, respectively in cancer cells and T-cells).

Spatial models There are not many spatial models in literature for the interaction between oncolytic virotherapy and the immune system, probably due to the complexities of the phenomena under investigation and the lack of medical data related to spatial distribution. The most common approach for PDEs is the free-boundary problem introduced in Friedman and Tao, 2003; Wu et al., 2001, which has been extended to include innate immune cells (Wu et al., 2004; Friedman et al., 2006), natural killer cells (Kim et al., 2018) and immune checkpoint inhibitors (Friedman and Lai, 2018; Kim et al., 2018; Storey and Jackson, 2021; Surendran et al., 2023).

Interactions between oncolytic viruses and the immune system may also be described through agent-based models (Storey and Jackson, 2021) and hybrid models (Jenner et al., 2022; Surendran et al., 2023). These approaches are able to describe several complex features, such as interactions with the stroma and with immune checkpoint inhibitors. Such biological details make the models hard to be approached with rigorous analytical techniques.

To our knowledge, the use of chemotaxis to model immune response to oncolytic viral injection has not been commonly employed. This motivates the agent-based and continuous models developed in Chapter 3. We keep the model simple enough to allow some mathematical tractability.

1.5 Mathematical models for hypoxia and its influence on cancer therapies

The two main motivations for the study of hypoxia in tumours are its effects on therapies (Zhuang et al., 2023) and cancer invasion (Barrak et al., 2020; Kao et al., 2016). We first restrict our attention to tumour development alone, with some hints on invasiveness, and then present extensions that take into account therapies. In both cases, oxygen concentration may either be modelled directly or be assumed to be stationary and independent of cancer. The former approach is clearly more complete, allowing the mutual interactions with the tumour to be characterised. On the other hand, in many cases, the assumption that oxygen is stationary allows us to decrease the model complexity and focus the attention on the effects on the tumour; furthermore, sometimes, this assumption enhances the mathematical tractability. A few models also consider the intratumoral vascular network reconstructed from experimental data (Villa et al., 2021a).

We remark that, although similar mathematical approaches have also been used in relation to other environmental fluctuations, for the sake of brevity, we here restrict our attention to the specific case of hypoxia.

1.5.1 Tumour development in hypoxic conditions

Discrete compartments A basic way to model the influence of hypoxia is through discrete compartments that evolve according to different dynamics. For example, in Martínez-González et al., 2012 tumour cells are considered to be either normoxic or hypoxic, cell loss is modelled through a necrotic population and transition rates depend on the oxygen concentration; it is assumed that hypoxic cells proliferate slower (*proliferation-survival trade-off*) and move faster (*proliferation-motility trade-off*) than normoxic cells. A similar approach is employed in Astanin and Preziosi, 2008 in the context of a mechanical multiphase model, in which normoxic and hypoxic cells are described by two different

phases and transitions between them happen at a rate dependent on environmental conditions; this model is used to describe the transition from aerobic to purely glycolytic metabolism (also known as *Warburg effect*).

The same strategy may be adapted to agent-based models: for example, in Rocha et al., 2021, cells are modelled at the individual level either as normoxic or hypoxic, with transitions between the two states that depend on the oxygen level; hypoxic cells are characterised by enhanced motility and this allows to analyse the tumour invasion lead by post-hypoxic cells, which maintain their hypoxic features even after reaching a more oxygenated environment. In Gatenby et al., 2007, a hybrid cellular automaton is developed and cells are associated with a label that depends on their adaptation to hypoxia and influences their dynamics; this label may change in relation to environmental conditions. Unlike the two previous situations, this model considers a broad spectrum of adaptation levels, although discrete.

It is also possible to adopt a hybrid approach and model some compartments with a continuous density-based representation and others with a discrete individual-based description.

> In Chapter 6, this last modelling approach is applied to the study of hypoxia-driven epithelial-to-mesenchymal transitions, with hypoxic cells more likely to be associated with the mesenchymal phenotype.

Continuous trait variables One may also consider a continuous spectrum of adaptation levels and a common way to do so is by the use of epigenetically structured equations similar to Eq. (1.1), with the reproduction rate R also depending on the oxygen concentration O. When R takes the form given by Eq. (1.2), this can be done by considering

$$r(y, O) := f(y) + g(y, O)$$

as in Ardaševa et al., 2020c; Ardaševa et al., 2020b. In this formula, $g(y, O)$ models the fitness related to the aerobic energy pathways, while $f(y)$ represents the one associated with anaerobic pathways. The functions are usually chosen in a way that allows rewriting the reproduction rate as

$$R(y, O, \rho) = a(O) - b(O)(y - \varphi(O))^2 - \kappa\rho$$

This formulation allows to consider the above-mentioned *proliferation-survival trade-off*. The same approach may also be adopted for the agent-based counterpart of these models (Ardaševa et al., 2020a). Furthermore, in some cases, spatial heterogeneity is also considered, either with epigenetic diffusion (Fiandaca et al., 2021; Villa et al., 2021a) or without it (Lorenzi et al., 2018): the heterogeneous spatial concentrations of oxygen leads to the selection of different cells' phenotypes in different parts of the spatial domain, with relevant consequences on the therapeutical level (as we explain below).

Alternatively, in Chiari et al., 2023b the reproduction rate takes the form of Eq. (1.3) with φ depending on the oxygen concentration, i.e.

$$R(y, O, \rho) = p(y, O)\left(1 - \frac{\rho}{K}\right) - \eta(y - \varphi(O))^2$$

As in the previous case, the fittest epigenetic trait is achieved for $y = \varphi(O)$. The main difference is that here the cell density always grows up to the same carrying capacity K, irrespective of the oxygen level (see also the discussion of Chapter 5).

The latter approach is adopted in Chapter 5 and serves as a base to include oncolytic virotherapy.

In hypoxic environments, continuous traits may also be included in agent-based models, as it is done in Gallaher et al., 2019 in the context of the *proliferation-migration trade-off*.

1.5.2 Impact of hypoxia on cancer therapies

We now explain how it is possible to build upon the previously presented models and include the heterogeneous effects on chemotherapy, radiotherapy and oncolytic virotherapy. We also briefly recall the standard mathematical description of the first two therapies.

Chemotherapy The effect of chemotherapy is usually modelled as an additional linear death term in the equation of cancer evolution, following the well-known log-kill hypothesis. In hypoxic conditions, chemotherapy is less effective due to the higher resistance of hypoxic cells (mainly caused by their slower metabolism) and the difficulties that the chemotherapeutic agent faces in reaching areas far from blood vessels. The latter feature clearly requires spatial effects; on the other hand, the former may be studied even in nonspatial settings and builds upon a vast literature that keeps into account some kind of resistance to therapies and its trade-off with proliferation (Almeida et al., 2019; Chisholm et al., 2015; Lorz et al., 2015; Pouchol et al., 2018; Stace et al., 2020). Chemotherapy in hypoxic situations was modelled in Lorenzi et al., 2018; Villa et al., 2021b.

Radiotherapy The survival fraction of tumour cells after radiotherapy is usually modelled in a linear-quadratic fashion, with coefficients α and β: this can be justified by the fact that cell death is caused by either a simultaneous break of both DNA strands or two consecutive breaks. The therapy may be considered as a jump process (and in this case the previous expression is an exponential) or as a continuous death process. Hypoxic conditions constitute an obstacle not only due to the resistance of hypoxic cells, but also because oxygen plays a direct role in the DNA damage caused by radiation. These two effects are usually taken into account by varying the parameters α and β as functions of the oxygen concentration and the epigenetic trait (Celora et al., 2021; Celora et al., 2023; Chiari et al., 2023a). On the other hand, it is also possible to consider models not epigenetically structured and take into account just oxygen concentration, as it is done in Hamis et al., 2019 in the context of agent-based models and in Kuznetsov and Kolobov, 2020; Lewin et al., 2018 for PDE models.

Oncolytic virotherapy The inefficient viral infection of hypoxic cells can be modelled as a direct influence of oxygen concentration on the infection rate, as done in Ramaj and Zou, 2023 in the case of ODEs and nested ODEs (the latter models infections in adjacent lymph nodes). The only spatial model that we know in this context is the one presented in Boemo and Byrne, 2019, in which the difficulties of treating hypoxic regions with standard therapies motivate the use of macrophages that release oncolytic viral particles when experiencing low oxygen concentrations.

To our knowledge, there are no epigenetically structured models for the influence of hypoxia on oncolytic virotherapy. This motivates the work presented in Chapter 5.

1.6 Contributions of the thesis

This chapter briefly introduced the biological context and presented the most common mathematical approaches to model cancer growth and oncolytic virotherapy available in the literature. Overall, most models suggest that oncolytic virotherapy cannot eradicate a tumour alone in most situations, which is in line with experimental observation. This thesis aims to improve the existing modelling approaches by focusing on the effects of several obstacles that prevent its success. In particular, we aim to address the following questions:

- What is the most suitable mathematical expression to model cell movement in the presence of oncolytic viral infections?
- How is virotherapy affected by physical obstacles that hinder viral diffusion in the tumour microenvironment?
- Is the immune response beneficial to the outcome of the virotherapy, or does it reduce the efficacy of the infection?
- Can a viral injection enhance the immune recognition of cold tumours?
- Does the emergence of some kind of resistance to the viral infection play any role in the efficacy of the therapy?
- What is the role of stochasticity in all the above-mentioned processes?
- How does hypoxia affect the virotherapy?
- Is it possible to effectively target hypoxic cells through oncolytic virotherapy?
- What is the most effective way to model epithelial-to-mesenchymal transitions driven by hypoxia?

Table 1.1 summarises the model variations investigated in the thesis. Some of the key findings are reported Table 7.1 of Chapter 7. The rest of the thesis is organised as follows.

In Chapter 2, we present some simple agent-based and continuum models for the infection of oncolytic viruses, which serve as a basis for most of the models developed later. We consider both undirected random cell movement (as in Eq. (1.6)) and pressure-driven cell movement (as in Eq. (1.7)). The model described in this chapter and most of the results shown have been published in Morselli et al., 2023; some sections have been significantly extended with respect to the published version. The author of the thesis was in charge of the conceptualisation of the work, the choice of the methodology, the development of the software, the writing process and the visualisation of the results, under the supervision of the other authors.

In Chapter 3, we include immune dynamics and explore its effects on oncolytic virotherapy. The model described in this chapter and the results shown have been submitted for publication (Morselli et al., 2024b). The author of the thesis was in charge of the conceptualisation of the work, the choice of the methodology, the development of the software, the writing process and the visualisation of the results, under the supervision of the other authors.

In Chapter 4, we present two additional extensions that consider explicit viral dynamics and cell heterogeneity. The models described in this chapter have been developed in collaboration with Marcello E. Delitala and Federico Frascoli. The author of the thesis was in charge of the conceptualisation of the work, the choice of the methodology, the development of the software used in Section 4.1, the writing process and the visualisation

Chapter	Stochasticity	Cell movement	Viral dynamics	Immune system	Heterogeneity
2	✓	undirected / pressure	✗	✗	✗
3	✓	undirected	✗	✓	✗
4 (Sec. 4.1)	✓	undirected / pressure	✓	✗	✗
4 (Sec. 4.2)	✓	undirected	✗	✗	✓
5	✗	pressure	✓	✗	✓
6	✓	undirected	NA	✗	✓

TABLE 1.1: Schematic structure of the models presented in the thesis. Undirected random cell movement refers to equations analogous to Eq. (1.6); pressure-driven cell movement refers to equations analogous to Eq. (1.7). Note that the viral dynamics do not apply to Chapter 6, as the model does not relate to virotherapy.

of the results, under the supervision of Marcello E. Delitala and Federico Frascoli; the software used in Section 4.2 was partially developed by Emma Ciccarelli in preparation for her master thesis (under the supervision of the author of the thesis, who also run all the simulations).

In Chapter 5, we develop an epigenetically structured model for the influence of hypoxia on oncolytic virotherapy. The model described in this chapter and the results shown have been submitted for publication (Morselli et al., 2024a). The author of the thesis was in charge of the conceptualisation of the work, the choice of the methodology, the writing process and the visualisation of the results, with the collaboration of Giulia Chiari under the supervision of Marcello E. Delitala and Federico Frascoli; the software was mainly developed by Giulia Chiari (with some minor contributions by the author of the thesis, who also run all the simulations).

In Chapter 6, we describe a novel approach for the description of cell heterogeneity at the genotypic and phenotypic level; this approach is then applied to the study of EMT. The model described in this chapter and the results shown have been published in Chiari et al., 2022. The author of the thesis contributed to the conceptualisation of the work, the choice of the methodology, the writing process and the visualisation of the results, under the supervision of Marcello E. Delitala and Marco Scianna; the software for the numerical simulations was developed and run by Giulia Chiari.

Finally, in Chapter 7, we present a global thesis conclusion and comment on possible research perspectives.

2 Agent-based and continuum models for oncolytic viruses' infection

In this chapter, we present a stochastic agent-based model describing infected and uninfected cells for solid tumours that interact with viruses in the absence of an immune response. Our model takes into account proliferation and death of uninfected tumour cells, death of infected tumour cells, infection of infected cells and cell movement. We present two alternative sets of rules governing the latter process (namely, undirected random cell movement and pressure-driven cell movement) and we show how this choice strongly influences therapy outcomes. Our intent is to compare different mechanisms for tumour development, capturing some of the constraints that diverse microenvironments pose on tumours development.

In the case of undirected movement, the corresponding continuum model is a diffusive Lotka–Volterra model with either logistic or exponential growth: this allows us to partially rely on previous analytical results on the subject (Dunbar, 1984). In this situation, we observe a good agreement between agent-based simulations and the numerical and analytical results of the continuum model. On the other hand, in the case of pressure-driven cell movement, the corresponding continuum model is a local cross-diffusion Lotka–Volterra model that we could not find in the literature (although it is similar to the systems studied in Bubba et al., 2020b; Carrillo et al., 2018; Gwiazda et al., 2019; Lorenzi et al., 2017). We observe a wide parameter range in which the infection of the agents remains confined to the centre of the tumour, even though the continuum model shows travelling waves of infection; outcomes appear to be more sensitive to stochasticity and uninfected regions appear harder to invade, giving rise to irregular, unpredictable growth patterns.

Our results show that the presence of spatial constraints in tumours' microenvironments limiting free expansion has a very significant impact on virotherapy. Outcomes for these tumours suggest a notable increase in variability. All these aspects can have important effects when designing individually tailored therapies where virotherapy is included.

This chapter is organised as follows. In Section 2.1, we introduce the two agent-based models. In Section 2.2, we formally derive their continuum counterparts. In Section 2.3, we present some classical analytical results for travelling wave solutions of the continuum models. In Section 2.4, we compare the results of numerical simulations of the agent-based models and the numerical solutions of the corresponding PDEs, showing their consistency with the analytical results. In Section 2.5, we discuss the main findings in light of existing experimental evidence *in vitro* and we provide some hints for future research.

The model described in this chapter and most of the results shown have been published in Morselli et al., 2023; the results of Sections 2.3 and 2.4.3 have been significantly extended with respect to the published version.

2.1 Description of the agent-based models

In this section, we describe the stochastic dynamics of the two agent-based models and introduce the different expressions of the probability of cell movement.

2.1.1 Agent-based models

In the agent-based modelling framework, each cell is an agent occupying a position on a discrete lattice. We consider two cell populations, uninfected and infected; the infection of a cell then corresponds to an agent passing from the former to the latter population. Cells can also move, reproduce and die. For ease of presentation, in this section, we only consider cells arranged along the one-dimensional real line $\mathbb{R}$, but there would be no additional difficulty in considering higher spatial dimensions. Since we carry out the comparisons between discrete and continuum models also in two spatial dimensions, in Remarks 2.1 and 2.2, we explain the small changes of the two-dimensional models.

Let us consider the temporal discretisation $t_n = \tau n$ with $n \in \mathbb{N}_0$, $0 < \tau \ll 1$ and the spatial discretisation $x_j = \delta j$, with $j \in \mathbb{Z}$, $0 < \delta \ll 1$; we assume τ to be small enough to guarantee that all the probabilities defined hereafter are smaller than 1. We denote the number of uninfected and infected cells that occupy position x_j at time t_n respectively by U_j^n and I_j^n; the corresponding densities are

$$u_j^n := \frac{U_j^n}{\delta}, \qquad i_j^n := \frac{I_j^n}{\delta}$$

The local pressure is assumed to be given by a barotropic relation of the form $\rho_j^n := \Pi(u_j^n + i_j^n)$. In the next sections we restrict to the case $\Pi(z) = z$ (so the pressure is actually the total cell density), but the discussion of this section is valid also for more general nondecreasing smooth functions $\Pi\colon [0, +\infty) \to [0, +\infty)$ such that $\Pi(0) = 0$: for example, one could think of the functional form proposed in Perthame et al., 2014. Although there might be differences in the way the system reaches the carrying capacity and how the model appears in the continuum limit, it seems that the overall behaviour of the tumour is not profoundly affected by different functional forms (Macfarlane et al., 2022).

Fig. 2.1 summarises the rules governing the dynamics of the agents. We consider two different movement mechanisms, i.e. undirected and pressure-driven, giving rise to different models. The rules for proliferation and death of uninfected cells, as well as death of infected cells and infection, are common for both models.

Pressure-dependent proliferation of uninfected cells We assume that the proliferation probability decreases as the pressure increases and stops at some homeostatic pressure $P > 0$; a pressure value greater than P results in the cell's death. Given a smooth decreasing function $G\colon [0, +\infty) \to \mathbb{R}$ such that $G(P) = 0$, we let an uninfected cell that occupies position x_j at time t_n reproduce with probability $\tau G(\rho_j^n)_+$, die with probability $\tau G(\rho_j^n)_-$, and remain quiescent with probability $1 - \tau G(\rho_j^n)_+ - \tau G(\rho_j^n)_- = 1 - \tau |G(\rho_j^n)|$. In these formulas, $z_+ := \max\{z, 0\}$ and $z_- := \max\{-z, 0\}$. When a reproduction takes place, a new cell is placed at the same lattice site. The fact that proliferation stops above P guarantees that, as $\tau \to 0$, a population of cells whose initial pressure is below the homeostatic value becomes less likely to acquire a pressure value above this level at later times. This kind of probability has already been employed in Chaplain et al., 2020.

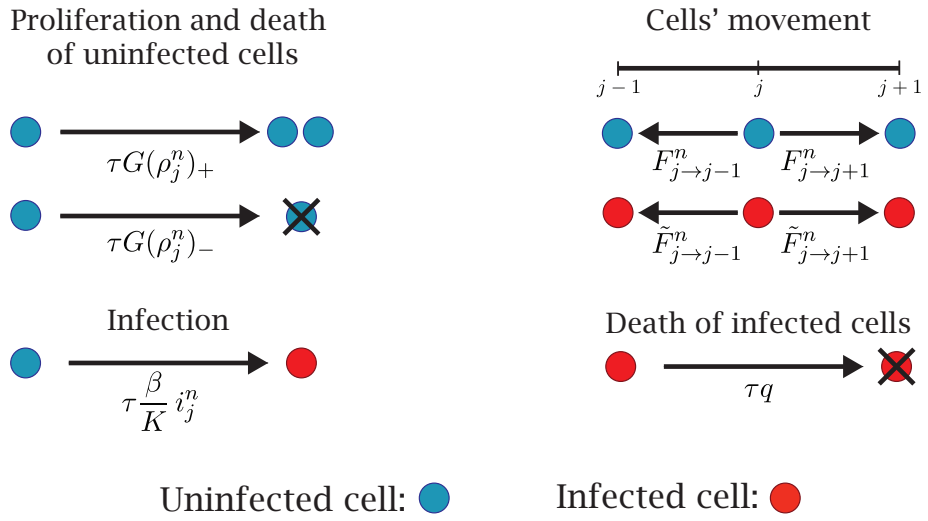

FIGURE 2.1: Schematic representation of the rules governing cell dynamics in the stochastic models. Uninfected cells are represented in blue and infected cells in red. Uninfected cells may proliferate or die according to the pressure value, move and become infected upon contact with infected cells. Infected cells may move and die with constant probability. We consider different expressions for the probabilities of movement, given respectively in Eqs. (2.2) and (2.3).

For the sake of simplicity, in the following sections, we mainly restrict our analysis to the logistic growth, i.e.

$$G(\rho) = p\left(1 - \frac{\rho}{P}\right) \tag{2.1}$$

where $p > 0$ is the maximal duplication rate. Let us observe that the carrying capacity of the system is $K := \Pi^{-1}(P)$; since in the case of our interest $\Pi(z) = z$, we actually have $P = K$. In the case of undirected cell movement, we also consider the case of pressure-independent proliferation, i.e. $G(\rho) \equiv p$; unlimited exponential growth is clearly not feasible in any biological scenario, but we could imagine that in some cases the carrying capacity is too high to give any significant contribution in the initial phases of the tumour dynamics.

Death of infected cells We do not model the proliferation of infected cells, as the virus disrupts the cellular machinery. Sometime after the infection, the cell undergoes lysis and dies: we assume that at every time step this happens with probability τq, where $q > 0$ is a constant death rate.

Infection We do not model explicitly the oncolytic virus, as we assume that its dynamics are faster than cellular dynamics and can thus be approximated by a quasi-steady state (as in Komarova and Wodarz, 2010; Novozhilov et al., 2006; see also Section 2.4.1). Thus, we assume that infection takes place upon contact between infected and uninfected cells with probability proportional to the density of infected cells. This means that an uninfected cell that occupies position x_j at time t_n becomes infected with probability $\tau\beta i_j^n / K$, where K is the carrying capacity and $\beta > 0$ is a constant infection rate. Although the carrying capacity could be easily incorporated in the infection parameter, this formulation allows the easy rescale of the cell densities by only modifying K and the initial conditions. This process is similar to the interaction between the tumour and the immune system described, for example, in Almeida et al., 2022; Almeida et al., 2023.

Cell movement As we already mentioned, we consider two different rules governing cell movement. In view of the formal derivation of the continuum models, it is convenient to adopt the same notation for both processes. We thus state that an uninfected cell that occupies position x_j at time t_n moves to the lattice point $x_{j\pm1}$ with probability $F^n_{j\to j\pm1}$ and remains at its initial position with probability $1 - F^n_{j\to j-1} - F^n_{j\to j+1}$. The same happens for the infected cells, but with probabilities $\tilde{F}^n_{j\to j\pm1}$ that in principle may be different from $F^n_{j\to j\pm1}$.

Let us now give the explicit expressions for these probabilities. The simplest model of movement assumes no influence of the cell density and no preferential direction of motion; in this case we set

$$F^n_{j\to j\pm1} := \frac{\theta_u}{2}, \qquad \tilde{F}^n_{j\to j\pm1} := \frac{\theta_i}{2} \tag{2.2}$$

with $\theta_u, \theta_i \in [0,1]$. This is a standard unbiased random walk.

On the other hand, since cellular proliferation is limited by a carrying capacity, it also makes sense to take into account a reduction of motility in a crowded environment and allow cells to only move following the pressure gradient: the probability of movement thus depends on the difference between the pressure at the initial position of the cell and the pressure at the target point. In this case, we set

$$F^n_{j\to j\pm1} := \theta_u \frac{(\rho^n_j - \rho^n_{j\pm1})_+}{2P}, \qquad \tilde{F}^n_{j\to j\pm1} := \theta_i \frac{(\rho^n_j - \rho^n_{j\pm1})_+}{2P} \tag{2.3}$$

where $z_+ := \max\{z, 0\}$, P is the homeostatic pressure and $\theta_u, \theta_i \in [0,1]$ as before. Observe that, if $\rho^n_j \le P$ for every j, then all the probabilities are between 0 and 1. This kind of reasoning and the probabilities associated have already been employed in Chaplain et al., 2020.

In the special case $\rho^n_j = P$ and $\rho^n_{j-1} = \rho^n_{j+1} = 0$ the two definitions give the same probability values; in any other case, the probabilities of movement given in Eq. (2.2) are higher than the ones given in Eq. (2.3). This, as we will see shortly, strongly affects the therapy outcomes.

2.2 Formal derivation of the corresponding continuum models

We now derive the continuum counterparts of the agent-based models described in the previous section, using techniques analogous to those employed in various references (Champagnat and Méléard, 2007; Johnston et al., 2015; Lorenzi et al., 2020; Macfarlane et al., 2022; Penington et al., 2011; Chaplain et al., 2020; Almeida et al., 2022; Almeida et al., 2023).

2.2.1 Uninfected cells

Uninfected cells can first move, then reproduce or die based on the pressure value and finally become infected, as explained in Section 2.1. The principle of mass balance gives the equation

$$\begin{aligned} u^{n+1}_j = &\left[F^n_{j-1\to j}\, u^n_{j-1} + F^n_{j+1\to j}\, u^n_{j+1} + (1 - F^n_{j\to j-1} - F^n_{j\to j+1}) u^n_j\right] \\ &\times \left[1 + \tau G(\rho^n_j)_+ - \tau G(\rho^n_j)_-\right]\left(1 - \tau \frac{\beta}{K} i^n_j\right) \end{aligned}$$

and using the algebraic relation $x_+ - x_- = x$, this simplifies to

$$u_j^{n+1} = \Big[F_{j-1\to j}^n\, u_{j-1}^n + F_{j+1\to j}^n\, u_{j+1}^n + (1 - F_{j\to j-1}^n - F_{j\to j+1}^n)u_j^n\Big] \times \Big[1 + \tau G(\rho_j^n)\Big]\Big(1 - \tau\frac{\beta}{K} i_j^n\Big)$$

Let us define

$$\Phi := -(F_{j\to j-1}^n + F_{j\to j+1}^n)u_j^n + F_{j-1\to j}^n u_{j-1}^n + F_{j+1\to j}^n u_{j+1}^n \tag{2.4}$$

so that the previous equation becomes

$$\begin{aligned} u_j^{n+1} &= (u_j^n + \Phi)\Big[1 + \tau G(\rho_j^n)\Big]\Big(1 - \tau\frac{\beta}{K} i_j^n\Big) \\ &= u_j^n + \tau G(\rho_j^n)u_j^n - \tau\frac{\beta}{K} u_j^n i_j^n + \Phi - \tau^2 G(\rho_j^n)\frac{\beta}{K} u_j^n i_j^n \\ &\quad + \tau\Phi\Big[G(\rho_j^n) - \frac{\beta}{K} i_j^n - \tau G(\rho_j^n)\frac{\beta}{K} i_j^n\Big] \end{aligned}$$

We now divide both sides of the previous equation by τ and rearrange the terms to get

$$\frac{u_j^{n+1} - u_j^n}{\tau} = G(\rho_j^n)u_j^n - \frac{\beta}{K} u_j^n i_j^n + \frac{1}{\tau}\Phi + H_1 \tag{2.5}$$

where

$$H_1 := -\tau G(\rho_j^n)\frac{\beta}{K} u_j^n i_j^n + \Phi\Big[G(\rho_j^n) - \frac{\beta}{K} i_j^n - \tau G(\rho_j^n)\frac{\beta}{K} i_j^n\Big]$$

We will shortly see that in the cases of interest H_1 is the sum of higher order terms and therefore vanishes as $\tau, \delta \to 0$.

Let us now assume that there are two functions $u \in C^2([0,+\infty)\times\mathbb{R})$ such that $u_j^n = u(t_n, x_j) = u$ and $i \in C^2([0,+\infty)\times\mathbb{R})$ such that $i_j^n = i(t_n, x_j) = i$ (from now on we omit the arguments of functions computed at (t_n, x_j)); thus, we can use Taylor expansions for u in time and space as follows

$$\begin{aligned} u_j^{n+1} &= u(t_n + \tau, x_j) = u + \tau\partial_t u + \mathcal{O}(\tau^2) \\ u_{j\pm1}^n &= u(t_n, x_j \pm \delta) = u \pm \delta\partial_x u + \frac{1}{2}\delta^2\partial_{xx}^2 u + \mathcal{O}(\delta^3) \end{aligned}$$

Furthermore, we are assuming that the function Π is smooth, so that $\rho = \Pi(u+i) \in C^2([0,+\infty)\times\mathbb{R})$ and we can use a Taylor expansion for ρ as well

$$\rho_{j\pm1}^n = \rho(t_n, x_j \pm \delta) = \rho \pm \delta\partial_x\rho + \frac{1}{2}\delta^2\partial_{xx}^2\rho + \mathcal{O}(\delta^3)$$

Let us now treat separately the cases in which movement does or does not depend on pressure.

Undirected cell movement In this case, we have $F_{j\to j\pm1}^n = F_{j\pm1\to j}^n = \theta_u$, which is a constant independent of n, j. We then obtain

$$\Phi = \theta_u(u_{j-1}^n + u_{j+1}^n - 2u_j^n) = \theta_u\delta^2\partial_{xx}^2 u + \mathcal{O}(\delta^3)$$

and thus

$$H_1 = -\tau G(\rho_j^n)\frac{\beta}{K}u_j^n i_j^n + \Big[G(\rho_j^n) - \frac{\beta}{K}i_j^n - \tau G(\rho_j^n)\frac{\beta}{K}i_j^n\Big]\Phi = \mathcal{O}(\tau) + \mathcal{O}(\delta^2)$$

Eq. (2.5) then becomes

$$\partial_t u + \mathcal{O}(\tau^2) = \theta_u \frac{\delta^2}{2\tau}\partial_{xx}^2 u + pu - \frac{\beta}{K}ui + \mathcal{O}(\tau) + \mathcal{O}(\delta^2)$$

Letting $\tau, \delta \to 0$ in such a way that $\frac{\delta^2}{2\tau} \to D$, we obtain

$$\partial_t u = \theta_u D\partial_{xx}^2 u + pu - \frac{\beta}{K}ui$$

Pressure-driven cell movement In this case, we modify the terms as follows:

$$F_{j\to j\pm1}^n := \theta_u \frac{(\rho_j^n - \rho_{j\pm1}^n)_+}{2P} = \frac{\theta_1}{2P}\Big(\mp\delta\partial_x\rho - \frac{1}{2}\delta^2\partial_{xx}^2\rho + \mathcal{O}(\delta^3)\Big)_+ = \mathcal{O}(\delta)$$

It is then easy to see that $H_1 \to 0$ as $\tau, \delta \to 0$, as each term is multiplied either by τ or by some F. We then use the Taylor expansion of u in Eq. (2.4) to get

$$\begin{aligned}\Phi &= -(F_{j\to j-1}^n + F_{j\to j+1}^n)u + F_{j-1\to j}^n\Big(u - \delta\partial_x u + \frac{1}{2}\delta^2\partial_{xx}^2 u + \mathcal{O}(\delta^3)\Big)\\ &\quad + F_{j+1\to j}^n\Big(u + \delta\partial_x u + \frac{1}{2}\delta^2\partial_{xx}^2 u + \mathcal{O}(\delta^3)\Big)\\ &= (F_{j-1\to j}^n - F_{j\to j-1}^n + F_{j+1\to j}^n - F_{j\to j+1}^n)u + \delta(-F_{j-1\to j}^n + F_{j+1\to j}^n)\partial_x u\\ &\quad + \frac{1}{2}\delta^2(F_{j-1\to j}^n + F_{j+1\to j}^n)\partial_{xx}^2 u + \mathcal{O}(\delta^3)\end{aligned}$$

Now, let us observe that

$$\begin{aligned}F_{j\pm1\to j}^n - F_{j\to j\pm1}^n &= \frac{\theta_1}{2P}[(\rho_{j\pm1}^n - \rho_j^n)_+ - (\rho_j^n - \rho_{j\pm1}^n)_+]\\ &= \frac{\theta_1}{2P}(\rho_{j\pm1}^n - \rho_j^n) = \frac{\theta_1}{2P}\Big(\pm\delta\partial_x\rho + \frac{1}{2}\delta^2\partial_{xx}^2\rho + \mathcal{O}(\delta^3)\Big)\end{aligned}$$

using the relation $x_+ - (-x)_+ = x_+ - x_- = x$. We therefore have

$$\Phi = \frac{\theta_u}{2P}\Big\{\delta^2\partial_{xx}^2\rho u + \delta[-(-\delta\partial_x\rho + \mathcal{O}(\delta^2))_+ + (\delta\partial_x\rho + \mathcal{O}(\delta^2))_+]\partial_x u + \mathcal{O}(\delta^3)\Big\}$$

Finally, Eq. (2.5) becomes

$$\begin{aligned}\partial_t u + \mathcal{O}(\tau^2) = G(\rho)u - \frac{\beta}{K}ui + \frac{\theta_u}{P}\,\frac{\delta^2}{2\tau}\Big\{&\partial_{xx}^2\rho u\\ &+ [(\partial_x\rho + \mathcal{O}(\delta))_+ - (-\partial_x\rho + \mathcal{O}(\delta))_+]\partial_x u + \mathcal{O}(\delta)\Big\} + H_1\end{aligned}$$

Letting $\tau, \delta \to 0$ in such a way that $\frac{\delta^2}{2\tau} \to D$ we arrive at the final result:

$$\begin{aligned}
\partial_t u &= \frac{\theta_u D}{P}\{\partial^2_{xx}\rho u + [(\partial_x \rho)_+ - (-\partial_x \rho)_+]\partial_x u\} + G(\rho)u - \frac{\beta}{K}ui \\
&= \frac{\theta_u D}{P}(\partial^2_{xx}\rho u + \partial_x \rho \partial_x u) + G(\rho)u - \frac{\beta}{K}ui \\
&= \frac{\theta_u D}{P}\partial_x(u\partial_x \rho) + G(\rho)u - \frac{\beta}{K}ui
\end{aligned}$$

2.2.2 Infected cells

Infected cells can first move, then die based on the pressure value, as explained in Section 2.1. Also, uninfected cells may be infected. The computations follow the same strategy of uninfected cells, so we only sketch the main points. The principle of mass balance gives the equation

$$\begin{aligned}
i_j^{n+1} = &\left[\tilde{F}^n_{j-1\to j}\, i^n_{j-1} + \tilde{F}^n_{j+1\to j}\, i^n_{j+1} + (1 - \tilde{F}^n_{j\to j-1} - \tilde{F}^n_{j\to j+1})i^n_j\right](1-\tau q) \\
&+ \tau\frac{\beta}{K} i^n_j (1 + \tau G(\rho^n_j))\left[F^n_{j-1\to j}\, u^n_{j-1} + F^n_{j+1\to j}\, u^n_{j+1} + (1 - F^n_{j\to j-1} - F^n_{j\to j+1})u^n_j\right]
\end{aligned}$$

which simplifies to

$$\begin{aligned}
i_j^{n+1} &= (1-\tau q)\left[\tilde{F}^n_{j-1\to j}\, i^n_{j-1} + \tilde{F}^n_{j+1\to j}\, i^n_{j+1} + (1 - \tilde{F}^n_{j\to j-1} - \tilde{F}^n_{j\to j+1})i^n_j\right] \\
&\quad + \tau\frac{\beta}{K} u^n_j i^n_j + \tau H_2 \\
&= \left[\tilde{F}^n_{j-1\to j}\, i^n_{j-1} + \tilde{F}^n_{j+1\to j}\, i^n_{j+1} - (\tilde{F}^n_{j\to j-1} + \tilde{F}^n_{j\to j+1})i^n_j\right] + (1-\tau q) i^n_j \\
&\quad + \tau\frac{\beta}{K} u^n_j i^n_j + \tau H_2 + \tau H_3 \\
&= \Psi + (1-\tau q) i^n_j + \tau\frac{\beta}{K} u^n_j i^n_j + \tau H_2 + \tau H_3
\end{aligned}$$

where

$$\Psi \coloneqq \tilde{F}^n_{j-1\to j}\, i^n_{j-1} + \tilde{F}^n_{j+1\to j}\, i^n_{j+1} - (\tilde{F}^n_{j\to j-1} + \tilde{F}^n_{j\to j+1})i^n_j$$

and

$$\begin{aligned}
H_2 &\coloneqq \tau G(\rho^n_j)\frac{\beta}{K} u^n_j i^n_j + \frac{\beta}{K} i^n_j (1 + \tau G(\rho^n_j)) \\
&\qquad \times \underbrace{\left[F^n_{j-1\to j}\, u^n_{j-1} + F^n_{j+1\to j}\, u^n_{j+1} - (F^n_{j\to j-1} + F^n_{j\to j+1})u^n_j\right]}_{=\Phi} \\
H_3 &\coloneqq -q\underbrace{\left[\tilde{F}^n_{j-1\to j}\, i^n_{j-1} + \tilde{F}^n_{j+1\to j}\, i^n_{j+1} - (\tilde{F}^n_{j\to j-1} + \tilde{F}^n_{j\to j+1})i^n_j\right]}_{=\Psi}
\end{aligned}$$

Dividing both sides by τ and rearranging the terms we get

$$\frac{i^{n+1}_j - i^n_j}{\tau} = \frac{1}{\tau}\Psi - q i^n_j + \frac{\beta}{K} u^n_j i^n_j + H_2 + H_3 \tag{2.6}$$

Let us now make the same regularity assumptions of the previous subsection and use the Taylor expansions for i to arrive at

$$i_j^{n+1} = i(t_n + \tau, x_j) = i + \tau \partial_t i + \mathcal{O}(\tau^2)$$
$$i_{j\pm1}^n = i(t_n, x_j \pm \delta) = i \pm \delta \partial_x i + \frac{1}{2}\delta^2 \partial_{xx}^2 i + \mathcal{O}(\delta^3)$$

Again, we treat separately the case in which movement does not depend on pressure and the case in which it does.

Undirected cell movement In this case, we have

$$\Phi = \theta_u(u_{j-1}^n + u_{j+1}^n - 2u_j^n) = \theta_u \delta^2 \partial_{xx}^2 u + \mathcal{O}(\delta^3)$$

and

$$\Psi = \theta_i(i_{j-1}^n + i_{j+1}^n - 2i_j^n) = \theta_i \delta^2 \partial_{xx}^2 i + \mathcal{O}(\delta^3)$$

This means that $H_2 + H_3 = \mathcal{O}(\tau) + \mathcal{O}(\delta^2)$. Eq. (2.6) then becomes

$$\partial_t i + \mathcal{O}(\tau^2) = \theta_i \frac{\delta^2}{2\tau} \partial_{xx}^2 i + \frac{\beta}{K} ui - qi + \mathcal{O}(\tau) + \mathcal{O}(\delta^2)$$

Letting $\tau, \delta \to 0$ in such a way that $\frac{\delta^2}{2\tau} \to D$ we obtain the required term:

$$\partial_t i = \theta_i D \partial_{xx}^2 i + \frac{\beta}{K} ui - qi$$

Pressure-driven cell movement In this case $F_{j\to j\pm1}^n$ and $\tilde{F}_{j\pm1\to j}^n$ are $\mathcal{O}(\delta)$. It is then easy to see that $H_2 + H_3 \to 0$ as $\tau, \delta \to 0$, as each term is multiplied either by τ, by some F or by some $\tilde{F}$. We can then repeat the calculations already performed for the uninfected cells to show that, letting $\tau, \delta \to 0$ in such a way that $\frac{\delta^2}{2\tau} \to D$ yields

$$\frac{1}{\tau}\Psi \to \frac{\theta_i D}{P} \partial_x(i \partial_x \rho)$$

Therefore, in the required limit Eq. (2.6) becomes

$$\partial_t i = \frac{\theta_i D}{P} \partial_x(i \partial_x \rho) + \frac{\beta}{K} ui - qi$$

2.2.3 Summary of the continuum models

In the case of undirected cell movement, we have obtained the following system of reaction-diffusion PDEs:

$$\begin{cases} \partial_t u(t,x) = D_u \partial_{xx}^2 u(t,x) + p u(t,x) G(\rho(t,x)) - \dfrac{\beta}{K} u(t,x) i(t,x) \\ \partial_t i(t,x) = D_i \partial_{xx}^2 i(t,x) + \dfrac{\beta}{K} u(t,x) i(t,x) - q i(t,x) \end{cases} \tag{2.7}$$

where $D_u := \theta_u D$ and $D_i := \theta_i D$.

If we take the function G as in Eq. (2.1) and $\rho = u + i$, then the system becomes

$$\begin{cases} \partial_t u = D_u \partial_{xx}^2 u + pu\left(1 - \dfrac{u+i}{K}\right) - \dfrac{\beta}{K} ui \\ \partial_t i = D_i \partial_{xx}^2 i + \dfrac{\beta}{K} ui - qi \end{cases} \tag{2.8}$$

This model is a simplified version of the one studied in Pooladvand et al., 2021, as here we do not consider viral dynamics explicitly. A similar diffusive Lotka–Volterra model with logistic growth has been studied in Dunbar, 1984; it is important to observe that in our case the infected cells, which play the role of predators, contribute to the saturation of the growth of uninfected cells, which play the role of prey, hence Eq. (2.8) cannot be adimensionalised exactly in the same way as the model in Dunbar, 1984.

On the other hand, if we take the function $G(\rho) \equiv p$, then the system becomes

$$\begin{cases} \partial_t u = D_u \partial_{xx}^2 u + pu - \dfrac{\beta}{K} ui \\ \partial_t i = D_i \partial_{xx}^2 i + \dfrac{\beta}{K} ui - qi \end{cases} \tag{2.9}$$

which is a simplification of the previous system. Observe that in this setting, the carrying capacity has no specific meaning and we only keep it as a scaling parameter of the infection rate in order to facilitate the comparison with the results obtained with the other models.

Remark 2.1 *When the spatial domain is the two-dimensional real plane $\mathbb{R}^2$ instead of the one-dimensional real line $\mathbb{R}$, the scalar index $j \in \mathbb{Z}$ should be replaced by the vector $\boldsymbol{j} = (j_x, j_y) \in \mathbb{Z}^2$ and the probability that a cell moves to one of the four neighbouring lattice points is $\theta_k/4$, with $k = u, i$. We then need to scale τ and δ in such a way that $\frac{\delta^2}{4\tau} \to D$. The corresponding continuum model is*

$$\begin{cases} \partial_t u(t,x) = D_u \Delta u(t,x) + pu(t,x)G(\rho(t,x)) - \dfrac{\beta}{K} u(t,x)i(t,x) \\ \partial_t i(t,x) = D_i \Delta i(t,x) + \dfrac{\beta}{K} u(t,x)i(t,x) - qi(t,x) \end{cases}$$

In the case of pressure-driven cell movement, we have obtained the following local cross-diffusion system:

$$\begin{cases} \partial_t u(t,x) = \dfrac{D_u}{P} \partial_x [u(t,x)\partial_x \rho(t,x)] + pu(t,x)G(\rho(t,x)) - \dfrac{\beta}{K} u(t,x)i(t,x) \\ \partial_t i(t,x) = \dfrac{D_i}{P} \partial_x [i(t,x)\partial_x \rho(t,x)] + \dfrac{\beta}{K} u(t,x)i(t,x) - qi(t,x) \end{cases} \tag{2.10}$$

where $D_u := \theta_u D$ and $D_i := \theta_i D$. This model can be thought as the natural generalisation to infections of the model presented in Perthame et al., 2014; Byrne and Drasdo, 2009. A similar system is studied in Gwiazda et al., 2019, although it is important to remark that our infection term does not fit in the framework of reaction terms considered in that paper.

If we take the function G as in Eq. (2.1) and $\rho = u + i$ (so that also $P = K$), then the system becomes

$$\begin{cases} \partial_t u = \dfrac{D_u}{K}\partial_x[u\partial_x(u+i)] + pu\Big(1 - \dfrac{u+i}{K}\Big) - \dfrac{\beta}{K}ui \\ \partial_t i = \dfrac{D_i}{K}\partial_x[u\partial_x(u+i)] + \dfrac{\beta}{K}ui - qi \end{cases} \tag{2.11}$$

Remark 2.2 *When the spatial domain is the two-dimensional real plane $\mathbb{R}^2$ instead of the one-dimensional real line $\mathbb{R}$, the scalar index $j \in \mathbb{Z}$ should be replaced by the vector $\boldsymbol{j} = (j_x, j_y) \in \mathbb{Z}^2$ and the probability that a cell moves to one of the four neighbouring lattice points is*

$$\theta_k \frac{(\rho_j^n - \rho_{j+\boldsymbol{e}}^n)_+}{4P}$$

with $k = u, i$ and $\boldsymbol{e} \in \{(\pm 1, 0), (0, \pm 1)\}$. As in the case of Remark 2.1, we need to scale τ and δ in such a way that $\frac{\delta^2}{4\tau} \to D$. The corresponding continuum model when G as in Eq. (2.1) and $\rho = u + i$ is

$$\begin{cases} \partial_t u = \dfrac{D_u}{K}\nabla \cdot [u\nabla(u+i)] + pu\Big(1 - \dfrac{u+i}{K}\Big) - \dfrac{\beta}{K}ui \\ \partial_t i = \dfrac{D_i}{K}\nabla \cdot [u\nabla(u+i)] + \dfrac{\beta}{K}ui - qi \end{cases}$$

2.3 Travelling waves for the continuum models

In view of the forthcoming comparison of the different models, it is useful to keep in mind some well-known analytical results about travelling waves. We first describe the equilibria of the corresponding nonspatial models, which serve as a starting point for the search of travelling wave solutions. We then recall some well-known results related to one dimensional waves and we describe some standard techniques that can be applied in more general situations. We then conclude by applying this considerations to the case of our interest.

2.3.1 Equilibria of the corresponding nonspatial models

We first recall that the system

$$\begin{cases} \dfrac{\mathrm{d}u}{\mathrm{d}t} = pu - \dfrac{\beta}{K}ui \\ \dfrac{\mathrm{d}i}{\mathrm{d}t} = \dfrac{\beta}{K}ui - qi \end{cases} \tag{2.12}$$

(which is the spatially homogeneous analog of Eq. (2.9)) has two equilibria, $(0, 0)$ and

$$\Big(\frac{qK}{\beta}, \frac{pK}{\beta}\Big) \tag{2.13}$$

The Jacobian matrix computed at the first equilibrium point has eigenvalues p and $-q$, so it is unstable; the Jacobian matrix computed at the second equilibrium point has eigenvalues $\pm \mathrm{i}\sqrt{pq}$, so it is neutrally stable.

Let us also recall that the system

$$\begin{cases} \dfrac{\mathrm{d}u}{\mathrm{d}t} = pu\left(1 - \dfrac{u+i}{K}\right) - \dfrac{\beta}{K}ui \\ \dfrac{\mathrm{d}i}{\mathrm{d}t} = \dfrac{\beta}{K}ui - qi \end{cases} \tag{2.14}$$

(which is the spatially homogeneous analogue of Eqs. (2.8) and (2.11)) has three equilibria: $(0,0)$, $(K,0)$ and

$$(u^*, i^*) := \left(\frac{qK}{\beta}, \frac{pK(\beta - q)}{\beta(\beta + p)}\right) \tag{2.15}$$

The Jacobian matrix computed at the first equilibrium point has eigenvalues p and $-q$, so it is unstable (recall that all the parameters are strictly positive). The Jacobian matrix computed at the second equilibrium point has eigenvalues $-p$ and $\beta - q$, so it is stable when $\beta < q$ (i.e., $i^* < 0$) and unstable when $\beta > q$ (i.e., $i^* > 0$). The expression for the eigenvalues of the Jacobian matrix computed at the last equilibrium point is more complicated, but their sum is $-\frac{pq}{\beta}$ and their product is $\frac{pq(\beta-q)}{\beta}$: hence, when $i^* > 0$ the eigenvalues are either both real and negative or complex with negative real part; in both cases, the equilibrium is stable.

Observe that, in the case of $\beta < q$ and positive initial data, the only possible outcome predicted by Eq. (2.14) is the extinction of infected cells and the growth of the uninfected cells to the carrying capacity, which in our biological interpretation corresponds to a complete failure of the treatment. As also pointed out in other works, the interplay between the infection rate and the death rate of infected cells is responsible, to some extent, for the success of the overall therapy (Jenner et al., 2018b; Pooladvand et al., 2021). Infections that start and develop too quickly seem to carry less ability to effectively control the tumour in the long run. This can be circumvented, to some extent, by encasing the virus in gels or implementing strategies to retard and prolong its release (Jenner et al., 2019; Pooladvand et al., 2021; Jenner et al., 2020; Jenner et al., 2018c). On the other hand, the case of an ineffective treatment does not exist mathematically in the case of Eq. (2.12), as the equilibrium values $(qK/\beta, pK/\beta)$ are positive for all values of the parameters. The shortcoming is the fact that for $\beta \ll q$, all the dynamics happen at much higher density levels than those involved in the case of logistic growth and, as such, appear biologically irrelevant. From now on, we focus on the situation $\beta > q$.

2.3.2 Travelling waves involving a single equation and linearisation

We recall that the equation

$$\partial_t u = D\partial^2_{xx} u + pu\left(1 - \frac{u}{K}\right) \tag{2.16}$$

admits as solutions travelling waves with speed at least $2\sqrt{Dp}$ and an initial condition with compact support evolves into a wave that travels with the minimal speed (Fisher, 1937; Kolmogorov et al., 1937). Any reaction-diffusion equation of the form $\partial_t u = D\partial^2_{xx} u + f(u)u$ such that $f'(0) = p$ has the same invasion speed $2\sqrt{D_u p}$ (Kolmogorov et al., 1937); this result can be easily obtained using standard linearisation techniques (Van Saarloos, 2003, §2.1), which we now briefly sketch for the sake of completeness.

Let us consider a nonlinear PDE

$$\partial_t \phi(t,x) = \mathcal{F}[\phi]$$

and let $\partial_t \phi(t,x) = \mathcal{L}[\phi]$ be its linearization close to 0; we assume that the state $\phi = 0$ is linearly unstable. Let us also assume that

$$\phi(0,x) = \int_{-\infty}^{+\infty} \bar{\phi}(k) e^{\mathrm{i}kx}\,\mathrm{d}k$$

(which means that $\bar{\phi}$ is the Fourier transform of the initial condition). We can then substitute $e^{-\mathrm{i}\omega(k)t+\mathrm{i}kx}$ in the linear equation to obtain the *dispersion relation* $\omega(k)$; then, we formally have

$$\phi(t,x) = \int_{-\infty}^{+\infty} \bar{\phi}(k) e^{\mathrm{i}kx-\mathrm{i}\omega(k)t}\,\mathrm{d}k$$

In the moving frame given by $\xi := x - v^* t$ the previous expression becomes

$$\phi(t,x) = \int_{-\infty}^{+\infty} \bar{\phi}(k) e^{\mathrm{i}kx-\mathrm{i}kv^*t-\mathrm{i}\omega(k)t+\mathrm{i}kv^*t}\,\mathrm{d}k = \int_{-\infty}^{+\infty} \bar{\phi}(k) e^{\mathrm{i}k\xi-\mathrm{i}[\omega(k)-v^*k]t}\,\mathrm{d}k \tag{2.17}$$

For ξ finite and $t \to +\infty$ we use the Laplace method to obtain that the dominant contribution of the integral is $e^{-\mathrm{i}[\omega(k^*)-v^*k^*]t}$, where k^* is given by the relation

$$\frac{\mathrm{d}[\omega(k)-v^*k]}{\mathrm{d}k}\Big|_{k^*} = 0 \implies v^* = \omega'(k^*)$$

In order to avoid exponential growth and decay, we must have $\Re\{\mathrm{i}[\omega(k^*)-v^*k^*]\} = 0$, which means

$$\Im[\omega(k^*)] - v^*\Im[k^*] = 0 \implies v^* = \omega'(k^*) = \frac{\Im[\omega(k^*)]}{\Im[k^*]}$$

We then approximate the integral of Eq. (2.17) and obtain

$$\phi(t,x) \approx \frac{1}{\sqrt{4\pi\hat{D}t}} e^{\mathrm{i}k^*\xi-\mathrm{i}\Re[\omega(k^*)]t} e^{-\xi^2/4\hat{D}t} \bar{\phi}(k^*) \quad \text{where } \hat{D} := \frac{\mathrm{i}}{2}\omega''(k^*)$$

$e^{\mathrm{i}k^*\xi}$ describes the *dominant spatial behaviour*, while $\hat{D}$ is the *effective diffusion coefficient*, which characterises the Gaussian correction to the exponential behaviour.

We can now apply these results to the equation

$$\partial_t \phi = D\partial_{xx}^2\phi + f(\phi)\phi$$

We have $\mathcal{L}[\phi] = D\partial_{xx}^2\phi + f'(0)\phi$ and thus

$$-\mathrm{i}\omega(k) = -Dk^2 + f'(0) \implies \omega(k) = \mathrm{i}(f'(0) - Dk^2), \quad \omega'(k) = -2\mathrm{i}Dk$$

Then from the equation $-2\mathrm{i}Dk^* = \Im[i(f'(0) - Dk^2)]/\Im[k]$ we easily obtain

$$k^* = \pm\mathrm{i}\sqrt{\frac{f'(0)}{D}}$$

which yields $v^* = \pm 2\sqrt{Df'(0)}$ (depending on the direction of the wave) and $\hat{D} = D$. A special case is $f(u)$ constant and equal to p, which corresponds to exponential growth.

On the other hand, the application of these techniques to an intrinsically nonlinear equation, such as

$$\partial_t u = \frac{D}{K}\partial_x(u\partial_x u) + f(u)u \tag{2.18}$$

does not give any meaningful information. In the specific case of the equation

$$\partial_t u = \frac{D}{K}\partial_x(u\partial_x u) + pu\left(1 - \frac{u}{K}\right) \tag{2.19}$$

it is known that there exist travelling wave solutions with speed at least $\sqrt{Dp/2}$ and an initial condition with compact support evolves into a wave that travels with the minimal speed (Aronson, 1980; Newman, 1980). The main difference with respect to Eq. (2.16) is the fact that initial data with compact support evolve into sharp waves with compact support.

2.3.3 Travelling waves involving two equations

We now focus our attention on travelling wave solutions of systems in the form of Eqs. (2.8), (2.9) and (2.11). We first recall that in Dunbar, 1984 it was proven that a system similar to Eq. (2.8) (in which "predators" do not contribute to the saturation of uninfected cells' growth) admits travelling waves connecting (u^*, i^*) to $(K, 0)$ with speed greater or equal to $2\sqrt{D_i(\beta - q)}$ and damped oscillations after the front of the wave may appear. Since we are mostly interested in the case of a tumour that is still expanding, it makes more sense to look for travelling waves connecting (u^*, i^*) to $(0, 0)$ and we expect to observe a race between the uninfected cells (evolving according to Eq. (2.16) in the absence of infected cells) and the infected cells at the centre of the tumour. This situation is shown in Fig. 2.2a and it is clearly more complex than the one examined in Dunbar, 1984. Let us observe that the density of a population of infected cells invading a region of uninfected cells at constant density $\hat{u}$ satisfies the equation

$$\partial_t i = D_i\partial^2_{xx} i + \left(\frac{\beta}{K}\hat{u} - q\right)i$$

According to the previous discussion about linearisation techniques, we expect infected cells to travel at speed $2\sqrt{D_i(\frac{\beta}{K}\hat{u} - q)}$; for $\hat{u} = K$ we recover the expression $2\sqrt{D_i(\beta - q)}$ (as it is shown in Fig. 2.2a).

To our knowledge there are no rigorous analytical results for travelling waves solving Eqs. (2.9) and (2.11). Since the substitution of the logistic growth with the exponential growth keeps the linear form of the equation unchanged, it is reasonable to expect that travelling waves are not too affected by this change: indeed, the numerical simulation in Fig. 2.2b confirms this expectation. We remark that, although the equilibrium given by Eq. 2.13 is only neutrally stable and not asymptotically stable, this does not prevent the formation of waves: indeed, the eigenvalues of the matrix

$$\begin{pmatrix} p - \frac{\beta}{K}i & -\frac{\beta}{K}u \\ \frac{\beta}{K}i & \frac{\beta}{K}u - q \end{pmatrix}\Bigg|_{(u,i)=(qK/\beta, pK/\beta)} + \begin{pmatrix} -D_u\sigma^2 & 0 \\ 0 & -D_i\sigma^2 \end{pmatrix} = \begin{pmatrix} -D_u\sigma^2 & -q \\ p & -D_i\sigma^2 \end{pmatrix}$$

are either both negative or complex with negative real part $-\frac{D_u + D_i}{2}\sigma^2$. In other words, the addition of diffusion to the system is enough to make the equilibrium asymptotically stable (see also Murray, 2003).

On the other hand, the situation of pressure-driven movement is more complicated. Clearly, an initial condition in which the function i has compact support surrounded by an area with $u = K$ cannot evolve into a travelling wave connecting $(K, 0)$ to (u^*, i^*), as the spatial movement of i is inhibited in the areas in which u is at carrying capacity (see Fig. 2.3a). As a consequence, the classical problem of a new predator or a new infection

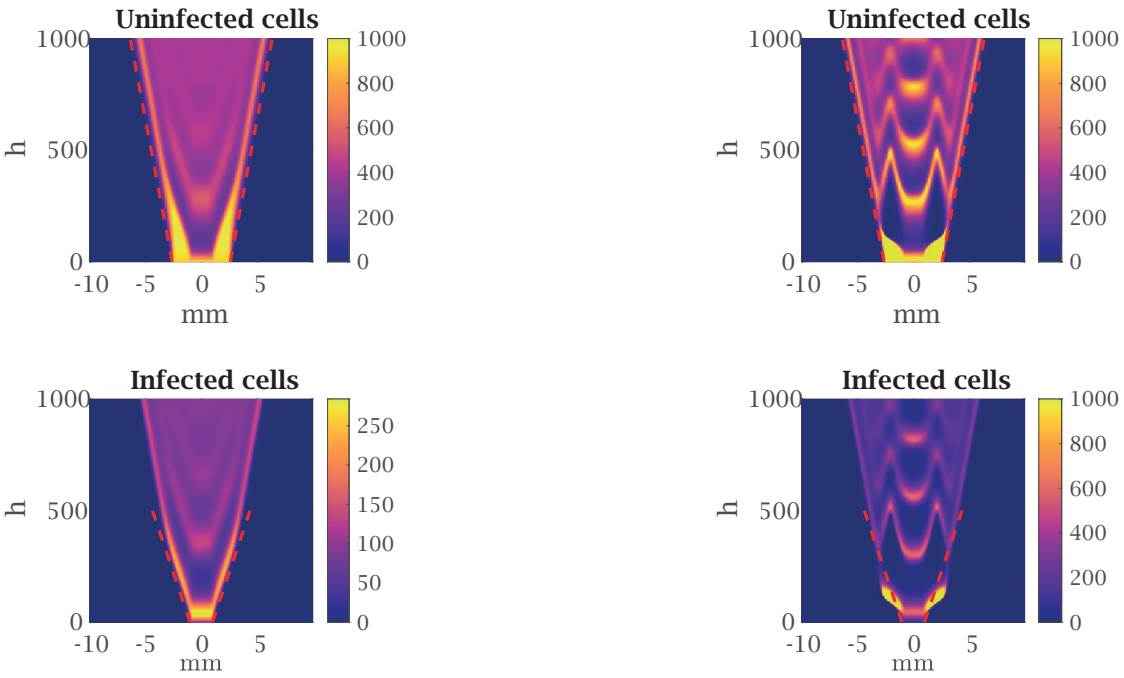

(a) diffusion and logistic growth

(b) diffusion and exponential growth

FIGURE 2.2: Numerical solutions of (a) Eq. (2.8) and (b) Eq. (2.9). Theoretical results correctly estimate the speeds of the travelling waves of uninfected cells in both cases and of infected cells in panel (a). The results are discussed more in-depth in the following sections. The parameters employed are the ones given in Table 2.1.

invading an established population makes no sense in this context. On the other hand, the numerical results in Fig. 2.3b show the existence of a travelling wave evolving from $(0,0)$ to (u^*, i^*). Let us also observe that the movement depends on the local density, so the speed expression $\sqrt{D_u p/2}$ is only valid when the invading front is at carrying capacity; when the front is smaller due to the infection, it also moves slower. In the case of Fig. 2.3b, the invading front is close enough to K, so that the value $\sqrt{D_u p/2}$ is still a good approximation for the speed of uninfected invasion.

Let us conclude this section by recalling the fact that all the speed wave expressions are accurate in one spatial dimension. In two spatial dimensions, the same formulas describe the asymptotic speed for the radially symmetric equation (see, for example, Murray, 2002, §13.2); our numerical simulations show that the formulas of this section approximate the wave speed well enough in the parameters' range of our interest.

2.4 Comparison between agent-based and continuum models

In this section, we compare numerical simulations for the agent-based models with the corresponding PDE systems.

2.4.1 Details of numerical simulations

Parameter values In Table 2.1, we list the parameters we adopt as a reference in the numerical simulations. Some simulations use other parameter values to explore different behaviours emerging from our model, as explained in the text.

Most of the parameters in the model have been estimated from the existing experimental literature. The maximal duplication rate in the logistic growth p has been taken

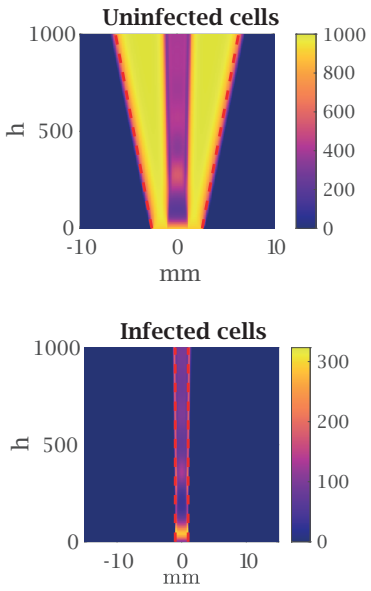

(a) pressure-driven movement and central infection

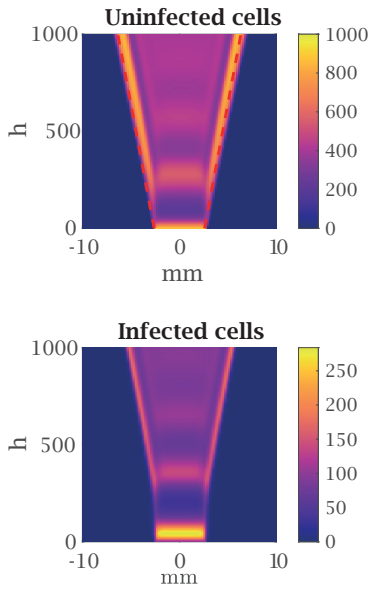

(b) pressure-driven movement and wide infection

FIGURE 2.3: Numerical solutions of Eq. (2.11) show that theoretical results correctly estimate the speed of the travelling waves for uninfected cells. The parameters employed are the ones given in Table 2.1, with the exception of the infection radius R_i in panel (b). Observe that a central initial infection remains constrained in the centre of the domain. The results are discussed in more depth in the following sections.

Parameter	Description	Value [Units]	Reference
p	maximal duplication rate of uninfected cells	1.87×10^{-2} [h^{-1}]	Ke et al., 2000
q	death rate of infected cells	4.17×10^{-2} [h^{-1}]	Ganly et al., 2000
D_u, D_i	diffusion coefficients (undirected movement)	1.88×10^{-4} [mm^2/h]	estimate based on Kim et al., 2006
D_u, D_i	diffusion coefficients (pressure-driven movement)	1.50×10^{-3} [mm^2/h]	estimate based on Kim et al., 2006
K^{1D}	tissue carrying capacity in one dimension	10^3 [cells/mm]	model estimate
K^{2D}	tissue carrying capacity in two dimensions	10^4 [cells/mm^2]	Lodish et al., 2008
β	infection rate	1.02×10^{-1} [h^{-1}]	estimate based on Friedman et al., 2006
R_u	initial radius of uninfected cells	2.6 [mm]	Kim et al., 2006
R_i	initial radius of infected cells	1 [mm]	model estimate

TABLE 2.1: Reference parameter set for this chapter.

equal to $\log(2)/37\ h^{-1} \approx 1.87 \times 10^{-2}\ h^{-1}$; the duplication time of 37 hours is approximately the highest among the ones reported in Ke et al., 2000 and has been chosen so that the exponential growth is not too fast. The death rate of infected cells q has been taken equal to $1/24\ h^{-1} = 4.17 \times 10^{-2}\ h^{-1}$, following Ganly et al., 2000.

The diffusion coefficient of uninfected cells D_u has been estimated from the experimental data of the U343 control group of Kim et al., 2006, as already done in Pooladvand et al., 2021: the tumour volume passes in 40 days from 70 mm^3 to 1000 mm^3, which corresponds to a change in the tumour radius from approximately 2.6 mm to approximately 6.2 mm; since in absence of viral infection the dynamic of uninfected cells follows Eq. (2.16) in the case of undirected movement and Eq. (2.19) in the case of pressure-driven movement, we can estimate the diffusion coefficient from the wave

speed formulas described in Section 2.3 and obtain

$$D_u = \frac{c^2}{4p} = \left(\frac{6.2 - 2.6 \text{ mm}}{40 \times 24 \text{ h}}\right)^2 \times \frac{1}{4 \times 1.87 \times 10^{-2} \text{ h}^{-1}} \approx 1.88 \times 10^{-4} \text{ mm}^2/\text{h}$$

in the former case and

$$D_u = \frac{2c^2}{p} \approx 8 \times 1.88 \times 10^{-4} \text{ mm}^2/\text{h} \approx 1.50 \times 10^{-3} \text{ mm}^2/\text{h}$$

in the latter case. We assume $D_i = D_u$, as a priori we have no reason to believe that the infection affects cellular movement.

In the agent-based models, cellular movement is governed by the parameters θ_u and θ_i. Having in mind the formal derivation of the continuum models, we set them according to the formula

$$\theta_k = \begin{cases} \dfrac{2\tau D_k}{\delta^2} & \text{in one dimension} \\ \dfrac{4\tau D_k}{\delta^2} & \text{in two dimensions} \end{cases} \tag{2.20}$$

where $k = u, i$ and τ, δ are the temporal and spatial discretisations. For the sake of simplicity, in the text, we always refer to the the variation of the diffusion coefficients (which have a clear macroscopic meaning), keeping in mind that θ_u and θ_i are adjusted accordingly.

The carrying capacity K has been estimated assuming that a cell has radius 10 μm$=10^{-2}$ mm (Lodish et al., 2008, §1.1): this implies that the carrying capacity is 10^2 cells/mm in one spatial dimension and 10^4 cells/mm^2 in two spatial dimensions. Since we observed that $K = 100$ cells/mm is too little to obtain a good agreement between agent-based and continuum models, we decided to increase it to $K = 1000$ cells/mm in the case of one spatial dimension.

Let us now estimate the infection rate β. In Friedman et al., 2006 the authors assume that oncolytic viruses have an infection rate of $\tilde{\beta} = 7 \times 10^{-10}$ mm^3/(viruses$\times$h) and cells have a carrying capacity of $\tilde{K} = 10^6$ cells/mm^3. Clearly, this value cannot be used directly in our model, which does not explicitly take viral dynamics into account. Let us assume that viral density satisfies the PDE

$$\partial_t v(t,x) = D_v \partial^2_{xx} v(t,x) + \alpha q i(t,x) - q_v v(t,x)$$

where D_v is the diffusion coefficient, α is the number of viruses released by the lysis when an infected cell dies, q is the death rate of infected cells (which is also present in our model) and q_v is the clearance rate of the virus. Since viral dynamics are faster than cellular dynamics, we can assume that the viral density is quasi-steady, leading to the algebraic relation

$$v(t,x) = \frac{\alpha q}{q_v} i(t,x)$$

We, therefore, have $\beta = \tilde{\beta}\alpha q \tilde{K}/q_v$, with the values of the parameters α and q_v to be chosen. We set $q_v = 1/6$ h^{-1} as in Mok et al., 2009. The viral load released by the death of infected cells depends highly on the type of virus and ranges from the value 157 ± 23.4 viruses/cell estimated in Workenhe et al., 2014 to the value 3500 viruses/cell of Chen et al., 2001; we chose an intermediate value of $\alpha = 580$ viruses/cell. In conclusion,

we have

$$\beta = \left(7 \times 10^{-10} \, \frac{\text{mm}^3}{\text{viruses} \times \text{h}}\right) \times \frac{580 \text{ viruses/cell} \times 1/24 \text{ h}^{-1}}{1/6 \text{ h}^{-1}} \times 10^6 \, \frac{\text{cells}}{\text{mm}^3} \approx 0.102 \text{ h}^{-1}$$

It is important to observe that the parameter β incorporates a wide variety of dynamics related to the virus; hence different parameter values could result in the same value of β: for example, if we assume a faster viral decay of $q_v = 1 \text{ h}^{-1}$ and a higher number of viruses released during lysis $\alpha = 3500$ viruses/cell as in Chen et al., 2001, then the value of β remains unchanged.

Finally, we use the following initial conditions

$$u_0(x) = \begin{cases} 0.9\,K & \text{for } |x| \leq R_u \\ 0 & \text{for } |x| > R_u \end{cases} \qquad i_0(x) = \begin{cases} 0.1\,K & \text{for } |x| \leq R_i \\ 0 & \text{for } |x| > R_i \end{cases} \tag{2.21}$$

The value of R_u has been set to 2.6 mm, as in Kim et al., 2006. Remembering that we postulate a central injection (Russell and Peng, 2018), we observe that it is not easy to find reliable estimates for the radius of the region occupied by infected cells right after such an injection. We thus chose the value $R_i = 1$ mm, which is slightly less than half of the tumour radius. In the model with undirected movement, initial conditions do not really affect the long-time dynamics of the system. On the other hand, varying initial conditions in the model with pressure-driven movement may result in opposite outcomes, as the infection is unable to propagate in areas of constant total density.

Numerical simulations are run until the final time $T = 1500$ h, since their behavior up to this moment is also representative of later dynamics. For the spatial domain $[-L, L]$ (or $[-L, L]^2$) we set $L = 10$ mm so that wavefronts do not hit the boundary before T and the domain is representative of typical extensions of solid tumours. Since some simulations of the model with pressure-driven movement have been performed with a higher value of D_u, D_i (and, consequently, a higher speed wave) in these situations L has been slightly increased.

Numerical simulations for the discrete models We used a temporal step $\tau = 0.02$ h and a spatial step of $\delta = 0.1$ mm both for the one-dimensional and the two-dimensional simulations. Some additional simulations (not shown) demonstrated that a further refinement on the grid does not result in a significant improvement of the agreement between discrete and continuous models, while greatly affecting the computation time. All simulations have been performed in MATLAB 2021B.

At every iteration, we first computed the sum of the two populations and then cell numbers are updated according to the rules described in Section 2.1. We first consider movement, then reproduction and death, finally infection. Zero-flux boundary conditions are implemented by not allowing cells at the boundary to leave the domain. This, however, does not have any particular influence on the results, as all the simulations are stopped before the wave front reaches the boundary.

Observe that the sum of the two populations is not updated during the iteration, in accordance with the formulas of Section 2.1. As a consequence, cell densities may fluctuate above the carrying capacity for short periods of time, before the dynamics make them decrease again. In order to avoid problems with the formula in Eq. (2.3), we truncate the pressure at the carrying capacity K. In the case of undirected movement, the fluctuations above the carrying capacity are more frequent because of the lack of movement inhibition in crowded regions (see Fig. 2.4); this, however, does not cause any problem in the formulation of the model.

Since we only need to keep track of the collective fate of cells in the same lattice point, we used the built-in MATLAB functions `binornd` and `mnrnd`, which compute random arrays according to binomial and multinomial distributions.

Figs. 2.4, 2.5, 2.6a-b, 2.7, 2.8, 2.9a-b, 2.10, 2.11 and 2.13 show the average of five simulations. On the other hand, Figs. 2.6 (with the exception of Figs. 2.6a-b), 2.9 (with the exception of Figs. 2.9a-b) and 2.14 have the purpose of explaining the influence of stochastic effects and therefore show a single simulation. Averaging simulations in two dimensions results in nonzero cell densities below $\frac{1}{\delta^2}$, which makes no sense in the case of a single simulation; for the sake of consistency, we decided to truncate these values to zero.

In order to allow reproducibility, a random seed has been set at the beginning of each new simulation, ranging from 1 to 5. In the figures representing a single simulation, only the one with random seed equal to 1 is shown. Fig. 2.12 shows the average of one hundred simulations, which were obtained using random seeds ranging from 1 to 100.

Numerical simulations for the continuum models Eqs. (2.8) and (2.11) complemented with homogeneous Neumann boundary conditions have been solved in MATLAB 2021B using the built-in function `pdepe`; in the two-dimensional case we exploited the radial symmetry of the equations. We considered a uniform discretisation of the spatial interval $[0, L]$ consisting of 500 points and a uniform discretisation of step 1 of the temporal interval $[0, T]$.

The application of this strategy to the simulation depicted in Figs. 2.10a, 2.11a caused some numerical instabilities. We solved this issue by using a forward upwind scheme for the transport term, following LeVeque, 2007. This method is able to deal with such instabilities even at long times if we take the discretisation $\Delta x = 0.05$, $\Delta t = 10^{-4}$. We then used the same algorithm for all the numerical solutions of Eq. (2.11) for the sake of coherence, with discretisations $\Delta x = 0.1$, $\Delta t = 10^{-4}$. In the two-dimensional case, we can rely upon the radial symmetry of the problem; hence, the analogue of Eq. (2.11) becomes

$$\begin{cases} \partial_t u = \dfrac{D_u}{K}\dfrac{1}{r}\partial_r[r\,u\partial_r(u+i)] + pu\left(1-\dfrac{u+i}{K}\right) - \dfrac{\beta}{K}ui \\ \partial_t i = \dfrac{D_i}{K}\dfrac{1}{r}\partial_r[r\,i\partial_r(u+i)] + \dfrac{\beta}{K}ui - qi \end{cases}$$

In the two-dimensional plots of the supplementary material of Morselli et al., 2023, we truncated the solutions at a value $\frac{1}{\delta^2}$ to be consistent with the representation of the agent-based model. We also use the same threshold $\frac{1}{\delta^2}$ to identify the wavefront, which is depicted in some of the figures. However, it is important to observe that in some simulations the density of infected cells is positive almost in the whole domain occupied by uninfected cells; the definition of the front as the location in which cell density is above $\frac{1}{\delta^2}$ makes visual comparison between the discrete and the continuous model clearer.

2.4.2 Undirected movement and logistic growth

We are now ready to compare numerical simulations for the agent-based models and the corresponding systems of PDE. We start from the model with standard diffusion and logistic growth since, in this case, there exist comprehensive analytical results for travelling waves. We first present the results obtained with the reference parameters listed in Table 2.1 in both one and two dimensions; we then investigate how different parameters allow us to obtain other spatial patterns.

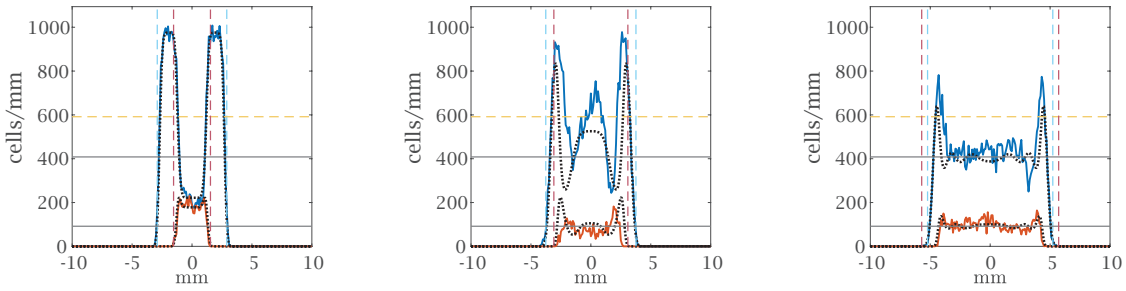

(a) $t = 80$ h (b) $t = 310$ h (c) $t = 700$ h

FIGURE 2.4: Comparison in one spatial dimension between numerical simulations of the discrete model with undirected movement and logistic growth (solid lines) and the numerical solution of Eq. (2.8) (dotted black lines) at three different times, with the parameters given in Table 2.1. For the agent-based model, the density of the uninfected cells is represented in blue and the density of infected cells in red. The vertical dashed lines represent the expected positions of the uninfected and infected invasion fronts, travelling respectively at speed $2\sqrt{D_u p}$ (blue lines) and $2\sqrt{D_i(\beta - q)}$ (red lines); the latter has no biological meaning in panel (c), as the infection cannot go beyond the uninfected front. The horizontal solid black lines show the equilibrium of the ODE given by Eq. (2.15) and the horizontal dashed yellow line represents the expected uninfected density at the front given by Eq. (2.22) (only relevant in panel (c)). The results of the agent-based model are averaged over five simulations and the maximum of the cell density axes corresponds to the maximum over time of this average (which is larger than the carrying capacity).

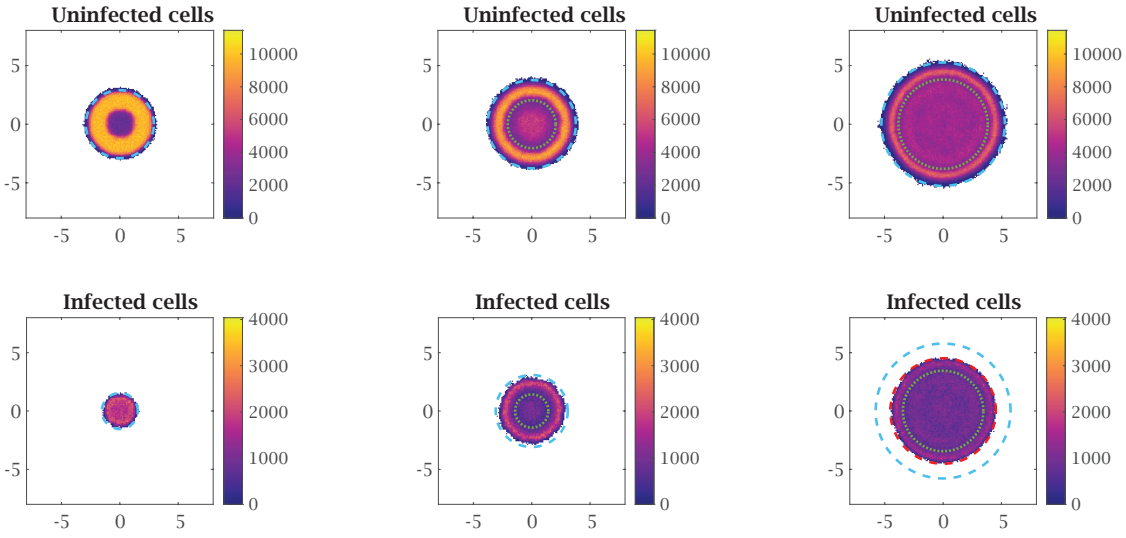

(a) $t = 80$ h (b) $t = 310$ h (c) $t = 710$ h

FIGURE 2.5: Numerical simulation of the discrete model with undirected movement and logistic growth in two spatial dimensions at three different times with the parameters given in Table 2.1. The dotted green circles represent the internal minimum of the numerical solution of Eq. (2.8) (not shown in panel (a), as this minimum is in 0). The dashed cyan circles represent the expected positions of the uninfected and infected invasion fronts, travelling respectively at speed $2\sqrt{D_u p}$ and $2\sqrt{D_i(\beta - q)}$. The latter has no biological meaning in panel (c), as the infection cannot go beyond the uninfected front; therefore, in this figure, we also show with a dashed red circle the front of the infected cells given by the numerical solution of Eq. (2.8). The results of the agent-based model are averaged over five simulations and the maximum of the colorbars for uninfected and infected cells correspond to the maximum over time of the averages (which for the uninfected cells is larger than the carrying capacity).

Reference parameters Fig. 2.4, along with the video accompanying it (see electronic supplementary material S2 of Morselli et al., 2023), shows an excellent quantitative agreement between numerical solutions of the system of PDEs (2.8) and the average over five numerical simulations of the agent-based model in one spatial dimension. At the beginning of the simulations, the central region of the tumour is quickly infected, while the outer region (which is only occupied by uninfected cells) grows up until reaching the carrying capacity. At the same time, a travelling wave of uninfected cells starts to invade the surrounding area at the speed $2\sqrt{D_u p}$ (vertical blue lines in Fig. 2.4), as predicted by theoretical results. As soon as the uninfected cells reach the carrying capacity, the invasion speed of the infected cells stabilises to the value $2\sqrt{D_i(\beta - q)}$ (vertical red lines in Fig. 2.4), which again confirms our expectations from analytical results. In the meantime, cell densities at the centre of the tumour converge with damped oscillations to the equilibrium of the corresponding ODE (horizontal solid black lines in Fig. 2.4), given by Eq. (2.15). This is shown in Fig. 2.4a.

The parameters we chose are such that $2\sqrt{D_u p} < 2\sqrt{D_i(\beta - q)}$, meaning that the infection eventually reaches the front of the wave of uninfected cells. This happens around time $t = 200$ h: as a consequence, the peak at the front starts to decrease for both populations and infected cells slow down (see Fig. 2.4b). The final peak of the uninfected cells is approximately

$$\bar{u} := \left(\frac{q}{\beta} + \frac{D_u p}{D_i \beta}\right) K = u^* + \frac{D_u p K}{D_i \beta} \tag{2.22}$$

which is the solution of the equation

$$2\sqrt{D_u p} = 2\sqrt{D_i\left(\frac{\beta}{K}\bar{u} - q\right)}$$

In other words, an uninfected population of cell density $\bar{u}$ is invaded by infected cells at speed $2\sqrt{D_u p}$, which is the speed of the uninfected front. A higher uninfected density at the front would result in a faster invasion of the infection, which would cause the front to decrease again; similarly, a smaller uninfected density at the front would slow down the infection and thus allow the uninfected front to grow. In our case, the density of the uninfected population is not constant, but the value $\bar{u}$ given in Eq. (2.22) is still a good approximation of the density at the front (see the horizontal dashed yellow line in Fig. 2.4c). As time passes, both front waves keep moving at the speed $2\sqrt{D_u p}$ and the central area; the fronts are followed by a few damped oscillations that converge to the equilibrium of the ODE. This is shown in Fig. 2.4c.

Fig. 2.5, along with the video accompanying it (see electronic supplementary material S3 of Morselli et al., 2023), shows that the same excellent agreement also holds in two spatial dimensions; the comparison with the continuum model and the analytical expressions of the wave speeds is shown through dashed and dotted coloured circles, as explained in the caption of the figure. Observe that, before cell densities converge to the equilibrium in the centre of the tumour, some concentric circles appear, in line with experimental observation (Wodarz et al., 2012); the internal circle, however, disappears as time passes.

Impact of the parameters on the treatment outcome Let us show how varying the parameters affects the success of the therapy, still for the case of growth that is unhindered by spatial or pressure constraints, but is only limited by carrying capacity. We only focus on two-dimensional simulations, but the one-dimensional case is analogous.

We start by analysing some instances of treatment failure. As we already pointed out in Section 2.3, the worst possible case is the situation in which the infection ceases after a

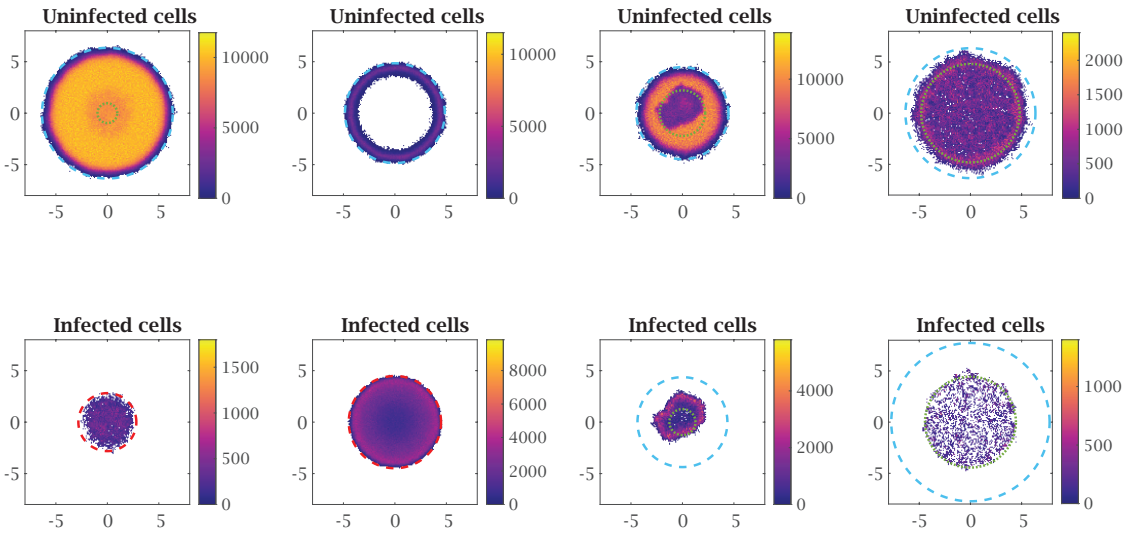

(a) $\beta = 4.86 \times 10^{-2}$ h^{-1}, $t = 1000$ h

(b) $q = 4.17 \times 10^{-3}$ h^{-1}, $t = 600$ h

(c) small initial conditions, $t = 500$ h

(d) $K = 10^3$ cells/mm, $t = 1000$ h

FIGURE 2.6: Numerical simulation of the discrete model with undirected movement in two spatial dimensions with different parameter values. The dotted green circles represent the internal minimum of the numerical solution of Eq. (2.8) (not shown when this minimum is in 0). The dashed cyan circles represent the expected positions of the uninfected invasion fronts, travelling at speed $2\sqrt{D_u p}$. The dashed red circles represent the front of the infected cells given by the numerical solution of Eq. (2.8). The parameters employed are the ones given in Table 2.1, with the exception of the infection rate β in panel (a) (which is set to 4.86×10^{-2} h^{-1}, i.e. less than half of the reference value), the death rate of infected cells q in panel (b) (which is set to 4.17×10^{-3} h^{-1}, i.e. one-tenth of the reference value), the initial conditions in panel (c) (whose densities are set to $0.09\,K$ for uninfected cells and $0.01\,K$ for infected cells, i.e. one-tenth of the reference values of Eq. (2.21)) and the carrying capacity K in panel (d) (which is set to 10^3 cells/mm; initial conditions are scaled accordingly). The first two figures are the averages over five simulations, while the last two represent single simulations. In both cases, the maximum of the colorbars for uninfected and infected cells correspond to the maximum over time of the quantity plotted, which for uninfected cells is larger than the carrying capacity (note the different values between different simulations).

finite time and uninfected cells grow at carrying capacity: this corresponds to parameter values such that $\beta < q$, which do not allow the equilibrium (u^*, i^*) to be positive. A more interesting case of failure, which has no analogue in the spatially homogeneous ODE, is the one in which the equilibrium (u^*, i^*) is positive and stable, the infected cells form a travelling wave, but the spread of the infection is smaller than the speed of the uninfected wave and so the outer region of the tumour is completely unaffected by the therapy. Fig. 2.6a shows this situation, obtained by decreasing the infection rate β with respect to the reference value. In this case, the value of u^* is more than 85% of the carrying capacity, so the invasion front is at carrying capacity and even in the central area the role of the infection is not really relevant, despite never ceasing completely. Similar situations are obtained whenever parameter values are such that

$$2\sqrt{D_i(\beta - q)} < 2\sqrt{D_u p}$$

If $D_u = D_i$, this condition is equivalent to $\beta < q + p$. We can thus conclude that, as we could easily expect, a decrease in the infection rate β or an increase either of the death rate of the infected cells q or the proliferation rate of the uninfected cells p with respect to the reference value makes the therapy less successful and, in extreme cases, useless. This scenario mimics, to some extent, that of an aggressively expanding tumour whose developing front is moving very fast, as in existing clinical settings (Eissa et al., 2018). We remark that our model assumes unrestricted tumour invasion in the surrounding tissues, allowing the front of the uninfected cell wave to escape from the infection indefinitely. This is a reasonable assumption for a tumour *in vitro*. On the other hand, the presence of physical obstacles in the tumour microenvironment that hinder tumour invasion *in vivo* may facilitate the infection of the whole tumour, reaching the equilibrium (u^*, i^*).

Whenever the infection reaches the boundary of the tumour (as in the reference situation), we can consider the therapy to be at least partially successful. Some variations of the parameter values then allow for the improvement of therapy achievements. For example, as the death rate of the infected cells q decreases, the infection propagates faster and u^* decreases, therefore the therapy becomes more effective. This situation is shown in Fig. 2.6b and captures the typical case when the virus has sufficient potency, as current clinical trials and therapeutic practice strive to achieve (Lawler et al., 2017; Hemminki et al., 2020). The centre of the tumour is almost completely void for most of the time, as the number of uninfected cells is negligible and the number of infected cells is quite small (although slightly bigger). At later times, some other inner circles emerge as a consequence of the damped oscillations leading to equilibrium; nevertheless, the emerging spatial structure can still be described as an empty ring. It is clear from these results that a way to make the therapy more efficient would be to increase β, as this would again result in a faster infection and a smaller uninfected population. A decrease of p would leave the number of uninfected cells at the equilibrium unchanged; yet, the tumour expansion would slow down and, as a consequence, the infection would reach the tumour boundary faster. Unlike the continuous model, the agent-based model may show extinction in finite time of both populations, which corresponds to the eradication of the tumour (not shown here). However, this would require changing parameters beyond the values that appear biologically meaningful. This is in line with results obtained from deterministic spatially homogenous models, for example, the simple one in Jenner et al., 2018c.

In all the cases described above, the results of the agent-based model perfectly agree with the ones given by the numerical solution of the corresponding PDE. Let us stress the fact that taking into account a single simulation in most cases reduces the quantitative agreement, but not the overall qualitative behavior: individual variations occur but a

$\beta < q$	uninfected cell wave at speed $2\sqrt{D_u p}$ and height K, no infection.
$q < \beta < q + \frac{D_u}{D_i} p$	uninfected cell wave at speed $2\sqrt{D_u p}$ and height K, central infection expanding at speed $2\sqrt{D_i(\beta - q)}$ without reaching the uninfected front; internal densities reach the values $\left(\frac{qK}{\beta}, \frac{pK(\beta-q)}{\beta(\beta+p)}\right)$.
$\beta > q + \frac{D_u}{D_i} p$	uninfected cell wave at speed $2\sqrt{D_u p}$ and height $\left(\frac{q}{\beta} + \frac{D_u p}{D_i \beta}\right) K$, infection up to the uninfected front; internal densities reach the values $\left(\frac{qK}{\beta}, \frac{pK(\beta-q)}{\beta(\beta+p)}\right)$.

TABLE 2.2: Summary of the different scenarios for the travelling waves as the infection rate β increases.

general, consistent trend is achieved.

Impact of stochasticity for lower cell densities We now present two simulations in which stochastic effects give rise to notable differences between the discrete and continuum approach, due to the fact that a smaller number of cells reduces the quality of the continuum approximation. This could correspond to a moderately extended tumour in its first stages of growth, for example. Fig. 2.6c shows the result of a single simulation with the parameters of Table 2.1 and smaller initial cell densities. Clearly, uninfected cells take longer than in the reference case to reach carrying capacity. As soon as they do, the infected area is much less regular than what the PDE predicts: this comes from the fact that the infection starts among a small number of cells and thus a few stochastic events affect the spatial distribution of the infection relevantly. As time passes, these differences tend to disappear.

Fig. 2.6d shows the situation in which the carrying capacity K is decreased and initial cell densities are scaled accordingly, in agreement with Eq. (2.21). At initial times, it is still possible to recognise the same qualitative behaviour of the PDEs, but as time passes, stochastic events drive the system into a very irregular spatial configuration.

Let us also mention what happens when we change the reference parameters for the scaled system (not shown here). If we decrease the death rate of infected cells, we still observe the void ring structure, although much less precise than the one of Fig. 2.6b. If the infection rate is decreased as in Fig. 2.6a, then the number of infected cells is so low that the infection undergoes extinction in a short time. We can, therefore, conclude that the PDEs remain a good description of the treatment outcome, even though the quantitative agreement is lost due to stochastic effects.

2.4.3 Undirected movement and exponential growth

We now analyse whether the growth of a small tumour that is not limited by the lack of external resources may be stopped only by viral infections. Unlimited exponential growth is clearly not feasible in any biological scenario, but we could imagine that in some cases, the carrying capacity is too high to make any significant contribution in the initial phases of the tumour dynamics. We thus let $G(\rho) \equiv p$ and study what happens in the situations we have analysed so far. It is important to remind once again that in case of unlimited growth the factor K does not represent the carrying capacity and it is only a scaling factor, which we keep for the sake of consistency with the other models; this factor affects the infection rate and the initial conditions. As in the previous case, we start presenting the results obtained with the reference parameters listed in Table 2.1 in both one and two dimensions; we then investigate how different parameters allow us to obtain other spatial patterns.

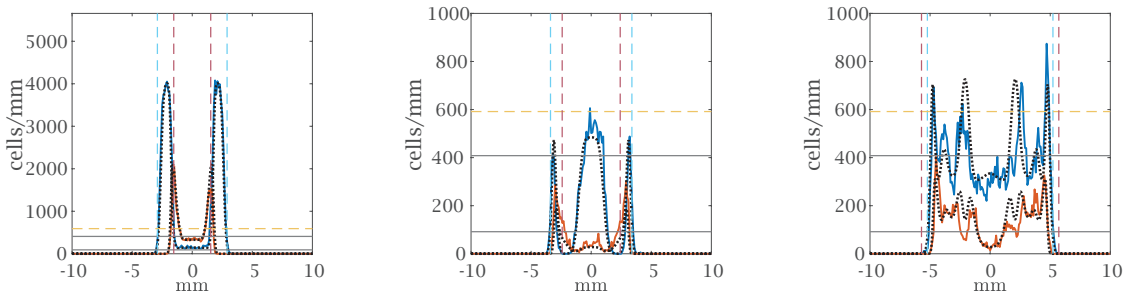

(a) $t = 80$ h (b) $t = 210$ h (c) $t = 700$ h

FIGURE 2.7: Comparison in one spatial dimension between numerical simulations of the discrete model with undirected movement and exponential growth (solid lines) and the numerical solution of Eq. (2.9) (dotted black lines) at three different times, with the parameters given in Table 2.1. For the agent-based model, the density of the uninfected cells is represented in blue and the density of infected cells in red. The vertical dashed lines represent the expected positions of the uninfected and infected invasion fronts for Eq. 2.15, travelling respectively at speed $2\sqrt{D_u p}$ (blue lines) and $2\sqrt{D_i(\beta - q)}$ (red lines); while the former is confirmed also in this case, the latter only holds when the uninfected population is at value K: we therefore observe that the invasion front is much faster in the first infection phase and then quickly slows down as the infection reaches the front of uninfected cells (see also Fig. 2.2b). The horizontal solid black lines show the equilibrium of the ODE given by Eq. (2.13) and the horizontal dashed yellow line represents the expected uninfected density at the front given by Eq. (2.22) (only relevant in panel (c)). The results of the agent-based model are averaged over five simulations. In panel (a), the maximum of the cell density axes of the panel (a) corresponds to the maximum over time of this average; in panels (b) and (c), the axes are scaled in order to enhance visibility.

Reference parameters Fig. 2.7 shows an excellent quantitative agreement between numerical solutions of the system of PDEs (2.9) and the average over five numerical simulations of the agent-based model in one spatial dimension. At the beginning of the simulations, the central region of the tumour is quickly infected, while the outer region (which is only occupied by uninfected cells) starts to grow exponentially and reaches much higher density values than in the case of logistic growth. As time passes, cell densities at the centre of the tumour slowly converge with damped oscillations to the equilibrium of the corresponding ODE, given by Eq. (2.13): since the ODE equilibrium is not asymptotically stable, this is only due to the stabilising effect of the diffusion; hence, this causes high oscillations that are still clearly observable at late times.

Uninfected cells do not form a travelling wave due to the unlimited growth. As discussed in Section 2.3, the speed of the invasion front in the absence of infection is $2\sqrt{D_u p}$ as in the case of Eq. (2.16). We also recall that the linear spreading speed of infected cells in a homogeneous region of uninfected cells with constant density $\bar{u}$ is $2\sqrt{D_i(\beta\bar{u} - q)}$; even though we do not have constant uninfected density, this formula is still a good approximation if we interpret $\bar{u}$ as the average density at the invasion front. It follows that the speed of infected cells increases as the number of uninfected cells grows until the infection eventually reaches the front of uninfected cells: this happens around time $t = 100$ h, which is approximately half the time it takes for the same process in the case of logistic growth; however, in this case, the peak of uninfected cells is more than five times the value of K.

After that, the peak of uninfected cells quickly drops to approximately the value $\bar{u}$ predicted by Eq. (2.22). Infected cells experience the same drop and the following dynamics at the invasion front resemble closely the ones observed in the case of logistic growth (except for the fact that the equilibrium of infected cells is now given by Eq. (2.12)). On the other hand, in the centre of the tumour, there are several secondary waves with a peak of size comparable to the front peak, which propagate both towards the interior and the exterior of the tumour. These waves are led by uninfected cells, with infected

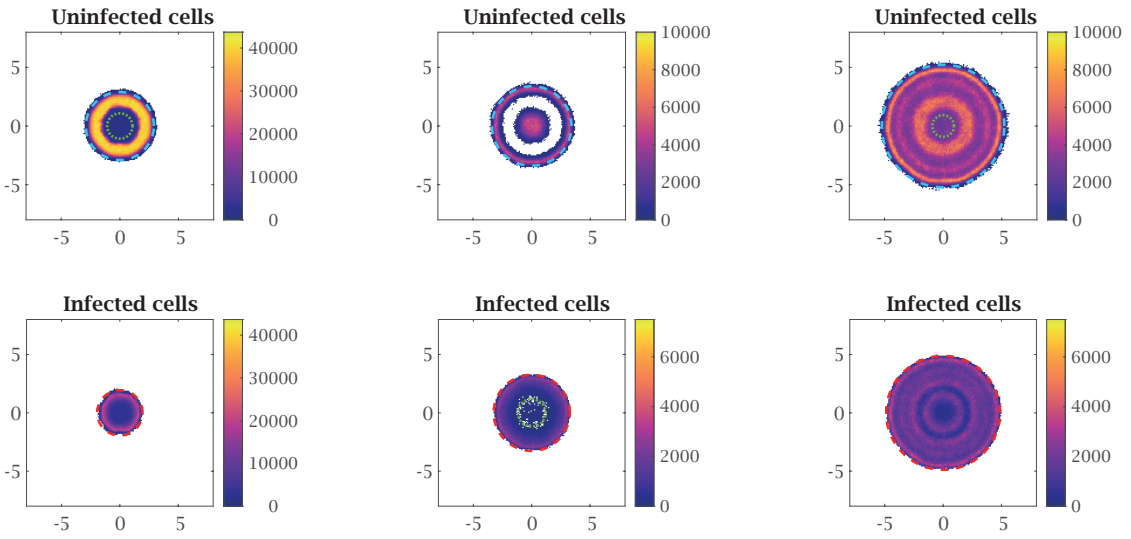

(a) $t = 80$ h (b) $t = 210$ h (c) $t = 700$ h

FIGURE 2.8: Numerical simulation of the discrete model with undirected movement and exponential growth in two spatial dimensions at three different times with the parameters given in Table 2.1. The dotted green circles represent the internal minimum of the numerical solution of Eq. (2.9) (not shown when this minimum is in 0). The dashed cyan circle represents the expected positions of the uninfected invasion front, travelling at speed $2\sqrt{D_u p}$. The dashed red circle represents the front of the infected cells given by the numerical solution of Eq. (2.9). The results of the agent-based model averaged over five simulations. In panel (a), the maximum of the colorbar corresponds to the maximum over time of this average; in panels (b) and (c), the colorbars are scaled in order to enhance visibility.

cells following: when two uninfected waves merge, they quickly disappear because they get surrounded by infected cells.

Fig. 2.8, along with the video accompanying it (see electronic supplementary material S4 of Morselli et al., 2023), shows that the same excellent agreement also holds in two spatial dimensions. Observe that, in this case, concentric circles persist even at long times.

The density values obtained with this model are probably too high to be realistic. Nevertheless, it is interesting to observe that infection alone is enough to stop an exponential growth, which otherwise would be unbounded.

Other parameters Let us now briefly mention how varying the parameters affects the success of the therapy. The situation of a highly effective therapy does not present any relevant difference with respect to the case of logistic growth, as it is clear by comparing Figs. 2.6b and 2.9b: the only difference is that inner circles are more visible and persistent at late times.

On the other hand, the case of an ineffective treatment does not exist mathematically, as the equilibrium given by Eq. (2.13) exists for all values of the parameter. Furthermore, the propagation speed of the infection increases as the number of infected cells increases: since the growth is unlimited, the infection will inevitably reach the front of the uninfected cells. The shortcoming is the fact that all the dynamics happen at much higher density levels, as Fig. 2.9a shows. This situation is probably unrealistic, so we should conclude that in this situation logistic growth describes the underlying biological phenomenon much better.

Lower cell densities Since there is no deterministic limit to cell growth, we expect that for low cell densities stochasticity plays a more important role in this model: indeed,

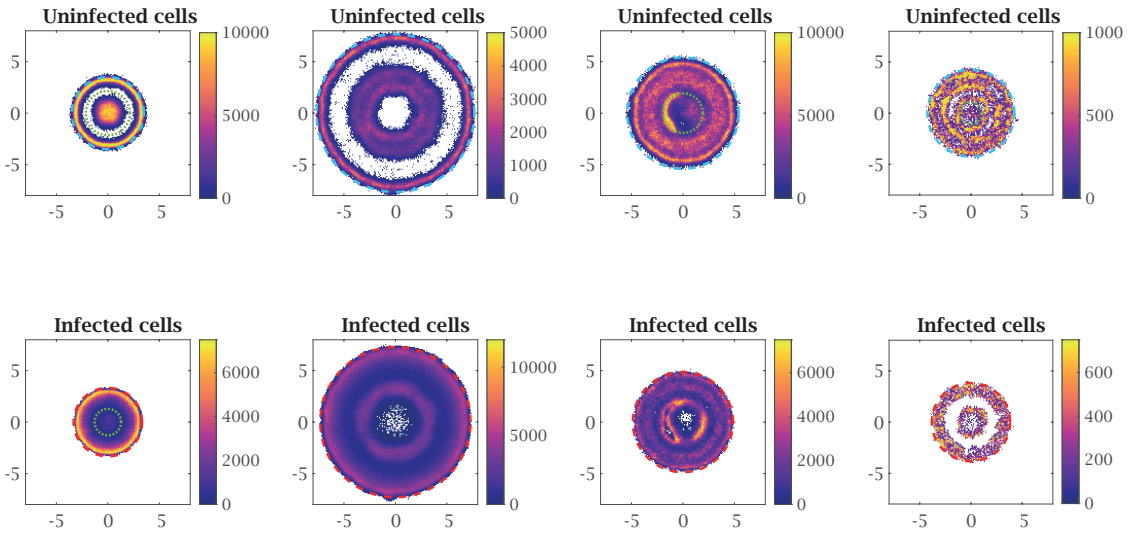

(a) $\beta = 4.86 \times 10^{-2}$ h^{-1}, $t = 240$ h

(b) $q = 4.17 \times 10^{-3}$ h^{-1}, $t = 1350$ h

(c) small initial conditions, $t = 750$ h

(d) $K = 10^3$ cells/mm, $t = 440$ h

FIGURE 2.9: Numerical simulation of the discrete model with undirected movement and exponential growth in two spatial dimensions, with different parameter values. The dotted green circles represent the internal minimum of the numerical solution of Eq. (2.9) (not shown when this minimum is in 0). The dashed cyan circles represent the expected positions of the uninfected invasion fronts, travelling at speed $2\sqrt{D_u p}$. The dashed red circles represent the front of the infected cells given by the numerical solution of Eq. (2.9). The parameters employed are the ones given in Table 2.1, with the exception of the infection rate β in panel (a) (which is set to 4.86×10^{-2} h^{-1}, i.e. less than half of the reference value), the death rate of infected cells q in panel (b) (which is set to 4.17×10^{-3} h^{-1}, i.e. one-tenth of the reference values), the initial conditions in panel (c) (whose densities are set to $0.09\,K$ for uninfected cells and $0.01\,K$ for infected cells) and the carrying capacity K in panel (d) (which in this case only affects the infection and is set to 10^3 cells/mm; initial conditions are scaled accordingly). The first two figures are the averages over five simulations, while the last two represent single simulations. The maximum values of the colorbars have been chosen in order to make the figures clear and are much smaller than the maximum reached by uninfected cell densities (note the different values between different simulations).

small fluctuation of the cell density may grow exponentially without any limit, leading the system significantly far from the average. Fig. 2.9c shows that scaling only the initial conditions leads again to spatial patterns much less regular than what the PDE predicts; furthermore, these features are still evident even for long times. Fig. 2.9d shows that as we scale the whole system by a factor of ten (i.e., both the initial conditions and the infection rate) we still maintain some qualitative agreement with the PDE, although the importance of stochastic effects is evident; we also observe that local peaks may get very high before the infection manages to control them.

Despite the increasing importance of stochasticity in this situation, it is important to observe that the PDE is still able to correctly predict the outcome of the therapy as parameters change.

2.4.4 Pressure-driven movement

Finally, let us discuss the numerical simulations for the model with pressure-driven movement and logistic growth. As we already pointed out, the linear spreading speed does not give any meaningful information. An additional difficulty comes from the fact that varying initial conditions may result in opposite therapy outcomes: this is a consequence of cells' inability to propagate in areas of constant total density. We will also see that the role of stochasticity is more important than in the previous models and in many cases the PDEs are unable to correctly predict the therapy outcome. This represents an important insight when assessing the efficiency of virotherapy for tumours that are either highly constrained or hard to infect or penetrate.

Given the intrinsic variability, we do not give a comprehensive description of all the possible outcomes in the way we did in the previous section and limit to the description of some cases of failure and success of the therapy, with a special emphasis on the situations in which results from the agent-based model and the PDE do not agree.

Reference parameters: ineffective treatment Let us first analyse Figs. 2.10a and 2.11a, which show an excellent quantitative agreement between numerical solutions of the system of PDEs (2.11) and the average over five numerical simulations of the agent-based model both in one and two spatial dimensions. Unlike the previous situations, this model predicts the infection to be confined at the centre of the tumour: this is due to the fact that the central infection quickly causes the total cell density to drop, while external uninfected cells proliferate; since cells cannot move towards an area with higher cell density, the outer cells are never going to be infected and the tumour keeps expanding at speed $\sqrt{D_u p/2}$ (vertical dashed blue line in 2.10a and dashed cyan circle in Fig. 2.11a), in the same way it would do in absence of treatment. This situation is similar to the case of ineffective infection already observed in Fig. 2.6a, but it is important to observe that here the infection rate has not been decreased with respect to the reference value. Therefore, it is clear that in this model constraints to cell movement are responsible for treatment failure.

It is important to remark that adding explicit viral dynamics to the model and allowing the virus to diffuse without any constraint due to crowding effects would result in an effective infection even in the case of pressure-driven cell movement (see Section 4.1), but does not entirely capture the realism of the process. We are considering a situation in which the virus faces some challenges in penetrating the tumour and thus cell movement is clearly a major driver of viral propagation.

Treatment success in the continuous setting Since treatment failure is due to the inability of the infection to propagate in the tumour, a simple solution to improve

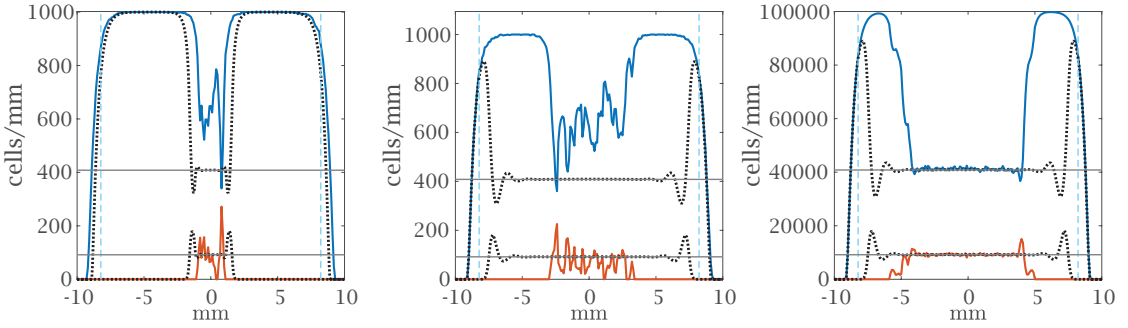

(a) reference (b) $R_i = R_u$ (c) $R_i = R_u$, $K = 10^5$ cells/mm

FIGURE 2.10: Comparison in one spatial dimension between numerical simulation of the discrete model with pressure-driven movement (solid lines) and the numerical solution of Eq. (2.11) (dotted black lines) at the same time $t = 1500$ h with different parameter values, all resulting in treatment failure according to the discrete model. For the agent-based model, the density of the uninfected cells is represented in blue and the density of infected cells in red. The vertical dashed blue lines represent the expected positions of the uninfected invasion front, travelling at speed $\sqrt{D_u p/2}$. The horizontal solid black lines show the equilibrium of the ODE given by Eq. (2.15). The parameters employed are the ones given in Table 2.1, with the exception of the infection radius R_i in panels (b) and (c) (which is set to 2.6 mm) and the carrying capacity K in panel (c) (which is set to 10^5 cells/mm). The results of the agent-based model are averaged over five simulations and the maximum of the cell density axes corresponds to the maximum of this average.

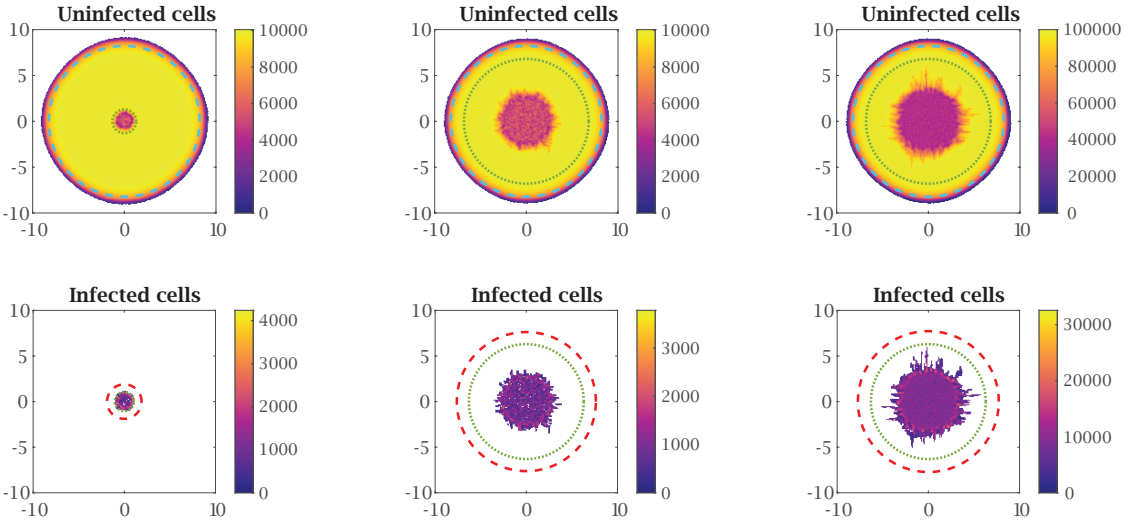

(a) reference (b) $R_i = R_u$ (c) $R_i = R_u$, $K = 10^5$ cells/mm^2

FIGURE 2.11: Numerical simulation of the discrete model with undirected movement in two spatial dimensions at the same time $t = 1500$ h with different parameter values, all resulting in treatment failure. The dotted green circles represent the internal minimum of the numerical solution of Eq. (2.11). The dashed cyan circles represent the expected positions of the uninfected invasion fronts, travelling at speed $\sqrt{D_u p/2}$. The dashed red circles represent the front of the infected cells given by the numerical solution of Eq. (2.11). The parameters employed are the ones given in Table 2.1, with the exception of the infection radius R_i in panels (b) and (c) (which is set to 2.6 mm) and the carrying capacity K in panel (c) (which is set to 10^5 cells/mm^2). The results of the agent-based model are averaged over five simulations and the maximum of the colorbars for uninfected and infected cells correspond to the maximum over time of the averages. Note the finger-like formations.

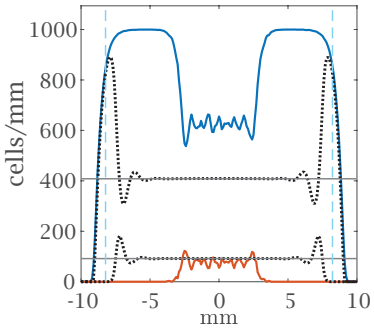

FIGURE 2.12: Comparison in one spatial dimension between numerical simulation of the discrete model with pressure-driven movement (solid lines) and the numerical solution of Eq. (2.11) (dotted black lines) at the same time $t = 1500$ h. The settings are the same ones as Fig. 2.10b, with the only difference that the results of the agent-based model are now averaged over one hundred simulations. This allows us to conclude that the mismatch is indeed consistently observed and should not be ignored.

outcomes could be to consider that infected cells are initially present in the whole tumour, i.e. take $R_i = R_u$ in Eq. (2.21). From the biological point of view, this corresponds to multiple locations for the initial viral injection in contrast to a single central injection, which has been considered so far. Figs. 2.10b and 2.11b indeed show that using this approach the PDEs predict infected cells to be at all times at the tumour front, giving rise to travelling waves qualitatively similar to the ones we observed in the model with undirected movement. Nevertheless, the agent-based model again shows an infection that fails to propagate in the whole tumour. This is due to the fact that, in this model, demographic stochasticity plays a much more important role than in previous models: any growth above the average of uninfected cells stops the movement of infected cells and hence cannot be compensated at later times by other processes. Let us also observe that the PDE predicts the presence of a very small infected cell density up to the uninfected invasion front: in the discrete model, this corresponds to a number of infected cells too low to guarantee a good quality of the continuous approximation (in these regards, see also the discussions in Johnston et al., 2020; Macfarlane et al., 2022). Taking the average over a higher number of realisations of the model does not significantly improve the agreement, since the stochasticity of each simulation is not affected (see Fig. 2.12). Overall, at this scale the discrete model cannot be accurately described by the continuum model.

According to the formal derivation of the PDEs from the agent-based model, an increase of cell number (which ensures that the evolution of the stochastic system diverges less from the average behaviour described by the continuum model) and a decrease of the temporal and spatial discretisation improve the quality of the continuum approximation. Hence, we scaled the system by setting $K = 10^5$ cells/mm in one dimension and $K = 10^5$ cells/mm^2 in two dimensions. While this increase has no biological justification, from the mathematical point of view it still makes sense to analyse at what scale we obtain good agreements between the discrete and the continuous model. Figs. 2.10c and 2.11c show that, despite an excellent quantitative agreement at initial times, stochastic events at some point inevitably cause external cells to start to grow: a positive feedback loop then promotes cellular growth until carrying capacity, stopping any further spatial propagation of the infection. We can thus conclude that only a further increase in the cell number could guarantee a better agreement between the discrete and the continuum model, although the biological meaning would be lost.

As we previously pointed out, although our model assumes unrestricted tumour invasion in the surrounding tissues, physical obstacles may hinder the growth *in vivo*. This might be particularly relevant for the kind of tumours that we consider in this

section, as the same constraints could affect both the tumour cells and the viral particles. The inhibition of the movement of cancer cells makes the tumour less aggressive and is beneficial for virotherapy, as a confined tumour is more likely to be fully infected. In the extreme case of a complete inhibition of cancer movement, a viral injection across the whole tumour would clearly be enough to decrease the tumour burden. On the other hand, the previous discussion explains how stochastic events prevent the infection from propagating in the full domain; such stochastic events are likely to take place well before a malignant tumour reaches an area in which cell movement is severely inhibited.

Treatment success in the discrete setting Let us now describe two parameter settings that allow the discrete model to create travelling waves, so that the therapy is at least partially successful. Figs. 2.11b and 2.11c show that in two dimensions the infection propagates more easily than in one dimension, as there is more space to overcome the unexpected growth of uninfected cells at single points; we therefore expect to observe travelling waves in two dimensions by changing the reference parameter values in ways less significant than in one dimension. Indeed, Fig. 2.13, along with the video accompanying it (see electronic supplementary material S6 of Morselli et al., 2023), shows that an increase in the number of cells and a decrease in the death rate of infected cells q give rise to a wave in the two-dimensional discrete model, in agreement with the numerical solution of the PDE. We recall that, in the model with undirected cell movement, the decrease of the parameter q is associated with a highly effective therapeutic outcome; we thus have an additional confirmation that in the discrete model, with pressure-driven movement, partial success is not viable.

As we have already mentioned, in one spatial dimension, a good propagation of infection in the discrete model is harder to achieve. The electronic supplementary video S5 of Morselli et al., 2023 shows that a good agreement between the agent-based model and the numerical solution of the PDE is still possible, but can only be attained in unrealistic parameter ranges. Observe that in that simulation the diffusion coefficients are much higher than the reference values, indicating again that cell movement is the main obstacle to overcome for full success.

In both cases, reasonable increases in the infection rate β do not lead to a more effective infection, as this causes a decrease in central cell density and creates the need for infected cells to move against a pressure gradient. Clearly, further increases of β allow for a fast eradication of the tumour in the case of spread infection and the problem caused by the inhibition of movement becomes irrelevant; this, however, can be attained only if we go beyond the biologically meaningful setting.

Other spatial patterns In this model, the role of stochasticity is so important that we can see irregular configurations even maintaining the carrying capacity at the reference value. Furthermore, let us set the death rate of infected cells at the same value of the simulation in Fig. 2.13, as otherwise the therapy would not be effective in the discrete model.

Fig. 2.14a shows that in this setting an increase of diffusion coefficients allows the infection to propagate until approximately 1000 h, when it starts to be blocked by the increase of the uninfected front. Observe how the stochastic events stopping the infection take place at different times in different locations, giving rise to interesting finger-shaped structures. The other simulations depicted in Fig. 2.14 have been obtained by considering a higher probability of movement of infected cells with respect to uninfected cells: while there is no clear biological evidence supporting this assumption, we may still interpret it as a way to indirectly incorporate in our model, for example, a viral diffusion that is

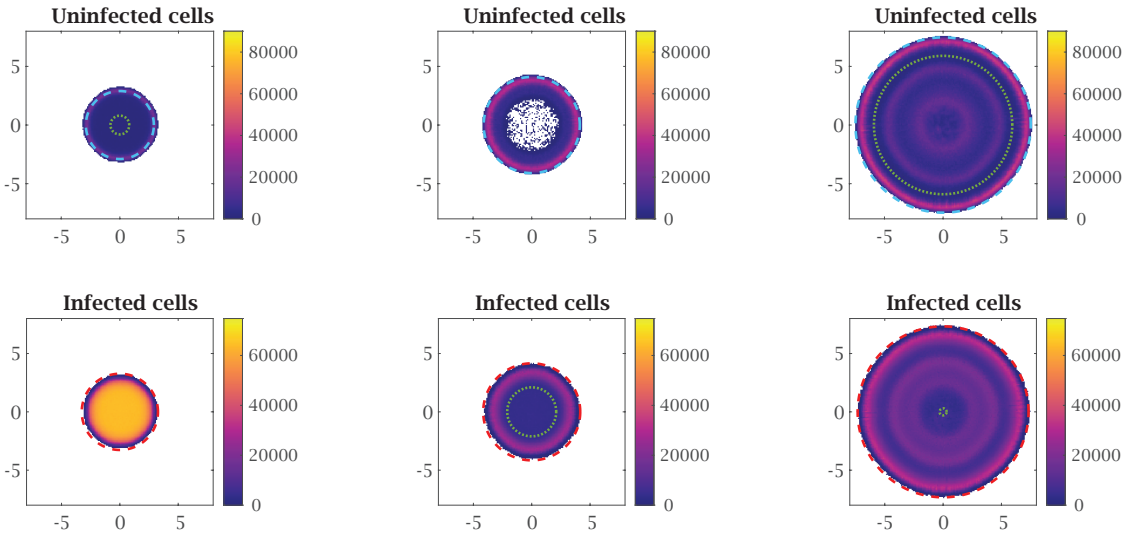

(a) $t = 80$ h (b) $t = 400$ h (c) $t = 1300$ h

FIGURE 2.13: Numerical simulation of the discrete model with pressure-driven movement in two spatial dimensions at three different times. The dotted green circles represent the internal minimum of the numerical solution of Eq. (2.11) (not shown when this minimum is in 0). The dashed cyan circles represent the expected positions of the uninfected invasion fronts in the absence of treatment, travelling at speed $\sqrt{D_u p/2}$. The dashed red circles represent the front of the infected cells given by the numerical solution of Eq. (2.11). The parameters employed are the ones given in Table 2.1, with the exception of the carrying capacity K (which is set to 10^5 cells/mm^2, i.e. ten times the reference value) and the death rate of infected cells q (which is set to 8.33×10^{-3} h^{-1}, i.e. one-fifth of the reference values). These parameter choices allow a perfect agreement between the discrete and the continuous model, although their biological value is disputable. The results of the agent-based model are averaged over five simulations and the maximum of the colorbars for uninfected and infected cells correspond to the maximum over time of the averages.

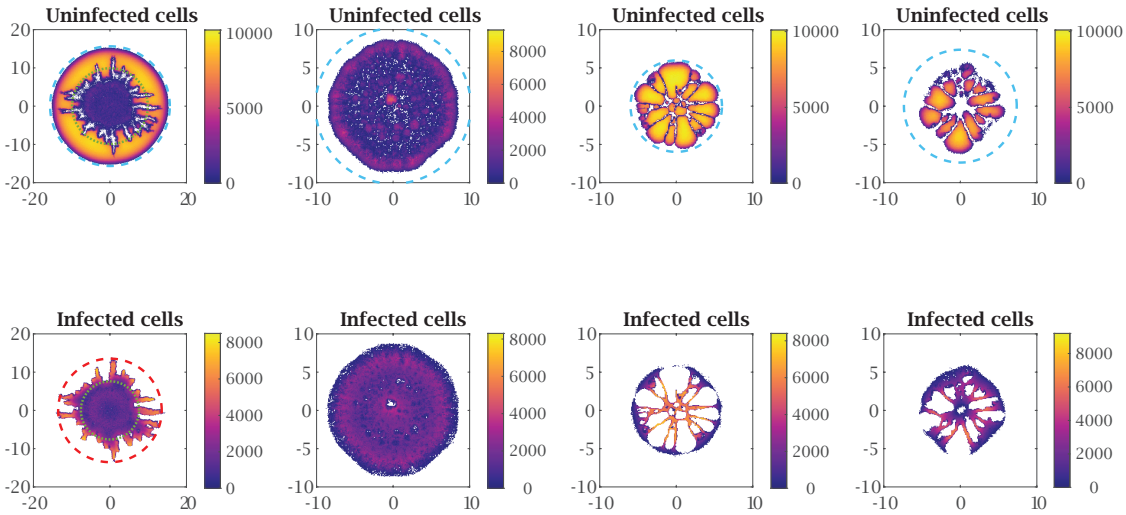

(a) high cell motility, $t = 1100$ h

(b) high motility of infected cells, $t = 900$ h

(c) very high motility of infected cells, $t = 900$ h

(d) high infection rate, $t = 900$ h

FIGURE 2.14: Numerical simulation of the discrete model with pressure-driven movement in two spatial dimensions with different parameter values. The dotted green circles in panel (a) represent the internal minimum of the numerical solution of Eq. (2.11). The dashed cyan circles represent the expected positions of the uninfected invasion fronts in the absence of treatment, travelling at speed $\sqrt{D_u p/2}$. The dashed red circle in panel (a) represents the front of the infected cells given by the numerical solution of Eq. (2.11). The parameters employed are the ones given in Table 2.1, with the exception of the death rate of infected cells q (which is set to 8.33×10^{-3} h^{-1}, i.e. one-fifth of the reference values), the diffusion coefficient of infected cells D_i (which is set to 1.50×10^{-1} mm^2/h, i.e. ten times the reference value) the diffusion coefficient of uninfected cells D_u in panels (a), (b) and (d) (which is set to 1.50×10^{-1} mm^2/h in panel (a), to 7.50×10^{-2} mm^2/h in panel (b) and to 3.00×10^{-3} mm^2/h in panel (d)) and the infection rate β in panel (d) (which is set to 2.04×10^{-1} h^{-1}, i.e. twice the reference value). The maximum of the colorbars for uninfected and infected cells correspond to the maximum over time of the simulation.

slightly more efficient in the tumour microenvironment (so that both cell-to-cell contacts and free viral particles contribute to new infections and thus the therapy is only partially inhibited by the pressure). Fig. 2.14b shows that the lower motility of uninfected cells allows the infection to occupy the whole tumour area. In few areas, uninfected cells manage to survive and become harder to be infected as they keep growing, but the therapy can still be considered effective. A further decrease of uninfected motility does not improve the situation: Fig. 2.14c shows that, despite a very effective initial infection, a few cells manage to survive and give rise to segregated structures that are almost impossible to infect, due to the low uninfected cell motility. In the majority of the tumour, uninfected cells are at carrying capacity and the tumour invasion of the surrounding tissues has been only slightly slowed down with respect to the case without infection. We can thus conclude that such a high difference in the motilities does not favour the therapy. Finally, let us consider again the value of D_u used for Fig. 2.14b and double the infection rate β: as we may expect, this kind of infection makes the pressure decrease in the infected areas and it is thus too fast to be effective. Fig. 2.14d shows the result of this simulation, which is much more similar to 2.14c than to 2.14a. It is interesting to observe that this strong segregation happens with parameter values quite close to the ones that would cause a highly effective treatment, indicating how delicate the balance between the different populations is. The general message is that a pressure-driven scenario generates patterns and structures that can be hard for the virus to clear.

2.5 Conclusions

A minimal, individual-based model for the infection of tumour cells due to oncolytic viruses, assuming two different mechanisms for cellular movement, has been developed. In both cases we formally derive the deterministic continuum counterpart and compare the numerical results in one and two spatial dimensions. The outcomes of the comparison are highly dependent on the rules governing cells' movement and show typical traits for failure and successful outcomes.

In the model with undirected cell movement, the solution of Eq. (2.8) faithfully mirrors the qualitative and quantitative properties of the results of the simulations of the agent-based model: this agreement is robust to parameter variations and holds even if the logistic growth is replaced by exponential growth. When lower cell densities are considered, the quantitative agreement is partially lost, but the PDEs are still able to correctly predict the treatment outcome. We can thus use our knowledge of the continuous model to better understand the outcome of the therapy in different parameter regimes and establish strategies and trends to help clinicians.

On the other hand, in the model with pressure-driven cell movement, the solution of Eq. (2.11) exhibits travelling waves in situations in which simulations of the agent-based model result in a localised infection in the centre of the tumour, especially in one dimension. From the mathematical point of view, this can be addressed by increasing the number of agents in the simulations and decreasing the temporal and spatial discretisations. However, from the biological point of view, it makes no sense to consider such a high cell density and stochastic effects cannot simply be neglected: therapy may fail only because of the inhibition of movement due to the pressure. This represents quite a hurdle from the treatment's perspective and suggests that, in the absence of an immune response, virotherapy is intrinsically limited for tumours whose microenvironments constrain cell movement.

Note also that the two-dimensional patterns obtained from the agent-based simulations are consistent with the ones discussed in the literature regarding oncolytic viral

infection: for example, in Wodarz et al., 2012 the authors describe filled rings (similar to our Figs. 2.5 and 2.6d), hollow rings (similar to our Fig. 2.6b), concentric rings (similar to our Figs. 2.9, 2.13) and disperse patterns (similar to our Figs. 2.6d, 2.9d, 2.14b) obtained both via in silico experiments and numerical simulations of an agent-based model. But, in Wodarz et al., 2012, only a single cell can occupy a lattice point and, therefore, concentric rings are due to stochasticity, whereas they are also originated by PDEs in our model. Results are also consistent with the spatial patterns observed in Kim et al., 2014, for glioma and ECM-degrading enzyme Chase-ABC. Structures like these appear to be universal whenever tumour expansion is hindered. The different spatial patterns are clearly associated to different degrees of therapeutic success: indeed, hollow rings correspond to a better outcome than filled rings or disperse patterns. Our results show how parameter variations are associated to the different structures, suggesting the features that an ideal oncolytic virus would need. For example, the decrease of the death rate of infected cells appears always beneficial; on the other hand, the increase of the infection rate may not be associated to a more effective treatment if spatial constraints are relevant. In any case, virotherapy alone appears unable to fully eradicate tumours.

We were also able to obtain segregated regions of uninfected cells (Figs. 2.14c and 2.14d) by considering a faster movement for infected cells in the agent-based model when diffusion is pressure-driven. This kind of results resembles those of stochastic invasion models (Lewis, 2000; Lewis and Pacala, 2000) and deterministic PDEs of predator and prey with an Allee effect, due to the instability of the propagation front (Li, 2015; Morozov et al., 2006; Petrovskii et al., 2005; Petrovskii et al., 2002). Unlike these two models, though, in our case the segregation is due to the combination of pressure's inhibition of movement and stochasticity. It is interesting to observe that, despite all the differences in the model, our results are in agreement with the observation of Li, 2015; Morozov et al., 2006; Petrovskii et al., 2005; Petrovskii et al., 2002 that this "patchy invasion" takes place for parameter values very close to the ones that would result in the extinction of both populations. This could be important from a therapeutic perspective, suggesting to exercise extra care when tumours' growth is subject to pressure-related effects.

In all these cases, the comparison between the discrete and the continuous approach allows us to better understand which phenomena are mainly driven by stochasticity and which others can be described equally well by deterministic rules. It is interesting to observe that the experiments *in vitro* of Wodarz et al., 2012 were performed in conditions that prevent long-range spread of the virus away from infected cells and the different patterns are observed in identical experimental conditions; this confirms our observation that, in constrained environments, stochasticity should be taken into account. Although our models do not have predictive power on those experiments, our results are still useful to highlight the mechanisms that determine different outcomes.

From the mathematical point of view, a rigorous way to characterise the travelling wave solutions of the system of PDEs (2.11) is lacking. While waves connecting $(K, 0)$ to (u^*, i^*) cannot be obtained starting from initial conditions in which the support of i is surrounded by an area where $u = K$ (and therefore, it is not possible to describe a homogeneous population invaded by a new infection or predator), our numerical simulations show that it makes sense to look for waves connecting $(0, 0)$ to (u^*, i^*), corresponding to the race between two expanding populations.

The models presented in this chapter do not include the immune response, whose interactions with oncolytic viruses are still not entirely clear (Hemminki et al., 2020). In recent years, the combination of oncolytic viruses with immunotherapy has shown promising results (see Engeland et al., 2022 for a review of the topic); hence we tackle such a shortcoming in the next chapter.

3 *Interactions of the immune system with oncolytic viral infections*

The interplay between oncolytic viruses and immune cells is twofold: oncolytic viruses are able to stimulate immune cells, not only against viral particles but also against tumour cells; conversely, an immune response that targets the oncolytic virus may prevent an effective infection in the whole tumour, making virotherapy inefficient (Shi et al., 2020). The complexities of these dynamics motivate the use of mathematical models to gain a deeper understanding, with the goal of suggesting optimal treatment schedules for the combination of virotherapy and immunotherapies.

In Chapter 2, we observed partial tumour remission in absence of the immune response in the case of unrestricted cell movement. The goal of the present chapter is to analyse the impact of the immune system in this situation, with the aim of determining whether eradication or long-term control of the tumour is attainable, at least in the absence of relevant physical constraints.

Immune interactions with a tumour involve several different types of immune cells, which are stimulated and inhibited by a large number of molecules. An accurate description of these processes goes beyond the scope of the present work. In order to facilitate some theoretical understanding of the model, we restrict our attention to a single type of immune cell, namely cytotoxic T-cells, with the ability to kill both infected and uninfected tumour cells. We then assume that tumour cells secrete chemoattractant and immune cells follow the chemotactic stimuli towards the tumour (see Painter, 2019 and the references therein); this leads to a hybrid and multiscale modelling approach. Although the derivation of this kind of model from microscopic rules is well-known (see Almeida et al., 2022 for the specific case of immune interactions with cancer and Bubba et al., 2020a; Charteris and Khain, 2014 for more general situations), we are not aware of any other work comparing agent-based and continuous models for the interactions between the immune system and oncolytic viruses.

We consider a tumour with poor immune infiltration (i.e., a *cold* tumour in the classification of Galon and Bruni, 2019) and assume that the infection by the oncolytic virus induces an immune anti-tumour response by increasing immune cell inflow and improving immune recognition. We also assume that the immune killing rate can be enhanced (e.g., by inhibition of the PD-1 and PD-L1 checkpoints (Iwai et al., 2002)) and we evaluate its consequences on the therapy. First, the spatially homogeneous ODE is considered, revealing that some parameter regions give rise to stable limit cycles: this is not surprising, as the same behaviour is also observed in similar models describing interactions of cancer with immune cells (Eftimie et al., 2011a), oncolytic virus (Baabdulla and Hillen, 2024; Jenner et al., 2018c; Jenner et al., 2019; Pooladvand et al., 2021) and both entities together (Eftimie et al., 2016). Then, the effects of the oscillations are explored in spatial models: in some situations, we observe the extinction of infected agents even though the continuous model shows the recurrence of infection. Overall, our results suggest that the enhancement of the immune response may either increase or decrease

the effectiveness of oncolytic virotherapy, depending on the time and location of the viral injection.

The chapter is organised as follows. In Section 3.1, we introduce the agent-based model and present its continuum counterpart. In Section 3.2, we formally derive its continuum counterpart. In Section 3.3, we study the equilibria of the spatially homogeneous ODE and the emergence of a stable limit cycle; this analysis provides some insights into the oscillations observed in the full system. In Section 3.4, we compare the results of numerical simulations of the agent-based model and the numerical solutions of the corresponding PDEs, comparing it with the situation in which the immune response is negligible. In Section 3.5, we discuss the main findings and provide some suggestions for future research.

The model described in this chapter and the results shown have been submitted for publication (Morselli et al., 2024b).

3.1 Description of the agent-based model

3.1.1 Agent-based model

We extend and improve upon the modelling framework described in Section 2.1 by including immune cells, which are described as agents that occupy a position on a discrete lattice in the same way as cancer cells. We also consider a chemoattractant secreted by cancer cells that guide the movement of immune cells; its concentration is described as a discrete, non-negative function. Observe that we are using a hybrid discrete-continuous modelling framework, since the chemoattractant concentration is the discretisation of a continuous function. For ease of presentation, in this section, we restrict our attention to one spatial dimension, but there would be no additional difficulty in considering higher spatial dimensions. In the following sections, we mainly focus on two spatial dimensions, so, in Remark 3.1, we explain the small difference in this situation.

Let us consider the temporal discretisation $t_n = \tau n$, with $n \in \mathbb{N}_0$, $0 < \tau \ll 1$, and the spatial domain $\Omega \subseteq \mathbb{R}$ with discretisation $x_j = \delta j$, with $j \in \mathbb{Z}$, $0 < \delta \ll 1$; we assume τ to be small enough to guarantee that all the probabilities defined hereafter are smaller than 1. We denote the number of immune cells, uninfected and infected cancer cells that occupy position x_j at time t_n respectively by Z_j^n, U_j^n and I_j^n; the corresponding densities are

$$z_j^n := \frac{Z_j^n}{\delta}, \qquad u_j^n := \frac{U_j^n}{\delta}, \qquad i_j^n := \frac{I_j^n}{\delta}$$

We then denote by ϕ_j^n the concentration of chemoattractant at time t_n and position x_j. Since the spatio-temporal scales for the chemoattractant's dynamics are very different from cellular ones, we describe them with a deterministic discrete balance equation, as in Almeida et al., 2022; Cooper and Kim, 2014. Table 3.1 summarises the variables of the hybrid agent-based model and their macroscopic counterparts; Fig. 3.1 summarises the rules governing the dynamics of the agent-based model. Cancer cells proliferate, move, become infected and die in the same way as in Chapter 2. The dynamics of the chemoattractant and of the immune cells represent a novelty with respect to our previous work and resemble some other models in the literature, as explained in the following. We assume that the infection stimulates the immune system by increasing the number of immune cells in the area and guiding them towards infected cells; once an immune cell comes in contact with a cancer cell, it is able to kill it even if it is not infected.

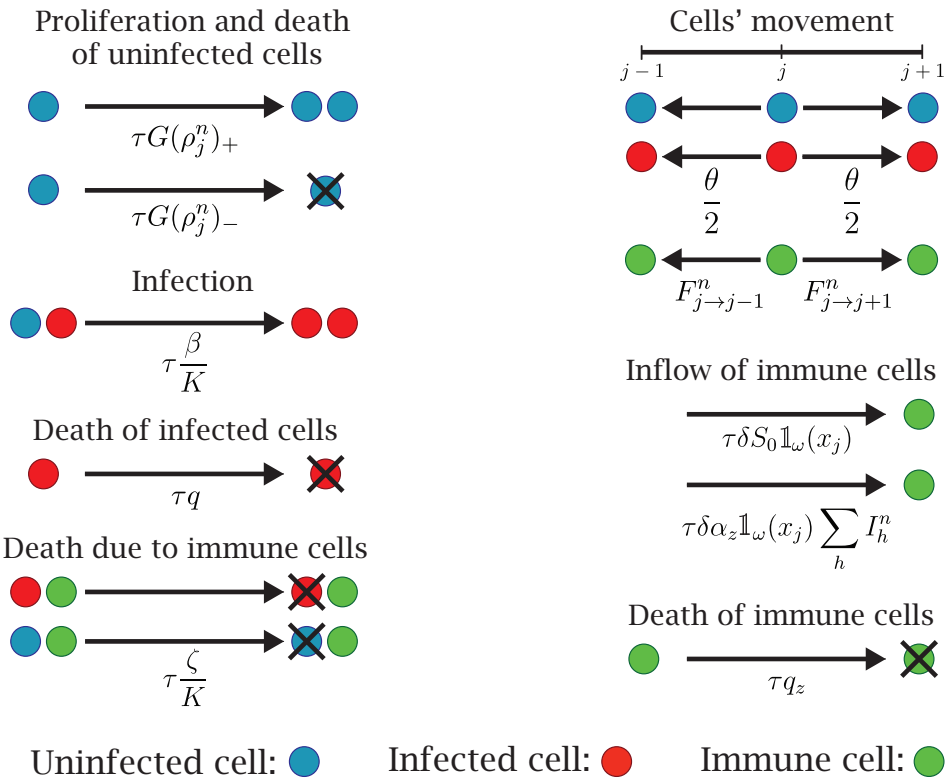

FIGURE 3.1: Schematic representation of the rules governing cell dynamics in the stochastic models. Uninfected cells are represented in blue, infected cells in red and immune cells in green. Uninfected cells may proliferate or die according to the total density, move, become infected upon contact with infected cells and die upon contact with immune cells. Infected cells may move, die with constant probability and die upon contact with immune cells. Immune cells may enter the domain, move with the probabilities given in Eq. (3.3) and die with constant probability. The model also considers the dynamics of the chemoattractant, which are not included in the figure due to the different modelling approach adopted (i.e., density-based and deterministic instead of individual-based and stochastic).

Quantity	Microscopic variable [Units]	Macroscopic variable [Units]
uninfected cancer cells	U_j^n [cells]	$u(t,x)$ [cells/mm^2]
infected cancer cells	I_j^n [cells]	$i(t,x)$ [cells/mm^2]
immune cells	Z_j^n [cells]	$z(t,x)$ [cells/mm^2]
chemoattractant	ϕ_j^n [μg/mm^2]	$\phi(t,x)$ [μg/mm^2]

TABLE 3.1: List of the variables for both approaches, with their units of measurement.

Basic dynamics of cancer cells We refer to Section 2.1 for the description of proliferation, infection, movement and death of cancer cells. In this chapter, we restrict our attention to the case of undirected random movement; furthermore, for the sake of simplicity, we consider that infected and uninfected cells move with the same probability, which we denote by θ.

Dynamics of the chemoattractant We assume that uninfected and infected cells produce chemoattractant at rates γ_ϕ and α_ϕ, respectively. We choose their values so that $\alpha_\phi \gg \gamma_\phi > 0$, in line with our assumption that the tumour is initially *cold* and the infection by the oncolytic virus is enough to induce an immune anti-tumour response, as often observed *in vivo* and *in vitro* (Galon and Bruni, 2019). Chemoattractant density cannot grow unlimited, therefore it saturates at $\phi^* > 0$. The chemoattractant also decays at rate $q_\phi > 0$ and diffuses. The resulting balance equation is

$$\phi_j^{n+1} = \phi_j^n + \tau D_\phi \frac{\phi_{j+1}^n + \phi_{j-1}^n - 2\phi_j^n}{\delta^2} + \tau(\alpha_\phi i_j^n + \gamma_\phi u_j^n)(\phi^* - \phi_j^n) - \tau q_\phi \phi_j^n \tag{3.1}$$

where $D_\phi > 0$ is the diffusion coefficient. This equation closely resembles the ones used in Almeida et al., 2022; Bubba et al., 2020a to model the evolution of a chemoattractant concentration.

Dynamics of immune cells We assume that there is a constant influx of immune cells into the microenvironment independent of the presence of cancer cells. In addition to this, we assume that infection by the oncolytic virus stimulates an immune response in the whole tumour. Hence, an immune cell appears at point x_j at time step t_n with probability $\tau\delta S_j^n$, given by

$$S_j^n = \left(S_0 + \alpha_z \sum_h I_h^n\right) \mathbb{1}_\omega(x_j) \tag{3.2}$$

where $\mathbb{1}_\omega$ is the indicator function of the set $\omega \subset \Omega$, $S_0 > 0$ is the base inflow rate and $\alpha_z > 0$ is the additional inflow rate due to the infection; the latter takes into account the total number of infected cells in the domain. In principle, we could vary ω to model the fact that some areas of the tumour are harder to reach for immune cells (e.g. due to poor vascularisation), although this goes beyond the scope of the present work. It is important to observe that the increase of the inflow due to infected cells is nonlocal, as in Almeida et al., 2022; this resembles the recruitment of immune cells from adjacent lymph nodes and the subsequent arrival through blood vessels.

We then assume that an immune cell that occupies position x_j at time t_n moves to the lattice point $x_{j\pm1}$ with probability $F_{j\to j\pm1}^n$ and remains at its initial position with probability $1 - F_{j\to j-1}^n - F_{j\to j+1}^n$. We include both undirected, random movement and chemotactic movement up the gradient of the chemoattractant: this latter part depends on the difference between the chemoattractant concentration at the initial position of the

cell and the concentration of chemoattractant at the target point. We therefore set

$$F^n_{j\to j\pm1} := \frac{\theta_z}{2} + \nu\frac{(\phi^n_{j\pm1} - \phi^n_j)_+}{2\phi^*} \tag{3.3}$$

where $z_+ := \max\{z, 0\}$, ϕ^* is the saturation density of the chemoattractant and $\theta_z, \nu \in [0, 1]$ with $\theta_z + \nu < 1$. Observe that, if $0 \le \phi^n_j \le \phi^*$ for every j, then all the probabilities are between 0 and 1. This kind of reasoning and the probabilities associated have already been employed in Almeida et al., 2022; Bubba et al., 2020a.

Finally, we assume that at every time step an immune cell dies with probability τq_z, where $q_z > 0$ is a constant death rate.

Cytotoxic action of the immune cells We assume that cancer cells may be killed by the cytotoxic action of immune cells upon contact; this happens at a rate proportional to the density of immune cells. To be precise, a cancer cell that occupies position x_j at time t_n dies with probability $\tau\zeta z^n_j/K$, where K is the carrying capacity and $\zeta > 0$ is a constant killing rate. For the sake of simplicity, we assume that the killing rate is the same for every cancer cell, although it could make sense to consider situations in which infected cells are more easily recognised by immune cells and, thus, are killed at a higher rate. This process is analogous to the infection of cancer cells described above.

3.2 Formal derivation of the corresponding continuum model

We now derive the continuum counterparts of the agent-based models described in the previous section, using techniques analogous to those employed in Section 2.2 and in the references mentioned there.

3.2.1 Uninfected cancer cells

Uninfected cells can first move, then reproduce or die based on the pressure value, then become infected and finally be killed by immune cells, as explained in Section 3.1. The principle of mass balance gives the equation

$$\begin{aligned} u^{n+1}_j = &\left[\frac{\theta}{2}u^n_{j-1} + \frac{\theta}{2}u^n_{j+1} + (1-\theta)u^n_j\right]\left[1 + \tau G(\rho^n_j)_+ - \tau G(\rho^n_j)_-\right] \\ &\times \left(1 - \tau\frac{\beta}{K}i^n_j\right)\left(1 - \tau\frac{\zeta}{K}z^n_j\right) \end{aligned}$$

where $rho^n_j := u^n_j + i^n_j$. Using the algebraic relation $x_+ - x_- = x$, this simplifies to

$$\begin{aligned} u^{n+1}_j = &\left[\frac{\theta}{2}u^n_{j-1} + \frac{\theta}{2}u^n_{j+1} + (1-\theta)u^n_j\right]\left[1 + \tau G(\rho^n_j)\right] \\ &\times \left(1 - \tau\frac{\beta}{K}i^n_j\right)\left(1 - \tau\frac{\zeta}{K}z^n_j\right) \end{aligned}$$

Let us define

$$\Phi := \frac{\theta}{2}u^n_{j-1} + \frac{\theta}{2}u^n_{j+1} - \theta u^n_j = \frac{\theta}{2}\delta^2\frac{u^n_{j-1} + u^n_{j+1} - 2u^n_j}{\delta^2}$$

so that the previous equation becomes

$$\begin{aligned}
u_j^{n+1} &= (u_j^n + \Phi)\Big[1 + \tau G(\rho_j^n)\Big]\Big(1 - \tau\frac{\beta}{K}i_j^n\Big)\Big(1 - \tau\frac{\zeta}{K}z_j^n\Big) \\
&= u_j^n + \tau G(\rho_j^n)u_j^n - \tau\frac{\beta}{K}u_j^n i_j^n - \tau\frac{\zeta}{K}u_j^n z_j^n + \Phi \\
&- \tau^2 G(\rho_j^n)\frac{\beta}{K}u_j^n i_j^n - \tau^2 G(\rho_j^n)\frac{\zeta}{K}u_j^n z_j^n + \tau^2\frac{\beta\zeta}{K^2}u_j^n i_j^n z_j^n + \tau^3 G(\rho_j^n)\frac{\beta\zeta}{K^2}u_j^n i_j^n z_j^n \\
&+ \tau\Phi\Big[G(\rho_j^n) - \frac{\beta}{K}i_j^n - \frac{\zeta}{K}z_j^n - \tau G(\rho_j^n)\frac{\beta}{K}i_j^n - \tau G(\rho_j^n)\frac{\zeta}{K}z_j^n + \tau\frac{\beta\zeta}{K^2}i_j^n z_j^n \\
&+ \tau^2 G(\rho_j^n)\frac{\beta\zeta}{K^2}i_j^n z_j^n\Big]
\end{aligned}$$

We now divide both sides of the previous equation by τ and rearrange the terms to get

$$\frac{u_j^{n+1} - u_j^n}{\tau} = G(\rho_j^n)u_j^n - \frac{\beta}{K}u_j^n i_j^n - \frac{\zeta}{K}u_j^n z_j^n + \frac{1}{\tau}\Phi + H_1 \tag{3.4}$$

and observe that every term of H_1 is multiplied either by τ or by Φ.

Let us now assume that there is a function $u \in C^2([0,+\infty)\times\mathbb{R})$ such that $u_j^n = u(t_n, x_j) = u$ (from now on we omit the arguments of functions computed at (t_n, x_j)); thus, we can use Taylor expansions for u in time and space as follows

$$\begin{aligned}
u_j^{n+1} &= u(t_n + \tau, x_j) = u + \tau\partial_t u + \mathcal{O}(\tau^2) \\
u_{j\pm1}^n &= u(t_n, x_j \pm \delta) = u \pm \delta\partial_x u + \frac{1}{2}\delta^2\partial_{xx}^2 u + \mathcal{O}(\delta^3)
\end{aligned}$$

This implies that

$$\Phi = \frac{\theta}{2}\delta^2\partial_{xx}^2 u + \mathcal{O}(\delta^3)$$

and thus $H_1 = \mathcal{O}(\tau) + \mathcal{O}(\delta^2)$. Eq. (3.4) then becomes

$$\partial_t u + \mathcal{O}(\tau^2) = \theta\frac{\delta^2}{2\tau}\partial_{xx}^2 u + G(\rho)u - \frac{\beta}{K}ui - \frac{\zeta}{K}uz + \mathcal{O}(\tau) + \mathcal{O}(\delta^2)$$

Letting $\tau, \delta \to 0$ in such a way that $\frac{\delta^2}{2\tau} \to \tilde{D}$, we obtain

$$\partial_t u = \theta\tilde{D}\partial_{xx}^2 u + G(\rho)u - \frac{\beta}{K}ui - \frac{\zeta}{K}uz$$

3.2.2 Infected cancer cells

Infected cells can first move, then die, as explained in Section 3.1. Also, uninfected cells may be infected. The principle of mass balance gives the equation

$$\begin{aligned}
i_j^{n+1} = &\Big[\frac{\theta}{2}i_{j-1}^n + \frac{\theta}{2}i_{j+1}^n + (1-\theta)i_j^n\Big](1 - \tau q)\Big(1 - \tau\frac{\zeta}{K}z_j^n\Big) \\
&+ \tau\frac{\beta}{K}i_j^n(1 + \tau G(\rho_j^n))\Big(1 - \tau\frac{\zeta}{K}z_j^n\Big)(u_j^n + \Phi)
\end{aligned}$$

which simplifies to

$$\begin{aligned} i_j^{n+1} &= (1-\tau q)\Big(1-\tau\frac{\zeta}{K}z_j^n\Big)(i_j^n+\Psi)+\tau\frac{\beta}{K}u_j^n i_j^n+\tau H_2 \\ &= i_j^n-\tau q i_j^n-\tau\frac{\zeta}{K}i_j^n z_j^n+\Psi+\tau H_3 \\ &\quad+\tau\frac{\beta}{K}u_j^n i_j^n+\tau H_2 \end{aligned}$$

where

$$\Psi := \frac{\theta}{2}i_{j-1}^n+\frac{\theta}{2}i_{j+1}^n-\theta i_j^n = \frac{\theta}{2}\delta^2\frac{i_{j-1}^n+i_{j+1}^n-2i_j^n}{\delta^2}$$

and

$$\begin{aligned} H_2 := \tau G(\rho_j^n)\frac{\beta}{K}u_j^n i_j^n-\tau\frac{\beta\zeta}{K^2}u_j^n i_j^n z_j^n-\tau^2 G(\rho_j^n)\frac{\beta\zeta}{K^2}u_j^n i_j^n z_j^n \\ +\frac{\beta}{K}i_j^n(1+\tau G(\rho_j^n))\Big(1-\tau\frac{\zeta}{K}z_j^n\Big)\Phi \\ H_3 := -q\Psi-\frac{\zeta}{K}z_j^n\Psi+\tau q\frac{\zeta}{K}i_j^n z_j^n+\tau q\frac{\zeta}{K}z_j^n\Psi \end{aligned}$$

Let us observe that every term of H_2 and H_3 is multiplied either by τ, Φ or Ψ. Dividing both sides by τ and rearranging the terms, we get

$$\frac{i_j^{n+1}-i_j^n}{\tau} = \frac{1}{\tau}\Psi-qi_j^n+\frac{\beta}{K}u_j^n i_j^n-\frac{\zeta}{K}i_j^n z_j^n+H_2+H_3 \tag{3.5}$$

Let us now assume that there is a function $i \in C^2([0,+\infty)\times\mathbb{R})$ such that $i_j^n = i(t_n,x_j) = i$, so that

$$\begin{aligned} i_j^{n+1} &= i(t_n+\tau,x_j) = i+\tau\partial_t i+\mathcal{O}(\tau^2) \\ i_{j\pm1}^n &= i(t_n,x_j\pm\delta) = i\pm\delta\partial_x i+\frac{1}{2}\delta^2\partial_{xx}^2 i+\mathcal{O}(\delta^3) \end{aligned}$$

This implies that

$$\Psi = \frac{\theta}{2}\delta^2\partial_{xx}^2 i+\mathcal{O}(\delta^3)$$

and thus $H_2+H_3 = \mathcal{O}(\tau)+\mathcal{O}(\delta^2)$. Eq. (3.5) then becomes

$$\partial_t i+\mathcal{O}(\tau^2) = \theta\frac{\delta^2}{2\tau}\partial_{xx}^2 i+\frac{\beta}{K}ui-\frac{\zeta}{K}iz-qi+\mathcal{O}(\tau)+\mathcal{O}(\delta^2)$$

Letting $\tau,\delta\to 0$ in such a way that $\frac{\delta^2}{2\tau}\to\tilde{D}$ we obtain

$$\partial_t i = \theta\tilde{D}\partial_{xx}^2 i+\frac{\beta}{K}ui-\frac{\zeta}{K}iz-qi$$

3.2.3 Chemoattractant

The chemoattractant is produced by cancer cells, decays at a constant rate and diffuses, as explained in Section 3.1; its dynamics are described by Eq. (3.1), which can be written

as

$$\frac{\phi_j^{n+1}-\phi_j^n}{\tau} = D_\phi \frac{\phi_{j+1}^n+\phi_{j-1}^n-2\phi_j^n}{\delta^2} + (\alpha_\phi i_j^n + \gamma_\phi u_j^n)(\phi^*-\phi_j^n) - q_\phi \phi_j^n \tag{3.6}$$

Let us now assume that there is a function $\phi \in C^2([0,+\infty)\times\mathbb{R})$ such that $\phi_j^n = \phi(t_n, x_j) = \phi$. Then clearly the discrete diffusion term converges to the second derivative of ϕ, hence for $\tau, \delta \to 0$ we obtain

$$\partial_t \phi = D_\phi \partial_{xx}^2 \phi + (\alpha_\phi i + \gamma_\phi u)(\phi^* - \phi) - q_\phi \phi$$

3.2.4 Immune cells

Immune cells can first move, then die, as explained in Section 3.1. Also, new immune cells may enter the domain. The principle of mass balance gives the equation

$$z_j^{n+1} = \left[F_{j-1\to j}^n z_{j-1}^n + F_{j+1\to j}^n z_{j+1}^n + (1 - F_{j\to j-1}^n - F_{j\to j+1}^n) z_j^n\right](1-\tau q_z) + \tau S_j^n$$

with

$$F_{j\to j\pm1}^n := \frac{\theta_z}{2} + \underbrace{\nu \frac{(\phi_{j\pm1}^n - \phi_j^n)_+}{2\phi^*}}_{=:\tilde{F}_{j\to j\pm1}^n}, \qquad S_j^n = \left(S_0 + \alpha_z \sum_h I_h^n\right) \mathbb{1}_\omega(x_j)$$

Observe that the source term is no longer multiplied by δ, since we are considering the cell density. The previous equation can be written as

$$\begin{aligned} z_j^{n+1} &= (z_j^n + \Xi)(1-\tau q_z) + \tau S_j^n \\ &= z_j^n + \Xi - \tau q_z z_j^n - \tau q_z \Xi + \tau S_j^n \end{aligned}$$

where

$$\begin{aligned} \Xi &:= \Xi_1 + \Xi_2 \\ \Xi_1 &:= \theta_z \frac{z_{j-1}^n + z_{j+1}^n - 2z_j^n}{2} \\ \Xi_2 &:= -(\tilde{F}_{j\to j-1}^n + \tilde{F}_{j\to j+1}^n) z_j^n + \tilde{F}_{j-1\to j}^n z_{j-1}^n + \tilde{F}_{j+1\to j}^n z_{j+1}^n \end{aligned}$$

Dividing both sides by τ and rearranging the terms, we get

$$\frac{z_j^{n+1}-z_j^n}{\tau} = \frac{\Xi}{\tau} - q_z z_j^n + S_j^n + q_z \Xi \tag{3.7}$$

Let us now assume that there is a function $z \in C^2([0,+\infty)\times\mathbb{R})$ such that $z_j^n = z(t_n, x_j) = z$, so that

$$\begin{aligned} z_j^{n+1} &= z(t_n+\tau, x_j) = z + \tau \partial_t z + \mathcal{O}(\tau^2) \\ z_{j\pm1}^n &= z(t_n, x_j \pm \delta) = z \pm \delta \partial_x z + \frac{1}{2}\delta^2 \partial_{xx}^2 z + \mathcal{O}(\delta^3) \end{aligned}$$

This implies that

$$\Xi_1 = \frac{\theta_z}{2}\delta^2 \partial_{xx}^2 z + \mathcal{O}(\delta^3)$$

Furthermore, the assumptions on ϕ imply that

$$\tilde{F}^n_{j\to j\pm1} = \frac{\nu}{2\phi^*}\Big(\pm\delta\partial_x\phi + \frac{1}{2}\delta^2\partial^2_{xx}\phi + \mathcal{O}(\delta^3)\Big)_+ = \mathcal{O}(\delta)$$

and we can easily conclude that $\Xi = \mathcal{O}(\delta)$. We then use the Taylor expansion of z in the definition of Ξ_2 to get

$$\begin{aligned}\Xi_2 &= -(\tilde{F}^n_{j\to j-1} + \tilde{F}^n_{j\to j+1})z + \tilde{F}^n_{j-1\to j}\Big(z - \delta\partial_x z + \frac{1}{2}\delta^2\partial^2_{xx}z + \mathcal{O}(\delta^3)\Big)\\ &\quad + \tilde{F}^n_{j+1\to j}\Big(z + \delta\partial_x z + \frac{1}{2}\delta^2\partial^2_{xx}z + \mathcal{O}(\delta^3)\Big)\\ &= (\tilde{F}^n_{j-1\to j} - \tilde{F}^n_{j\to j-1} + \tilde{F}^n_{j+1\to j} - \tilde{F}^n_{j\to j+1})z + \delta(-\tilde{F}^n_{j-1\to j} + \tilde{F}^n_{j+1\to j})\partial_x z\\ &\quad + \frac{1}{2}\delta^2(\tilde{F}^n_{j-1\to j} + \tilde{F}^n_{j+1\to j})\partial^2_{xx}z + \mathcal{O}(\delta^3)\end{aligned}$$

Now, let us observe that

$$\begin{aligned}\tilde{F}^n_{j\pm1\to j} - \tilde{F}^n_{j\to j\pm1} &= \frac{\nu}{2\phi^*}[(\phi^n_j - \phi^n_{j\pm1})_+ - (\phi^n_{j\pm1} - \phi^n_j)_+]\\ &= \frac{\nu}{2\phi^*}(\phi^n_j - \phi^n_{j\pm1}) = \frac{\nu}{2\phi^*}\Big(\mp\delta\partial_x\phi - \frac{1}{2}\delta^2\partial^2_{xx}\phi + \mathcal{O}(\delta^3)\Big)\end{aligned}$$

using the relation $x_+ - (-x)_+ = x_+ - x_- = x$. We therefore have

$$\Xi_2 = \frac{\nu}{2\phi^*}\Big\{-\delta^2\partial^2_{xx}\phi z + \delta[-(\delta\partial_x\phi + \mathcal{O}(\delta^2))_+ + (-\delta\partial_x\phi + \mathcal{O}(\delta^2))_+]\partial_x z + \mathcal{O}(\delta^3)\Big\}$$

Finally, Eq. (3.7) becomes

$$\begin{aligned}\partial_t z + \mathcal{O}(\tau^2) = \theta_z\frac{\delta^2}{2\tau}\partial^2_{xx}z + \mathcal{O}(\frac{\delta^3}{\tau}) + \frac{\nu}{\phi^*}\frac{\delta^2}{2\tau}\Big\{&-\partial^2_{xx}\phi z\\ &+ [-(\partial_x\phi + \mathcal{O}(\delta))_+ + (-\partial_x\phi + \mathcal{O}(\delta))_+]\partial_x z + \mathcal{O}(\delta)\Big\} - q_z z + S^n_j + \mathcal{O}(\delta)\end{aligned}$$

Let us now observe that

$$\sum_h I^n_h = \sum_h i^n_h\,\delta = \sum_h i(t_n, x_h)\delta \xrightarrow{\delta\to0} \int_\Omega i(t_n, y)\,\mathrm{d}y$$

which means that

$$S^n_j = \Big(S_0 + \alpha_z\sum_h I^n_h\Big)\mathbb{1}_\omega(x_j) \xrightarrow{\delta\to0} \Big(S_0 + \alpha_z\int_\Omega i(t_n, y)\,\mathrm{d}y\Big)\mathbb{1}_\omega(x_j) =: S(t_n, x_j)$$

Letting $\tau, \delta \to 0$ in such a way that $\frac{\delta^2}{2\tau} \to \tilde{D}$ we arrive at the final result:

$$\begin{aligned}\partial_t z &= \theta_z\tilde{D}\partial^2_{xx}z + \frac{\nu\tilde{D}}{\phi^*}\{-\partial^2_{xx}\phi z + [-(\partial_x\phi)_+ + (-\partial_x\phi)_+]\partial_x z\} - q_z z + S\\ &= \theta_z\tilde{D}\partial^2_{xx}z + \frac{\nu\tilde{D}}{\phi^*}(-\partial^2_{xx}\phi z - \partial_x\phi\partial_x z) - q_z z + S\\ &= \theta_z\tilde{D}\partial^2_{xx}z - \frac{\nu\tilde{D}}{\phi^*}\partial_x(z\partial_x\phi) - q_z z + S\end{aligned}$$

3.2.5 Summary of the continuum model

The system we have formally obtained is the following:

$$\begin{cases} \partial_t u(t,x) = & D\partial^2_{xx}u(t,x) + pu(t,x)\Big(1 - \dfrac{u(t,x)+i(t,x)}{K}\Big) - \dfrac{\beta}{K}u(t,x)i(t,x) \\ & -\dfrac{\zeta}{K}u(t,x)z(t,x) \\ \partial_t i(t,x) = & D\partial^2_{xx}i(t,x) + \dfrac{\beta}{K}u(t,x)i(t,x) - qi(t,x) - \dfrac{\zeta}{K}i(t,x)z(t,x) \\ \partial_t z(t,x) = & D_z\partial^2_{xx}z(t,x) - \dfrac{\chi}{\phi_{\max}}\partial_x(z(t,x)\partial_x\phi(t,x)) - q_z z(t,x) + S(t,x) \\ \partial_t \phi(t,x) = & D_\phi\partial^2_{xx}\phi(t,x) + (\alpha_\phi i(t,x) + \gamma_\phi u(t,x))\,(\phi^* - \phi(t,x)) - q_\phi\phi(t,x) \end{cases} \tag{3.8}$$

where $D := \theta\tilde{D}$, $D_z := \theta_z\tilde{D}$, $\chi := \nu\tilde{D}$ and

$$S(t,x) := \left(S_0 + \alpha_z \int_\Omega i(t,y)\,\mathrm{d}y\right)\mathbb{1}_\omega(x)$$

The first two equations are the ones of Eq. (2.8) with the addition of the death term related to the immune system; we therefore expect to recover similar results for small ζ. This system resembles some of the models discussed in Painter, 2019 for the interactions between cancer and different kinds of immune cells, with the relevant differences being that one of our equations is integro-differential (as in Almeida et al., 2022) and that the infection significantly affects the dynamics, spatially and temporally.

In the next section, we consider the two-dimensional radially equivalent version of this problem. Hence, we assume that

$$\omega := \{\, \boldsymbol{x} \in \Omega \mid |\boldsymbol{x}| \le R \,\} \tag{3.9}$$

with $R > 0$; this corresponds to the situation of a well-vascularised tumour in which immune cells can easily reach any point of the domain or that of a solid tumour that is easily accessible by the immune system both from the histological and topological point of view. The system of PDEs then becomes

$$\begin{cases} \partial_t u = D\dfrac{1}{r}\partial_r(r\,\partial_r u) + pu\Big(1 - \dfrac{u+i}{K}\Big) - \dfrac{\beta}{K}ui - \dfrac{\zeta}{K}uz \\ \partial_t i = D\dfrac{1}{r}\partial_r(r\,\partial_r i) + \dfrac{\beta}{K}ui - qi - \dfrac{\zeta}{K}iz \\ \partial_t z = D_z\dfrac{1}{r}\partial_r(r\,\partial_r z) - \dfrac{\chi}{\phi_{\max}}\dfrac{1}{r}\partial_r(rz\,\partial_r\phi) - q_z z + S \\ \partial_t \phi = D_\phi\dfrac{1}{r}\partial_r(r\,\partial_r\phi) + (\alpha_\phi i + \gamma_\phi u)\,(\phi^* - \phi) - q_\phi\phi \end{cases} \tag{3.10}$$

with

$$S(t,r) := \left(S_0 + 2\pi\alpha_z \int_0^r i(t,s)s\,\mathrm{d}s\right)\mathbb{1}_{[0,R]}(r)$$

Remark 3.1 *When the spatial domain is the two-dimensional real plane $\mathbb{R}^2$ instead of the one-dimensional real line $\mathbb{R}$, the scalar index $j \in \mathbb{Z}$ should be replaced by the vector $\boldsymbol{j} = (j_x, j_y) \in \mathbb{Z}^2$ and the probability that a cell moves to one of the four neighbouring lattice points is $\theta_k/4$, with $k = u, i$. We then need to scale τ and δ in such a way that $\frac{\delta^2}{4\tau} \to \tilde{D}$.*

3.3 Corresponding ODE model and bifurcation analysis

Before comparing the agent-based and the continuous model, it is useful to consider a homogeneous spatial configuration and analyse the equilibria of the corresponding ODE model and their stability. The chemoattractant has the sole purpose of guiding immune cells, therefore it can be neglected in this nonspatial model. Hence, we now consider the system

$$\begin{cases} \dfrac{\mathrm{d}u}{\mathrm{d}t} = pu\Big(1 - \dfrac{u+i}{K}\Big) - \dfrac{\beta}{K}ui - \dfrac{\zeta}{K}uz \\ \dfrac{\mathrm{d}i}{\mathrm{d}t} = \dfrac{\beta}{K}ui - qi - \dfrac{\zeta}{K}iz \\ \dfrac{\mathrm{d}z}{\mathrm{d}t} = \alpha i - q_z z + S_z \end{cases} \tag{3.11}$$

It is important to observe that the inflow of immune cells in Eq. (3.8) depends on the total number of infected cells and not just on the local infected cell density. If we consider that u, i and z are homogeneous in the spatial domain Ω and $\omega = \Omega$, then

$$\mathbb{1}_\omega(x) \int_\Omega i(t,y)\,\mathrm{d}y = \int_\Omega i(t)\,\mathrm{d}y = |\Omega|\, i(t)$$

Hence, in this situation, the parameter α in Eq. (3.11) corresponds to the parameter α_z of Eqs. (3.8) and (3.2) multiplied by the measure of the set Ω (denoted by $|\Omega|$).

The equilibria are $(0, 0, \frac{S_z}{q_z})$, $(K - \frac{\zeta S_z}{pq_z}, 0, \frac{S_z}{q_z})$, (u^*, i^*, z^*) and $(0, -\frac{qq_zK}{\alpha\zeta} - \frac{S_z}{\alpha}, -\frac{qK}{\zeta})$. The latter exists only for $\alpha, \zeta \neq 0$; it is always negative, so we can neglect it. The third one is defined by the expressions

$$u^* := \frac{qK}{\beta} + \zeta z^*, \qquad i^* := \frac{Kpq_z(\beta - q) - S_z\beta(\zeta + \frac{p}{\beta}\zeta)}{\beta[q_z(\beta + p) + \alpha(\zeta + \frac{p}{\beta}\zeta)]}, \qquad z^* := \frac{\alpha}{q_z} i^* + \frac{S_z}{q_z} \tag{3.12}$$

When $\alpha = S_z = 0$, we recover the equilibria in the absence of the immune response (see also Chapter 2). As α and S_z increase, u^* increases and i^* decreases. Similarly, when $\zeta = 0$, the equilibria are analogous to the situation without immune response (although the value of z at the equilibrium may not be 0).

The Jacobian matrix computed at the equilibrium point $(0, 0, \frac{S_z}{q_z})$ has eigenvalues $(-q_z, p - \frac{S_z\zeta}{Kq_z}, -q - \frac{S_z\zeta}{Kq_z})$ and the Jacobian matrix computed at the equilibrium point $(K - \frac{\zeta S_z}{pq_z}, 0, \frac{S_z}{q_z})$ has eigenvalues $(-q_z, -p + \frac{S_z\zeta}{Kq_z}, \beta - q - \frac{S_z(\beta\zeta + p\zeta)}{Kpq_z})$. The first equilibrium is stable when

$$Kpq_z < S_z\zeta$$

corresponding to the situation in which the uninfected cell density of the second equilibrium is negative. This means that the immune system alone may be able to eradicate the tumour without the need for any oncolytic virus. The second equilibrium is stable in case neither the first equilibrium is stable nor $i^* > 0$. In this case, the oncolytic virotherapy is not effective and the outcome of the therapy depends entirely on the immune response. Let us observe that the density of uninfected cells $K - \frac{\zeta S_z}{pq_z}$ is increasing in the parameters ζ, S_z and decreasing in p, q_z: while a complete tumour eradication is unattainable, we may still keep the tumour at an acceptable size if the immune response is strong enough.

The expressions for the eigenvalues of the Jacobian matrix computed at the third equilibrium point are more complicated. Numerical simulations show that, in the parameter region where $i^* > 0$, either this equilibrium is stable or there appears a stable limit cycle. Fig. 3.2 shows numerical bifurcation diagrams for the parameters α, β and

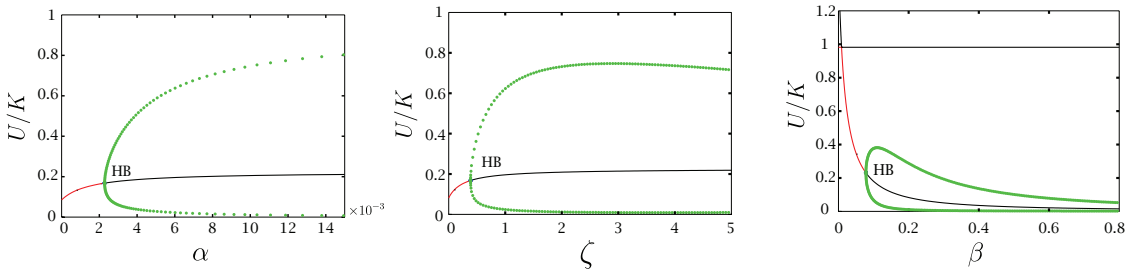

FIGURE 3.2: One parameter bifurcations in α, ζ and β of Eq. (3.11), with other parameters as in Table 3.2. The immune killing rate ζ has been set to the base value 0.50 h^{-1}. In order to facilitate comparison with the forthcoming two-dimensional simulations, we set $\alpha = \pi r^2 \alpha_z$ with $r = 5$ mm (corresponding to a late stage of tumour growth). The green dots show the maximum and minimum values of U/K during the oscillations of the stable limit cycle. The solid lines show the value of the equilibrium of U divided by K; the line is red if the equilibrium is stable and black if it is unstable. Hopf bifurcations are denoted by HB. Observe that for low values of β the infection-free equilibrium close to carrying capacity is stable.

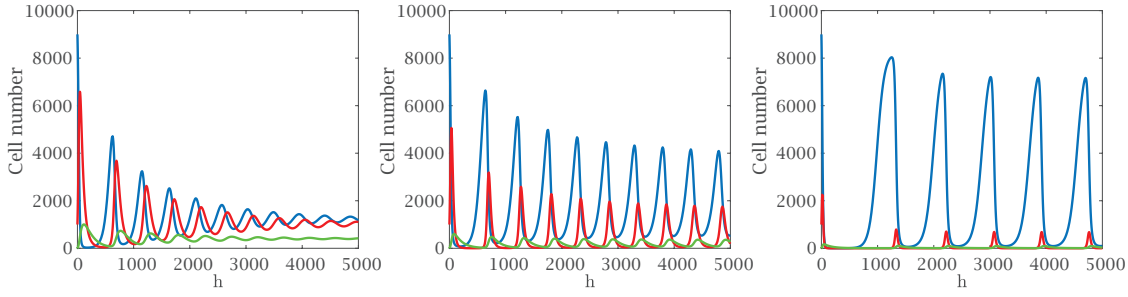

(a) $\zeta = 0.01$ h^{-1} (b) $\zeta = 0.50$ h^{-1} (c) $\zeta = 5.00$ h^{-1}

FIGURE 3.3: Numerical simulation of Eq. (3.11) with the parameters as in Table 3.2 and different values of the immune killing rate ζ. As in Fig. 3.2, we set $\alpha = \pi r^2 \alpha_z$ with $r = 5$ mm. Uninfected tumour cells are plotted in blue, infected tumour cells in red and immune cells in green. The oscillations become wider as ζ increases, in accordance with the bifurcation diagram of Fig. 3.2b.

Parameter	Description	Value [Units]	Reference
p	maximal duplication rate of uninfected cells	1.87×10^{-2} [h^{-1}]	Ke et al., 2000
q	death rate of infected cells	8.34×10^{-3} [h^{-1}]	model estimate
D	diffusion coefficients of cancer cells	1.88×10^{-4} [mm^2/h]	estimate based on Kim et al., 2006
β	infection rate	1.02×10^{-1} [h^{-1}]	estimate based on Friedman et al., 2006
K	tissue carrying capacity	10^4 [cells/mm^2]	Lodish et al., 2008
D_ϕ	diffusion coefficients of chemoattractant	3.33×10^{-2} [mm^2/h]	Matzavinos et al., 2004
ϕ^*	saturation density of chemoattractant	2.92 [$\mu g/mm^2$]	Gao et al., 2014
α_ϕ	secretion of chemoattractant by infected cells	2.50×10^{-4} [$mm^2/(h \cdot cells)$]	model estimate
γ_ϕ	secretion of chemoattractant by uninfected cells	5.00×10^{-6} [$mm^2/(h \cdot cells)$]	model estimate
q_ϕ	decay of chemoattractant	8.33×10^{-2} [h^{-1}]	Cooper and Kim, 2014
D_z	diffusion coefficients of immune cells	4.20×10^{-3} [mm^2/h]	Almeida et al., 2022
χ	chemotactic coefficient of immune cells	1.65×10^{-1} [mm^2/h]	model estimate
q_z	death rate of immune cells	7.50×10^{-3} [h^{-1}]	Hao et al., 2014
S_0	base inflow rate of immune cells	5.00×10^{-2} [cells/($mm^2 \cdot h$)]	model estimate
α_z	inflow rate of immune cells due to the infection	3.75×10^{-5} [$(mm^2 \cdot h)^{-1}$]	model estimate
ζ	immune killing rate of cancer cells	0.50 or 5.00 [h^{-1}]	model estimate
R_u	initial radius of uninfected cells	2.60 [mm]	Kim et al., 2006
R_i	initial radius of infected cells	1.00 [mm]	model estimate

TABLE 3.2: Reference parameter set used in this chapter.

ζ. The diagrams were obtained using the software `auto`, which allows the study of the stability of equilibria and limit cycles through numerical continuation. In all three cases, we observe the appearance of a Hopf bifurcation; in these continuations, the other parameters of Eq. (3.11) are set to the values of Table 3.2. The size of the oscillations of the limit cycle increases as α and ζ increase, and decreases as β increases. As a consequence, the enhancement of the immune response may significantly decrease the effectiveness of the therapy. However, it is fundamental to also consider that, in some cases, the oscillations have a minimum very close to zero, as it is clear from the time series of Fig. 3.3: if we take into account a discrete number of cells, they may go extinct when approaching the minimum due to stochastic events and the following regrowth may not take place. Variations of the parameter p never result in a bifurcation of this equilibrium (at least when all the other parameters are within the range of our interest), but the size of the oscillations during the convergence decreases as p increases; a few particular parameter combinations result into a monotone convergence towards the equilibrium (e.g., for a high value of p).

3.4 Comparison between agent-based and continuum models

In this section, we compare numerical simulations for the agent-based model with the corresponding PDE system. It is useful to recall that, in the absence of an immune response, the uninfected cells form a travelling wave invading the surrounding area at speed $2\sqrt{Dp}$ and infected cells invading a region in which uninfected cells are at

carrying capacity form a travelling wave moving at speed $2\sqrt{D(\beta - q)}$, as discussed in Chapter 2. These results cannot be easily generalised to Eq. (3.8), as the chemotactic movement of immune cells does not fall within this framework. We may still expect that uninfected cells invade a region where the number of immune cells can be neglected and thus the expression $2\sqrt{Dp}$ is still a good approximation of the invasion speed. However, we should not expect the considerations about the equilibria of Eq. (3.11) to directly apply to the expanding central region, due to both chemotaxis and the nonlocal term in the equation.

3.4.1 Details of numerical simulations

Parameter values The majority of the parameters of the model have been estimated from the empirical literature, while a few others are specific to our formulation of the model and have been set to reasonable values in order to reproduce plausible dynamics. The parameters p, D, K and β assume the values listed in Table 3.2, which are the same used in Chapter 2. On the other hand, the basic death rate of infected cells q has been decreased to 8.34×10^{-3} h^{-1}, which is one-fifth of the value used in Chapter 2. This is due to the fact that, in the current model, q does not take into account the death of infected cells due to immune killing, which is considered separately.

The diffusion coefficient of the chemoattractant D_ϕ has been taken equal to 3.33×10^{-2} mm^2/h following Matzavinos et al., 2004. The saturation density of the chemoattractant ϕ^* and the secretion rates of chemoattractant by infected cells α_ϕ have been adapted from the values reported in Jenner et al., 2022, which fit the data of IFN γ taken from Gao et al., 2014. The value of ϕ^* has been obtained by rescaling the estimate of Jenner et al., 2022 to our two-dimensional setting, yielding a value of 2.92 μg/mm^2. The secretion rate reported in Jenner et al., 2022 refers to a single CD4$^+$T and these cells are assumed to be stimulated by infected tumour cells; we have adapted their value to our setting by dividing it by the carrying capacity K, obtaining the value $\alpha_\phi = 2.50 \times 10^{-4}$ mm^2/(h·cells). Since we are assuming that immune cells are much less stimulated by uninfected tumour cells, we have set the secretion rate of chemoattractant by uninfected cells γ_ϕ to 5.00×10^{-6} mm^2/(h·cells), which still allows obtaining a considerable reduction of the tumour load when the infection stimulates the immune system. The decay of chemoattractant q_ϕ has been taken equal to 8.3×10^{-2} h^{-1}, as in Cooper and Kim, 2014.

While it is clear from experimental results that the speed of an immune cell is around 1.08 mm/h (Textor et al., 2011), the estimate of the diffusion and chemotactic coefficients D_z and χ from this consideration constitute a particular challenge. The diffusion coefficient of immune cells has been set to $D_z = 4.20 \times 10^{-3}$ mm^2/h, as in Almeida et al., 2022, noting that similar values are used elsewhere in the literature (such as in Atsou et al., 2020). We remark that, following the approach of Hillen and Swan, 2016; Othmer and Hillen, 2002, one could estimate a value in the same order of magnitude relying on reasonable biological assumptions (although the precise quantities needed are hard to estimate). We performed several simulations of our agent-based model to conclude that for $\chi = 1.65$ mm^2/h immune cells move toward a gradient of chemoattractant similar to the one present in our simulations (i.e., the stationary profile of the chemokines for the initial condition of our simulations) with an average speed of approximately 0.6 mm/h. We decrease this value to $\chi = 0.165$ mm/h^2 to avoid an excessive concentration of immune cells; the resulting average speed is around 0.06 mm/h, which is plausible considering that immune cells face many physical obstacles in penetrating the tumour microenvironment.

The death rate of immune cells q_z has been taken equal to 7.5×10^{-3} h^{-1}, which is the value used in Hao et al., 2014 for T4 cells. The base inflow rate of immune cells S_0 has

been set to 5.00×10^{-2} cells/(mm^2·h) in order to have a density of immune cells inside the tumour coherent with experimental observations (Chatzopoulos et al., 2020; Yasuda et al., 2011). The additional inflow rate of immune cells due to the infection α_z is one of the main peculiarities of our model and summarises several biological processes; hence, it is hard to find meaningful estimates in the literature. We have set it to 3.75×10^{-5} (mm^2·h)$^{-1}$, which allows us to have an immune cell density comparable with the aforementioned experimental references. The same problem arises with the immune killing rate of cancer cells ζ: since the model is very sensitive to this parameter, we compare the differences between setting it to 0.50 h^{-1} and 5.00 h^{-1}, corresponding respectively to weak and enhanced immune responses.

In our simulations, we consider a spatial domain $\Omega := [-L, L]^2$ with $L = 10$ mm and we adopt zero-flux boundary conditions. We define ω as in Eq. (3.9) in order to maintain the radial symmetry of the problem, with $R = L$. The initial conditions are

$$u_0(\boldsymbol{x}) = \begin{cases} 0.9\ K & \text{for } |\boldsymbol{x}| \leq R_u \\ 0 & \text{for } |\boldsymbol{x}| > R_u \end{cases} \qquad i_0(\boldsymbol{x}) = \begin{cases} 0.1\ K & \text{for } |\boldsymbol{x}| \leq R_i \\ 0 & \text{for } |\boldsymbol{x}| > R_i \end{cases} \tag{3.13}$$

where R_u and R_i are respectively the initial radius of uninfected and infected cells; initial conditions for z and ϕ are 0 across the whole domain. The reference case with $R_u > R_i$ corresponds to the intratumoral injection of the virus (Jin et al., 2021). On the other hand, in some simulations, we assume that $R_u = R_i$, which corresponds to an infection of the whole domain: since we consider a tumour that can be infiltrated by the immune system without major obstacles, it is reasonable to assume that this could be obtained with an intravenous administration of the virus (Jin et al., 2021).

Numerical simulations for the discrete models We used a temporal step $\tau = 0.02$ h and a spatial step of $\delta = 0.1$ mm, as already done in Chapter 2. All simulations have been performed in MATLAB 2021B.

At every iteration, the cell numbers and the chemoattractant density are updated according to the rules described in Section 3.1. We first consider movement, then reproductions and deaths of all cell populations, the inflow of immune cells, infections and finally chemoattractant dynamics. Since we only need to keep track of the collective fate of cells in the same lattice point, we again used the built-in MATLAB functions `binornd` and `mnrnd`. Zero-flux boundary conditions for cell populations are implemented by not allowing cells at the boundary to leave the domain. The density of the chemoattractant is updated through the two-dimensional analogue of Eq. (3.1); Neumann boundary conditions are then implemented by considering additional grid points outside the domain, with the same density value as the boundary points of the grid.

The one-dimensional plots in Figs. 3.4a, 3.5 and 3.6a are obtained by averaging ten simulation. The cell sums of Fig. 3.17 are obtained by averaging five simulations (although the cell sum obtained from a single simulation does not show any significant difference). All the two-dimensional plots show a single simulation. We remark that, in all cases, we performed at least five simulations and did not observe any relevant qualitative difference with respect to the result shown; the only exception is Fig. 3.13 and the electronic supplementary material S6 of Morselli et al., 2024b, as explained in the following.

In order to allow reproducibility, a random seed has been set at the beginning of each new simulation. In the figures representing a single simulation, only the one with random seed equal to 1 is shown (with the exception of the electronic supplementary material S6 of Morselli et al., 2024b, in which it has been set to 4, and Fig. 3.11, in which it varies between 2 and 5).

Numerical simulations for the continuum models The system of equations (3.10) has been solved with a finite difference scheme explicit in time, using the discretisations $\Delta t = 10^{-4}$, $\Delta x = 0.01$; such a low space step allows to appropriately describe the high peaks of immune cells of some simulations. The only exceptions are the simulations of Fig. 3.9, which are run for a very long time in a bigger domain: there, the discretisation for space is $\Delta x = 0.02$, which guarantees stability at late times without the need to decrease the time step. We used a forward upwind scheme for the chemotactic term in the equation for immune cell density, following LeVeque, 2007; this is a common strategy to deal with this kind of equations (Almeida et al., 2022; Bubba et al., 2020a). The integrals are computed through the built-in MATLAB function `trapz`, which is based on a linear interpolation of functions. We also use again the threshold $\frac{1}{\delta^2}$ to identify the wavefront of infected cells in the solution of the PDE; this allows us to be consistent with the representation of the agent-based model.

3.4.2 Interactions between the tumour and the immune system in the absence of virotherapy

We first describe the behaviour of the model without oncolytic viral infection, in order to better understand the basic interactions between the tumour and the immune system. Fig. 3.4 shows an excellent qualitative agreement between numerical solutions of the system of PDEs (3.10) with $i_0(\boldsymbol{x}) = 0$ and a single simulation of the agent-based model. The number of immune cells involved is so low that stochastic fluctuations cannot be neglected; hence, the quantitative difference between the two modelling approaches is significant; however, it is enough to consider the average over ten simulations to obtain an improved quantitative agreement. For the sake of clarity, Fig. 3.4a represents the central section of the domain, i.e. the set $[-L, L] \times \{0\}$. At the beginning of the simulation, there are no immune cells in the domain, hence the tumour starts to grow towards the carrying capacity and to invade the surrounding area at the speed $2\sqrt{Dp}$ (vertical blue lines in Fig. 3.4a). In the meantime, immune cells enter the domain at the constant rate S_0. Although uninfected cells secrete much less chemoattractant than infected cells, the high number of cells guarantees a chemoattractant secretion sufficient to guide immune cells. Therefore, the immune cell density stabilises around the equilibrium value S_0/q_z (lower horizontal black line in Fig. 3.4a) only far from the tumour, while it is higher inside the tumour and almost 0 around the boundary due to chemotaxis. The presence of immune cells decreases the tumour cell density to approximately $K - \frac{\zeta}{p} z(t, \boldsymbol{x})$ (the upper horizontal black line in Fig. 3.4a uses the value $z(t, 0)$ for simplicity).

As time passes, the area of the tumour increases and the total number of immune cells reaches a steady state; this is due to our assumption that uninfected tumour cells are unable to stimulate the immune system. As a consequence, immune cell density decreases and tumour cell density increases. The maximum density of the chemoattractant stabilises around a value slightly larger than 1 μg/mm^2, which is slightly more than a third of ϕ^* (see Fig. 3.7b). Overall, the total number of tumour cells increases in time, although at a lower rate than it would do in the absence of an immune response.

When the immune killing action is enhanced, clearly, the tumour cell density decreases, as Fig. 3.5 shows. It is important to observe that in this situation, even though the total number of immune cells does not change, the immune cell density inside the tumour is smaller than before: this is due to the fact that fewer tumour cells secrete less chemoattractant (the maximum value is now around 0.85 μg/mm^2, as shown in Fig. 3.7b); as a consequence, the chemotactic component of the immune cell movement is weaker than before and the immune density is more homogeneous in the whole domain due to diffusion. The tumour is still very far from eradication and even a more effective immune

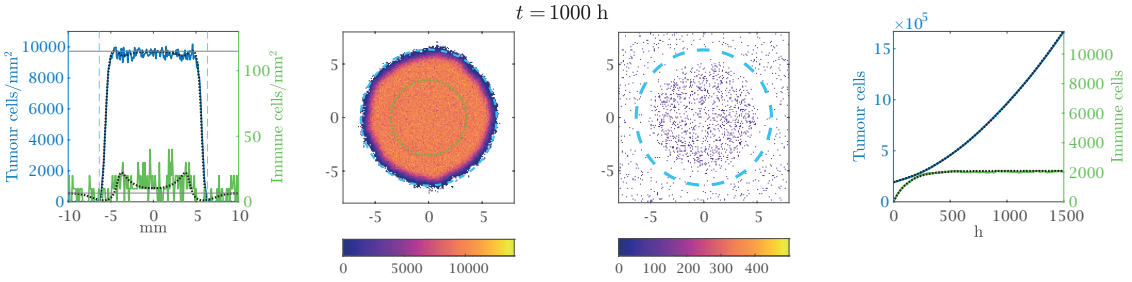

(a) Central section (b) Tumour cells (c) Immune cells (d) Total cell number

FIGURE 3.4: Numerical simulations of the agent-based model with the parameters given in Table 3.2 and $\zeta = 0.50\,\mathrm{h}^{-1}$ in the absence of oncolytic viral infection (i.e., with $R_i = 0$). Panel (a) represents cell densities obtained on the horizontal section of the domain $[-L, L] \times \{0\}$ by averaging ten simulations: the density of the uninfected tumour cells is the blue solid line and the density of the immune cells is the green solid line; observe that the scales are different. The dotted black lines show the numerical solution of Eq. (3.10). The vertical blue dashed lines represent the expected positions of the uninfected invasion front, travelling at speed $2\sqrt{D_u p}$. The horizontal solid black lines show respectively the equilibrium of the ODE for the immune cell density in the absence of infected cells S_0/q_z (the actual concentration is larger inside the tumour due to chemotaxis) and the expected central tumour density $K - \frac{\zeta}{p} z(t, 0)$ with $t = 1000$ h. All the other panels show the result of a single simulation. The dashed cyan circles in panels (b) and (c) represent the expected positions of the tumour invasion front, travelling at speed $2\sqrt{D_u p}$. The dotted green circle in panel (b) represents the internal minimum of the numerical solution of Eq. (3.10). In panel (d), solid lines refer to the agent-based model and dotted lines refer to the continuum model. In all the cases, the maximum of the axes and the colorbars correspond to the maximum over time of the quantity plotted.

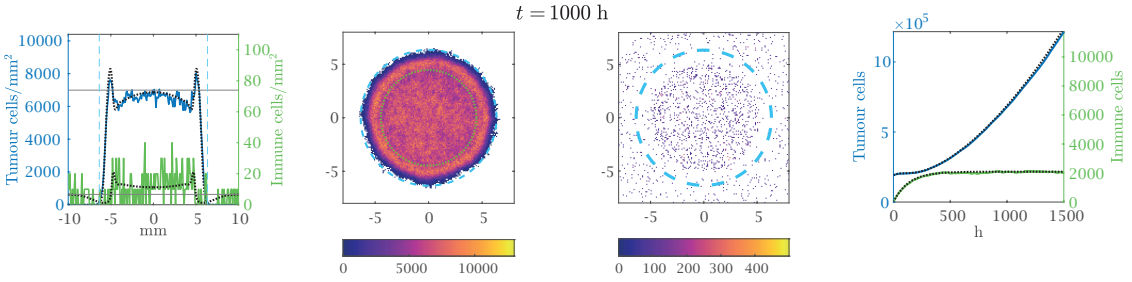

(a) Central section (b) Tumour cells (c) Immune cells (d) Total cell number

FIGURE 3.5: Numerical simulations of the agent-based model with the parameters given in Table 3.2 and $\zeta = 5.00\,\mathrm{h}^{-1}$ in the absence of oncolytic viral infection (i.e., with $R_i = 0$). All the graphical elements have the same meaning as Fig. 3.4.

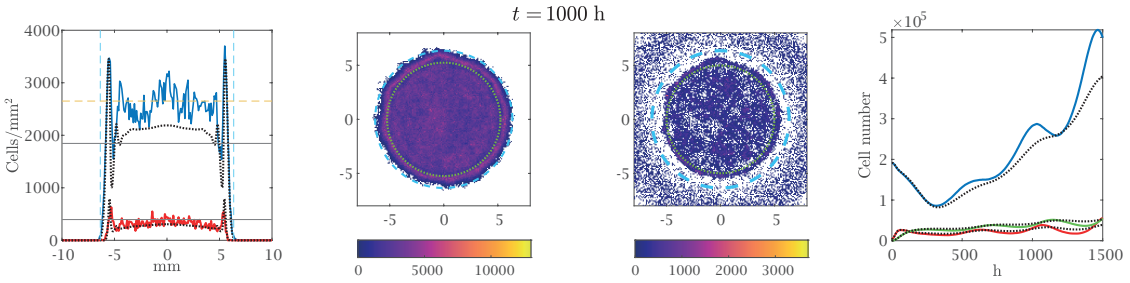

(a) Central section (b) Tumour cells (c) Immune cells (d) Total cell number

FIGURE 3.6: Numerical simulations of the agent-based model with the parameters given in Table 3.2, $\zeta = 0.50\,\mathrm{h}^{-1}$ and central oncolytic viral infection. Panel (a) represents cell densities on the horizontal section of the domain $[-L, L] \times \{0\}$ obtained by averaging ten simulations: the density of the uninfected tumour cells is the blue solid line and the density of the infected tumour cells is the red solid line; immune cell density is not shown, as it would superimpose the infected tumour cell density. The dotted black lines show the numerical solution of Eq. (3.10). The vertical blue dashed lines represent the expected positions of the uninfected invasion front, travelling at speed $2\sqrt{D_u p}$. The horizontal solid black lines show the equilibrium of the ODE given by Eq. (3.12) with the value $\alpha = \alpha_z \pi r(t)^2$, where $r(t)$ is the radius of infected cells at time $t = 1000$ h. All the other panels show the result of a single simulation. The dashed cyan circles in panels (b) and (c) represent the expected positions of the tumour invasion front, travelling at speed $2\sqrt{D_u p}$. The dotted green circle in panels (b) and (c) represents the internal minimum of the numerical solution of Eq. (3.10). In panel (d), solid lines refer to the agent-based model (uninfected, infected and immune cells are represented respectively in blue, red and green) and dotted lines refer to the continuum model. The maximum of the axes and the colorbars correspond to the maximum over time of the quantity plotted, except panel (a), in which the maximum was scaled to enhance readability.

system may not be able to eradicate the mass completely, as a few tumour cells do not secrete enough chemoattractant to guide immune cells. This is in line with the empirical observation that immunotherapy alone usually cannot eradicate cold tumours (Galon and Bruni, 2019). We remark that an analogous situation is observed when the immune inflow is multiplied by a factor of ten (not shown), i.e. no eradication is achieved even when the immune inflow is highly enhanced.

3.4.3 Central infection by oncolytic virus and weak immune response

Expanding on the results of the previous section, we now investigate the effects of an oncolytic viral infection on the immune response and tumour growth. Fig. 3.6, along with the videos accompanying it (see electronic supplementary material S2 and S3 of Morselli et al., 2024b), shows an excellent quantitative agreement between numerical solutions of the system of PDEs (3.10) and the average over ten numerical simulations of the agent-based model. The dynamics in this reference situation are very similar to the ones described in Chapter 2 in the absence of an immune response; therefore, we briefly present the major ideas. At the beginning of the simulation, the central region of the tumour is quickly infected; the outer region starts to grow, but does not reach carrying capacity due to the immune response. The invasion speed of uninfected cells is $2\sqrt{Dp}$ (vertical blue lines in Fig. 3.6), as predicted by theoretical results. On the other hand, the invasion speed of the infected cells in the uninfected region is slightly less than $2\sqrt{D(\beta - q)}$ (vertical red lines in Fig. 3.6), which is the speed value observed in the absence of immune response; the reason is that the density of uninfected cells is below K. The highest peak of immune cell density corresponds to the invasion front of infected cells, as this is the region of the steepest gradient of chemokines. In the central region, the chemokines' density is constantly at ϕ^*; hence, the chemotactic component of the movement is weaker and the density of immune cells is almost constant due to the diffusion, although at a value much higher than S_0/q_z.

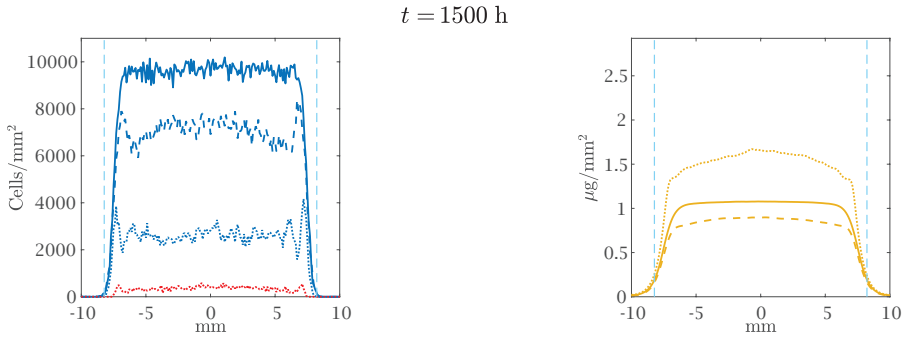

(a) Tumour cells (b) Chemoattractant

FIGURE 3.7: Comparison of cell densities (a) and chemoattractant concentration (b) for the three previous numerical simulations. The solid lines refer to the case of Fig. 3.4, i.e., $\zeta = 0.50\,\mathrm{h}^{-1}$ and $R_i = 0$. The dashed lines refer to the case of Fig. 3.5, i.e., $\zeta = 5.00\,\mathrm{h}^{-1}$ and $R_i = 0$. The dotted lines refer to the case of Fig. 3.5, i.e., $\zeta = 0.50\,\mathrm{h}^{-1}$. All the other parameters take the values given in Table 3.2. The vertical blue dashed lines represent the expected positions of the uninfected invasion front, travelling at speed $2\sqrt{D_u p}$. The results of the agent-based model are averaged over ten simulations and the maximum of the axes corresponds to the maximum over time of these averages: in panel (a), the maximum corresponds to the maximum value of the simulation in Fig. 3.4; in panel (b), the maximum takes the value ϕ^*, which is achieved in the simulation of Fig. 3.6.

The parameters we chose are such that the infection eventually reaches the front of the wave of uninfected cells around time $t = 200$ h; as a consequence, the peak at the front starts to decrease for both populations and infected cells slow down. The final peak of the uninfected cells is approximately the value given in Eq. (2.22), which allows the infected front to move at speed $2\sqrt{Dp}$ in absence of infection. The fact that all the formulas related to the invasion speeds are not affected by the immune system is not surprising, since the linearised equations do not change. On the other hand, the central densities are affected by immune cells: the exact values are hard to predict due to the presence of the chemotactic term, but we can verify that uninfected cell density is higher than in the absence of immune response and infected cell density is lower, as predicted by the analysis of Eq. (3.11). As time progresses, both front waves keep moving at speed $2\sqrt{Dp}$ and central densities of tumour cells and immune cells have some oscillations while converging towards an equilibrium. In the central region, the chemokines' density decreases to approximately 1.5 μg/mm^2 due to the reduced amount of cells (see Fig. 3.7): this is still higher than the values we observed in the absence of viral infection and enough to guide a high number of immune cells towards the tumour, although the peak of immune cell density at the boundary of the tumour is lower than at earlier times.

It is interesting to observe that, overall, the immune response reduces the efficacy of the infection: in comparison to the results of Chapter 2, the invasion speed of the infected cells is lower, the equilibrium value of uninfected cells is higher and the one of infected cells is lower (see Eq. (3.12) and the comments thereafter). This suggests that some care is needed when virotherapy is combined with immunotherapy. Despite this difference, most of the conclusions of Chapter 2 to optimise virotherapy remain valid: as it is clear from Eq. (3.12), the efficacy of the infection increases as β increases and q decreases.

3.4.4 Emergence of oscillations

The discussion of Section 3.3 suggests that some parameter ranges may lead to persistent oscillations in the centre of the domain. We should also take into account that these oscillations may be biologically relevant even if they converge towards a stable equilibrium, as the convergence may be very slow. Fig. 3.8 along with the video accompanying it

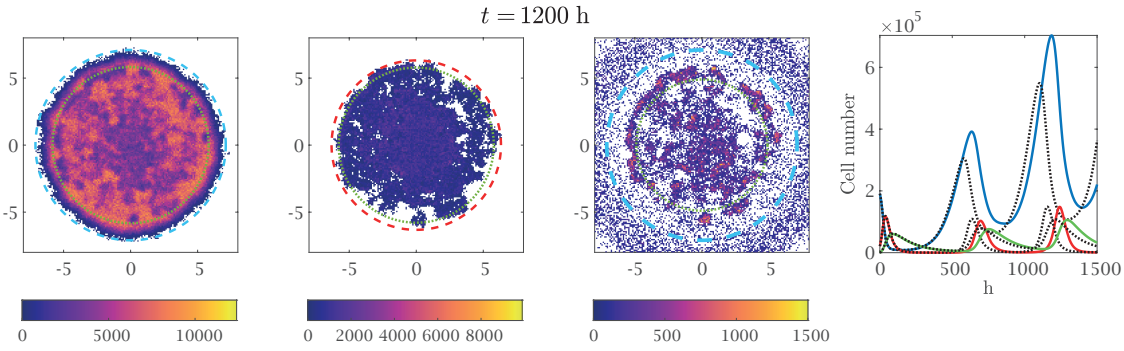

(a) Uninfected tumour cells (b) Infected tumour cells (c) Immune cells (d) Total cell number

FIGURE 3.8: A single numerical simulation of the agent-based model with the parameters given in Table 3.2, $\zeta = 0.50\,\mathrm{h}^{-1}$ and wide oncolytic viral infection (i.e., $R_i = R_u$). The dashed cyan circles in panels (a) and (c) represent the expected positions of the tumour invasion front, travelling at speed $2\sqrt{D_u p}$. The dotted green circles in panels (a), (b) and (c) represent the internal minimum of the numerical solution of Eq. (3.10). The dashed red circle in panel (b) represents the front given by the numerical solution of Eq. (3.10). In panel (d), solid lines refer to the agent-based model (uninfected, infected and immune cells are represented respectively in blue, red and green) and dotted lines refer to the continuum model. In all the cases the maximum of the axes and the colorbars correspond to the maximum over time of the quantity plotted.

(see electronic supplementary material S4 of Morselli et al., 2024b), indeed shows an example of this situation: the only difference with respect to the reference case is the initial condition $R_i = R_u$ (i.e., the initial viral injection covers the whole domain); we, therefore, expect the same asymptotic behaviour of the reference situation, but up to time $t = 1500$ h the difference is very significant. This can be explained by noting that the initial number of infected cells is higher; hence, more immune cells are involved, which causes wider oscillations. It is interesting to observe that the oscillations of the agent-based model are delayed with respect to the ones of the continuum model (this is easy to see from the total number of cells): when the infected cell density is very low, stochasticity becomes relevant and, in some regions, infected cells go extinct; hence, the following infected cell regrowth is at first inhomogeneous and it takes some time to diffuse in the whole domain. The spatial inhomogeneities quickly disappear, and the delay in the oscillations is the main difference between the two modelling approaches.

This example suggests that oscillations may bring the cell density to such low levels that the agents go extinct, even though the continuum model predicts recurrence. Infected cells are much more likely to be eradicated than uninfected cells since even a small population of the latter tends to regrow; this means that, in practice, most of the time after the first oscillation, the tumour keeps growing as it would do in the absence of virotherapy. It makes sense to take the bifurcation diagrams of Section 3.3 as a starting point and study whether system (3.10) has the same behaviour as parameters vary. Fig. 3.9 indeed shows that, as ζ increases, the oscillations that appear show an increasing maximum value and a decreasing minimum value, suggesting that, in the agent-based model, both uninfected and infected cells should become close to eradication. The influence of the parameter p is more interesting: the stability of the equilibrium (u^*, i^*, z^*) appears independent of its value, but the size of the oscillations during the convergence decreases as p increases (see Fig. 3.9); this leads to the counter-intuitive result that a fast-growing tumour has a more predictable behaviour under therapy than one with slower growth.

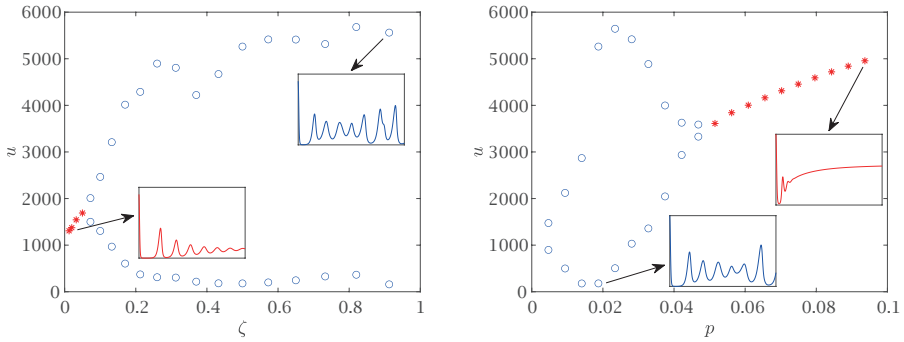

FIGURE 3.9: Oscillations at the origin from numerical simulations of the PDE for different values of ζ and p, with the other parameters as in Table 3.2, $\zeta = 0.50\ \mathrm{h}^{-1}$ in panel (b) and the chemotactic coefficient χ reduced to $1.65 \times 10^{-2}\ \mathrm{mm}^2/\mathrm{h}$ (i.e., one-tenth of the reference value) in order to guarantee numerical stability for all the parameter values under investigation. The simulations are run respectively until 4000 h and 3500 h on circular domains of radius 20 mm and 25 mm in order to avoid boundary effects. The blue dots show the maximum and minimum values of $u(\cdot, 0)$ during the oscillations after $t = 3000$ h (when present). The red stars show the value of u in the centre at the last time in cases where oscillations dampen significantly.

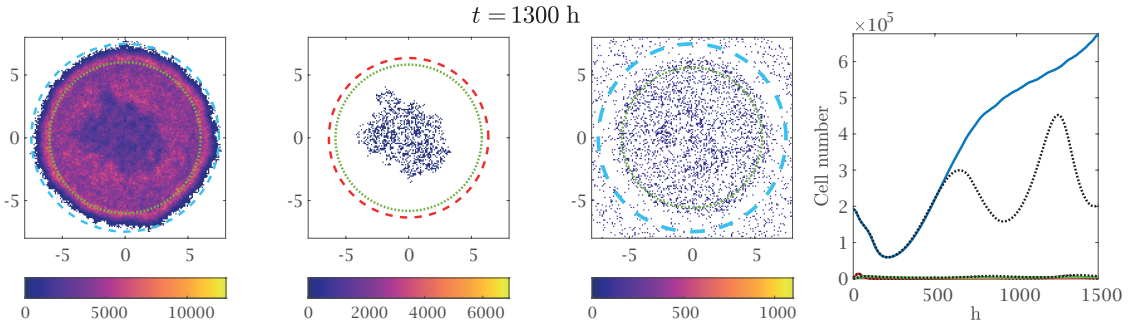

(a) Uninfected tumour cells (b) Infected tumour cells (c) Immune cells (d) Total cell number

FIGURE 3.10: A single numerical simulation of the agent-based model with the parameters given in Table 3.2, $\zeta = 5.00\,\mathrm{h}^{-1}$ and central oncolytic viral infection. The dashed cyan circles in panels (a) and (c) represent the expected positions of the tumour invasion front, travelling at speed $2\sqrt{D_u p}$. The dotted green circles in panels (a), (b) and (c) represent the internal minimum of the numerical solution of Eq. (3.10). The dashed red circle in panel (b) represents the front given by the numerical solution of Eq. (3.10). In panel (d), solid lines refer to the agent-based model (uninfected, infected and immune cells are represented respectively in blue, red and green) and dotted lines refer to the continuum model. In all the cases the maximum of the axes and the colorbars correspond to the maximum over time of the quantity plotted.

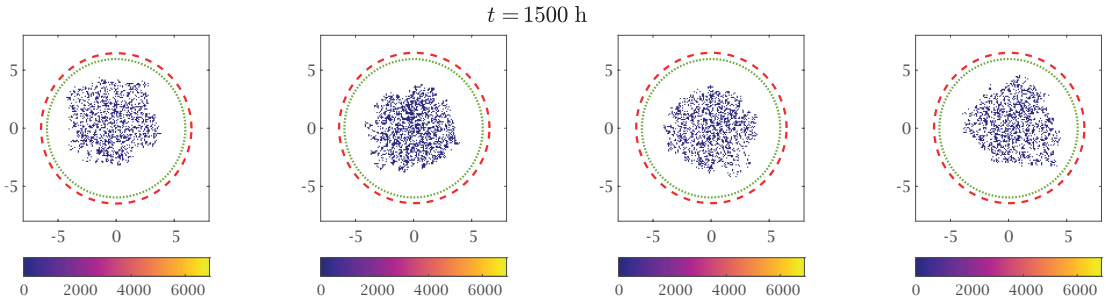

FIGURE 3.11: Comparison between four different simulations of the agent-based model with the parameters given in Table 3.2, $\zeta = 5.00\,\mathrm{h}^{-1}$ and central oncolytic viral infection. These simulations use the same parameter values as the simulation in Fig. 3.10 and only differ by the random seed. The dotted green circles represent the internal minimum of the numerical solution of Eq. (3.10). The dashed red circles represent the front given by the numerical solution of Eq. (3.10). The maximum of the colorbars is the same as in Fig. 3.10b to facilitate the comparison.

3.4.5 Enhanced immune response in the presence of viral infection

The previous discussion motivates our interest in exploring different parameter ranges. While the increase of the infection rate β may be challenging to implement biologically, the enhancement of the immune response appears more feasible, for example, through the use of immune checkpoint inhibitors or other immune boosting techniques (T-cell transfer, immune system modulators, etc.). Fig. 3.10 along with the video accompanying it (see electronic supplementary material S5 of Morselli et al., 2024b), shows this situation, with the immune killing rate of cancer cells increased to 5.00 h^{-1}. The central region of the tumour is quickly infected and the total cancer cell density decreases significantly shortly after due to the action of immune cells. When the central cell concentration is very low, the immune cells move quickly towards the outer region of the tumour, as it secretes more chemoattractant. As the number of infected cells decreases, the inflow of immune cells significantly reduces: as a consequence, around time $t = 200$ h, while the cell density in the outer region is still decreasing, the central uninfected cell density starts to increase again due to the absence of infected and immune cells. The agent-based model and the continuum model show an excellent quantitative agreement up to approximately $t = 490$ h, when we observe the recurrence of the infection only in the continuum model, which also stimulates again the immune system. In the agent-based model, infected cells are extinct in most of the domain; hence, the second infection is less efficient because it takes more time for the infected cells to diffuse again in the whole tumour. It is interesting to observe that the infection remains confined in the centre of the tumour even at later times due to the strong immune response. Overall, the dynamics of the two models differ significantly: Fig 3.11 shows that the same behaviour is consistently observed in all the agent-based simulations we performed in these settings. In the agent-based model, the cancer cell number at later times is significantly higher than in the case of Fig. 3.6, meaning that the stronger immune response decreases the efficacy of the therapy.

The main reason for the failure of the therapy in the previous case is the fact that the immune response is strong enough to eradicate infected cells, but too weak to do the same with uninfected cells. A possible solution is to try and increase the immune cell density: a natural way to do so is having more infected cells to increase immune inflow; in the previous case, the infection was stopped before reaching the tumour boundary, therefore we now assume that the initial infection is spread in the whole tumour so that we avoid such issue. The result is shown in Fig. 3.12. In this situation, the tumour is infected everywhere and the immune cells kill all infected cells and most of the uninfected cells.

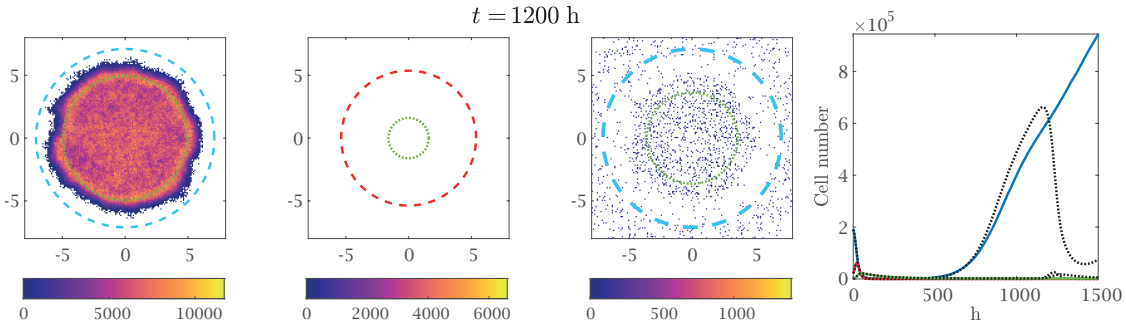

(a) Uninfected tumour cells (b) Infected tumour cells (c) Immune cells (d) Total cell number

FIGURE 3.12: A single numerical simulation of the agent-based model with the parameters given in Table 3.2, $\zeta = 5.00\,\mathrm{h}^{-1}$ and wide oncolytic viral infection (i.e., $R_i = R_u$). The dashed cyan circles in panels (a) and (c) represent the expected positions of the tumour invasion front, travelling at speed $2\sqrt{D_u p}$. The dotted green circles in panels (a), (b) and (c) represent the internal minimum of the numerical solution of Eq. (3.10). The dashed red circle in panel (b) represents the front given by the numerical solution of Eq. (3.10). In panel (d), solid lines refer to the agent-based model (uninfected, infected and immune cells are represented respectively in blue, red and green) and dotted lines refer to the continuum model. In all the cases the maximum of the axes and the colorbars correspond to the maximum over time of the quantity plotted.

As time passes, the number of immune cells in the domain decreases; the few remaining uninfected cells left secrete too little chemoattractant to guide the immune action; hence, they start to regrow. Despite the low cell numbers involved, stochasticity does not play a key role in the process: we performed thirty identical simulations with different random seeds and they all showed the same qualitative behaviour and negligible quantitative differences. Overall, the regrowth is only slightly delayed with respect to the continuum model. At long times, this situation is even worse than the previous one, since the infection has completely extinguished; nevertheless, the initial tumour reduction is still remarkable and should not be neglected.

It is interesting to observe that the increase of immune cell density at later times (due, for example, to CAR-T therapy (He et al., 2023)) is not enough alone to eradicate the few tumour cells left, as T-cells are unable to effectively detect tumour cells (not shown). On the other hand, for higher chemoattractant secretion rates, the immune system may be able to keep the few surviving cancer cells under control and, in some cases, even to completely eradicate the tumour. In this setting, we observe a significant effect of stochasticity due to the very low uninfected cell number involved; hence, we performed one hundred simulations and compared the final cell number for three different values of the chemoattractant secretion rates, as shown in Fig. 3.13. When α_ϕ has the reference value and $\gamma_\phi = \alpha_\phi$ (Fig. 3.13a), tumour eradication is observed only in a few simulations and, in some others, the tumour appears under control for a long time (see supplementary material S6 for an example of this); nevertheless, the majority of the simulations show recurrence. As the values of α_ϕ and γ_ϕ increase (Fig. 3.13b), eradication becomes more likely to happen; in the few cases in which recurrence is observed, it happens later. When the secretion rates are even higher (Fig. 3.13c), the immune system appears able to eradicate the tumour in the wide majority of cases. As the secretion rates increase, the number of simulations in which the tumour is not completely eradicated becomes negligible. These scenarios could be interpreted as the situation of a tumour with a very high mutational burden that is well recognised by the immune cells in the area, despite not stimulating the immune system by itself (see, for example, the review O'Donnell et al., 2018 and type 1 tumours described there); it is therefore highly likely that such a tumour never reaches a significant size, as any attempt to grow would be immediately stopped by the immune cells already present in the area. Our results

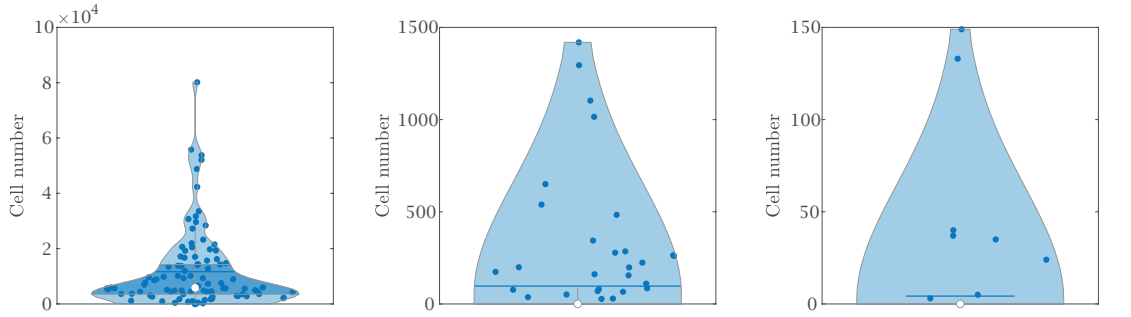

(a) $\alpha_\phi = \gamma_\phi = 2.50 \times 10^{-4}$ mm^2/(h·cells) (b) $\alpha_\phi = \gamma_\phi = 3.75 \times 10^{-4}$ mm^2/(h·cells) (c) $\alpha_\phi = \gamma_\phi = 4.50 \times 10^{-4}$ mm^2/(h·cells)

FIGURE 3.13: Violin plots of the final cell number at time $t = 1500$ obtained from one hundred simulations of the agent-based model with the parameters given in Table 3.2, $\zeta = 5.00\,\mathrm{h}^{-1}$, wide oncolytic viral infection (i.e., $R_i = R_u$) and different chemoattractant secretion rates. The blue dots show the single results, not shown when they are at 0; this happens in 6% of simulations of panel (a), 72% of simulations in panel (b) and 92% of simulations in panel (c). The white dots show the median and the blue horizontal lines show the average. The dark blue areas show the region between the first and the third quartile; in panel (c), this is not shown, as both quartiles coincide with 0. Randomness plays a very important role in therapeutic outcomes.

show that immunovirotherapy could be efficient in the few cases in which this kind of tumour evades immune control. However, it appears unlikely that a direct increase in the chemokine secretion of uninfected tumour cells could be implemented clinically. We remark that, in all these situations, the agent-based model differs significantly from the continuous model, which always shows tumour relapse.

3.4.6 Different treatment protocols

The best outcome that we have achieved so far without changing the chemoattractant secretion rate is a temporary tumour remission in the situation of an initial infection that affects the whole area of the tumour. It is natural to wonder whether the same result can be obtained when the initial infection is only in the centre. Fig. 3.14, along with the video accompanying it (see electronic supplementary material S7 of Morselli et al., 2024b), shows that this is possible if the immune killing rate is increased at time $t = 200$ h, corresponding to the moment in which the infected front reaches the tumour boundary. This is because the number of infected cells at that time is enough to stimulate an appropriate immune response, and its spread configuration allows the immune system to attack every area of the tumour. The following dynamics are similar to the ones of Fig. 3.12, except that the relapse is slightly faster.

Our goal is now to exploit this temporary remission and try to achieve a better therapeutic outcome, keeping in mind that a persistent infection reduces the tumour burden for indefinitely long times (as in Fig. 3.6). A possible solution would be to have a second viral injection when the tumour starts to relapse, but this is challenging for several reasons. First of all, it is not clear when this should be done: on the one hand, we do not want to wait until the tumour is too big as this is inconvenient for the patient; on the other hand, if we do it early when the number of cells is too low, the infection quickly dies away. A second challenge is the location of the injection: the spatial configuration during the remission is very sparse and it is impossible to predict where the infection should start in order to be effective. We ignore the second issue, assuming that the virus may easily reach any area of the tumour, and focus on the first one. We assume that the immune system is enhanced all the time and the first wide injection is followed by a second one at time $t = 900$ h; we assume that this second viral injection causes 30% of the tumour cells to become infected, irrespective of their location. Fig. 3.15, along with

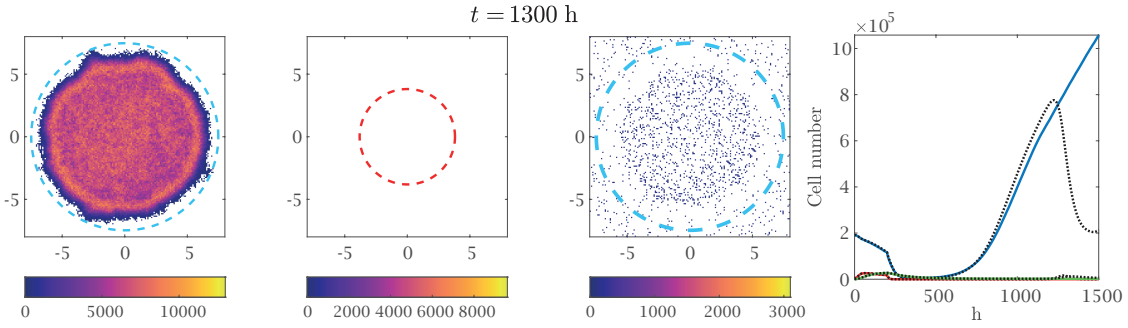

(a) Uninfected tumour cells (b) Infected tumour cells (c) Immune cells (d) Total cell number

FIGURE 3.14: A single numerical simulation of the agent-based model with the parameters given in Table 3.2, central oncolytic viral infection, $\zeta = 0.50\,\mathrm{h}^{-1}$ up to time $t = 200$ h and $\zeta = 5.00\,\mathrm{h}^{-1}$ afterwards. The dashed cyan circles in panels (a) and (c) represent the expected positions of the tumour invasion front, travelling at speed $2\sqrt{D_u p}$. The dashed red circle in panel (b) represents the front given by the numerical solution of Eq. (3.10). The internal minimum of the numerical solution of Eq. (3.10) is not shown, as it is in 0 in all three cases. In panel (d), solid lines refer to the agent-based model (uninfected, infected and immune cells are represented respectively in blue, red and green) and dotted lines refer to the continuum model. In all the cases the maximum of the axes and the colorbars correspond to the maximum over time of the quantity plotted.

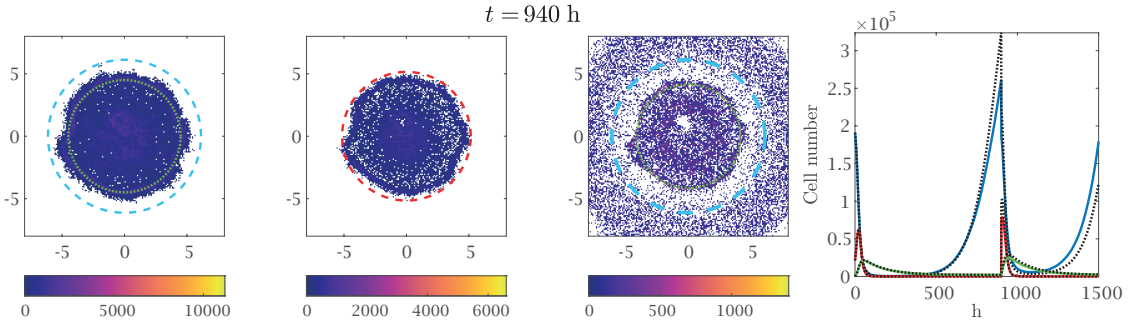

(a) Uninfected tumour cells (b) Infected tumour cells (c) Immune cells (d) Total cell number

FIGURE 3.15: A single numerical simulation of the agent-based model with the parameters given in Table 3.2, $\zeta = 5.00\,\mathrm{h}^{-1}$ and wide oncolytic viral infection (i.e., $R_i = R_u$); a second viral injection is performed at time $t = 900$ h, infecting 30% of cells everywhere. The dashed cyan circles in panels (a) and (c) represent the expected positions of the tumour invasion front, travelling at speed $2\sqrt{D_u p}$. The dotted green circles in panels (a), (b) and (c) represent the internal minimum of the numerical solution of Eq. (3.10) (not shown when this minimum is in 0). The dashed red circle in panel (b) represents the front given by the numerical solution of Eq. (3.10). In panel (d), solid lines refer to the agent-based model (uninfected, infected and immune cells are represented respectively in blue, red and green) and dotted lines refer to the continuum model. In all the cases the maximum of the axes and the colorbars correspond to the maximum over time of the quantity plotted.

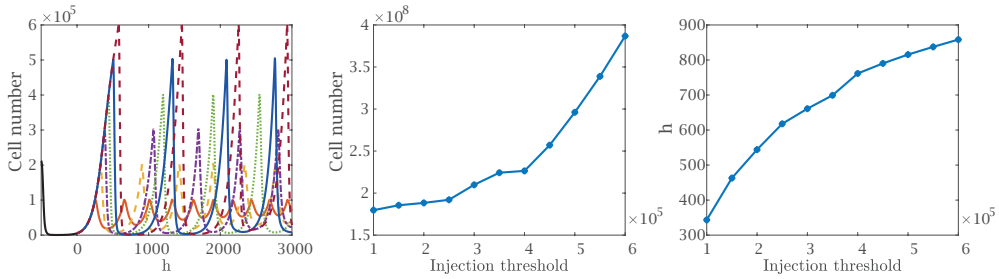

(a) Evolution of tumour cell number (b) Total tumour cell number (c) Average time between consecutive injections

FIGURE 3.16: Numerical solutions of Eq. (3.10) with the parameters given in Table 3.2, $\zeta = 5.00\,\mathrm{h}^{-1}$ and wide oncolytic viral infection (i.e., $R_i = R_u$); after the first 500 h, a new wide viral injection is performed in the whole tumour as soon as the cell count reaches a given threshold (decided a priori) and as a result 30% of cells in every location become infected. Panel (a) shows the total tumour cell numbers for some thresholds. Panels (b) and (c) show respectively the total tumour cell number from $t = 0$ h to $t = 3000$ h and the average time between two consecutive injections for different values of the threshold at which the injection is performed.

the video accompanying it (see electronic supplementary material S8 of Morselli et al., 2024b), shows that we can indeed keep the tumour under control for a longer period of time, although in the end we always observe recurrence.

This suggests that a good therapeutical approach could be to perform periodic repeated viral injections: let us now focus on optimising the schedule. Fig. 3.15 shows a very good quantitative agreement between numerical solutions of the system of PDEs (3.10) and single numerical simulations of the agent-based model. We exploit this fact to reduce our attention to the continuum model and simulate an automatic viral injection when the cell count reaches a fixed threshold decided a priori. Fig. 3.16 shows that, as this threshold increases, the minimum tumour size achieved decreases, but the total area under the curve increases. An ideal treatment would require very frequent viral injections, but its implementation in real life may be inconvenient. Nonetheless, for some chronic conditions where the patient requires lifelong, periodic monitoring, this approach should not be completely discarded.

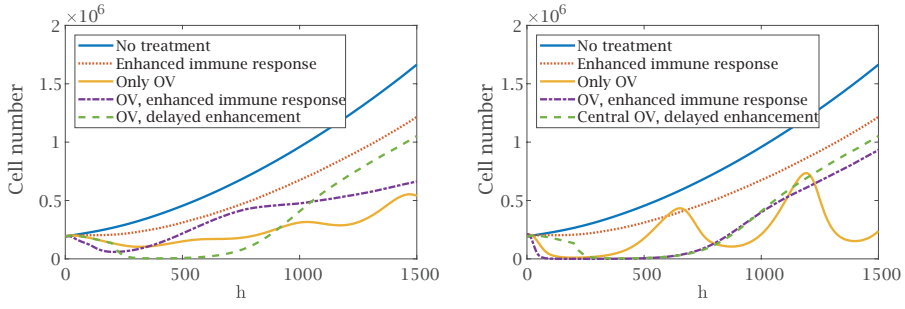

(a) Central viral injection (b) Wide viral injection

FIGURE 3.17: Comparison between the sum of tumour cells obtained as the average of five agent-based simulations in different regimes in case of central viral injection (a) and wide viral injection (b). It is here evident that the enhancement of the immune system during virotherapy may worsen the outcome. The delay of the enhancement in the case of central injection is very similar to the case of a wide injection with the immune system enhanced from the beginning.

3.5 Conclusions

A minimal, hybrid discrete-continuum model for the interactions between tumour cells, oncolytic viruses and the immune system has been developed. The deterministic continuum counterpart is formally derived and the numerical results of the two approaches are compared. The main assumption is that the tumour under investigation is immunologically cold (i.e., its immunogenicity is very low) and the viral infection stimulates an immune response.

The continuum model is an excellent approximation of the underlying microscopic model in several cases. This allows us to improve our understanding of the therapeutical outcome in different settings, relying on some analytical insights coming from the analysis of the nonspatial model and performing extensive numerical simulations in a reasonable amount of time. On the other hand, in some situations, we observe significantly different behaviours between the two models. The main explanation for this is the appearance of oscillations that bring the cell density to very low levels: the continuum model may then exhibit a quick regrowth, which does not take place in the same way in the agent-based model due to the extinction of a cell population in some locations. This extinction is more likely to happen for infected cells, since uninfected cells have the ability to regrow; therefore, it appears as a major obstacle to the effectiveness of immunovirotherapy. Even though stochasticity plays a key role in the process, it is still possible to predict when the phenomenon may be observed based on the bifurcations of the corresponding ODE (which mirrors the oscillations of the spatial continuum model). We remark on the importance of taking into account also the transient behaviour of the system, since oscillations may dampen on a time scale much longer than the biologically meaningful one.

Our results show that, according to the continuum model, any immune response has the tendency to decrease the effectiveness of the virotherapy. This holds true for the agent-based model whenever oscillations are absent or too weak to drive the uninfected cell number very low; in the latter situation, the partial extinction of the solely infected populations may result in a complete failure of virotherapy. On the other hand, stronger oscillations are sometimes able to lead all the cancer cells close to extinction in the individual-based model. This happens when the infection has the possibility to propagate in the whole tumour before the enhancement of the immune system; hence, it can only be achieved if the time and location of the therapies are correctly calibrated. Fig. 3.17 summarises the total number of cells of the agent-based model in different scenarios, clearly showing that the combination of treatments may worsen the outcome; this result is in line with several experimental evidence (Filley and Dey, 2017). At the final time of the simulations $t = 1500$ h, the best outcome is achieved through virotherapy alone and any kind of immune enhancement worsens it. On the other hand, other treatment protocols show much more promising results at earlier times. Even though our model shows recurrence of the tumour at later times in most cases, such a low number of cells suggests that it would be possible to completely eradicate the tumour (e.g., by implementing an additional therapy) or at least to keep it under control (e.g., by repeated viral injections, as shown in Fig. 3.16).

It is fundamental to keep in mind that there are several factors that may hinder this partial success. First, we assume that immune cells kill uninfected and infected cells at exactly the same rate, but it would be reasonable to assume that infected cells are more easily recognised and killed: this highlights the risk that the immune response could stop the infection and the need to enhance it only when a sufficient number of infected cells are present. Furthermore, our model neglects spatial constraints or immunorefractory aspects of some tumour microenvironments that could affect the viral diffusion and the

immune infiltration inside the tumour, which are well-known obstacles to the success of both virotherapy (as already discussed in Chapter 2) and immunotherapy (Almeida et al., 2022) administered alone. On the other hand, in the present work, we only take into account an increase in the immune killing rate that resembles a generic immune-boosting therapy, such as immune checkpoint inhibition. Several immunotherapies have shown their success when combined with oncolytic virotherapy (Shi et al., 2020), such as, but not limited to, adoptive T-cell transfer (Krabbe et al., 2021), CAR-T (He et al., 2023), CAR-T and BiTE (Wing et al., 2018). It could, therefore, be interesting to analyse whether the combination of different immunotherapies could partially overcome the above-mentioned obstacles by refining and augmenting our model.

From the mathematical point of view, it could also be important to perform a rigorous analysis of the PDE that we have obtained. It is well-known that chemotactic models may lead to blow-up in finite time (Hillen and Painter, 2009); hence, the well-posedness for long times may not be completely trivial.

The rest of the models of oncolytic virotherapy presented in the thesis focus on different aspects of the therapy and do not consider immune response for the sake of simplicity. Nevertheless, it is important to keep in mind that in some situations the immune system may significantly affect the dynamics, as demonstrated in the current chapter.

4 Viral dynamics and cells' heterogeneity in discrete and continuous models

All the models analysed so far rely on the two assumptions of quasi-steadiness of the virus and homogeneity of cancer populations. The present chapter aims to relax those assumptions and explore the outcomes to understand their influence on the models better. We here neglect the immune response for the sake of simplicity and extend the modelling framework of Chapter 2 in different ways than the one presented in Chapter 3.

This chapter is organised as follows. In Section 4.1, we include explicit viral dynamics to the models of Chapter 2 and explore the consequences of this inclusion. In Section 4.2, we present the discrete model of infections with heterogeneous uninfected cells, derive its continuum counterpart, present a preliminary asymptotic analysis and compare numerical simulations of discrete and continuous models. In Section 4.3, we discuss the results in the context of the other chapters and provide some hints for future research.

The models described in this chapter have been developed in collaboration with Marcello E. Delitala and Federico Frascoli; some of the results of Section 4.2 have been obtained with Emma Ciccarelli in preparation for her master thesis. Although the findings are not ready for publication at the present stage, they still provide meaningful insights in the thesis context, bridging the gap between the two previous chapters (concerning homogeneous populations and without viral dynamics) and the following one (relating to a heterogeneous population and with viral dynamics).

4.1 Explicit viral dynamics

4.1.1 Description of the agent-based models

We again build upon the modelling framework presented in Section 2.1 and include viral particles, whose concentration is described by a discrete non-negative function analogous to the one relative to the chemoattractant in Chapter 3. As a consequence, the modelling framework is again hybrid discrete-continuous. As in the previous chapters, we restrict our attention to one spatial dimension in the formulation of the models and refer to Remarks 2.1 and 2.2 for the adaptation to two spatial dimensions.

Let us consider the temporal discretisation $t_n = \tau n$ with $n \in \mathbb{N}_0$, $0 < \tau \ll 1$ and the spatial discretisation $x_j = \delta j$, with $j \in \mathbb{Z}$, $0 < \delta \ll 1$; we assume τ to be small enough to guarantee that all the probabilities defined hereafter are smaller than 1. We denote the number of uninfected and infected cells that occupy position x_j at time t_n respectively by U_j^n and I_j^n; the corresponding densities are

$$u_j^n := \frac{U_j^n}{\delta}, \qquad i_j^n := \frac{I_j^n}{\delta}$$

The local pressure is again given by a barotropic relation of the form $\rho_j^n := \Pi(u_j^n + i_j^n)$ and we restrict to the case $\Pi(z) = z$ (hence, the pressure is actually the total cell density). We then denote by v_j^n the concentration of viral particles at time t_n and position x_j. Since the spatio-temporal scales for the viruses' dynamics are very different from cellular ones, we describe them with a discrete balance equation; we remark that this equation contains stochastic elements, as will be explained shortly.

The rules governing the dynamics of the agents correspond precisely to the ones presented in Chapter 2 and depicted in Fig. 2.1, with the only exception of the infection, which here involves the viral concentration. We then consider an additional equation for the evolution of the viral density.

Dynamics of cancer cells We refer to Section 2.1 for the description of the proliferation, movement and death of cancer cells. Here, we consider both undirected random movement and pressure-driven movement. For the sake of brevity, we restrict our attention to logistic growth.

The main difference concerning the models studied in Chapters 2 and 3 is the infection, which in this case is caused by contact between uninfected cells and viral particles. This means that an uninfected cell that occupies position x_j at time t_n becomes infected with probability $\tau\tilde{\beta}v_j^n/K$, where K is the carrying capacity and $\tilde{\beta} > 0$ is a constant infection rate; we use the tilde as a "friendly" reminder that it does not coincide with the parameter β used in Chapters 2 and 3.

Dynamics of the virus We assume that infected cells release viral particles when they die due to lysis. Since cell death is stochastic, the balance equation for viral density needs to take it into account. The virus also decays at rate $q_v > 0$ and diffuses. The resulting balance equation is

$$v_j^{n+1} = v_j^n + \tau D_v \frac{v_{j+1}^n + v_{j-1}^n - 2v_j^n}{\delta^2} + \frac{\alpha L_j^n}{\delta} - \tau q_v v_j^n \tag{4.1}$$

where $D_v > 0$ is the diffusion coefficient and L_j^n denotes the number of infected cells at position x_j that die at time t_n; this last term is multiplied by α, which is the number of viral particles released, and divided by δ to pass from the number of the particles to the density. This equation closely resembles Eq. (3.1), with the main difference given by the presence of stochasticity.

4.1.2 Corresponding continuum models

The derivation of the continuum counterparts of the previously described individual models for cancer cells is almost identical to the computations performed in Section 2.2, with the only difference that now the term $\tau\tilde{\beta}v_j^n/K$ replaces $\tau\beta i_j^n/K$. On the other hand, the continuum counterpart of Eq. (4.1) follows the same approach adopted for the chemoattractant in Section 3.2: we first take the expected values of Eq. (4.1) and rearrange the terms to obtain

$$\frac{v_j^{n+1} - v_j^n}{\tau} = D_v \frac{v_{j+1}^n + v_{j-1}^n - 2v_j^n}{\delta^2} + \alpha \frac{q\mathbb{E}[I_j^n]}{\delta} - q_v v_j^n$$

Parameter	Description	Value [Units]	Reference
p	maximal duplication rate of uninfected cells	1.87×10^{-2} [h^{-1}]	Ke et al., 2000
q	death rate of infected cells	4.17×10^{-2} [h^{-1}]	Ganly et al., 2000
D_u, D_i	diffusion coefficients (undirected movement)	1.88×10^{-4} [mm^2/h]	estimate based on Kim et al., 2006
D_u, D_i	diffusion coefficients (pressure-driven movement)	1.50×10^{-3} [mm^2/h]	estimate based on Kim et al., 2006
K^{1D}	tissue carrying capacity in one dimension	10^3 [cells/mm]	model estimate
K^{2D}	tissue carrying capacity in two dimensions	10^4 [cells/mm^2]	Lodish et al., 2008
q_v	virus clearance rate	1.67×10^{-1} or 1.00 [h^{-1}]	Mok et al., 2009, model estimate
α	viral burst size	580 or 3500 [viruses/cells]	Workenhe et al., 2014; Chen et al., 2001
$\tilde{\beta}$	infection rate	7.00×10^{-4} [h^{-1}]	Friedman et al., 2006
D_v	virus diffusion coefficient	3.6×10^{-2} [mm^2/h]	Kim et al., 2006
R_u	initial radius of uninfected cells	2.6 [mm]	Kim et al., 2006
R_v	initial radius of oncolytic virus	0.5 [mm]	Pooladvand et al., 2021
R_i	initial radius of infected cells	0 [mm]	

TABLE 4.1: Parameters set for the models of infection with viral dynamics

where $\mathbb{E}[\cdot]$ is the expected value. We then assume that there is a function $v \in C^2([0, +\infty) \times \mathbb{R})$ such that $v_j^n = v(t_n, x_j) = v$ and let $\tau, \delta \to 0$ to get

$$\partial_t v = D_v \partial_{xx}^2 v + \alpha q i - q_v v$$

In the case of undirected cell movement, we have the following system of reaction-diffusion PDEs:

$$\begin{cases} \partial_t u = D_u \partial_{xx}^2 u + pu\left(1 - \dfrac{u+i}{K}\right) - \dfrac{\tilde{\beta}}{K} uv \\ \partial_t i = D_i \partial_{xx}^2 i + \dfrac{\tilde{\beta}}{K} uv - qi \\ \partial_t v = D_v \partial_{xx}^2 v + \alpha q i - q_v v \end{cases} \tag{4.2}$$

In the case of pressure-driven cell movement, we have the following local cross-diffusion system:

$$\begin{cases} \partial_t u = \dfrac{D_u}{K} \partial_x [u \partial_x (u+i)] + pu\left(1 - \dfrac{u+i}{K}\right) - \dfrac{\tilde{\beta}}{K} uv \\ \partial_t i = \dfrac{D_i}{K} \partial_x [u \partial_x (u+i)] + \dfrac{\tilde{\beta}}{K} uv - qi \\ \partial_t v = D_v \partial_{xx}^2 v + \alpha q i - q_v v \end{cases} \tag{4.3}$$

We will see shortly that several of the previously analysed characteristic features of Eq. (2.11) disappear due to viral spatial diffusion.

4.1.3 Comparison between agent-based and continuum models

We now compare numerical simulations for the agent-based models and the corresponding PDE systems. All the simulations are performed with the techniques described in

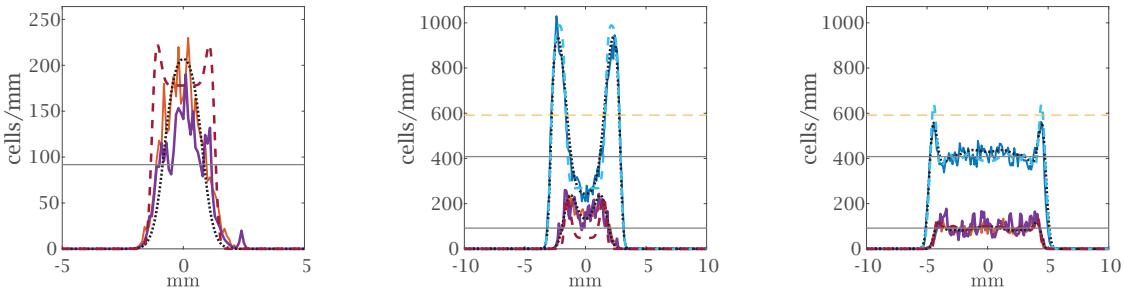

(a) $t = 80$ h (b) $t = 150$ h (c) $t = 700$ h

FIGURE 4.1: Comparison in one spatial dimension between numerical simulations of the discrete model with undirected cell movement (solid lines), the numerical solution of Eq. (2.8) (dashed lines) and the numerical solution of Eq. (4.2) (dotted black lines) at three different times, with the parameters given in Table 4.1, $\alpha = 3500$ viruses/cells and $q_v = 1$ h^{-1}. The viral density of the agent-based model is multiplied by $q_v/(\alpha q)$ to allow the comparison with cell numbers; on the other hand, the viral density for Eq. (4.2) is not shown, as it would superimpose with infected cells. For the agent-based model, the densities of uninfected cells, infected cells and virus are represented respectively in blue, red and purple; the numerical solutions of Eq. (2.8) are represented using the same colours. The horizontal solid black lines show the equilibrium of the ODE given by Eq. (2.15) (with $\beta = \tilde{\beta}\alpha q/q_v$) and the horizontal dashed yellow line represents the expected uninfected density at the front given by Eq. (2.22) (only relevant in panel (c)). The results of the agent-based model are averaged over five simulations. The maximum of the cell density axes in panels (b) and (c) corresponds to the maximum over time of this average (which is larger than the carrying capacity); on the other hand, in panel (a), it has been reduced to allow the comparison between infected cells and virus (and, as a consequence, uninfected cells are not shown).

Section 2.4.1. We use the following initial conditions:

$$u_0(x) = \begin{cases} 0.9\,K & \text{for } |x| \leq R_u \\ 0 & \text{for } |x| > R_u \end{cases} \qquad i_0(x) = 0 \qquad v_0(x) = \begin{cases} V_0 & \text{for } |x| \leq R_v \\ 0 & \text{for } |x| > R_v \end{cases} \tag{4.4}$$

with $V_0 = 2.67 \times 10^4$ in one spatial dimension and $V_0 = (2.67 \times 10^3)^2$ in two spatial dimensions; these values are obtained by appropriately rescaling the one used in Pooladvand et al., 2021, which comes from the number of viral particles used in Kim et al., 2006.

The parameters are set to the same values adopted in Chapter 2, with the only exception of $\tilde{\beta}$, q_v, α, D_v and R_v that are not present in those models. The spatial diffusion coefficient of viral particles D_v has been set to 3.6×10^{-2} mm^2/h, as in Friedman et al., 2006, and the viral injection radius R_v is taken equal to 0.5 mm, following Pooladvand et al., 2021; the values of the other three parameters have been already discussed in Chapter 2. We report the full parameters list in Table 4.1 for the reader's convenience.

As explained in Chapter 1, if the virus is assumed to be quasi-steady, then the infection rate β can be obtained as a combination of several parameters related to viral dynamics, given by Eq. (1.9). Our first goal now is to remove the quasi-steadiness assumption and test how different combinations of α and q_v that maintain their ratio approximately constant affect the dynamics, comparing it with the corresponding model from Chapter 2. We then describe the appearance of oscillations, which do not occur for a quasi-steady virus.

High viral burst size and high viral decay We start by considering the higher values of α and q_v from Table 4.1, chosen in such a way that the ratio $\tilde{\beta}\alpha q/q_v$ corresponds approximately to the reference value of β from Chapter 2. Fig. 4.1 shows an excellent quantitative agreement between numerical solutions of the system of PDEs (4.2) and the average over five numerical simulations of the corresponding agent-based model in one

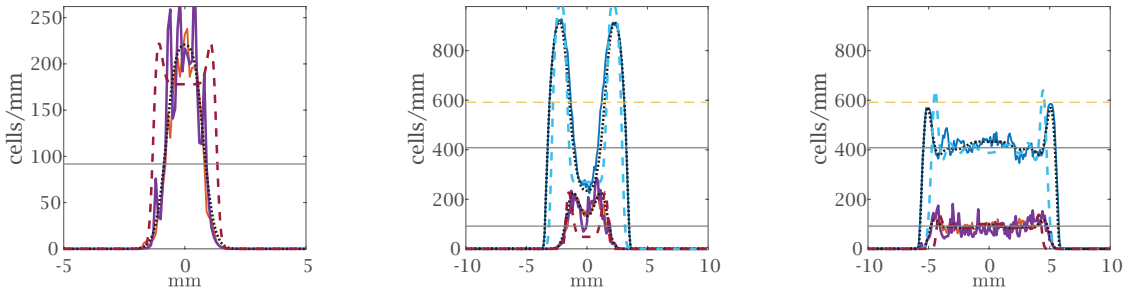

(a) $t = 80$ h (b) $t = 150$ h (c) $t = 700$ h

FIGURE 4.2: Comparison in one spatial dimension between numerical simulations of the discrete model with pressure-driven cell movement (solid lines), the numerical solution of Eq. (2.8) (dashed lines) and the numerical solution of Eq. (4.2) (dotted black lines) at three different times, with the parameters given in Table 4.1, $\alpha = 3500$ viruses/cells and $q_v = 1\ \mathrm{h}^{-1}$. We remark that the diffusion coefficient in Eq. (2.8) was modified to keep the propagation speed constant. All the graphical elements have the same meaning as in Fig. 4.1. Observe that, this time, the maximum value reached by the average uninfected cell density is lower than the carrying capacity.

spatial dimension. Furthermore, the approximation

$$i = \frac{q_v}{\alpha q} v$$

holds most of the time, even in the agent-based model (despite some small stochastic fluctuations), as it is evident from Fig. 4.1a. The initial invasion profile of infected cells is different from the one obtained by the two-equation model in Eq. (2.8), since it is now affected by the fast viral diffusion. Nevertheless, the invasion speed is approximately the same; as a consequence, after an initial transient time, the uninfected cell density is almost indistinguishable from the one resulting from Eq. (2.8) (Fig. 4.1b-c). At later times, Fig. 4.1c shows the formation of travelling waves remarkably similar to the ones already described in Chapter 2, with the same speed and the same values of the internal equilibria. The only slight difference regards the uninfected cell density at the front, which can be explained by the higher infection infiltration when viral dynamics are considered explicitly.

The same excellent agreement is also observed for pressure-driven movement, as shown in Fig. 4.2. The behaviour is very similar to the one observed in the previous case. Let us recall that, in Chapter 2, we observed that an initial central infection remains localised in the case of pressure-driven movement without explicit viral dynamics; this is in sharp contrast with the outcome shown in Fig. 4.2: indeed, in the present situation, viral particles can reach the outer region of the tumour without any obstacle and the constraints of cell movement do not stop the propagation of the infection. The similarity of this situation to the case of undirected cell movement suggests that it makes more sense to compare it to Eq. (2.8) than to Eq. (2.11). We remark that the comparison requires the adaptation of the diffusion coefficient to keep the propagation speed constant (as listed in Table 4.1). The only relevant differences between undirected movement and standard diffusion appear to be the maximum value reached by uninfected cell density, which is higher in the former situation, and the profile of the final invasion front, which, in the latter case, is compactly supported and invades the surrounding tissues slightly faster. For $D_v = 0$, we recover the dynamics described in Chapter 2. Overall, we can conclude that spatial viral dynamics have a more substantial effect on the evolution of the system than cellular spatial dynamics.

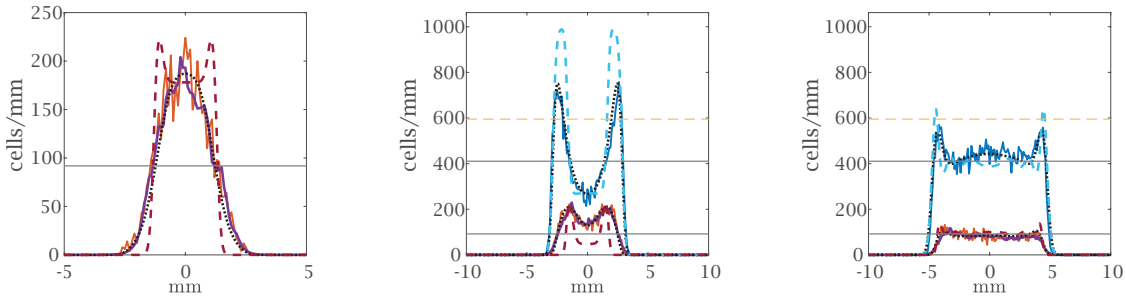

(a) $t = 80$ h (b) $t = 150$ h (c) $t = 700$ h

FIGURE 4.3: Comparison in one spatial dimension between numerical simulations of the discrete model with undirected cell movement (solid lines), the numerical solution of Eq. (2.8) (dashed lines) and the numerical solution of Eq. (4.2) (dotted black lines) at three different times, with the parameters given in Table 4.1, $\alpha = 580$ viruses/cells and $q_v = 1.67 \times 10^{-1}$ h^{-1}. All the graphical elements have the same meaning as Fig. 4.1.

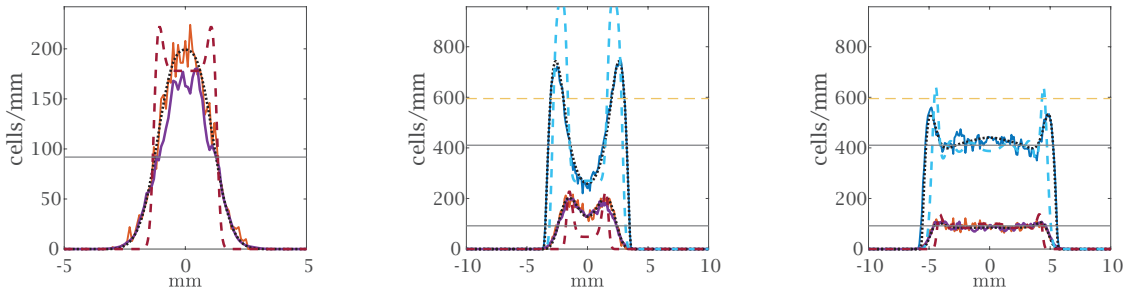

(a) $t = 80$ h (b) $t = 150$ h (c) $t = 700$ h

FIGURE 4.4: Comparison in one spatial dimension between numerical simulations of the discrete model with pressure-driven cell movement (solid lines), the numerical solution of Eq. (2.8) (dashed lines) and the numerical solution of Eq. (4.2) (dotted black lines) at three different times, with the parameters given in Table 4.1, $\alpha = 580$ viruses/cells and $q_v = 1.67 \times 10^{-1}$ h^{-1}. We remark that the diffusion coefficient in Eq. (2.8) was modified to keep the propagation speed constant. All the graphical elements have the same meaning as Fig. 4.1.

Low viral burst size and low viral decay Let us now consider lower values of α and q_v, keeping their ratio approximately as in the previous case. Fig. 4.3 shows again an excellent quantitative agreement between numerical solutions of the system of PDEs (4.2) and the average over five numerical simulations of the corresponding agent-based model in one spatial dimension. Even though the quasi-steadiness of the virus still holds, this time, the system's transient behaviour significantly differs from the solution of Eq. (2.8). Fig. 4.3a shows that the lower viral decay rate allows for the viral particles to move further; hence, the viral infection reaches the boundary of the tumour faster than in the previous case; as a consequence, uninfected cells start to decrease their numbers earlier (Fig. 4.3b). This difference does not affect the system's asymptotic behaviour, as it is clear from Fig. 4.3c.

Fig. 4.4 shows that the same excellent agreement is also observed for pressure-driven cell movement. Once again, the dynamics are very similar to the case of undirected cell movement, which confirms our previous observation that the infective dynamics are affected mainly by viral spatial dynamics.

Emergence of oscillations As we anticipated in Chapter 1, it is well known that solutions of Eq. 4.2 may exhibit persistent oscillations for some parameter values; this is in line with the fact that the nonspatial model

$$\begin{cases} \dfrac{\mathrm{d}u}{\mathrm{d}t} = pu\left(1 - \dfrac{u+i}{K}\right) - \dfrac{\tilde{\beta}}{K}uv \\ \dfrac{\mathrm{d}i}{\mathrm{d}t} = \dfrac{\tilde{\beta}}{K}uv - qi \\ \dfrac{\mathrm{d}v}{\mathrm{d}t} = \alpha qi - q_v v \end{cases} \tag{4.5}$$

presents a Hopf bifurcation. Fig. 4.5 shows the bifurcation in the parameter α, obtained using the software `auto`, which allows to study the stability of equilibria and limit cycles through numerical continuation. Fig. 4.6 shows the time series for three different values of α. We remark that a similar behaviour is also observed, for example, as $\tilde{\beta}$ increases or as q_v decreases. The one-dimensional setting is not ideal for studying oscillations, as the lower amount of cells involved may cause extinctions in the agent-based model due to stochasticity, which are not biologically relevant. We therefore now consider the previous models in two spatial dimensions, remarking that in this case extinctions may actually be associated with the biological relevance of random events (as in the cases described in Chapter 3).

For undirected cell movement, Fig. 4.7 shows an overall excellent quantitative agreement between numerical solutions of the system of PDEs (4.2) and the average over five numerical simulations of the corresponding agent-based model in two spatial dimensions. After the initial infection reaches the tumour boundary, the number of cancer cells decreases significantly; as a consequence, stochasticity becomes relevant, and in some regions, cells go extinct. Fig. 4.7a shows the inhomogeneous pattern of uninfected cells caused by this. As time passes, the spatial inhomogeneities quickly disappear, and both models show similar persistent oscillations in the tumour centre around the equilibrium values (coherently with what the bifurcation diagram shows). A slight delay of the oscillations is the main difference between the two modelling approaches: this is easy to see from the total number of cells, depicted in Fig. 4.9. The invasion speed of the tumour in the surrounding area is still $2\sqrt{Dp}$ and the uninfected cell density at the front is approximately given by Eq. (2.22), despite some fluctuations. It is interesting to

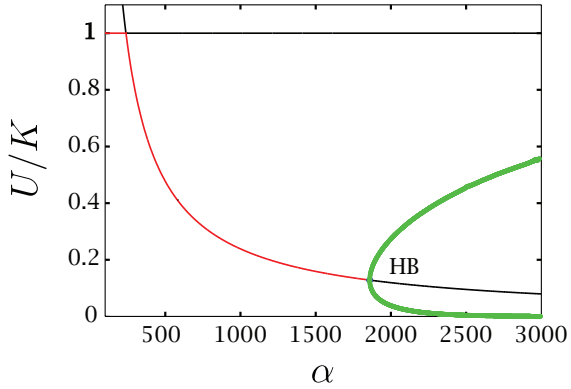

FIGURE 4.5: One parameter bifurcation in α of Eq. (4.5), with other parameters as in Table 4.1 and $q_v = 0.167\,\mathrm{h}^{-1}$. The green dots show the maximum and minimum values of U/K during the stable limit cycle oscillations. The solid lines show the equilibrium value of U divided by K; as in previous bifurcation diagrams, the line is red if the equilibrium is stable and black if it is unstable. Hopf bifurcations are denoted by HB. Observe that for low values of α, the infection-free equilibrium close to carrying capacity is stable.

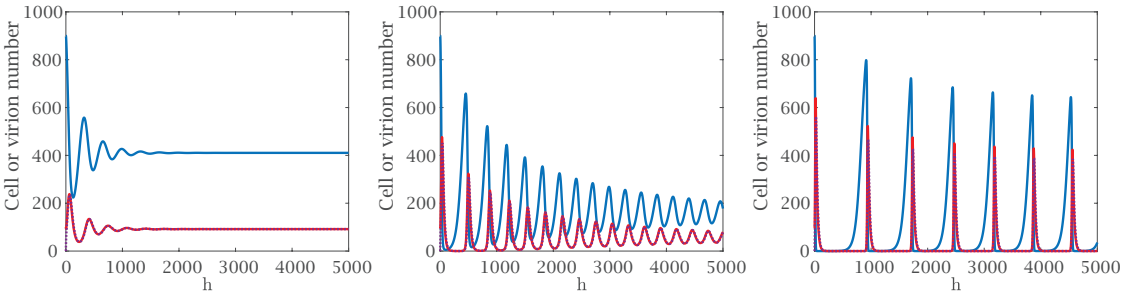

(a) $\alpha = 580$ viruses/cells (b) $\alpha = 15000$ viruses/cells (c) $\alpha = 3500$ viruses/cells

FIGURE 4.6: Numerical simulation of Eq. (3.11) with the parameters as in Table 4.1 and different values of the viral burst size α. The solid blue lines represent uninfected cells, the solid red lines infected cells and the dotted purple lines represent viral density multiplied by $q_v/(\alpha q)$; the two latter quantities superimpose almost exactly. The oscillations become wider as α increases, in accordance with the bifurcation diagram of Fig. 4.5.

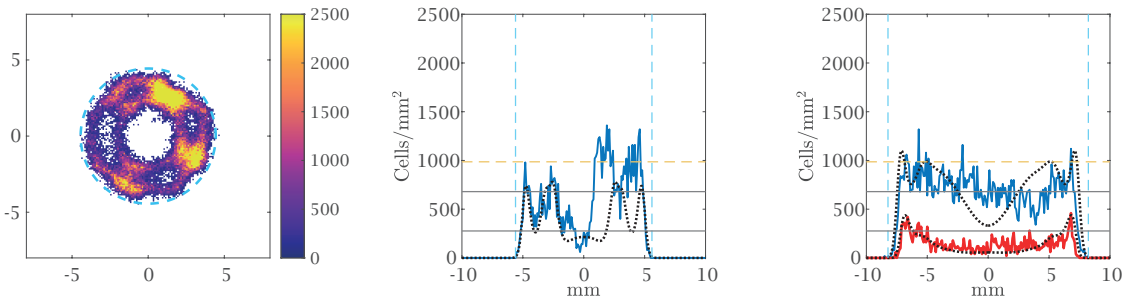

(a) uninfected cells, $t = 490$ h (b) uninfected cells, $t = 800$ h (c) $t = 1500$ h

FIGURE 4.7: Numerical simulations with the parameters given in Table at three different times, with the parameters given in Table 4.1, $\alpha = 3500$ viruses/cells and $q_v = 1.67 \times 10^{-1}$ h^{-1}. Panel (a) shows uninfected cell density from a single simulation to show the impact of stochasticity; the dashed cyan circle represents the expected positions of the tumour invasion front, travelling at speed $2\sqrt{D_u p}$. Panels (b) and (c) represent cell densities obtained on the horizontal section of the domain $[-L, L] \times \{0\}$ obtained by averaging five simulations: the density of the uninfected tumour cells is the blue solid line and the density of the infected tumour cells is the red solid line (not shown in panel (b) to avoid the superimposition with uninfected cell density); the viral density is not shown to improve readability. The solutions of Eq. (4.2) are represented with dotted black lines. The vertical blue dashed lines represent the expected positions of the uninfected invasion front, travelling at speed $2\sqrt{D_u p}$. The horizontal solid black lines show the equilibrium of the ODE given by Eq. (2.15) (with $\beta = \tilde{\beta}\alpha q/q_v$) and the horizontal dashed yellow line represents the expected uninfected density at the front given by Eq. (2.22) (only relevant in panel (c)). The maximum of the axes and the colorbars were scaled to enhance readability and are much lower than the maximum over time of the quantity plotted.

remark that highly dynamic patterns may emerge when viral injections at multiple sites are considered (Baabdulla and Hillen, 2024).

The situation is different in the case of pressure-driven movement. As in the previous case, the number of cancer cells decreases significantly after the initial infection reaches the tumour boundary and, in some regions, cells go extinct, originating inhomogeneous patterns. However, the subsequent regrowth does not allow a fast spatial spread due to the slow movement that cells experience when the pressure is so low. Fig. 4.8b indeed shows that uninfected cells take a long time in the agent-based model to move from the hollow ring into the central region; on the other hand, in the case of the PDE, the repopulation is much faster: there is never a complete extinction in the centre and the repopulation is caused by regrowth rather than movement. This difference is particularly evident from the second peak in Fig. 4.9. The difference between the two models tends to disappear as time passes, but Fig. 4.8c still shows some dissimilarities. Both models show an invasion speed much lower than $\sqrt{D_u p/2}$, due to the very low cell density involved (approximately one-tenth of the carrying capacity); this is a significant difference from the case of undirected cell movement and, as a result, the overall cell numbers involved are lower in the second case (see Fig. 4.9).

Fig. 4.9 also shows the comparison with the solution of Eq. (2.8) to remark once again that oscillations cannot be obtained in the two-equations model even for high infection rates. In the case of effective infections, only pressure-driven movement results in a slower invasion speed of the tumour; in this respect, it appears to be closer to the biological situation.

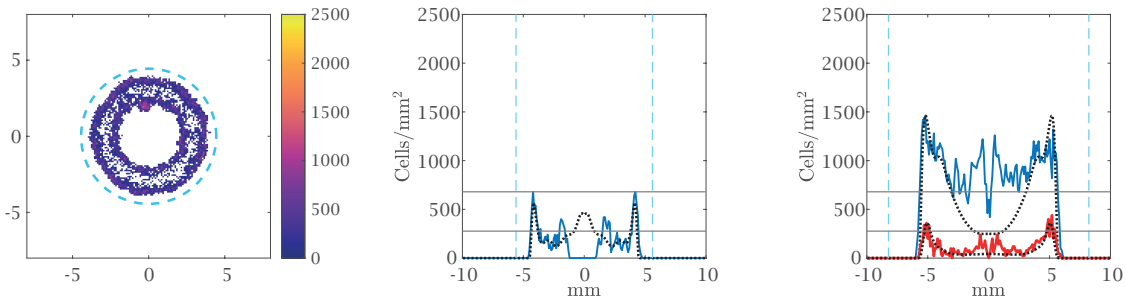

(a) uninfected cells, $t = 490$ h (b) uninfected cells, $t = 800$ h (c) $t = 1500$ h

FIGURE 4.8: Numerical simulations with the parameters given in Table at three different times, with the parameters given in Table 4.1, $\alpha = 3500$ viruses/cells and $q_v = 1.67 \times 10^{-1}$ h^{-1}. All the graphical elements have the same meaning as per Fig. 4.8, with the usual modifications needed to switch between undirected and pressure-driven movement.

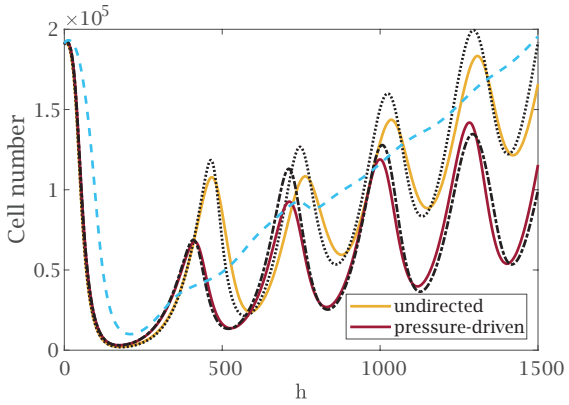

FIGURE 4.9: Comparison between the sum of tumour cells in different scenarios. Solid lines represent the average of five agent-based simulations in the case of undirected cell movement (yellow) and pressure-driven cell movement (red). All the other lines represent the sum of cells obtained from the continuous models: the dotted black line refers to the solution of Eq. (4.2), the dashed-dotted black line to the solution of Eq. (4.3) and the dashed blue line to the solution of Eq. (2.8); the last line has a different colour to highlight the fact that it is related to a two-equations model, which does not exhibit persistent oscillations.

4.2 Infection with an epigenetically structured uninfected population

We now add to the uninfected compartment an epigenetic heterogeneity that affects proliferation and infection. In this way, we can analyse how the emergence of resistance to the viral infection affects the outcome of the virotherapy. Several mechanisms may be involved in the process, such as interferon-mediated resistance, epigenetic modifications, hypoxia-mediated inhibition and virus-entry barriers (Bhatt et al., 2021). The model we develop in this chapter considers a generic kind of resistance without focusing on any specific situation; on the other hand, Chapter 5 is devoted to the application of this modelling approach to the resistance acquired by hypoxic cancer cells.

We assume a trade-off between the proliferation rate and the resistance to the infection, which is not specific of oncolytic virotherapy: for example, in Lorenzi et al., 2021b, this phenomenon is investigated in the framework of a host–parasite system. In the context of our interest, we may imagine that a higher speed of the metabolic activity is associated with both higher reproductive rate and faster viral infection, as both processes rely on the cell machinery to translate proteins; this situation is particularly relevant when hypoxia is considered, as we explain in the next chapter.

For the sake of simplicity, we neglect spatial obstacles and restrict our attention to the case of undirected cell movement without explicit viral dynamics: this setting does not present any substantial difference in the infection dynamics with respect to the models with explicit viral dynamics and any kind of cell movement, as explained in the previous section. We also restrict our attention to the case in which uninfected and infected cells follow the same rules for the movement.

4.2.1 Description of the agent-based models

Once again, our starting point is the modelling framework presented in Section 2.1, to which we now add an epigenetic structure on uninfected cells. We therefore consider an additional variable $y \in Y := [0,1]$ that affects uninfected cells' dynamics and assume that higher values of y are associated with slow proliferation and increased resistance to viral infection; we further assume that, once a cell becomes infected, the heterogeneity is lost. In addition to the temporal discretisation $t_n = \tau n$ with $n \in \mathbb{N}_0$, $0 < \tau \ll 1$ and the spatial discretisation $x_j = \delta j$, with $j \in \mathbb{Z}$, $0 < \delta \ll 1$, we now need to consider also an epigeneitc discretization $y_k = \chi k$ with k integer number between 0 and $[1/\chi]$, $0 < \chi \ll 1$. As usual, we assume τ to be small enough to guarantee that all the probabilities defined hereafter are smaller than 1. We denote the number of uninfected and infected cells that occupy position x_j at time t_n (with epigenetic trait y_k in the case of uninfected cells) respectively by $U^n_{j,k}$ and I^n_j; the corresponding densities are

$$u^n_{j,k} := \frac{U^n_{j,k}}{\delta\chi}, \qquad I^n_j := \frac{I^n_j}{\delta}$$

The slight change of notation with respect to the previous chapters highlights the difference between the uninfected population, which is epigenetically structured, and the infected population, which is not.

Dynamics of uninfected cells Proliferation, undirected movement and infection of uninfected cancer cells follow rules analogous to the ones described in Chapter 2, with the relevant difference that we now consider an epigenetic trait that affects proliferation and infection.

We only consider undirected random movement and assume that an uninfected cell moves to an adjacent lattice point with probability $\theta_x/2$, where $\theta_x \in [0,1]$, and remains at its initial position with probability $1-\theta_x$. Epigenetic mutations take place exactly in the same way, with the probability of switching to an adjacent epigenetic characterisation depending on a different parameter $\theta_y \in [0,1]$.

The proliferation and death of an uninfected cell with epigenetic trait y_k that occupies position x_j at time t_n now depends on the function

$$G(y,\rho) := p\Big(r(y) - \frac{\rho}{K}\Big) \tag{4.6}$$

where the total cell density at time t_n and position x_j is

$$\rho_j^n := \sum_{k=0}^{[1/\chi]} u_{j,k}^n + I_j^n$$

and $K > 0$ is the carrying capacity. The maximal duplication rate $p > 0$ and $r\colon Y \to [0,1]$ is a decreasing function that models the dependence on the epigenetic trait. In this sense, we consider y as the normalised level of expression of a set of genes responsible for the trade-off between proliferation and resistance to hypoxia: $y = 0$ corresponds to the highest intrinsic proliferation rate and the highest infection rate; conversely, $y = 1$ corresponds to the lowest intrinsic proliferation rate and the lowest infection rate.

Similarly, we assume that an uninfected cell with epigenetic trait y_k that occupies position x_j at time t_n becomes infected upon contact with infected cells with probability $\tau\beta(y_k)I_j^n/K$, where $\beta\colon Y \to \mathbb{R}$ is a decreasing function that gives the epigenetic-dependent infection rate, in line with the trade-off described above.

Dynamics of infected cells Infected cells are modelled by a single compartment, as they are not affected by the epigenetic structure. We refer to Section 2.1 for the description of the movement and death of such cells. Here, we consider undirected random movement and the probabilities are the same as those of uninfected cells.

4.2.2 Derivation of the corresponding continuum model

We now derive the continuum counterparts of the agent-based models described in the previous section, using techniques analogous to those employed in Section 2.2 and in the references mentioned there.

Uninfected cells Uninfected cells can first move and change their epigenetic trait, then reproduce or die based on the pressure value and finally become infected. The principle of mass balance gives the equation

$$\begin{aligned} u_{j,k}^{n+1} = &\Big[(1-\theta_y)\frac{\theta_x}{2}u_{j-1,k}^n \frac{\theta_y}{2}\frac{\theta_x}{2}(u_{j-1,k+1}^n + u_{j-1,k-1}^n) \\ &+ (1-\theta_y)\frac{\theta_x}{2}u_{j+1,k}^n + \frac{\theta_y}{2}\frac{\theta_x}{2}(u_{j+1,k+1}^n + u_{j+1,k-1}^n) + \\ &+ (1-\theta_y)(1-\theta_x)u_{j,k}^n + \frac{\theta_y}{2}(1-\theta_x)(u_{j,k+1}^n + u_{j,k-1}^n)\Big] \\ &\times \Big[1 + \tau G(y_k, \rho_j^n)\Big] \times \Big[1 - \tau\frac{\beta(y_k)}{K}I_j^n\Big] \end{aligned}$$

which can be written as

$$\begin{aligned} u_{j,k}^{n+1} = &\Big[u_{j-1,k}^n(1-\theta_y)\frac{\theta_x}{2} + u_{j-1,k+1}^n\frac{\theta_y}{2}\frac{\theta_x}{2} + u_{j-1,k-1}^n\frac{\theta_y}{2}\frac{\theta_x}{2} \\ &+ u_{j+1,k}^n(1-\theta_y)\frac{\theta_x}{2} + u_{j+1,k+1}^n\frac{\theta_y}{2}\frac{\theta_x}{2} + u_{j+1,k-1}^n\frac{\theta_y}{2}\frac{\theta_x}{2} \\ &+ u_{j,k}^n(1-\theta_y)(1-\theta_x) + u_{j,k+1}^n\frac{\theta_y}{2}(1-\theta_x) + u_{j,k-1}^n\frac{\theta_y}{2}(1-\theta_x)\Big] \\ &\times\Big[1+\tau G(y_k,\rho_j^n)\Big]\times\Big[1-\tau\frac{\beta(y_k)}{K}I_j^n\Big] \end{aligned} \tag{4.7}$$

Let us now assume that there are two functions $u \in C^2([0,+\infty)\times\mathbb{R}\times Y)$ such that $u_{j,k}^n = u(t_n, x_j, y_k) = u$ (from now on we omit the arguments of functions computed at (t_n, x_j, y_k)); thus, we can use Taylor expansions for u as follows

$$\begin{aligned} u(t+\tau,x,y) &= u + \tau\partial_t u + \mathcal{O}(\tau^2) \\ u(t,x,y\pm\chi) &= u \pm \chi\partial_y u + \frac{\chi^2}{2}\partial_{yy}^2 u + \mathcal{O}(\chi^3) \\ u(t,x\pm\delta,y) &= u \pm \delta\partial_x u + \frac{\delta^2}{2}\partial_{xx}^2 u + \mathcal{O}(\delta^3) \\ u(t,x+\delta,y\pm\chi) &= u + \delta\partial_x u \pm \chi\partial_y u + \frac{\delta^2}{2}\partial_{xx}^2 u + \frac{\chi^2}{2}\partial_{yy}^2 u \pm \delta\chi\partial_{xy}^2 u + \mathcal{O}(\delta^3) + \mathcal{O}(\chi^3) \\ u(t,x-\delta,y\pm\chi) &= u - \delta\partial_x u \pm \chi\partial_y u + \frac{\delta^2}{2}\partial_{xx}^2 u + \frac{\chi^2}{2}\partial_{yy}^2 u \mp \delta\chi\partial_{xy}^2 u + \mathcal{O}(\delta^3) + \mathcal{O}(\chi^3) \end{aligned}$$

After some simplifications, Eq. (4.7) becomes

$$\partial_t u + \mathcal{O}(\tau^2) = \frac{\theta_x\delta^2}{2\tau}\partial_{xx}^2 u + \frac{\theta_y\chi^2}{2\tau}\partial_{yy}^2 u + G(y,\rho)u - \frac{\beta(y)}{K}Iu + \mathcal{O}(\tau) + \mathcal{O}(\delta^2) + \mathcal{O}(\delta\chi)$$

Letting $\tau,\delta,\chi \to 0$ in such a way that $\frac{\delta^2}{2\tau} \to \tilde{D}_x$ and $\frac{\chi^2}{2\tau} \to \tilde{D}_y$, we obtain the equation

$$\partial_t u = \tilde{D}_y\partial_{yy}^2 u + \tilde{D}_x\partial_{xx}^2 u + G(y,\rho)u - \frac{\beta(y)}{K}\,I$$

Infected cells Infected cells can first move, then die based on the pressure value. Also, uninfected cells may be infected: as explained previously, the dynamics are unaffected by the epigenetic trait after the infection; hence, we do not need to keep track of it. The principle of mass balance gives the equation

$$I_j^{n+1} = (1-\tau q)\Big[\frac{\theta_x}{2}I_{j-1}^n + \frac{\theta_x}{2}I_{j+1}^n + (1-\theta_x)I_j^n\Big] + \tau I_j^n\sum_k\frac{\beta(y_k)}{K}\chi u_{j,k}^n$$

We remark that the density of infected cells is obtained by dividing the cell number only by δ, while the density of uninfected cells requires the additional division by χ: this leads to the multiplication of $u_{j,k}^n$ by χ. The previous equation then simplifies to

$$\frac{I_j^{n+1}-I_j^n}{\tau} = \theta_x\frac{\delta^2}{2\tau}\frac{I_{j-1}^n + I_{j+1}^n - 2I_j^n}{\delta^2} - qI_j^n - q\frac{\theta_x}{2}\delta^2\Big(\frac{I_{j-1}^n + I_{j+1}^n - 2I_j^n}{\delta^2}\Big) + I_j^n\sum_k\frac{\beta(y_k)}{K}\chi u_{j,k}^n$$

Let us observe that, for $\chi \to 0$,

$$\sum_k \beta(y_k)\chi u^n_{j,k} \to \int_Y \beta(y)u(t,x,y)\,\mathrm{d}y$$

Let us also assume that there is a function $I \in C^2([0,+\infty)\times\mathbb{R})$ such that $I^n_j = I(t_n, x_j) = I$, so that

$$I^{n+1}_j - I^n_j = \tau\partial_t I + \mathcal{O}(\tau^2)$$
$$I^n_{j-1} + I^n_{j-1} - 2I^n_j = \delta^2\partial^2_{xx} I + \mathcal{O}(\delta^3)$$

Therefore, letting $\tau, \delta, \chi \to 0$ in such a way that $\frac{\delta^2}{2\tau} \to \tilde{D}_x$ and $\frac{\chi^2}{2\tau} \to \tilde{D}_y$, we obtain the equation

$$\partial_t I(t,x) = D_x\partial^2_{xx} I(t,x) + I(t,x)\int_Y \frac{\beta(y)}{K}u(t,x,y)\,\mathrm{d}y - qI(t,x)$$

Summary of the continuum model We have formally obtained the following system of PIDEs:

$$\begin{cases} \partial_t u(t,x,y) = D_y\partial^2_{yy}u(t,x,y) + D_x\partial^2_{xx}u(t,x,y) + R(y,\rho,I)u(t,x,y) \\ \partial_t I(t,x) = D_x\partial^2_{xx}I(t,x) + I(t,x)\int_Y \frac{\beta(y)}{K}u(t,x,y)\,\mathrm{d}y - qI(t,x) \\ \rho(t,x) := \int_Y u(t,x,y)\,\mathrm{d}y + I(t,x) \end{cases} \tag{4.8}$$

where $D_x = \tilde{D}_x\theta_x$, $D_y = \tilde{D}_y\theta_y$ and

$$R(y,\rho,I) := p\Big(r(y) - \frac{\rho(t,x)}{K}\Big) - \frac{\beta(y)}{K}\,I(t,x)$$

It is also convenient to define the uninfected total cell density

$$\hat{u}(t,x) := \int_Y u(t,x,y)\,\mathrm{d}y \tag{4.9}$$

This system is the same one studied in Lorenzi et al., 2021b, with the addition of spatial dynamics. We may expect a travelling wave to originate from the equation: in the centre, the cell densities reach the steady state predicted in the absence of spatial dynamics (although the spatial diffusion may have some effects on that), while, at the front, there is a prevalence of cells with epigenetic variable close to 0.

Following Lorenzi et al., 2021b, we define $r(y)$ and $\beta(y)$ as

$$r(y) := 1 - \eta y^2, \qquad \beta(y) := \beta_0 + \zeta(1-y)^2$$

With this choice, we have

$$R(y,\rho,I) = g(I) - h(I)(y-\varphi(I))^2 - p\frac{\rho}{K}$$

where

$$h(I) := p\eta + \frac{\zeta}{K}I \qquad \varphi(I) := \frac{\zeta I}{h(I)K} \qquad g(I) := p - \frac{\beta_0+\zeta}{K}I + h(I)\varphi(I)^2$$

We can, therefore, interpret $\varphi(I)$ as the fittest epigenetic trait when the density of infected cells corresponds to I.

4.2.3 Preliminary formal asymptotic analysis

We now conduct a formal asymptotic analysis to compute the theoretical equilibrium values. Building upon the methods employed in Lorenzi and Painter, 2022; Lorenzi et al., 2021a; Villa et al., 2021a, we introduce a small parameter ε and assume that

$$D_x = D_y = \varepsilon^2$$

Furthermore, we use the time scaling $t \mapsto \frac{t}{\varepsilon}$ (which allows us to study the long-time behaviour of the system) and define

$$u_\varepsilon(t,x,y) := u\Big(\frac{t}{\varepsilon},x,y\Big), \qquad I_\varepsilon(t,x) := I\Big(\frac{t}{\varepsilon},x\Big)$$

The previous system thus becomes

$$\begin{cases} \varepsilon\partial_t u_\varepsilon(t,x,y) = \varepsilon^2\partial^2_{yy}u_\varepsilon(t,x,y) + \varepsilon^2\partial^2_{xx}u_\varepsilon(t,x,y) + R(y,\rho_\varepsilon(t,x),I_\varepsilon(t,x))\ u_\varepsilon(t,x,y) \\ \varepsilon\partial_t I_\varepsilon(t,x) = \varepsilon^2\partial^2_{xx}I_\varepsilon(t,x) + I_\varepsilon(t,x)\int_Y \beta(y)u_\varepsilon(t,x,y)\,\mathrm{d}y - qI_\varepsilon(t,x) \\ \rho_\varepsilon(t,x) := \int_Y u_\varepsilon(t,x,y)\,\mathrm{d}y + I_\varepsilon(t,x) \end{cases} \tag{4.10}$$

Let us observe that, letting $\varepsilon \to 0$ and assuming that all the functions converge, we immediately get from the second equation

$$I(t,x) = 0 \quad \text{or} \quad \int_Y \frac{\beta(y)}{K}u(t,x,y)\,\mathrm{d}y = q \tag{4.11}$$

We then make for uninfected cells the real phase WKB ansatz (Barles et al., 1990; Evans and Souganidis, 1989; Fleming and Souganidis, 1986), as it is common in the Hamilton–Jacobi approach presented, for example, in Diekmann et al., 2005; Lorz et al., 2011; Perthame, 2006; Perthame and Barles, 2008

$$u_\varepsilon(t,x,y) = e^{\frac{n_\varepsilon(t,x,y)}{\varepsilon}}$$

This implies

$$\partial_t u_\varepsilon = \frac{\partial_t n_\varepsilon}{\varepsilon}u_\varepsilon, \quad \partial_x u_\varepsilon = \frac{\partial_x n_\varepsilon}{\varepsilon}u_\varepsilon \quad \partial^2_{xx}u_\varepsilon = \Big(\frac{(\partial_x n_\varepsilon)^2}{\varepsilon^2} + \frac{\partial^2_{xx}n_\varepsilon}{\varepsilon}\Big)u_\varepsilon$$

and an analogous expression for $\partial^2_{yy}u_\varepsilon$. The first equation of Eq. (4.10) yields

$$\varepsilon\frac{\partial_t n_\varepsilon}{\varepsilon}u_\varepsilon = \varepsilon^2\Big(\frac{(\partial_y n_\varepsilon)^2}{\varepsilon^2} + \frac{\partial^2_{yy}n_\varepsilon}{\varepsilon}\Big)u_\varepsilon + \varepsilon^2\Big(\frac{(\partial_x n_\varepsilon)^2}{\varepsilon^2} + \frac{\partial^2_{xx}n_\varepsilon}{\varepsilon}\Big)u_\varepsilon + R(y,\rho_\varepsilon,I_\varepsilon)u_\varepsilon$$

and this simplifies to

$$\partial_t n_\varepsilon = (\partial_y n_\varepsilon)^2 + \varepsilon\partial^2_{yy}n_\varepsilon + (\partial_x n_\varepsilon)^2 + \varepsilon\partial^2_{xx}n_\varepsilon + R(y,\rho_\varepsilon,I_\varepsilon)$$

Letting $\varepsilon \to 0$ and assuming convergence, we obtain

$$\partial_t n = (\partial_y n)^2 + (\partial_x n)^2 + R(y,\rho,I) \tag{4.12}$$

All the functions without the subscript ε are the leading order terms of the asymptotic expansion.

Let us assume that, for every $\varepsilon > 0$, the initial condition $n_\varepsilon(0,x,y)$ is a uniformly concave function of y; for example, we could think that, at $t = 0$, tumour cells that occupy the same position are mainly in the same phenotypic state and so the local cell phenotypic distribution $y \mapsto u_\varepsilon(0,x,y)$ is a sharp Gaussian-like function (meaning that $n_\varepsilon(0,x,y) = -(y - \varphi_\varepsilon(x))^2$, for some appropriate function φ_ε). Since $y \mapsto R(y,\rho,I)$ is a concave function of y, we also expect n to be a strictly concave function of y (Mirrahimi and Perthame, 2015; Perthame and Barles, 2008). We then define

$$\bar{y}(t,x) \coloneqq \arg\max_{y\in Y} n(t,x,y)$$

Let us fix $x \in \mathrm{supp}(\rho)$. The fact that $\rho_\varepsilon(t,x) < +\infty$ for all ε implies that

$$n(t,x,\bar{y}(t,x)) = \max_{y\in Y} n(t,x,y) = 0$$

The concavity of $y \mapsto n(t,x,y)$ for every t and x implies that

$$u_\varepsilon(t,x,y) \overset{*}{\rightharpoonup} \hat{u}(t,x)\,\delta_{\bar{y}(t,x)}$$

in the meaning of weak-$*$ convergence of measures, i.e.

$$\int_Y \psi(y) u_\varepsilon(t,x,y) \xrightarrow{\varepsilon\to 0} \psi(\bar{y})\hat{u}(t,x) \quad \forall \psi \in C^0(Y)$$

This is in line with the concentration results that are typically obtained for similar equations (Lorenzi et al., 2018; Mirrahimi and Perthame, 2015; Perthame, 2006). Furthermore, the definition of $\bar{y}(t,x)$ trivially implies

$$\partial_y n(t,x,\bar{y}(t,x)) = 0$$

We also observe that

$$0 = \frac{\partial}{\partial t} n(t,x,\bar{y}(t,x)) = \partial_t n(t,x,y)|_{y=\bar{y}(t,x)} + \cancel{\partial_y n(t,x,y)|_{y=\bar{y}(t,x)}}\,\partial_t \bar{y}(t,x)$$

implying that $\partial_t n(t,x,\bar{y}(t,x)) = 0$; similarly, $\partial_x n(t,x,\bar{y}(t,x)) = 0$. We evaluate Eq. (4.12) in $y = \bar{y}(t,x)$ to get

$$R(\bar{y},\rho,I) = \partial_t n - (\partial_y n)^2 - (\partial_x n)^2 = 0 \tag{4.13}$$

We can also differentiate Eq. (4.12) with respect to y to get

$$\partial^2_{ty} n = 2\partial_y n\,\partial^2_{yy} n + 2\partial_y n\,\partial^2_{xy} n + \partial_y R(y,\rho,I)$$

which computed at $y = \bar{y}(t,x)$ yields

$$\partial^2_{ty} n(t,x,\bar{y}(t,x)) = \partial_y R(\bar{y}(t,x),\rho(t,x),I(t,x))$$

If we look for a homogeneous steady state, then the previous equation implies

$$\partial_y R(\bar{y},\rho,I) = 0 \tag{4.14}$$

Let us also note that

$$\int_Y \beta(y) u_\varepsilon(t,x,y)\,\mathrm{d}y \to \beta(\bar{y})\hat{u}(t,x)$$

due to the previous observation that $u_\varepsilon \overset{*}{\rightharpoonup} \hat{u}\,\delta_{\bar{y}}$. As a consequence, Eqs. (4.11), (4.13) and (4.14) constitute a system of three equations in the three variables $\hat{u}, I, \bar{y}$, which in principle can be solved. Let us first focus on the infection-free case of Eq. (4.11), i.e. $I = 0$. The other two variables solve the system

$$\begin{cases} R(\bar{y}, \hat{u}, 0) = p\left(1 - \eta\bar{y}^2 - \dfrac{\hat{u}}{K}\right) = 0 \\ \partial_y R(\bar{y}, \hat{u}, 0) = 2p\bar{y} = 0 \end{cases}$$

whose only solution is clearly $\bar{y} = 0$, $\hat{u} = K$. For $I \neq 0$, we need to solve the system

$$\begin{cases} \hat{u} = \dfrac{q}{\beta(\bar{y})} \\ R(\bar{y}, \hat{u} + I, I) = g(I) - h(I)(\bar{y} - \varphi(I))^2 - p\dfrac{\hat{u} + I}{K} = 0 \\ \partial_y R(\bar{y}, \hat{u} + I, I) = 2h(I)(\bar{y} - \varphi(I)) = 0 \end{cases} \tag{4.15}$$

The last equation implies $\bar{y} = \varphi(I)$, hence we need to solve the following equation in I:

$$R\left(\varphi(I), \frac{qK}{\beta(\varphi(I))} + I, I\right) = g(I) - p\frac{\frac{q}{\beta(\varphi(I))} + I}{K} = 0$$

This last equation is too complicated to be studied analytically; hence, in the following we restrict our attention to numerical solutions.

This approach may also be useful in characterising travelling waves.

4.2.4 Comparison between agent-based and continuum models

We now compare numerical simulations for the agent-based model and the corresponding system of PDEs. All the simulations are performed with the techniques described in Section 2.4.1. We use the following initial conditions:

$$u_0(x, y) = \begin{cases} 0.9\,K & \text{for } |x| \leq R_u,\ y \in Y \\ 0 & \text{for } |x| > R_u,\ y \in Y \end{cases} \qquad i_0(x) = \begin{cases} 0.1\,K & \text{for } |x| \leq R_i \\ 0 & \text{for } |x| > R_i \end{cases} \tag{4.16}$$

The parameters are set to the same values adopted in Chapter 2, with the only exception of η, β_0, ζ and D_y that specifically refer to the epigenetic structure. The epigenetic diffusion coefficient of tumour cells D_y is not easily accessible in the empirical literature and it has been taken from previous mathematical models about epigenetically structured populations: we set it to 5.00×10^{-6} h^{-1}, as in Celora et al., 2021. Furthermore, we set $\beta_0 = 1.02 \times 10^{-3}$ h^{-1}. The other two additional parameters, η and ζ, are set to arbitrary values that give rise to interesting dynamics: the goal of this section is in fact the description of general behaviours associated with heterogeneous infections that may vary in specific biological settings (for instance, the one analysed in Chapter 5, which refers to hypoxia). We report the full parameters list in Table 4.2 for the reader's convenience.

In order to facilitate the comparison, we define the average epigenetic trait

$$\mu(t, x) := \frac{\int_Y y u(t, x, y)\,\mathrm{d}y}{\hat{u}(t, x)}$$

with $\hat{u}$ as defined in Eq. (4.9). The infinite speed of propagation associated with spatial diffusion implies that $\hat{u}(t, x) > 0$ for all $t > 0$ and $x \in \mathbb{R}$; hence, the previous quantity

Parameter	Description	Value [Units]	Reference
p	maximal duplication rate of uninfected cells	1.87×10^{-2} [h^{-1}]	Ke et al., 2000
q	death rate of infected cells	4.17×10^{-2} [h^{-1}]	Ganly et al., 2000
D_x	diffusion coefficients (undirected movement)	1.88×10^{-4} [mm^2/h]	estimate based on Kim et al., 2006
K^{1D}	tissue carrying capacity in one dimension	10^3 [cells/mm]	model estimate
D_y	cell epigenetic diffusion coefficient	5.00×10^{-6} [h^{-1}]	Celora et al., 2021
η	intrinsic selection gradient	5.00×10^{-1} [non dim.]	model estimate
β_0	infection rate	1.02×10^{-3} [h^{-1}]	model estimate
ζ	selection gradient related to infection	2.00×10^{-1} [non dim.]	model estimate
R_u	initial radius of uninfected cells	2.6 [mm]	Kim et al., 2006
R_i	initial radius of infected cells	1 [mm]	model estimate

TABLE 4.2: Parameter set for the models of infections with epigenetically structured uninfected cells. The parameters η and ζ are non dimensional (abbreviated as "non dim.").

is properly defined. Analogous definitions can be employed for the agent-based model whenever the uninfected cell density is not zero.

Fig. 4.10 shows an excellent quantitative agreement between numerical solutions of the system of PDEs (4.8) and the average over five numerical simulations of the agent-based model in one spatial dimension. At the beginning of the simulations, uninfected cells with low epigenetic traits are quickly infected in the centre of the tumour; consequently, the average epigenetic trait increases. In the meantime, uninfected cells start to invade the surrounding area at speed $2\sqrt{D_u p}$ (vertical blue lines in Fig. 4.10): this invasion is mainly led by cells that proliferate at rate close to the maximal one. It is interesting to observe that the excellent agreement of the average epigenetic trait is lost in the outer region of the tumour: stochasticity appears more relevant due to the very low number of individuals involved; nevertheless, this does not significantly affect the overall dynamics.

As time passes, dynamics start to diverge significantly from the ones described in Chapter 2 due to the emergence of resistance to the infection in the centre of the tumour. The selected epigenetic trait strongly differs in different locations. In the centre, the theoretical equilibria are a good approximation for the values reached in the numerical simulations: this is clear from Fig. 4.11, which shows the evolution in time of the different uninfected subpopulations of the agent-based model at the centre of the domain; stochastic effects are evident, but the selected subpopulations are the ones we would expect from our theoretical analysis. On the other hand, spatial effects should not be neglected in the invasion front. Overall, the tumour becomes insensitive to the infection while maintaining its invasion properties unchanged. This suggests that the emergence of resistance may constitute a significant obstacle to oncolytic virotherapy.

4.3 Conclusions

In this chapter, we presented two extensions of the individual-based models studied in Chapter 2. In both cases, we formally derived the deterministic continuum counterpart and compared the numerical results, finding an excellent agreement.

When viral dynamics are included in the models, the rules governing viral spatial movement appear to affect the infection more significantly than the rules governing cell

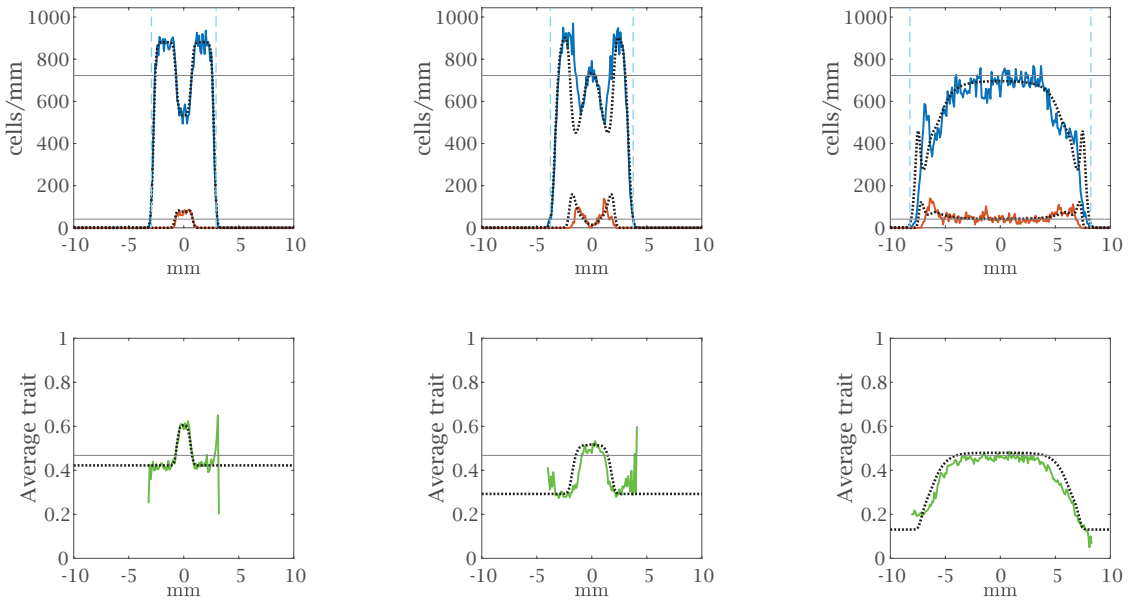

(a) $t = 90$ h (b) $t = 310$ h (c) $t = 1500$ h

FIGURE 4.10: Comparison in one spatial dimension between numerical simulations of the discrete model epigenetically structured uninfected cells (solid lines) and the numerical solution of Eq. (4.8) (dotted black lines) at three different times, with the parameters given in Table 4.2. For the agent-based model, the densities of uninfected and infected cells are represented respectively in blue and red in the upper panel (for uninfected cells, we consider the sum of the subpopulations); the average epigenetic trait is shown in green in the lower panel (in all the points in which it is well-defined). The horizontal black lines show the theoretical equilibria approximation of asymptotic equilibria, obtained by solving Eq. (4.15) The vertical dashed blue lines represent the expected position of the uninfected invasion front, travelling at speed $2\sqrt{D_u p}$. The results of the agent-based model are averaged over five simulations and the maximum of the cell density axes corresponds to the maximum over time of this average (which is larger than the carrying capacity).

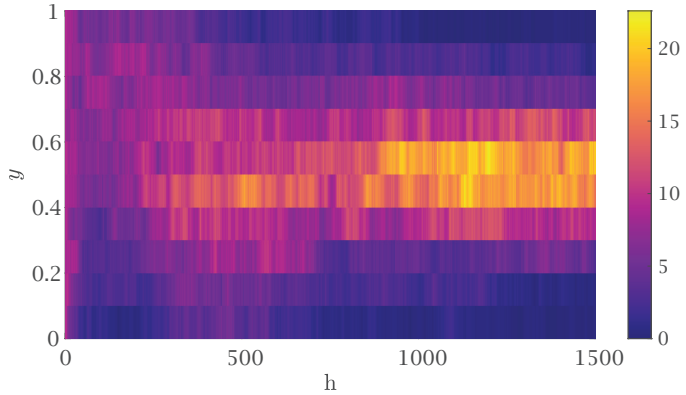

FIGURE 4.11: Evolution in time of the uninfected subpopulations of the agent-base model at the centre of the domain, i.e., the lattice point corresponding to $x = 0$. The results of the agent-based model are averaged over five simulations and the maximum of the cell density axes corresponds to the maximum over time of this average. We remark that the theoretical analysis yields the epigenetic value $\bar{y} \approx 0.47$.

movement. On the other hand, cell movement still retains its influence on the tumour invasion: only pressure-driven movement describes a slower invasion for low tumour cell numbers. This should be kept into account when the clinical consequences of the therapy are analysed. Overall, undirected movement (with or without viral diffusion) and pressure-driven movement without viral diffusion exhibit similar behaviour in regards to the spread of the infection throughout a tumour. The presence of the viral population may also lead to the appearance of persistent oscillations, which, however, do not affect the overall outcome in the same relevant way as we observed in Chapter 3.

When the heterogeneity of uninfected cells is considered, the emergence of a subpopulation resistant to viral infection may significantly hinder the success of the therapy. Although this resistance comes at the cost of a lower proliferation rate, the tumour growth does not slow down significantly due to the presence of high proliferative cells close to the invasion front that try to escape from the infection. In practice, the design of oncolytic virotherapy should consider that the efficacy may be significantly reduced if the tumour evolves toward an epigenetic characterisation in which cells are less susceptible to the infection, even if such evolution is correlated with a lower reproduction rate. These considerations are particularly relevant for hypoxic tumours, which may require a different treatment (see Chapter 5). Our preliminary theoretical analysis correctly predicts the equilibrium values in the centre of the tumour for both discrete and continuous models. Nevertheless, the spatial epigenetic heterogeneity is not trivial and a complete formal asymptotic analysis along the lines presented in this chapter may shed light or, at least, predict outcomes in some parameter regimes.

The results presented in this chapter may be improved and extended in several ways, both from the mathematical and the modelling perspectives. To our knowledge, a rigorous characterisation of the travelling waves that we observed is still lacking in most of the situations under investigation. In the case of explicit viral dynamics, the invasion speed of the virus in an uninfected tumour appears to depend on several parameters related to the virus and it could be interesting to elucidate further these relations. A deeper understanding og the phenomena could also help to reach a full characterisation of the limit of the parameters in Eq. (4.3) in which we recover Eq. (2.11): this clearly happens for $D_v = 0$, as previously mentioned; our simulations show that a high viral decay might be associated to a slower invasion of the infection in the tumour, so that phenomena similar to the ones analysed in Chapter 2 might be recovered. In the case of the epigenetically structured model, a rigorous analysis has only been performed in the spatially homogeneous situation (Lorenzi et al., 2021b). The formal asymptotic approach we adopted in this chapter could be extended to analyse spatial heterogeneity.

From the modelling point of view, the inclusion of viral dynamics is a natural step towards the study of how the tumour microenvironment affects viral diffusion, improving the insights obtained in Chapter 2: a few models have already taken it into account (Pooladvand and Kim, 2022) and additional experimental evidence may help to find a suitable mathematical description of the interactions between viral particles and the physical obstacles of the tumour microenvironment. Regarding the structured model, a natural extension is its application to some specific kinds of heterogeneity that cause a proliferation-resistance trade-off. The next chapter is devoted to one of such extensions, to analyse the influence of hypoxia on oncolytic virotherapy.

5 *Influence of hypoxia on oncolytic virotherapy*

As explained in Chapter 1, hypoxia reduces the effectiveness of several cancer therapies (Zhuang et al., 2023). In the context of oncolytic virotherapy, the impact of hypoxia on therapeutic efficacy is twofold (Sheng Guo, 2011). Firstly, hypoxic regions within tumours harbour cells less susceptible to viral infection and replication due to reduced metabolic activity and altered cellular signalling pathways. Secondly, the physiological adaptations of tumour cells to hypoxia, such as enhanced glycolytic metabolism and resistance to apoptosis, can confer resistance to viral-induced cell death. It is important to remark that the previous considerations are not universal: indeed, some particular oncolytic viruses can specifically target receptors that are upregulated in case of the lack of oxygen (Sadri et al., 2023; Sheng Guo, 2011). Understanding how hypoxia influences the interaction between oncolytic viruses and tumour cells is crucial for optimising treatment strategies and overcoming therapeutic resistance. Mathematical modelling is pivotal in unravelling these complexities and optimising therapeutic outcomes.

In the previous chapter, we presented a continuous epigenetically structured model that considers a trade-off involving the proliferation rate and the resistance to the infection of the uninfected compartment. Continuous structuring variables are also commonly employed to model heterogeneous levels of adaptation to hypoxia (see Section 1.5), easily allowing to model a trade-off between the proliferation rate and the resistance to hypoxic conditions. We now combine both trade-offs and assume that less proliferative cells have slower metabolic activity, resulting in a higher resistance to hypoxia and a lower infection rate in the presence of oncolytic virus. This approach allows us to include the influence of oxygen concentration on the dynamics of resistance to virotherapy described in the previous chapter.

More in detail, our model incorporates both spatial and phenotypic heterogeneity of tumour cells, along with the dynamics of oxygen concentration and viral infection; the model is formulated using a combination of PDEs and PIDEs, explicitly accounting for the spatial gradients of oxygen within the tumour. To our knowledge, the resulting model constitutes a novelty with respect to the existing literature. Such a modelling approach allows us to perform a formal asymptotic analysis of simplified settings to compute the homogeneous equilibrium values.

Due to the model's complexity, we here restrict our attention to the deterministic continuum setting. It is important to keep in mind that a formal derivation from the underlying individual based model is also possible and follows the same strategy adopted in previous chapters without any significant additional challenge.

In this chapter, we aim to

- characterise the impact of hypoxia on viral infection and investigate how oxygen gradients within tumours affect the spatial distribution and replication of the

tumour and the oncolytic viruses, with a focus on regions of severe hypoxia versus normoxic areas;

- explore evolutionary dynamics and analyse how hypoxia-induced adaptations in tumour cells influence their susceptibility to viral infection, the epigenetic composition of the tumour, and the emergence of resistant phenotypes over time;
- consider the trade-off between proliferation rate and resistance to hypoxia in view of optimising therapeutic strategies to enhance the efficacy of oncolytic virotherapy in hypoxic tumour environments.

This chapter is organised as follows. In Section 5.1, we introduce the model. In Section 5.2, we present a formal asymptotic analysis and obtain the equations that define the spatially homogeneous equilibrium values. In Section 5.3, we present numerical results in the two situations of stationary and variable oxygen concentration, comparing them to the theoretical results; we also mention the situation of a virus that specifically targets hypoxic cells, looking towards the combination of several therapies. Finally, in Section 5.4, we summarise the main results and present next steps and future perspectives.

The model described in this chapter and the results shown have been submitted for publication (Morselli et al., 2024a).

5.1 Model description

As in Chapter 4, we consider the epigenetic heterogeneity of uninfected cancer cells; we now assume that it affects resistance to hypoxia in addition to proliferation and infection. The dynamics of infected cells, instead, are not affected by epigenetic characteristics, hence we model them as a homogeneous population.

Let us denote by $t \in [0, +\infty)$ the time variable, by $\boldsymbol{x} \in \Omega$ the space variable, with $\Omega \subset \mathbb{R}^2$ and by $y \in Y$ the epigenetic variable, with $Y := [0, 1]$. We consider uninfected and infected cancer cells, whose densities are described respectively by the functions $u\colon [0, +\infty) \times \Omega \times Y \to [0, +\infty)$ and $I\colon [0, +\infty) \times \Omega \to [0, +\infty)$. We also define the uninfected total cell density as

$$U(t, x) := \int_Y u(t, x, y)\, \mathrm{d}y \tag{5.1}$$

and the total cancer cell density as

$$\rho(t, \boldsymbol{x}) := I(t, \boldsymbol{x}) + U(t, \boldsymbol{x}, y) \tag{5.2}$$

Finally, we consider viral density, described by the function $v\colon [0, +\infty) \times \Omega \to [0, +\infty)$, and oxygen concentration, described by the function $O\colon [0, +\infty) \times \Omega \to [0, +\infty)$. We now describe in detail the rules governing all the dynamics.

Uninfected cancer cells Uninfected cells may move via pressure-driven movement, change their epigenetic trait, reproduce, become infected and die due to environmental selection; this last process is the main addition to the model considered in Chapter 4. We assume a trade-off between proliferation and resistance to both hypoxia and viral infection. In this sense, we consider y as the level of expression of a set of genes responsible for this trade-off and, as previously, normalise it so that $y = 0$ and $y = 1$ are, respectively, the lowest and highest possible expressions: $y = 0$ corresponds to highest intrinsic proliferation rate, lowest resistance to hypoxia and highest infection rate; conversely

$y = 1$ corresponds to lowest intrinsic proliferation rate, highest resistance to hypoxia and lowest infection rate. As previously explained, the biological motivation for this choice is the fact that viral replication relies on the host cell translational machinery, which, in turn, is affected by hypoxia: indeed, protein synthesis is often shut down in response to stresses such as hypoxia and this slows down also cell proliferation (Sheng Guo, 2011). The evolution of uninfected cells is described by the equation

$$\begin{aligned}\partial_t u(t,\boldsymbol{x},y) =& R(y,\rho(t,\boldsymbol{x}),O(t,\boldsymbol{x}),v(t,\boldsymbol{x}))\, u(t,\boldsymbol{x},y) \\ &+ D_y \underbrace{\partial^2_{yy} u(t,\boldsymbol{x},y)}_{\text{random mutation}} + \underbrace{D_{\boldsymbol{x}} \nabla_{\boldsymbol{x}} \cdot (u(t,\boldsymbol{x},y) \nabla \rho(t,\boldsymbol{x}))}_{\text{pressure-driven movement}}\end{aligned}$$

with

$$R(y,\rho,O,v) = \big(\underbrace{P(y,\rho)}_{\text{proliferation}} - \underbrace{S(y,O)}_{\text{selection}}\big) - \underbrace{\beta(y)\, v}_{\text{infection}}$$

Random epigenetic mutations are described by a diffusive term in y with coefficient D_y. Cancer cells also move with coefficient $D_{\boldsymbol{x}}$ in space against the gradient of the total cancer cell density $\rho(t,\boldsymbol{x})$. Furthermore, uninfected cancer cells proliferate at a rate determined by the intrinsic proliferation rate $p(y)$ and the local cancer cell density $\rho(t,\boldsymbol{x})$, according to the logistic growth term

$$P(y,\rho) = p(y)\left(1 - \frac{\rho}{K}\right) \tag{5.3}$$

Uninfected cells may also die because of the environmental selection driven by oxygen concentration. The fittest trait, according to oxygen availability, is determined by the function

$$\varphi(O) := \begin{cases} 1 & \text{if } O \le O_m \\ \dfrac{O_M - O}{O_M - O_m} & \text{if } O_m < O < O_M \\ 0 & \text{if } O \ge O_M \end{cases} \tag{5.4}$$

Thus, the selective term is expressed through a quadratic function of the distance of trait y from the fittest one:

$$S(y,O) = \eta(y - \varphi(O))^2 \tag{5.5}$$

where η is the selection gradient. Finally, uninfected cancer cells are infected by the virus according to the density of virions and the infection rate $\beta(y)$. Note that y is directly involved in the selection term; it also affects proliferation and infection through the coefficients $p(y)$ and $\beta(y)$. To catch the above-described trade-off, we set

$$p(y) = p_M - (p_M - p_m)y, \qquad \beta(y) = \beta_m + (\beta_M - \beta_m)y \tag{5.6}$$

Observe that both functions are increasing in y.

We remark that the terms for proliferation and selection are the same ones adopted in Chiari et al., 2023b. In absence of infections, the cell density always grows up to the same carrying capacity K irrespective of the oxygen level: this constitutes a significant difference with respect to some previous modelling approaches of hypoxic tumours (such as the ones employed in Ardaševa et al., 2020c; Ardaševa et al., 2020a; Fiandaca et al., 2021; Villa et al., 2021a) and allows us to consider virotherapy as the only cause of cancer reduction in hypoxic conditions.

Infected cancer cell Infected cells may move and die; uninfected cells may also become infected. The dynamics are described by the equation

$$\partial_t I(t,\boldsymbol{x}) = \underbrace{D_x \nabla \cdot (I(t,\boldsymbol{x}) \nabla \rho(t,\boldsymbol{x}))}_{\text{pressure-driven movement}} + \underbrace{v(t,\boldsymbol{x}) \int_Y \beta(y) u(t,\boldsymbol{x},y)\, \mathrm{d}y}_{\text{infection}} - \underbrace{q_I I(t,\boldsymbol{x})}_{\text{death}}$$

The movement follows the same law as that of uninfected cells, as there is no reason to assume that the infection has some effect on that. All the susceptible cells that undergo infection are collected in the same population. Finally, infected cells die at rate q_I.

We again assume that infected cells do not proliferate, as the virus disrupts the cellular machinery, and are not affected by environmental conditions due to their short life. As a consequence, they lack all the processes affected by the epigenetic trait, which motivates their absence of epigenetic structure.

Oncolytic virus The virus is injected into the tumour, then diffuses in space with coefficient D_v and decays with rate q_v. The lysis of an infected cell releases α viral particles. The dynamics are described by the equation

$$\partial_t v(t,\boldsymbol{x}) = \underbrace{D_v \Delta v(t,\boldsymbol{x})}_{\text{diffusion}} + \underbrace{\alpha q_I I(t,\boldsymbol{x})}_{\text{release}} - \underbrace{q_v v(t,\boldsymbol{x})}_{\text{natural decay}} + \underbrace{v_{\text{inj}}(\boldsymbol{x}) \delta_{T_{\text{inj}}}(t)}_{\text{viral injection}} \tag{5.7}$$

The injection is modelled through a Dirac delta, which corresponds to a jump in the viral concentration at time T_{inj}; the spatial profile of the injection is given by the function v_{inj}. Apart from the injection term, this equation is the same as the ones employed in Eqs. (4.2) and (4.3).

Oxygen The oxygen is delivered by tissue vascularisation with a space-dependent intensity $Q(\boldsymbol{x})$, diffuses in space with diffusion coefficient D_O and is then consumed both by healthy tissue and cancer cells. The resulting equation is

$$\partial_t O(t,\boldsymbol{x}) = \underbrace{D_O \Delta O(t,\boldsymbol{x})}_{\text{diffusion}} - \underbrace{q_O O(t,\boldsymbol{x})}_{\text{natural decay}} - \underbrace{\lambda \rho(t,\boldsymbol{x}) O(t,\boldsymbol{x})}_{\text{cancer cell consumption}} + \underbrace{Q(\boldsymbol{x})}_{\text{source}} \tag{5.8}$$

We assume that healthy cells initially fill the tissue up to carrying capacity and their oxygen consumption is indirectly modelled through the decay at rate q_O. As the tumour grows, healthy cells are replaced by cancer cells, which consume more oxygen: the additional consumption is captured by the term $\lambda \rho(t,\boldsymbol{x}) O(t,\boldsymbol{x})$. Observe that both infected and uninfected cells are responsible for oxygen consumption in the same way.

Summary of the model Collecting all the equations together, the evolution of the system reads:

$$\begin{cases} \partial_t u(t,\boldsymbol{x},y) = D_y \partial^2_{yy} u(t,\boldsymbol{x},y) + D_x \nabla_x \cdot (u(t,\boldsymbol{x},y) \nabla \rho(t,\boldsymbol{x})) + P(y,\rho(t,\boldsymbol{x}))\, u(t,\boldsymbol{x},y) - \\ \qquad\qquad - S(y,O(t,\boldsymbol{x}))\, u(t,\boldsymbol{x},y) - \beta(y)\, u(t,\boldsymbol{x},y)\, v(t,\boldsymbol{x}) \\ \partial_t I(t,\boldsymbol{x}) = D_x \nabla \cdot (I(t,\boldsymbol{x}) \nabla \rho(t,\boldsymbol{x})) + v(t,\boldsymbol{x}) \int_Y \beta(y) u(t,\boldsymbol{x},y)\, \mathrm{d}y - q_I I(t,\boldsymbol{x}) \\ \partial_t v(t,\boldsymbol{x}) = D_v \Delta v(t,\boldsymbol{x}) + \alpha q_I I(t,\boldsymbol{x}) - q_v v(t,\boldsymbol{x}) + v_{\text{inj}}(\boldsymbol{x}) \delta_{T_{\text{inj}}(t)} \\ \partial_t O(t,\boldsymbol{x}) = D_O \Delta O(t,\boldsymbol{x}) - q_O O(t,\boldsymbol{x}) - \lambda \rho(t,\boldsymbol{x}) O(t,\boldsymbol{x}) + Q(\boldsymbol{x}) \\ \rho(t,\boldsymbol{x}) \coloneqq \int_Y u(t,\boldsymbol{x},y)\, \mathrm{d}y + I(t,\boldsymbol{x}) \end{cases} \tag{5.9}$$

with the previously defined $\rho(t,\boldsymbol{x})$ in Eq. (5.2), $P(y,\rho(t,\boldsymbol{x}))$ in Eq. (5.3), $S(y,O(t,\boldsymbol{x}))$ in Eq. (5.5) based on $\varphi(O(t,\boldsymbol{x}))$ in Eq. 5.4, and $p(y)$ and $\beta(y)$ set as in Eq. (5.6). We keep the oxygen source $Q(x)$ in general form and change it according to the biological setting we aim to reproduce.

We define the Cauchy problem by imposing the initial conditions

$$\begin{cases} u(0,\boldsymbol{x},y) = u_0(\boldsymbol{x},y) \\ I(0,\boldsymbol{x}) = 0 \\ v(0,\boldsymbol{x}) = 0 \\ O(0,\boldsymbol{x}) = O_0(\boldsymbol{x}) \end{cases} \tag{5.10}$$

where $u_0(\boldsymbol{x},y)$ and $O_0(\boldsymbol{x})$ will be defined in the context of the various scenarios in Section 5.3; we always assume that the tumour initially grows without viral infection and the therapy is administered after some time. Moreover, we impose no flux boundary conditions on ∂Y, i.e.

$$\partial_y u(t,\boldsymbol{x},0) = \partial_y u(t,\boldsymbol{x},1) = 0$$

corresponding to the fact that the epigenetic trait cannot assume values below 0 or above 1. Finally, we also impose no flux boundary condition for all $u(t,\boldsymbol{x},y)$, $I(t,\boldsymbol{x})$, $v(t,\boldsymbol{x})$ and $O(t,\boldsymbol{x})$ at $\partial\Omega$, meaning that these quantities cannot leave the spatial domain.

5.2 Formal asymptotic analysis

We now conduct a formal asymptotic analysis analogous to the one performed in Section 4.2 to compute the theoretical equilibrium values. As in Section 4.2, we introduce a small parameter ε and assume that

$$D_x = \varepsilon, \qquad D_y = D_v = D_O = \varepsilon^2$$

Furthermore, we use the time scaling $t \mapsto \frac{t}{\varepsilon}$ (which allows to study the long-time behaviour of the system) and define

$$u_\varepsilon(t,\boldsymbol{x},y) \coloneqq u\Big(\frac{t}{\varepsilon},\boldsymbol{x},y\Big), \qquad I_\varepsilon(t,\boldsymbol{x}) \coloneqq I\Big(\frac{t}{\varepsilon},\boldsymbol{x}\Big),$$
$$v_\varepsilon(t,\boldsymbol{x}) \coloneqq v\Big(\frac{t}{\varepsilon},\boldsymbol{x}\Big) \qquad O_\varepsilon(t,\boldsymbol{x}) \coloneqq O\Big(\frac{t}{\varepsilon},\boldsymbol{x}\Big)$$

The system of Eq. (5.9) then becomes

$$\begin{cases} \varepsilon\partial_t u_\varepsilon(t,\boldsymbol{x},y) = \varepsilon^2\partial^2_{yy} u_\varepsilon(t,\boldsymbol{x},y) + \varepsilon\nabla_{\boldsymbol{x}}\cdot(u_\varepsilon(t,\boldsymbol{x},y)\nabla\rho_\varepsilon(t,\boldsymbol{x})) \\ \qquad\qquad + R(y,\rho_\varepsilon(t,\boldsymbol{x}),O_\varepsilon(t,\boldsymbol{x}),v_\varepsilon(t,\boldsymbol{x}))\; u_\varepsilon(t,\boldsymbol{x},y) \\ \varepsilon\partial_t I_\varepsilon(t,\boldsymbol{x}) = \varepsilon\nabla\cdot(I_\varepsilon(t,\boldsymbol{x})\nabla\rho_\varepsilon(t,\boldsymbol{x})) + v_\varepsilon(t,\boldsymbol{x})\int_Y \beta(y)u(t,\boldsymbol{x},y)\,\mathrm{d}y - q_I I(t,\boldsymbol{x}) \\ \varepsilon\partial_t v_\varepsilon(t,\boldsymbol{x}) = \varepsilon^2\Delta v_\varepsilon(t,\boldsymbol{x}) + \alpha q_I I_\varepsilon(t,\boldsymbol{x}) - q_v v_\varepsilon(t,\boldsymbol{x}) \\ \varepsilon\partial_t O_\varepsilon(t,\boldsymbol{x}) = \varepsilon^2\Delta O_\varepsilon(t,\boldsymbol{x}) - q_O O_\varepsilon(t,\boldsymbol{x}) - \lambda\rho_\varepsilon(t,\boldsymbol{x})O_\varepsilon(t,\boldsymbol{x}) + Q(\boldsymbol{x}) \\ \rho_\varepsilon(t,\boldsymbol{x}) \coloneqq \int_Y u_\varepsilon(t,\boldsymbol{x},y)\,\mathrm{d}y + I_\varepsilon(t,\boldsymbol{x}) \end{cases} \tag{5.11}$$

Let us observe that, letting $\varepsilon \to 0$ and assuming that all the functions converge, we immediately get from the third equation that

$$v(t,\boldsymbol{x}) = \frac{\alpha q_I}{q_v} I(t,\boldsymbol{x}) \tag{5.12}$$

and from the second equation that

$$I(t,\boldsymbol{x}) = 0 \quad \text{or} \quad \int_Y \beta(y) u(t,\boldsymbol{x},y)\,\mathrm{d}y = \frac{q_I I(t,\boldsymbol{x})}{v(t,\boldsymbol{x})} = \frac{q_v}{\alpha} \tag{5.13}$$

Furthermore, the fourth equation yields

$$O(t,\boldsymbol{x}) = \frac{Q(\boldsymbol{x})}{q_O + \lambda\rho(t,\boldsymbol{x})} \tag{5.14}$$

and, for simplicity, we assume that the oxygen source is spatially homogeneous so that $Q(t,\boldsymbol{x}) \equiv Q$. It is important to remark that the system may not converge to an equilibrium: indeed, some parameter values will shortly show that central oscillations persist even for very long times, similar to the ones described in Section 4.1 (see also electronic supplementary material S9 of Morselli et al., 2024a),.

We then make for uninfected cells the real phase WKB ansatz

$$u_\varepsilon(t,\boldsymbol{x},y) = e^{\frac{n_\varepsilon(t,\boldsymbol{x},y)}{\varepsilon}}$$

This implies

$$\partial_t u_\varepsilon = \frac{\partial_t n_\varepsilon}{\varepsilon} u_\varepsilon, \quad \nabla_{\boldsymbol{x}} u_\varepsilon = \frac{\nabla_{\boldsymbol{x}} n_\varepsilon}{\varepsilon} u_\varepsilon \quad \partial^2_{yy} u_\varepsilon = \Big(\frac{(\partial_y n_\varepsilon)^2}{\varepsilon^2} + \frac{\partial^2_{yy} n_\varepsilon}{\varepsilon}\Big) u_\varepsilon$$

The first equation of Eq. (5.11) yields

$$\varepsilon \frac{\partial_t n_\varepsilon}{\varepsilon} u_\varepsilon \;=\; \varepsilon^2 \Big(\frac{(\partial_y n_\varepsilon)^2}{\varepsilon^2} + \frac{\partial^2_{yy} n_\varepsilon}{\varepsilon}\Big) u_\varepsilon + \varepsilon \Big(\frac{\nabla_{\boldsymbol{x}} n_\varepsilon}{\varepsilon} \cdot \nabla\rho_\varepsilon + \Delta\rho_\varepsilon\Big) u_\varepsilon + R(y,\rho_\varepsilon,O_\varepsilon,v_\varepsilon) u_\varepsilon$$

and this simplifies to

$$\partial_t n_\varepsilon = (\partial_y n_\varepsilon)^2 + \varepsilon \partial^2_{yy} n_\varepsilon + \nabla_{\boldsymbol{x}} n_\varepsilon \cdot \nabla\rho_\varepsilon + \varepsilon\Delta\rho_\varepsilon + R(y,\rho_\varepsilon,O_\varepsilon,v_\varepsilon)$$

Letting $\varepsilon \to 0$ and assuming convergence, we obtain

$$\partial_t n = (\partial_y n)^2 + \nabla_{\boldsymbol{x}} n \cdot \nabla\rho + R(y,\rho,O,v) \tag{5.15}$$

All the functions without the subscript ε are the leading order terms of the asymptotic expansion.

Under the concavity hypotheses explained in Section 4.2, we expect n to be a strictly concave function of y; we define

$$\bar{y}(t,\boldsymbol{x}) := \arg\max_{y\in Y} n(t,\boldsymbol{x},y)$$

Let us fix $\boldsymbol{x} \in \mathrm{supp}(\rho)$. The fact that $\rho_\varepsilon(t,\boldsymbol{x}) < +\infty$ for all ε implies that

$$n(t,\boldsymbol{x},\bar{y}(t,\boldsymbol{x})) = \max_{y\in Y} n(t,\boldsymbol{x},y) = 0$$

As in Section 4.2, the concavity of $y \mapsto n(t,x,y)$ for every t and x implies that

$$u_\varepsilon(t,x,y) \overset{*}{\rightharpoonup} U(t,x)\,\delta_{\bar{y}(t,x)}$$

Furthermore, the definition of $\bar{y}(t,x)$ trivially implies

$$\partial_y n(t,\boldsymbol{x},\bar{y}(t,\boldsymbol{x}))=0$$

We also observe that

$$0=\frac{\partial}{\partial t}n(t,\boldsymbol{x},\bar{y}(t,\boldsymbol{x}))=\partial_t n(t,\boldsymbol{x},y)|_{y=\bar{y}(t,\boldsymbol{x})}+\cancel{\partial_y n(t,\boldsymbol{x},y)|_{y=\bar{y}(t,\boldsymbol{x})}}\partial_t\bar{y}(t,\boldsymbol{x})$$

implying that $\partial_t n(t,\boldsymbol{x},\bar{y}(t,\boldsymbol{x}))=0$; similarly, $\nabla_{\boldsymbol{x}} n(t,\boldsymbol{x},\bar{y}(t,\boldsymbol{x}))=0$. We evaluate Eq. (5.15) in $y=\bar{y}(t,\boldsymbol{x})$ to get

$$\begin{aligned}[p_M+(p_m-p_M)y]\Big(1-\frac{\rho}{K}\Big)-\eta(y-\varphi(O))^2-[\beta_M+(\beta_m-\beta_M)y]v=\\ =R(\bar{y},\rho,O,v)=\partial_t n-(\partial_y n)^2-\nabla_{\boldsymbol{x}} n\cdot\nabla\rho=0\end{aligned}\tag{5.16}$$

We can also differentiate Eq. (5.15) with respect to y to get

$$\partial^2_{ty}n=2\partial_y n\,\partial^2_{yy}n+\partial_y\nabla_{\boldsymbol{x}} n\cdot\nabla\rho+\nabla_{\boldsymbol{x}} n\cdot\partial_y\nabla\rho+\partial_y R(y,\rho,O,v)$$

which computed at $y=\bar{y}(t,\boldsymbol{x})$ yields

$$\partial^2_{ty}n(t,\boldsymbol{x},\bar{y}(t,\boldsymbol{x}))=\partial_y\nabla_{\boldsymbol{x}} n(t,\boldsymbol{x},\bar{y}(t,\boldsymbol{x}))\cdot\nabla\rho(t,\boldsymbol{x})+\partial_y R(\bar{y}(t,\boldsymbol{x}),\rho(t,\boldsymbol{x}),O(t,\boldsymbol{x}),v(t,\boldsymbol{x}))$$

If we look for a homogeneous steady state, then the previous equation implies

$$\partial_y R(\bar{y},\rho,O,v)=(p_m-p_M)\Big(1-\frac{\rho}{K}\Big)-2\eta(y-\varphi(O))-(\beta_m-\beta_M)v=0\tag{5.17}$$

As in Section 4.2, we also have

$$\int_Y\beta(y)u_\varepsilon(t,\boldsymbol{x},y)\,\mathrm{d}y\to\beta(\bar{y})\bar{U}$$

With this observation, Eqs. (5.12), (5.13), (5.14), (5.16) and (5.17) constitute a system of five equations in the five variables $\bar{U},\bar{I},\bar{v},\bar{O},\bar{y}$, which in principle can be solved.

Let us first focus on the infection-free case of Eq. (5.13), i.e. $\bar{I}=0$. This clearly implies $\bar{v}=0$ and the other three variables solve the system

$$\begin{cases}R(\bar{y},\bar{U},\bar{O},0)=p(\bar{y})\Big(1-\dfrac{\bar{U}}{K}\Big)-\eta(\bar{y}-\varphi(\bar{O}))^2=0\\ \partial_y R(\bar{y},\bar{U},\bar{O},0)=(p_m-p_M)\Big(1-\dfrac{\bar{U}}{K}\Big)-2\eta(\bar{y}-\varphi(\bar{O}))=0\\ \bar{O}=\dfrac{Q}{q_O+\lambda\bar{U}}\end{cases}\tag{5.18}$$

From the first two equations, we obtain

$$1-\frac{\bar{U}}{K}=\frac{\eta(y-\varphi(\bar{O}))^2}{p(\bar{y})}=\frac{2\eta(y-\varphi(\bar{O}))}{(p_m-p_M)}$$

which admits two solutions: the first one is $\bar{U} = K, \bar{y} = \varphi(\bar{O})$; the second one is

$$\bar{y} = \frac{2p_M}{p_M - p_m} - \varphi(\bar{O}) > \frac{2p_M}{p_M - p_m} - 1 = \frac{p_M + p_m}{p_M - p_m} > 1$$
$$\bar{U} = K + \frac{4\eta p(\varphi(\bar{O}))}{(p_m - p_M)^2} > K$$

but it clearly has no biological meaning. We then obtain the oxygen concentration from the third equation of Eq. (5.18). The first equilibrium is given by

$$\bar{U} = K, \qquad \bar{O} = \frac{Q}{q_O + \lambda K}, \qquad \bar{y} = \varphi(\bar{O})$$

The second equilibrium could be obtained by computing the solutions of a second-degree equation in $\bar{O}$; given the complexity of the expressions and the lack of biological meaning, we omit further details.

Let us now assume $\bar{I} \neq 0$, which according to Eq. (5.13) implies

$$\bar{U} = \frac{q_v}{\alpha\beta(\bar{y})}$$

This leads to the system

$$\begin{cases} \bar{U} = \dfrac{q_v}{\alpha[\beta_M + (\beta_m - \beta_M)\bar{y}]} \\ \bar{v} = \dfrac{\alpha q_I}{q_v}\,\bar{I} \\ \bar{O} = \dfrac{Q}{q_O + \lambda(\bar{U} + \bar{I})} \\ R(\bar{y}, \bar{U} + \bar{I}, \bar{O}, \bar{v}) = [p_M + (p_m - p_M)\bar{y}]\left(1 - \dfrac{\bar{U} + \bar{I}}{K}\right) - \eta(\bar{y} - \varphi(\bar{O}))^2 \\ \qquad\qquad - [\beta_M + (\beta_m - \beta_M)\bar{y}]\bar{v} = 0 \\ \partial_y R(\bar{y}, \bar{U} + \bar{I}, \bar{O}, \bar{v}) = (p_m - p_M)\left(1 - \dfrac{\bar{U} + \bar{I}}{K}\right) - 2\eta(\bar{y} - \varphi(\bar{O})) - (\beta_m - \beta_M)\bar{v} = 0 \end{cases} \tag{5.19}$$

The above system is too complicated to be studied analytically; hence, we mainly consider numerical solutions. Although six solutions exist, only one is biologically meaningful in the parameter range that we consider. A more useful expression can be obtained by solving the equation $\partial_y R = 0$ in $\bar{y}$:

$$\bar{y} = \varphi(\bar{O}) + \frac{1}{2\eta}\left[-(p_M - p_m)\left(1 - \frac{\rho}{K}\right) + (\beta_M - \beta_m)\bar{v}\right] \tag{5.20}$$

This formula has a straightforward interpretation: $\varphi(\bar{O})$ is the epigenetic trait selected by the oxygen concentration; the fittest trait tends to decrease when the total cell population ρ is low due to the different proliferation rates of cell lines in a situation of low competition; at the same time, it grows in the presence of viral infection that targets proliferative cells and it reduces if the infection targets hypoxic cells. We remark that this formula may yield a value of $\bar{y}$ outside the interval $[0, 1]$, which has no meaning in our formulation of the model: when this happens, we should expect the fittest trait to be 0 if $\bar{y} < 0$ and 1 if $\bar{y} > 1$.

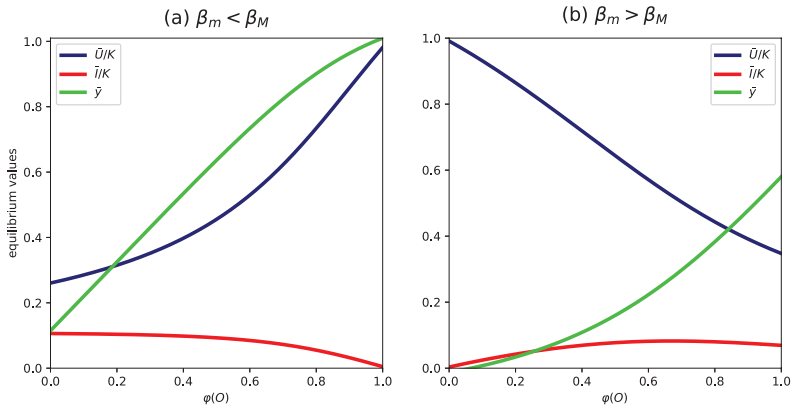

FIGURE 5.1: Numerical solution of Eq. 5.21 showing the equilibria in different oxygen conditions. The parameters in panel (a) take the values listed in Table 5.1. In panel (b), the values of β_M and β_m are switched to reproduce the situation of oncolytic viruses that specifically target hypoxic cells. In both cases, $\varphi(\bar{O})$ ranges between 0 and 1.

A simpler situation is obtained by assuming that tumour dynamics do not significantly affect oxygen density so that $\bar{O}$ is given a priori; in this case, the system becomes

$$\begin{cases} \bar{U} = \dfrac{q_v}{\alpha[\beta_M + (\beta_m - \beta_M)\bar{y}]} \\ \bar{v} = \dfrac{\alpha q_I}{q_v}\,\bar{I} \\ R(\bar{y}, \bar{U}+\bar{I}, \bar{O}, \bar{v}) = [p_M + (p_m - p_M)\bar{y}]\left(1 - \dfrac{\bar{U}+\bar{I}}{K}\right) - \eta(\bar{y} - \varphi(\bar{O}))^2 \\ \qquad\qquad - [\beta_M + (\beta_m - \beta_M)\bar{y}]\bar{v} = 0 \\ \partial_y R(\bar{y}, \bar{U}+\bar{I}, \bar{O}, \bar{v}) = (p_m - p_M)\left(1 - \dfrac{\bar{U}+\bar{I}}{K}\right) - 2\eta(\bar{y} - \varphi(\bar{O})) - (\beta_m - \beta_M)\bar{v} = 0 \end{cases} \tag{5.21}$$

It is then possible to obtain a third-degree equation for $\bar{y}$, which in principle can be solved; however, the explicit solutions are still too complicated to give any useful information. Fig. 5.1 shows the numerical solution of Eq. (5.21) that is biologically meaningful. In the reference situation ($\beta_m < \beta_M$), the equilibrium values of $\bar{U}$ and $\bar{y}$ increase as the oxygen values decrease; when the values of β_M and β_m are switched, we observe the inverse behaviour. The effect of oxygen variations on $\bar{I}$ is more complex, as its value is almost constant for a wide range of oxygen values and then significantly decreases only when the oxygen concentration is very low (or very high).

So far, we have focused our discussion on the spatially homogeneous situation. To our knowledge, spatial dynamics in this context have not been studied analytically, not even in simpler settings (such as the one of Section 4.2). Nevertheless, given the forthcoming numerical simulations, it is helpful to recall some elementary facts from the previous chapters. If we neglect the epigenetic structure, the one-dimensional dynamics of uninfected cells in the absence of viral infection follow the equation

$$\partial_t u(t,x) = D_x \partial_x (u(t,x)\partial_x u(t,x)) + p\left(1 - \frac{u(t,x)}{K}\right)u(t,x)$$

It is well-known that there exist travelling waves solutions of this equation with speed at least $\sqrt{D_x K p/2}$ and an initial condition with compact support evolves into a wave that travels with the minimal speed (Aronson, 1980; Newman, 1980). The addition of infection due to cell-to-cell contact originates travelling waves of the two populations

Parameter	Description	Value [Units]	Reference
p_M	maximal duplication rate	2.88×10^{-2} [h^{-1}]	Ke et al., 2000
p_m	minimal duplication rate	1.44×10^{-2} [h^{-1}]	Martínez-González et al., 2012
K	tissue carrying capacity	10^6 [cells/mm^3]	Lodish et al., 2008
D_x	cell spatial diffusion coefficient	1.30×10^{-9} [(mm×cells×h)$^{-1}$]	estimate based on Kim et al., 2006
η	selection rate by oxygen	2.08×10^{-2} [h^{-1}]	model estimate
D_y	cell epigenetic diffusion coefficient	5.00×10^{-6} [h^{-1}]]	Celora et al., 2021
β_M	maximal infection rate	7.00×10^{-10} [mm^3/(viruses×h)]	Friedman et al., 2006
β_m	minimal infection rate	1.75×10^{-10} [mm^3/(viruses×h)]	model estimate
q_I	death rate of infected cells	4.17×10^{-2} [h^{-1}]	Ganly et al., 2000
q_v	virus clearance rate	1.67×10^{-1} [h^{-1}]	Mok et al., 2009
α	viral burst size	1000 [viruses/cells]	model estimate
D_v	virus diffusion coefficient	3.6×10^{-2} [mm^2/h]	Kim et al., 2006
$O_{\max}$	maximal oxygen concentration	2.16×10^{-3} [$mm^3_{O_2}/mm^3_{plasma}$]	McKeown, 2014; Pittman, 2011
O_M	oxygen normoxic threshold	1.71×10^{-3} [$mm^3_{O_2}/mm^3_{plasma}$]	McKeown, 2014; Pittman, 2011
O_m	oxygen hypoxic threshold	2.28×10^{-4} [$mm^3_{O_2}/mm^3_{plasma}$]	McKeown, 2014; Pittman, 2011
q_O	oxygen physiological decay rate	5.60×10^{-1} [h^{-1}]	estimate based on Wagner et al., 2011
λ	oxygen consumption rate	6.55×10^{-4} [mm^3/(cell×h)]	estimate based on Grimes et al., 2014
D_O	oxygen diffusion coefficient	3.60 [mm^2/h]	Mueller-Klieser and Sutherland, 1984

TABLE 5.1: Parameter set for the model of infection in hypoxic conditions.

(uninfected and infected), with the uninfected proliferative cells trying to escape from the infected cells (see Chapter 2); the addition of a viral population does not significantly change this picture (see Section 4.1). It is important to remark that an efficient infection results in a wavefront much lower than the carrying capacity, whose invasion speed is lower than $\sqrt{D_x K p/2}$.

5.3 Numerical results

In this section, we describe the results of numerical simulations and compare them with the theoretical analysis performed in Section 5.2. After the description of the numerical details, for the sake of simplicity, we first consider a stationary oxygen distribution independent of time, corresponding to a situation in which the tumour does not influence the oxygen distribution: while this is clearly an oversimplification, it allows us to focus our attention on the tumour's evolutionary and infectious dynamics. We then analyse the full model, which includes oxygen dynamics, taking into account different configurations of oxygen sources. Finally, we briefly mention the case of a virus that specifically infects hypoxic cells, looking towards combining oncolytic virotherapy with other treatments.

5.3.1 Details of numerical simulations

Parameter values Table 5.1 lists the parameters we adopt as a reference in the numerical simulations. The majority of the parameters has been estimated from the empirical literature, while a few others are specific to our formulation of the model and have been set to reasonable values in order to reproduce plausible dynamics. Our two-dimensional simulations represent the section of a tumour that is approximately homogeneous along the third spatial dimension (which can, therefore, be neglected), and parameters are estimated in a three-dimensional setting.

The maximal duplication rate of uninfected cells p_M, corresponding to the normoxic situation, has been taken equal to $\log(2)/24\ \text{h}^{-1} \approx 2.88 \times 10^{-2}\ \text{h}^{-1}$; the duplication time of 24 hours is among the fastest values reported in Ke et al., 2000 for glioblastoma. On the other hand, we assume that severely hypoxic cells duplicate in 48 hours, as done in Martínez-González et al., 2012: this leads to a minimal proliferation rate $p_m = 1.44 \times 10^{-2}\ \text{h}^{-1}$. The carrying capacity K has been estimated assuming that a cell has diameter 10 μm$= 10^{-2}$ mm (Lodish et al., 2008, §1.1): this implies that the carrying capacity is 10^6 cells/mm^3.

The spatial diffusion coefficient of tumour cells D_x has been estimated from the experimental data of the U343 control group of Kim et al., 2006, as already done in the previous chapters. In their experiments, the tumour volume passes in 40 days from 70 mm^3 to 1000 mm^3, which corresponds to a change in the tumour radius from approximately 2.6 mm to approximately 6.2 mm. Hypoxia may play some role in the process, but this is not taken into account in their data: for the sake of simplicity, we assume a moderately hypoxic situation so that the proliferation rate takes the value $p(0.5)$ (i.e., the average between p_M and p_m). Hence, the dynamics of uninfected cells in the absence of viral infection follow the equation

$$\partial_t u(t,\boldsymbol{x}) = D_x \nabla_{\boldsymbol{x}} \cdot (u(t,\boldsymbol{x}) \nabla u(t,\boldsymbol{x})) + p(0.5)\Big(1 - \frac{u(t,\boldsymbol{x})}{K}\Big) u(t,\boldsymbol{x})$$

We recall that an initial condition with compact support evolves into a wave that travels with the minimal speed $\sqrt{D_x K p(0.5)/2}$. This yields the estimate

$$\begin{aligned} D_x = \frac{2c^2}{Kp} &= \Big(\frac{6.2 - 2.6\ \text{mm}}{40 \times 24\ \text{h}}\Big)^2 \times \frac{2}{10^6 \times \text{cells/mm}^3 \times 2.16 \times 10^{-2}\,\text{h}^{-1}} \\ &\approx \frac{1.30 \times 10^{-3}\ \text{mm}^2/\text{h}}{10^6 \times \text{cells/mm}^3} \approx 1.30 \times 10^{-9}\ (\text{mm} \times \text{cells} \times \text{h})^{-1} \end{aligned}$$

We assume that this coefficient is the same also for infected cells, as a priori we have no reason to believe that the infection affects cellular movement.

The death rate of uninfected tumour cells due to oxygen-driven selection η and the epigenetic diffusion coefficient of tumour cells D_y are not easily accessible in the empirical literature; hence they have been adapted from previous mathematical papers about epigenetically structured populations: their values have been set respectively to $1/48\ \text{h}^{-1} \approx 4.16 \times 10^{-2}\ \text{h}^{-1}$, which is of the same magnitude of the value used in Chiari et al., 2023b, and $5.00 \times 10^{-6}\ \text{h}^{-1}$, as in Celora et al., 2021.

The maximal infection rate of the oncolytic virus β_M has been set to 7.00×10^{-10} mm^3/(viruses$\times$h), as in Friedman et al., 2006; their model does not explicitly take into account hypoxia, so we assume that they consider normoxic conditions. Since we are unaware of any experimental estimate of infection rate under hypoxic conditions, we set β_m to one-fourth of the value of β_m. The death rate of infected cells q_I has been taken equal to $1/24\ \text{h}^{-1} = 4.17 \times 10^{-2}\ \text{h}^{-1}$, following Ganly et al., 2000. The clearance rate

of the virus has been set to $1/6$, as in Mok et al., 2009. The viral load released by the death of infected cells depends highly on the type of virus and ranges from the value 157 viruses/cells estimated in Workenhe et al., 2014 to the value 3500 viruses/cells of Chen et al., 2001; we chose an intermediate value of $\alpha = 1000$ viruses/cells. It is important to remark that all these values are highly dependent on the exact type of oncolytic virus employed; our choices allow us to model significant differences in the effectiveness of oncolytic virotherapy as the oxygen level varies. We remark that the outcome of the therapy is mostly determined by the aggregate value $\beta\alpha q_I/q_v$, hence similar dynamics may also be obtained by different parameter combinations that maintain the ratio unchanged (as explained in Chapter 4). The spatial diffusion coefficient of viral particles D_v has been set to 3.6×10^{-2} mm^2/h, as in Friedman et al., 2006.

We consider the oxygen thresholds defined in McKeown, 2014: the oxygen partial pressure (pO_2) in arterial blood is 70 mmHg and we consider this as the maximal oxygen concentration ($O_{\max}$); the physiological pO_2 ranges approximately between 57 mmHg and 30.4 mmHg, so we consider the higher value as the normoxic threshold O_M, keeping in mind that we may observe lower oxygen values also in healthy tissue; the pathological hypoxic pO_2 value is 7.6 mmHg, which we consider as O_m. All these pressure values are converted in volume ratios by multiplying them by the solubility constant $3 \cdot 10^{-5}\,\mathrm{mm}^3_{O_2}/(\mathrm{mm}^3{}_{\text{plasma}} \times \text{mmHg})$ (Pittman, 2011).

We assume that the oxygen decay is due to the consumption of the healthy cells in the region. According to Wagner et al., 2011, cells have an average rate of oxygen utilisation of $9.00 \times 10^{-15}\,\mathrm{mol}/(\text{cell} \times \text{h})$, corresponding approximately to $2.02 \times 10^{-7}\,\mathrm{mm}_{O_2}/(\text{cells} \times \text{h})$, but this value may vary several orders of magnitude among different cell types. We therefore assume that a single healthy cell consumes six times this amount of oxygen when the available oxygen level is at $O_{\max}$ and the consumption scales linearly with the oxygen concentration, meaning that the consumption in the case of unitary cell density is given by $O(t, \boldsymbol{x})$ multiplied by

$$\frac{1.21 \times 10^{-6}\,\mathrm{mm}^3_{O_2}}{\text{cell} \times \text{h}} \frac{1}{O_{\max}} = 5.60 \times 10^{-4}\,\mathrm{mm}^3/(\text{cell} \times \text{h})$$

Considering K as the healthy cell density in the absence of a tumour, we obtain a decay rate $q_O = 5.60 \times 10^2\,\mathrm{h}^{-1}$. We adopt a similar way of reasoning for the consumption by cancer cells, starting from the fact that the consumption of a single cell is estimated to be $2.62 \times 10^{-6}\,\mathrm{mm}_{O_2}/(\text{cells} \times \text{h})$ (Grimes et al., 2014) and assuming again that this is only possible when the oxygen level is $O_{\max}$. We then assume that cancer cells take the place of healthy cells, meaning that they cause an additional consumption of

$$\lambda = \frac{2.62 \times 10^{-6}\mathrm{mm}_{O_2}/(\text{cells} \times \text{h})}{O_{\max}} - \frac{q_O}{K} = 6.55 \times 10^{-4}\,\mathrm{mm}^3/(\text{cell} \times \text{h})$$

The oxygen diffusion coefficient D_O has been set to 3.60 mm^2/h, as in Mueller-Klieser and Sutherland, 1984.

Numerical simulations are run until the final time $T = 2500$ h since their behaviour up to that moment is also representative of later dynamics; the only exception is the electronic supplementary video S9 of Morselli et al., 2024a, in which the final time is $T = 3500$ h to highlight the persistence of the oscillations. For the spatial domain $\Omega = [-L, L]^2$, we set $L = 10$ mm so that in most cases, wavefronts do not hit the boundary before T and the domain is representative of typical extensions of solid tumours.

Numerical method Numerical simulations use a finite volume method developed by adapting the procedures presented in Carrillo et al., 2015; Bessemoulin-Chatard and Filbet, 2012 to our problem. We discretise the space Ω with a uniform mesh consisting of the cells

$$C_{j,k} := [x_{1,j-\frac{1}{2}}, x_{1,j+\frac{1}{2}}] \times [x_{2,k-\frac{1}{2}}, x_{2,k+\frac{1}{2}}]$$

for $j = 0, \dots, N_{x_1}$, $k = 0, \dots, N_{x_2}$. Similarly, we discretise the space $\Omega \times Y$ with the cells

$$C_{j,k,m} := [x_{1,j-\frac{1}{2}}, x_{1,j+\frac{1}{2}}] \times [x_{2,k-\frac{1}{2}}, x_{2,k+\frac{1}{2}}] \times [y_{m-\frac{1}{2}}, y_{m+\frac{1}{2}}]$$

for $j = 0, \dots, N_{x_1}$, $k = 0, \dots, N_{x_2}$, and $m = 0, \dots, N_y$. The sizes of the cells are thus respectively $\Delta x_1 \times \Delta x_2$ and $\Delta x_1 \times \Delta x_2 \times \Delta y$, where

$$\Delta x_i = \frac{2L}{N_{x_i} + 1} \quad (i = 1, 2) \qquad \Delta y = \frac{1}{N_y + 1}$$

We set $N_{x_i} = 200$ and $N_y = 20$.

The equations for infected cells, viruses and oxygen are not epigenetically structured and are of the form

$$\partial_t f(t, \boldsymbol{x}) = \mathcal{M}(t, \boldsymbol{x}) + \mathcal{R}(t, \boldsymbol{x})$$

where $\mathcal{M}(t, \boldsymbol{x})$ regulates the movement and $\mathcal{R}(t, \boldsymbol{x})$ the reactions. We adopt a splitting method, considering separately the movement and reaction terms. The quantity of our interest is

$$f_{j,k}(t) = \frac{1}{\Delta x_1 \Delta x_2} \int_{C_{j,k}} f(t, \boldsymbol{x}) \, \mathrm{d}\boldsymbol{x}$$

We begin with the conservative part $\mathcal{M}(t, x)$, which is given by

$$\mathcal{M}(t, \boldsymbol{x}) = D\Delta_{\boldsymbol{x}} f = D\nabla \cdot (\nabla_{\boldsymbol{x}} f)$$

in the case of virus and oxygen and by

$$\mathcal{M}(t, \boldsymbol{x}) = D\nabla \cdot (\Phi(t, \boldsymbol{x}) f), \qquad \Phi(t, \boldsymbol{x}) = \nabla_{\boldsymbol{x}} \rho(t, \boldsymbol{x})$$

in the case of infected cells. In both situations, $\mathcal{M}$ involves the divergence of some quantity, hence the semi-discrete scheme takes the form

$$\frac{\mathrm{d}f}{\mathrm{d}t} = -D \frac{M_{j+\frac{1}{2},k}(t) - M_{j-\frac{1}{2},k}(t)}{\Delta x_1} - D \frac{M_{j,k+\frac{1}{2}}(t) - M_{j,k-\frac{1}{2}}(t)}{\Delta x_2} \tag{5.22}$$

where M is given by

$$M_{j+\frac{1}{2},k} = -\partial_{x_1} f_{j+\frac{1}{2},k} \qquad M_{j,k+\frac{1}{2}} = -\partial_{x_2} f_{j,k+\frac{1}{2}}$$

in the case of spatial diffusion and by

$$M_{j+\frac{1}{2},k} = (\Phi^1_{j+\frac{1}{2},k})^+ f_{j,k} + (\Phi^1_{j+\frac{1}{2},k})^- f_{j+1,k} \qquad M_{j,k+\frac{1}{2}} = (\Phi^2_{j,k+\frac{1}{2}})^+ f_{j,k} + (\Phi^2_{j,k+\frac{1}{2}})^- f_{j,k+1}$$

in the case of pressure-driven movement. In this second case, $\Phi^1 := \partial_{x_1} \Phi$ and $\Phi^2 := \partial_{x_2} \Phi$ are the components of Φ along the x_1 and x_2 axis respectively; furthermore, $(\cdot)^+$ and $(\cdot)^-$ indicate respectively the positive and negative part of their arguments, i.e., $(\cdot)^+ = \max\{0, \cdot\}$ and $(\cdot)^- = \min\{0, \cdot\}$. Since our scheme is of order zero, the reconstruction of the function is piecewise constant and thus assumes the same values at all the

interfaces. In all the cases, the derivatives in the middle points are evaluated as

$$(\partial_{x_1} f)_{j+\frac{1}{2},k} = \frac{f_{j+1,k} - f_{j,k}}{\Delta x_1}, \qquad (\partial_{x_2} f)_{j,k+\frac{1}{2}} = \frac{f_{j,k+1} - f_{j,k}}{\Delta x_2}$$

while the derivatives in the nodes are evaluated as

$$(\partial_{x_1} f)_{j,k} = \frac{f_{j+1,k} - f_{j-1,k}}{2\Delta x_1}, \qquad (\partial_{x_2} f)_{j,k} = \frac{f_{j,k+1} - f_{j,k-1}}{2\Delta x_2}$$

We use a uniform time discretisation of size $\Delta t = 5 \times 10^{-1}$ h and denote with apex l the discretised time step, i.e., $t^l = l\Delta t$. At all the iterations, we check that Δt satisfies the positivity-preserving CFL for infected cells, namely

$$\Delta t \leq \Delta \mathcal{T}_l := \min \left\{ \frac{\Delta x_1}{4\Phi_M^1}, \frac{\Delta x_2}{4\Phi_M^2} \right\}$$

where $\Phi_M^1 = \max_{j,k} \left(|\Phi^{1\,l}_{j+\frac{1}{2},k}| \right)$ and $\Phi_M^2 = \max_{j,k} \left(|\Phi^{2\,l}_{j,k+\frac{1}{2}}| \right)$. In the case of standard diffusion, the CFL is time-independent and is given by

$$\Delta t \leq \min \left\{ \frac{(\Delta x_1)^2}{4D}, \frac{(\Delta x_2)^2}{4D} \right\}$$

The fast oxygen dynamics require a refined temporal discretisation. Hence, we set $\Delta t_O = 6.95 \times 10^{-5}$ (which is one-tenth of the maximum size required by the CFL condition for oxygen) and perform several sub-iterations just for the oxygen while maintaining all the other quantities constant.

For the reaction term $\mathcal{R}(t, \boldsymbol{x})$, we adopt a simple forward Euler method for the time derivative. We set the discretised initial condition $f^0_{j,k}$ provided for each $j = 0, \dots, N_{x_1}$ and for $k = 0, \dots, N_{x_2}$, being $f^l_{j,k}$ the numerical approximation of $f_{j,k}(t^l)$. The complete splitted numerical scheme reads

$$\begin{cases} f^{l+\frac{1}{2}}_{j,k} = f^l_{j,k} - D\dfrac{\Delta t}{\Delta x_1}\left(M^l_{j+\frac{1}{2},k} - M^l_{j-\frac{1}{2},k}\right) - D\dfrac{\Delta t}{\Delta x_2}\left(M^l_{j,k+\frac{1}{2}} - M^l_{j,k-\frac{1}{2}}\right) \\ f^{l+1}_{j,k} = f^{l+\frac{1}{2}}_{j,k} + \Delta t\, R^{l+\frac{1}{2}}_{j,k} \end{cases}$$

for $l = 1, \dots, N_l$. We also set no flux boundary conditions.

The equation for uninfected cells is epigenetically structured and takes the form

$$\frac{\partial f}{\partial t}(t, \boldsymbol{x}, y) = \mathcal{M}(t, \boldsymbol{x}, y) + \mathcal{R}(t, \boldsymbol{x}, y)$$

where

$$\mathcal{M}(t, \boldsymbol{x}, y) = D_{\boldsymbol{x}} \nabla_{\boldsymbol{x}} \cdot (\Phi(t, \boldsymbol{x}) f) + D_y \Delta_y f$$

Therefore, we are now interested in the quantity

$$f_{j,k}(t) = \frac{1}{\Delta x_1 \Delta x_2 \Delta_y} \int_{C_{j,k,m}} f(t, \boldsymbol{x}, y)\, \mathrm{d}\boldsymbol{x}\, \mathrm{d}y$$

The semi-discrete scheme of the equation takes a form analogous to Eq. (5.22), which requires the following definitions:

$$M_{j+\frac{1}{2},k,m} = (\Phi^1_{j+\frac{1}{2},k,m})^+ f_{j,k,m} + (\Phi^1_{j+\frac{1}{2},k,m})^- f_{j+1,k,m}$$
$$M_{j,k+\frac{1}{2},m} = (\Phi^2_{j,k+\frac{1}{2},m})^+ f_{j,k,m} + (\Phi^2_{j,k+\frac{1}{2},m})^- f_{j,k+1,m}$$
$$N_{j,k,m+\frac{1}{2}} = -\partial_y f_{j,k,m+\frac{1}{2}}$$

The corresponding splitted numerical scheme is

$$\begin{cases} f^{l+\frac{1}{3}}_{j,k,m} = f^l_{j,k,m} - \dfrac{\Delta t}{\Delta x_1}\left(M^l_{j+\frac{1}{2},k,m} - M^l_{j-\frac{1}{2},k,m}\right) - \dfrac{\Delta t}{\Delta x_2}\left(M^l_{j,k+\frac{1}{2},m} - M^l_{j,k-\frac{1}{2},m}\right) \\ f^{l+\frac{2}{3}}_{j,k,m} = f^{l+\frac{1}{3}}_{j,k,m} - \dfrac{\Delta t}{\Delta y}\left(N^{l+\frac{1}{3}}_{j,k,m+\frac{1}{2}} - N^{l+\frac{1}{3}}_{j,k,m-\frac{1}{2}}\right) \\ f^{l+1}_{j,k,m} = f^{l+\frac{2}{3}}_{j,k,m} + \Delta t\, R^{l+\frac{2}{3}}_{j,k,m} \end{cases}$$

Initial conditions and viral injection In all the simulations, we start with an uninfected tumour of the form

$$u_0(\boldsymbol{x}, y) = \begin{cases} A_u\, e^{-\frac{|x-x_0|^2}{\theta_x} - \frac{(y-y_0)^2}{\theta_y}} & \text{if } A_u\, e^{-\frac{|x-x_0|^2}{\theta_x} - \frac{(y-y_0)^2}{\theta_y}} > 1 \\ 0 & \text{otherwise} \end{cases} \tag{5.23}$$

The truncation is performed in order to have an initial condition with compact support; the form of the equations is such that the solution will still be compactly supported at all times (Aronson, 1980; Newman, 1980). In all the simulations we set $\boldsymbol{x}_0 = (0, 0)$, $y_0 = \varphi(O(0, \boldsymbol{x}_0))$, $\theta_x = 0.5$, $\theta_y = 0.5$. The parameter A_u is set to

$$A_u = \frac{7.19 \times 10^4 \text{ cell/mm}^3}{\displaystyle\int_Y e^{-\frac{(y-y_0)^2}{\theta_y}}\, \mathrm{d}y}$$

This choice allows a maximal initial total cell density equal to $\frac{K}{10}$, irrespective of the value of y_0. We then assume that viral injection is performed after some time so that the tumour can adapt to the environment. In most of the cases, we perform a central viral injection as soon as the tumour reaches a given size: in mathematical terms, we set

$$T_{\text{inj}} := \inf\left\{\, t \in [0, +\infty) \;\middle|\; d(t) \geq d_{\text{inj}} \,\right\} \tag{5.24}$$

where d_{inj} is the tumour size at which we choose to inject the virus and

$$d(t) := \operatorname{diam}\left\{ \boldsymbol{x} \in \Omega \;\middle|\; \rho(\boldsymbol{x}, t) \geq \frac{K}{10} \right\}$$

We recall that the diameter of a general set E is defined as

$$\operatorname{diam} E := \sup\left\{\, |\boldsymbol{x}_1 - \boldsymbol{x}_2| \;\middle|\; \boldsymbol{x}_1, \boldsymbol{x}_2 \in E \,\right\}$$

In the particular situation of a circle, this definition coincides with the standard diameter; in general, the diameter is the longest length found inside the set. This choice is based on the assumption that small tumours cannot be clinically detected, hence the therapy may only start when cancer cells reach a density of at least one-tenth of the carrying

capacity in a large region. We set $d_{\text{inj}} = 5.2$ mm, as in Kim et al., 2006 and the central viral injection takes the form

$$v_{\text{inj}}(\boldsymbol{x}) = A_v \, e^{-\frac{|\boldsymbol{x}-\boldsymbol{x}_0|^2}{\theta_v}} \tag{5.25}$$

with $A_v = 7 \times 10^9$, $\theta_v = 0.5$. This allows for a total number of viral particles in agreement with the experiments performed in Kim et al., 2006.

5.3.2 Stationary oxygen

The most elementary situation is obtained by considering that the oxygen concentration is constant in space and time. We focus on three oxygen values, namely O_M (normoxia), O_m (severe hypoxia) and their average $\frac{O_m+O_M}{2}$ (physiological hypoxia), whose corresponding selected traits are respectively 1, 0 and 0.5; other values produce intermediate situations. We then consider inhomogeneous oxygen distributions, which resemble more biologically meaningful situations.

To make the comparison between the epigenetic composition and spatial characterisation more straightforward, we introduce the *average epigenetic trait*, defined as

$$\mu(t,\boldsymbol{x}) := \frac{\int_Y y u(t,\boldsymbol{x},y)\,\mathrm{d}y}{U(t,\boldsymbol{x})} \qquad \text{for all } (t,\boldsymbol{x}) \text{ such that } U(t,\boldsymbol{x}) \neq 0$$

Observe that this condition is not satisfied in the whole domain due to the compact support of u.

Homogeneous oxygen distribution and no viral infection As a starting point, it is helpful to observe how a tumour evolves in these environmental conditions without treatment, as shown in Fig. 5.2 (for the sake of clarity, the figure represents the central section of the domain, i.e. the set $[-L, L] \times \{0\}$). Overall, we observe the behaviour predicted by the theoretical asymptotic analysis in all the cases. The three initial conditions are given by Eq. (5.23) with $y_0 = \varphi(O)$. However, the density ρ at the beginning is much lower than K; hence, unless we are in a normoxic situation, the fittest epigenetic trait is lower than $\varphi(O)$, as predicted by Eq. (5.20); on the other hand, in the normoxic situation, $\varphi(O) = 0$ is already the lowest attainable value. As time passes, the cell density grows close to carrying capacity and the cancer starts to invade the surrounding area at a speed approximately proportional to the square root of the proliferation rate. In the hypoxic scenarios, the fittest epigenetic trait grows with ρ until reaching the value $\varphi(O)$; however, that trait is never completely selected due to epigenetic diffusion. An important consequence of the presence of different epigenetic characteristics is that ρ is always slightly below K, as the oxygen selection never completely stops: this effect is especially evident in the hypoxic situation, in which the slow proliferation contrasts the selective pressure less effectively. It is important to observe that in all cases, the average epigenetic traits are lower at the invasion front due to the lower total densities and increase as we get close to the tumour centre. High oxygen levels are associated with more proliferative tumours, which reach carrying capacity earlier and invade the surrounding tissues faster.

Homogeneous oxygen distribution and virotherapy From the previous discussion, it could appear that hypoxic tumours do not constitute a significant threat; however, this situation overturns in the presence of treatment, as the adaptation to hypoxia makes the tumour less susceptible to therapies. Indeed, Fig. 5.3, along with the video accompanying it (see electronic supplementary material S2 of Morselli et al., 2024a), shows the effect of oncolytic virotherapy on the tumours described above. The different growth rates imply

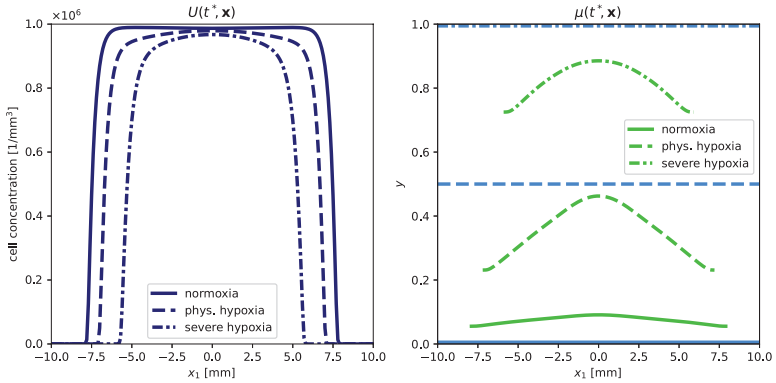

FIGURE 5.2: Results of the numerical simulation without viral infection for stationary oxygenation, for three spatially homogeneous oxygen condition: $O = O_M$ (solid lines), $O = \frac{O_M + O_m}{2}$ (dashed lines), and $O = O_m$ (dot-dashed lines). We plot the solutions at time $t^* = 1500$ h. Only the horizontal section is shown to facilitate the comparison. The blue lines in the left plot represent the profile of uninfected cancer cells $U(t^*, \boldsymbol{x})$. In the right plot, the green lines show the average epigenetic trait $\mu(t^*, \boldsymbol{x})$ and the light-blue lines show the fittest trait selected by the environment $\varphi(O(t^*, \boldsymbol{x}))$.

that the viral injection is performed at different times in the three situations: this happens respectively around $t = 426$ h for normoxia, 471 h for physiological hypoxia and 609 h for severe hypoxia. To facilitate the comparison between the different scenarios, Fig. 5.3 shows the section of the simulation approximately 1800 h after the viral injection. In all three cases, the central region of the tumour is quickly infected and viral particles reach the tumour front in a relatively short time due to their fast diffusion. In the severely hypoxic case, this initial successful infection might appear surprising. Still, it can be easily explained by the fact that at T_{inj} the tumour has not reached the carrying capacity yet and the epigenetic characteristics are still not fully adapted to the environment (the lack of complete adaptation is also true in the other cases, but less evident).

The following dynamics appear quite different in the three cases. In the normoxic case (Fig. 5.3a), cell densities at the centre of the tumour converge with damped oscillations to the equilibrium predicted by the theoretical analysis. The average of the epigenetic traits in the central area sensibly increases right after the viral injection, then oscillates towards the equilibrium. It is interesting to observe that epigenetic traits at the invasion front are lower since, in this area, both ρ and I are lower; this is in line with the observation of Section 4.2 that the tumour invasion is guided by the most proliferative cells. The situation is qualitatively similar in the physiologically hypoxic case (Fig. 5.3b), but the equilibrium value for ρ is higher. The spatial difference of the average epigenetic trait is much more evident than in the previous case: the convergence to the equilibrium value is slower than before and takes place mainly from the lower side. While these two situations can be described as partial successes of the therapy, the severely hypoxic case (Fig. 5.3c) is clearly a complete failure: the tumour density decreases only for a short time, after which it starts to regrow up to around 90% of carrying capacity, with a tiny fraction of infected cells (not shown here, see electronic supplementary material S2 of Morselli et al., 2024a); we remark that such a low number of cells may correspond a situation of extinction due to stochastic events. After approximately 400 h, the infection relapses, which causes a small decrease in the total cell density followed by a subsequent regrowth towards the theoretical equilibrium. The convergence is extremely slow and it is clear from Fig. 5.3c that 1800 h after the viral injection the dynamics are still far from the equilibrium. This can be explained by the fact that the smaller growth rate slows down all the evolutionary dynamics, hence it takes longer for the fittest trait to be selected. Furthermore, the model is restricted to values $y \leq 1$, hence the theoretical

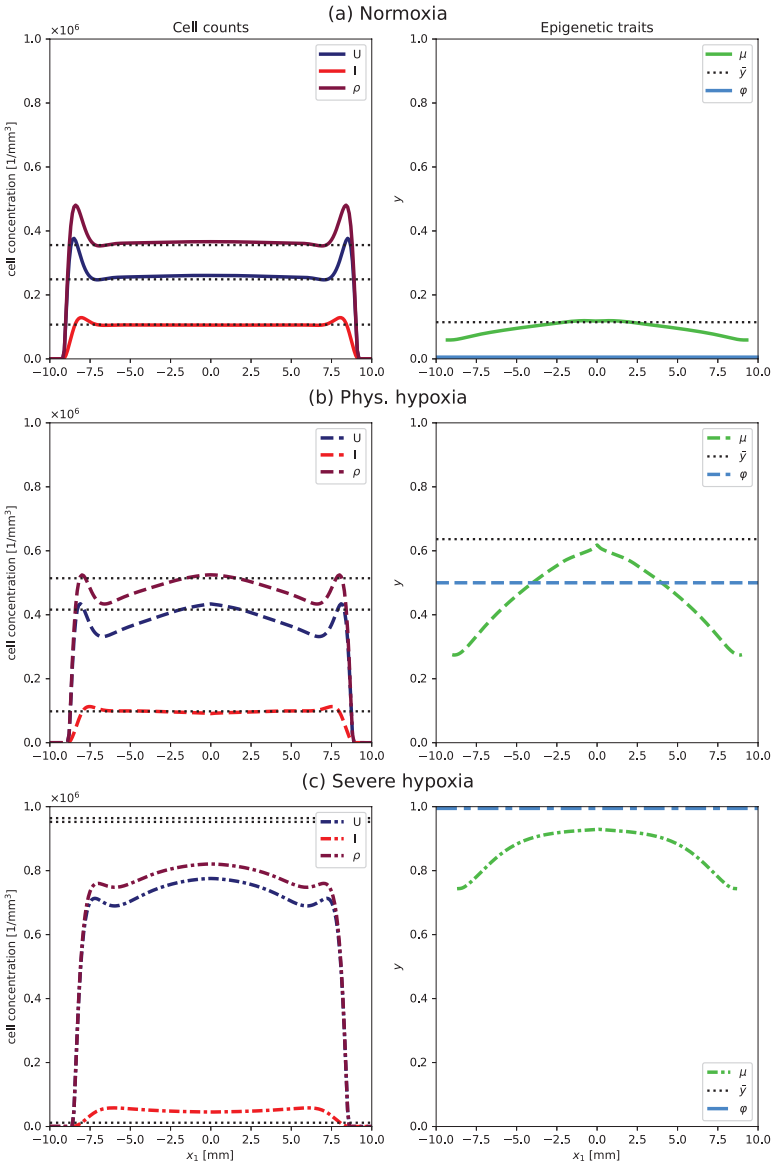

FIGURE 5.3: Results of the numerical simulations for stationary oxygen at time t^*, corresponding to approximately 1800 h after viral injection, for three spatially homogeneous oxygen conditions: $O = O_M$ (solid lines, panel (a)), $O = \frac{O_M + O_m}{2}$ (dashed lines, panel (b)), and $O = O_m$ (dot-dashed lines, panel (c)). Only the horizontal section is shown to facilitate the comparison. The first column shows $U(t^*, \boldsymbol{x})$ in blue, $I(t^*, \boldsymbol{x})$ in red, and $\rho(t^*, \boldsymbol{x})$ in purple. The second column provides the average epigenetic trait $\mu(t^*, \boldsymbol{x})$ in green and $\varphi(O(t^*, \boldsymbol{x}))$ in light blue. The black lines show the theoretical approximation of asymptotic equilibria, obtained by solving Eq. (5.21); in panel (c), $\bar{y}(t^*, \boldsymbol{x})$ is not shown, as it is higher than 1.

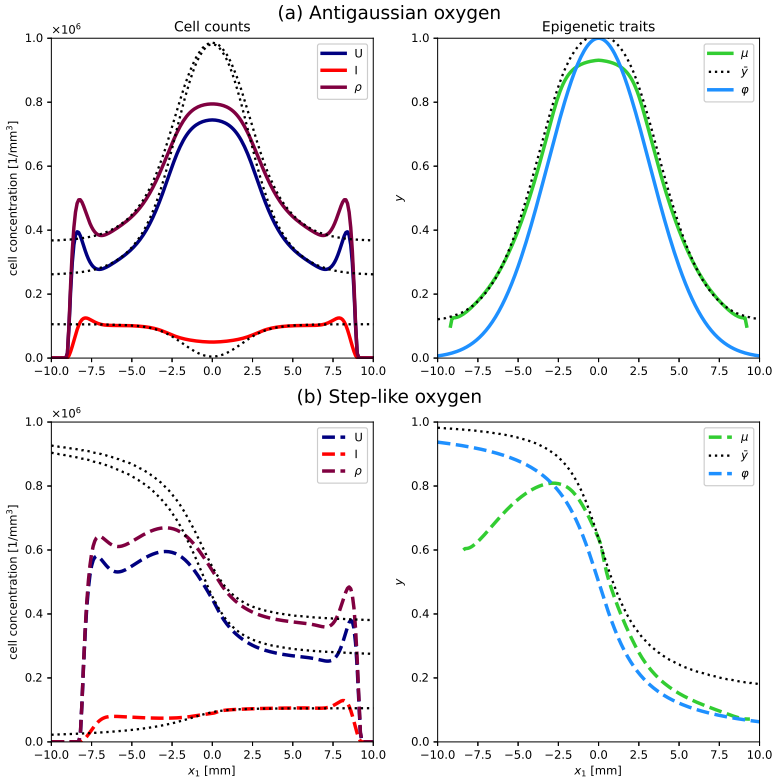

FIGURE 5.4: Results of the numerical simulations for stationary oxygen with antigaussian and step-like profiles at time t^* corresponding to approximately 1800 h after viral injection. Only the horizontal section is shown to facilitate the comparison with the equilibria. All the graphical elements have the same meaning as in Fig. 5.3.

value $\bar{y} > 1$ is unattainable; the convergence to 1 necessarily takes place from below and this makes the uninfected population more susceptible to the infection. We remark that longer numerical simulations confirm the convergence towards 1 with the associated cell densities (not shown). However, the equilibrium is reached only after a very long time; therefore, from the application point of view, we should note that the treatment outcome is slightly better than expected (although still unsuccessful).

Inhomogeneous oxygen distribution We now increase the model complexity by considering spatial homogeneities of the oxygen. We consider the following oxygen spatial profiles:

1. $O(\boldsymbol{x}) = O_m + (O_M - O_m)e^{\frac{|\boldsymbol{x}|^2}{20}}$ (antigaussian);
2. $O(\boldsymbol{x}) = O_m + \left[\frac{1}{2} + \frac{1}{\pi}\arctan\left(\frac{x_1}{2}\right)\right](O_M - O_m)$ (step-like profile).

The first profile is chosen to qualitatively resemble the oxygen distribution obtained after the tumour's consumption and we expect to observe dynamics that are somehow similar to the ones described below when we drop the stationarity assumption. The second one represents a tumour that grows at the boundary between two regions with significantly different vascularisation.

The numerical results of these two cases are shown in Fig. 5.4, along with the videos accompanying it (see electronic supplementary materials S3 and S4 of Morselli et al., 2024a),. We again represent the solutions approximately 1800 h after the viral injections, which take place respectively at times $t = 565$ h and $t = 470$ h. The extremely slow

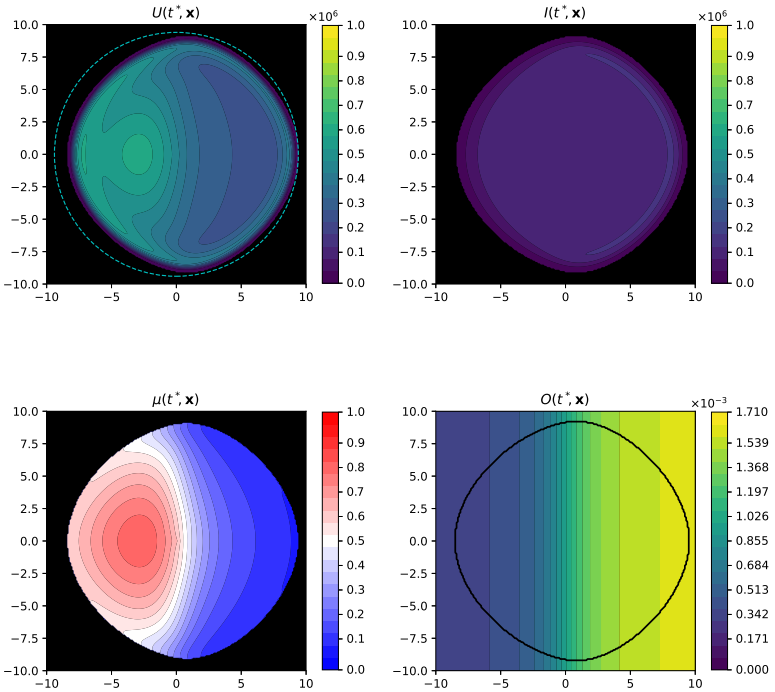

FIGURE 5.5: Results of the numerical simulations for stationary oxygen with step-like profile at time t^* corresponding to approximately 1800 h after viral injection. We now show the densities in the whole domain to highlight the anisotropy. The circle in the plot of $U(t^*, \boldsymbol{x})$ is centred in $(0, 0)$ and the radius is the distance from the origin of the furthest point $\boldsymbol{x}$ such that $\rho(t^*, \boldsymbol{x}) > 0$. On the other hand, the dark line in the plot of $O(t^*, \boldsymbol{x})$ encloses the region in which $\rho(t^*, \boldsymbol{x}) > 0$.

growth in the first situation is due to the severely hypoxic conditions that characterise the initial phase: although this is probably unrealistic, later dynamics appear more comparable to biologically meaningful scenarios. In both cases, we observe behaviours coherent with the previous findings, with the invasion led by slightly more proliferative cells and the slower convergence to the theoretical equilibrium in the hypoxic areas. The significance of these situations is the emergence of new selective dynamics that occur when the tumour reaches areas with different oxygen levels: in this respect, the effectiveness of virotherapy differs significantly from point to point.

Another significant aspect is the nonsymmetrical configuration of the step-like profile, which allows us to analyse the influence of the oxygenation on the invasion speed. Fig. 5.5 shows the simulation result in the whole domain. It is clear that the average epigenetic trait at the front significantly differs in different directions. We recall that, in the case of pressure-driven movement, the invasion speed is higher for high cell proliferation rate and high cell density. In the case of our interest, fast proliferation is associated with effective viral infection, which results in a lower cell density: as a consequence, a priori, it is not trivial to understand which conditions are associated with a faster invasion. The circle in Fig. 5.5 elucidates this aspect by showing that the fastest invasion still occurs in the most oxygenated area.

5.3.3 Inclusion of oxygen dynamics

In the previous section, we started with a basic model with homogeneous and stationary oxygenation, considering different concentration levels; we subsequently included complexity in the model by considering spatial heterogeneity. We now continue this progressive enrichment of the model toward realistic biological scenarios and consider

the whole dynamics of Eq. (5.9), in which oxygen varies both in space and time according to Eq. (5.8). A spatially heterogeneous oxygen source allows us to consider vessels of different sizes and, thus, with variable blood flow.

We consider a source of the form

$$Q(\boldsymbol{x}) = q_O \bar{O}(\boldsymbol{x})$$

where $\bar{O}(\boldsymbol{x})$ is the oxygen profile that we would observe in the absence of the tumour. We remark that the actual oxygen distribution is always below these values due to the increased oxygen consumption of cancer cells. We consider the following oxygen profiles:

1. $\bar{O}(\boldsymbol{x}) = O_M$ (normoxia);
2. $\bar{O}(\boldsymbol{x}) = 3\,O_m$ (hypoxia);
3. $\bar{O}(\boldsymbol{x}) = 3\,O_m + \left[\frac{1}{2} + \frac{1}{\pi}\arctan\left(\frac{x_1}{2}\right)\right](O_{\max} - 3\,O_m)$ (step-like source).
4. $\bar{O}(\boldsymbol{x}) = 3\,O_m + (O_M - 3\,O_m)\sum_{k=1}^{3} e^{-\frac{|\boldsymbol{x}-\boldsymbol{x}_k|^2}{15}}$ with $\boldsymbol{x}_1 \coloneqq (-4,4)$, $\boldsymbol{x}_2 \coloneqq (3,-6)$ and $\boldsymbol{x}_3 \coloneqq (6,-3)$ (source with three peaks).

The homogeneous sources aim at reproducing uniformly vascularised tissues, which, in the absence of a tumour, are either normoxic or physiologically hypoxic. The step-like source models a tissue with two distinguishable areas due to different oxygen inflow rates. Finally, the last source profile constitutes an example of a tissue in which heterogeneous vascularisation leads to a varied oxygen profile.

We use as initial condition $O_0(\boldsymbol{x})$ the steady state of Eq. (5.8), i.e., the solution of the equation

$$D_O \Delta O(t,\boldsymbol{x}) - q_O O(t,\boldsymbol{x}) - \lambda \rho(0,\boldsymbol{x}) O(t,\boldsymbol{x}) + Q(\boldsymbol{x}) = 0$$

where $\rho(0,\boldsymbol{x}) = \int_\Omega u_0(x,y)\,\mathrm{d}y$ and u_0 is given in Eq. (5.23). We remark that our parameter choice allows to have the same values of $\rho(0,\boldsymbol{x})$ for all y_0; as a consequence, it still makes sense to define $y_0 = \varphi(O_0(\mathbf{0}))$.

The results are collected in Figs. 5.6 and 5.7, along with the videos accompanying it (see electronic supplementary materials S5, S6, and S7 of Morselli et al., 2024a),. The arrangement of plots in Fig. 5.6 is analogous to Fig. 5.3, with the inclusion of $\varphi(O(0,\boldsymbol{x}))$ in the right panels: this allows to quantify the variation in time of the oxygen concentration due to tumour growth and the consequent evolution of the trait selected by environmental conditions. Fig. 5.7 shows the simulation result in the whole domain and highlights how the source heterogeneity affects the dynamics.

In all four cases, the initial tumour growth causes a drop in oxygen concentration, reducing the environmentally optimal epigenetic trait; consequently, the tumour growth progressively slows down. The variation of oxygen level is a new selective pressure, which could not be considered in the stationary oxygen situation. The dynamics in the centre of the tumour are characterized by a progressive adaptation, with the oxygen that reduces as the cell density grows and the average epigenetic trait that increases as the oxygen density decreases. We remark that in this initial phase, the actual fittest trait is always lower than the one selected by the environment due to the distance from carrying capacity; as time passes, this difference becomes less evident. In the meantime, the invasion fronts are more oxygenated, which contributes to the selection of proliferative traits in this area; this behaviour resembles the dynamics observed in the case of antigaussian stationary oxygen distribution. Spatial heterogeneity affects the invasion in the cases of step-like and multiple peak sources.

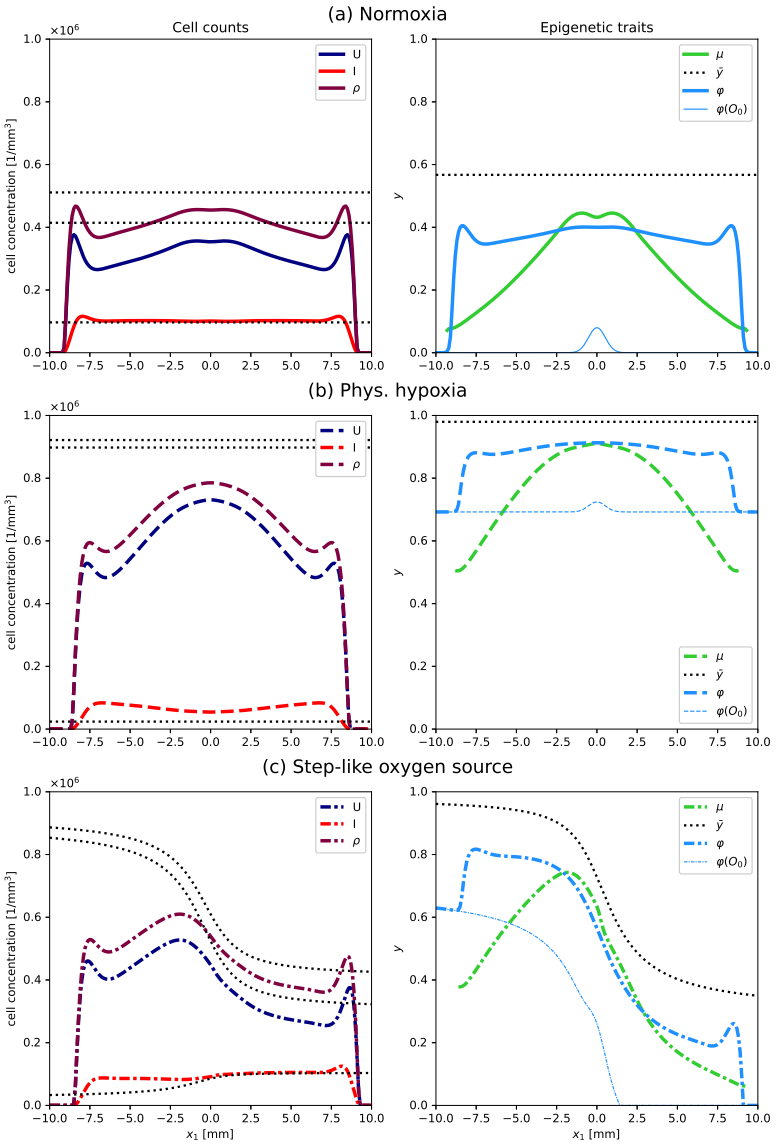

FIGURE 5.6: Comparison of the results obtained from numerical simulation of the full model at time t^*, corresponding to approximately 1800 h after viral injection. Three spatial oxygen conditions are considered: normoxia (solid lines, panel (a)), hypoxia (dashed lines, panel (b)), and step profile (dot-dashed lines, panel (c)). For explicit formulation, see the main text. All the graphical elements have the same meaning as in Fig. 5.3. In addition, a thinner light blue line in the right panels provides the φ profile at the initial state. The equilibria are now computed from Eq. (5.19).

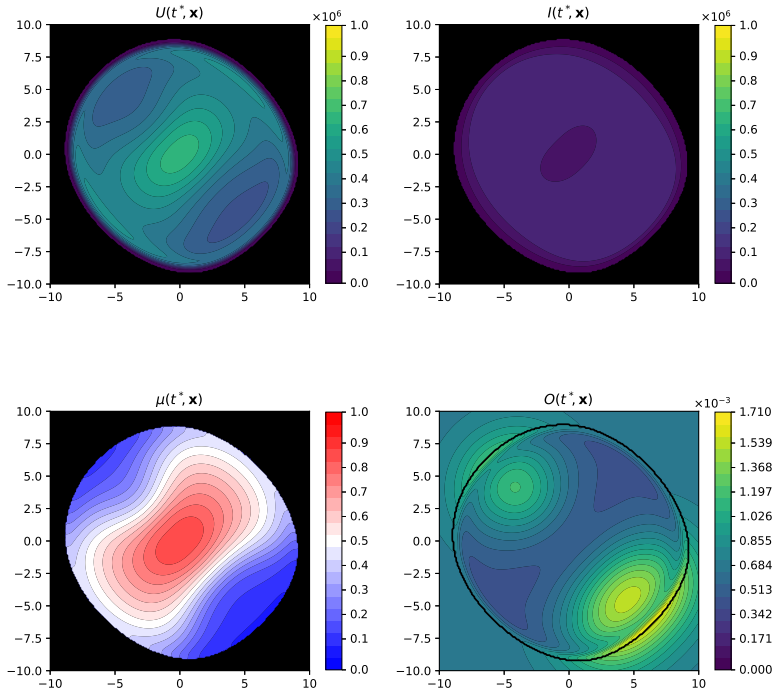

FIGURE 5.7: Results of the numerical simulation for the full model with oxygen source with three peaks at time t^* corresponding to approximately 1800 h after viral injection. We now show the densities in the whole domain to highlight the anisotropy. The dark line in the plot of $O(t^*, \boldsymbol{x})$ encloses the region in which $\rho(t^*, \boldsymbol{x}) > 0$.

As with stationary oxygen, the viral injection constitutes an additional selective pressure. The virotherapy causes a significant decrease in the cancer population, which allows the reoxygenation of the tissue. Nevertheless, the initial selective pressure of the infection appears more relevant than the environmental pressure, and the average epigenetic trait significantly increases. As time passes, the infection is more effective in the well-oxygenated areas: this keeps the cancer population low and avoids an excessive reduction in the oxygen concentration, which would result in a less effective infection. Conversely, in the less oxygenated areas, the tumour grows up to close to carrying capacity; hence, the oxygen concentration reduces further and the environmental conditions contribute to the selection of cells resistant to the infection.

Fig. 5.6 shows that the solutions of the equation approach the theoretical estimates, but the convergence is slower than in the case of stationary oxygen. This is particularly evident in the hypoxic areas due to the slow evolutionary dynamics related to the low growth rate, as already observed for stationary oxygen, and it is now accentuated by the fact that it takes time for the oxygen distribution to reach equilibrium. Furthermore, our tools do not allow to characterise the wavefront, whose dynamics are significantly far from equilibrium. Nevertheless, the theoretical values still provide significant information regarding the success of the therapy.

Overall, the main dynamics observed in Subsection 5.3.2 can be replicated without fixing a priori the oxygen distribution (which is not representative of realistic biological scenarios); oxygen dynamics significantly enriches the evolutionary dynamics. Initial condition referable as normoxic (Fig. 5.6a) or physiologically hypoxic (Fig. 5.6b) in the absence of the tumour become respectively physiologically and severely hypoxic due to cancer: in this sense, these two settings can be considered as a "trait d'union" with the previous simulations. Similar dynamics can also be observed in the presence of more complex oxygen sources, such as the three-peaked source of Fig. 5.7: this suggests that

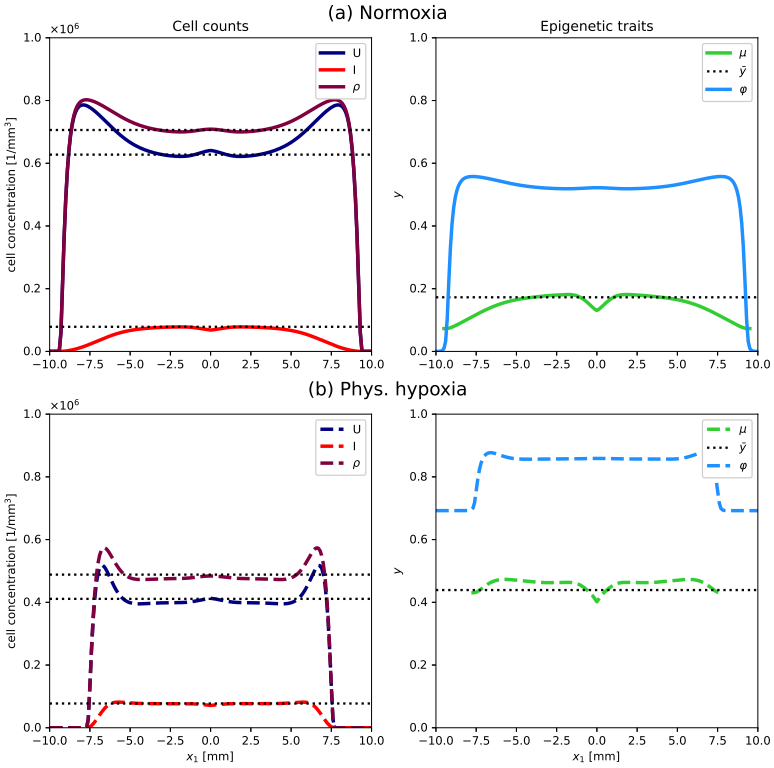

FIGURE 5.8: Comparison of the results obtained from numerical simulation of the full model in the case of hypoxia-targeting oncolytic viruses at time t^*, corresponding to approximately 1500 h after viral injection. We now consider an earlier time than in the previous simulations, as the infection in this case promotes the selection of more proliferative cells and, at later times, we would observe boundary effects in the normoxic case. Two spatial oxygen conditions are considered: normoxia (solid lines, panel (a)) and hypoxia (dashed lines, panel (b)); the oxygen sources are the same as in Figs. 5.6a-b. All the graphical elements have the same meaning as in Fig. 5.3.

the knowledge of the oxygen distribution in a tumour may predict the outcome of the virotherapy in clinical settings.

5.3.4 Hypoxia-specific oncolytic viruses

All the simulations presented so far rely on the assumption that viral infection is less effective in hypoxic cells: this can be explained by their slower metabolic activity, which also affects the translation of viral proteins (Sheng Guo, 2011). Nevertheless, one should note that some particular oncolytic viruses can specifically target receptors that are upregulated in case of the lack of oxygen (Sadri et al., 2023; Sheng Guo, 2011). This property appears particularly promising in light of the ineffectiveness of most classic cancer therapies in hypoxic conditions (Zhuang et al., 2023).

Therefore, we revert the previous trade-off and exchange the values of β_M and β_m, so that the function $\beta(y)$ is increasing; the rest of the model remains unchanged. The asymptotic analysis of Section 5.2 does not rely on any characterisation of the values of β and all the equations obtained are still valid: the only relevant difference is the fact that Eq. (5.20) now predicts a decrease of the fittest value in the presence of viral infection. The equilibrium values depicted in Fig. 5.1b indeed shows that the virotherapy's effectiveness increases as the oxygen concentration decreases, in line with the biological situation we aim to model.

Fig. 5.8, along with the video accompanying it (see electronic supplementary material S8 of Morselli et al., 2024a), shows the full model results for the oxygen sources

corresponding to normoxia and hypoxia. In the case of normoxia (Fig. 5.8a), we observe the failure of the therapy: despite the persistence of the infection, the uninfected cell density is now approximately twice the value observed in Fig. 5.6a; furthermore, the expansion of the tumour is much faster than in the case of virotherapy with standard viruses that target non-hypoxic cells. Both these phenomena are caused by the fact that viral infection selects cells with a value of the epigenetic trait lower than the one selected by environmental conditions alone, which are both more proliferative and more resistant to the infection. Interestingly, the results are not trivial: indeed, a priori, one could expect that the hypoxic condition caused by the tumour growth would be associated with a large number of hypoxic cells, which are effectively targeted by the virus. Our mathematical model is thus helpful to shed light on these complex interactions.

The situation of physiological hypoxia appears much more promising (Fig. 5.8b). Again, we observe a decrease in the average epigenetic trait caused by virotherapy, as expected from the theoretical results; consequently, the tumour's invasion speed is also higher. Nevertheless, the cell lines selected are not too resistant to the infection and the tumour cell density appears comparable to that observed in the case of normoxia treated by a standard virus. The important consequence is that the effectiveness of oncolytic virotherapy can be increased by selecting the most appropriate kind of virus based on the oxygenation of the tumour.

The comparison between the two kinds of oncolytic viruses in the case of physiological hypoxia is further elucidated in Fig. 5.9, in which we consider the total number of cancer cells in the domain

$$M(t) := \int_\Omega \rho(t, \boldsymbol{x}) \, \mathrm{d}\boldsymbol{x}$$

We also consider the evolution in time of the proportion of cells killed by environmental selection and the proportion of tumour cells infected at a given instant, respectively

$$\Gamma_S(t) := \frac{\eta}{M(t)} \int_Y \int_\Omega (y - \varphi(O(t, \boldsymbol{x})))^2 u(t, \boldsymbol{x}, y) \, \mathrm{d}\boldsymbol{x} \, \mathrm{d}y,$$
$$\Gamma_I(t) := \frac{1}{M(t)} \int_Y \int_\Omega \beta(y) u(t, \boldsymbol{x}, y) v(t, \boldsymbol{x}) \, \mathrm{d}\boldsymbol{x} \, \mathrm{d}y$$

In all cases, the main contribution to cell death is caused by viral infection, meaning that the therapy is always at least partially effective. The solid lines refer to the situation in which the oxygen concentration is not affected by the tumour and allow us to understand the role of oxygen dynamics; for the sake of brevity, this simulation is only performed in the case $\beta_m < \beta_M$. The comparison with the analogous simulation of the full model (dashed lines) shows that more cells are killed by environmental selection in the case of variable oxygen: indeed, hypoxia exerts a more significant action when the tumour needs to adapt to an evolving environment. The viral infection is more efficient in the latter case since it takes a long time for the tumour to fully adapt to the hypoxic state and become resistant to the infection. When the hypoxia-specific virus is considered, the infection appears significantly more effective. It is also remarkable that the environmental selection is more relevant in the last situation: indeed, the value of $\bar{y}$ given by Eq. (5.20) is now much lower than $\varphi(O)$ (see again Figs. 5.6b and 5.8b), as for $\beta_M < \beta_m$ both terms in the square bracket are negative; in other words, the infection favours cells that are less resistant to hypoxia. We should therefore conclude that the therapeutic effectiveness is also due to environmental selection.

Although the use of hypoxia-selective oncolytic viruses appears promising, our findings also stress that tumour eradication is still far from achieved. Furthermore, the cell lines selected are the most proliferative; hence, if the viral infection stopped for

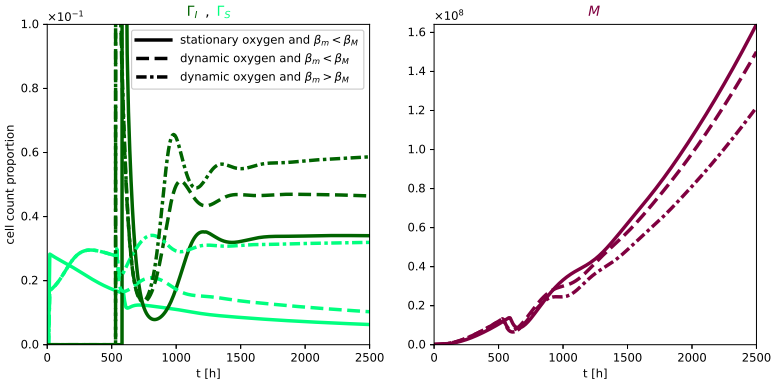

FIGURE 5.9: Comparison of the time evolution of the proportion of cells killed by environmental selection Γ_I, the proportion of tumour cells infected at a given instant Γ_S and the total number of cancer cells M in the cases of stationary oxygen and $\beta_m < \beta_M$ (solid lines), dynamic oxygen and $\beta_m < \beta_M$ (dashed lines), dynamic oxygen and $\beta_m > \beta_M$ (dot-dashed lines). In the case of stationary oxygen, the oxygen concentration is the equilibrium value of the corresponding model with dynamic oxygen (as depicted in the right panel of Fig. 5.6b), with the equilibria computed again from Eq. (5.19).

some external reason (such as immune response), the tumour would quickly regain its aggressiveness. Nonetheless, it is essential to observe that the average epigenetic trait is significantly reduced with respect to the one that environmental conditions would select; consequently, the tumour is now sensitive to standard treatments that lose their effectiveness in hypoxic conditions. This suggests that a hypoxic tumour could be effectively treated using a combination of therapies targeting cells with different degrees of adaptation to hypoxia (Sheng Guo, 2011).

5.4 Conclusions

In this chapter, we introduced a novel oncolytic virotherapy model that considers the epigenetic evolution of cancer cells due to viral infection and hypoxia. By integrating viral dynamics, tumour evolution, and spatial oxygen gradients, our model provides new insights into how hypoxic conditions within tumours affect the efficacy of oncolytic viral therapies. Numerical simulations are coherent with the theoretical results obtained by a formal asymptotic analysis of simplified settings and show how environmental conditions influence the capability of the virus to control tumour mass expansions and, in particular, underscore the significant impact of oxygen availability on viral infection rates, tumour cell susceptibility and the overall success of virotherapy. We considered some simple configurations of oxygen sources to capture the fundamental dynamics. Our results suggest that hypoxia may constitute a significant obstacle to the success of oncolytic virotherapy. Furthermore, the infection contributes to selecting a subpopulation of cells well adapted to hypoxia, which may be hard to kill even with other therapies. Hypoxic tumours appear to be more effectively treated with oncolytic viruses specifically targeting hypoxic cells, although tumour eradication still appears hard to achieve.

Our findings highlight several crucial aspects for optimising virotherapy: the presence of hypoxic regions can severely limit the spread and replication of standard oncolytic viruses; in contrast, hypoxia-specific viruses are particularly effective in these areas. This suggests that therapeutic strategies need to account for spatial oxygen level variations. The evolutionary dynamics of tumour cells under hypoxic stress and virotherapy pressure can lead to the emergence of resistant phenotypes, indicating the need for adaptive treatment protocols that can mitigate resistance development. One critical takeaway is

the importance of considering the spatial heterogeneity of oxygen levels when designing and implementing oncolytic virotherapy protocols. The model predicts that hypoxia can significantly alter the distribution and effectiveness of viral therapy, thereby affecting overall treatment outcomes. Additionally, the role of tumour cells' adaptation to hypoxic conditions highlights the necessity for dynamic treatment strategies that can respond to changes in the tumour microenvironment.

The key assumption of this work is that, in general, the slower metabolic activity of hypoxic cells is associated with a less effective viral infection. This has been modelled by considering an infection rate β that depends on the adaptation of cells to hypoxia. Our choice is motivated by the existing literature (Lorenzi et al., 2021b) and the possibility of obtaining some theoretical insights. Other approaches would also be possible: for example, one may directly consider the dependence of viruses on the host translational machinery to translate viral proteins; this would correspond to a viral burst size α that depends on the oxygen concentration or on the level of metabolic activity of the cell (which could correspond to the variable y).

There are several promising directions for future research and the results may be extended in several ways, both from the mathematical and the modeling perspectives. From the mathematical point of view, the formal asymptotic analysis of Section 5.2 may constitute a good starting point for characterising the travelling waves shown in the numerical simulations, at least in simplified settings (as already mentioned in the conclusion of Chapter 4). From a biological point of view, we aim to develop a model to study the interaction of oncolytic virotherapy and radiotherapy, which aligns with the clinical interest of combining the two therapies. Radiotherapy is well-known to decrease its effectiveness in hypoxic conditions and several mathematical models similar to the one in the present work have been developed to investigate this phenomenon (Celora et al., 2021; Chiari et al., 2023a). Although the combination with oncolytic viruses that decrease their efficacy due to hypoxia does not appear beneficial, using hypoxia-targeting oncolytic viruses could be promising.

Overall, our work contributes to a deeper understanding of the complexities of oncolytic virotherapy under hypoxic conditions and lays the groundwork for developing more effective and personalised cancer treatments. In this context, mathematical models could help design the optimal combination, considering contemporary, subsequent, or alternating treatments and investigating doses, orders and timing according to the environmental conditions.

As a final remark, we observe that the effects of hypoxia on the tumour's development involve several aspects and are not restricted to therapies. Indeed, the next chapter is devoted to the effects on cells' migratory abilities.

6 A novel heterogeneity-based hybrid modelling approach for EMT in tumours

In this chapter, we describe a theoretical/computational approach that allows characterising cells both at the *genotypic* and at the *phenotypic* level. In other words, each value of a variable is set to correspond to a given sequence of genes, which determines the cell's potential. A distinct *mathematical representation*, i.e., pointwise/discrete or density-based/continuous, is instead employed to distinguish cells with respect to their (possibly dichotomic) phenotype/effective behaviour, which is established by gene transcription and, therefore, expression levels. In this respect, the subpopulation of cells with a given phenotype is represented by a set of particles, whereas the remaining group of individuals, characterised by the alternative phenotype, is represented by a continuous density function. The phenotype corresponds to the actual behaviour within the range of the possibilities that the genotype allows: as a consequence, the cell's behaviour is primarily affected by the phenotype and the actual performance is regulated by its potential.

By defining a bubble function that represents a plausible spatial distribution of the mass of a single individual, we then implement the passage between the two descriptive instances. This strategy, firstly proposed in Colombi et al., 2017; Scianna and Colombi, 2017, allows to model the phenomenon of *phenotypic plasticity*, that is, the ability of cells to switch back and forth among multiple phenotypes while maintaining unaltered their genotype (Holzel et al., 2012). In particular, we here assume that phenotypic conversions are triggered by environmental signals, dependent on cell genetic traits and affected by randomness. Including the last aspect represents a significant novelty with respect to the previously-cited works (Colombi et al., 2017; Scianna and Colombi, 2017).

The proposed modelling approach is able to capture and represent genetic and phenotypic heterogeneity among a given system of cells, as well as selected mechanisms underlying phenotypic plasticity. Therefore, its possible applications span a broad spectrum of phenomena since the evolution of aggregates of cells, from small clusters to large populations, is typically determined by cooperative dynamics and interactions between the component individuals differing both at the DNA and the protein level. For instance, in most collective cell movement, few specialised individuals, able to sense environmental chemical signals, typically behave as a patterning guidance for the rest of the system, which instead passively displaces only due to adhesion (see Ilina and Friedl, 2009; Khalil and Friedl, 2010 and the references therein). It is the case of angiogenic processes, where a small number of endothelial cells forming the walls of pre-existing vessels acquire a leader/tip phenotype, representing migratory cues for the neighbouring individuals with a follower/stalk behaviour (Boareto et al., 2016). These mechanisms are triggered by several diffusing growth factors (e.g., vascular endothelial growth factor – VEGF, hepatocyte growth factors – HGF) and mediated by the well-known Delta-Notch signalling pathways (Liu et al., 2013; Williams et al., 2006). Similarly, during skin repair after injury, the cells located at the front of the epidermal monolayers that invade the wounded region are characterised by actin-rich lamellipodia and pseudopodia, which

allow active movement, and are able to synthesise a new basement membrane, whereas individuals at the rear regions only passively displace dragged by cell–cell adhesive interactions.

This chapter focuses on applying the modelling framework to tumour growth, with special emphasis on the *epithelial-to-mesenchimal transition (EMT)*. Genome instability is among the *hallmarks of cancer* described in Section 1.1 and the altered gene expression affects cellular behaviour. We consider three different sequences of genes corresponding to three values of the trait variable; as explained above, this characterises a cell's potential abilities. On the other hand, phenotypic plasticity is often triggered by external signals that may come from neighbouring cells or from the surrounding environment; these signals evolve on a time scale much faster than genetic mutations and this justifies the employment of our modelling approach. We, therefore, model genotype and phenotype separately: genetic mutations are neglected and phenotypic switches correspond to a change in behaviour. We adopt a continuous description for *epithelial* cells, which are characterised by a high proliferative ability and undergo slow collective dynamics mainly guided by intercellular communication. *Mesenchymal* cells are instead described individually and this allows us to easily track their individual directional movement in response to environmental cues; their poor miotic activity allows us to neglect their reproduction. These assumptions give rise to a 3×2 matrix of cell behaviours (see also Fig. 6.4a).

This chapter is organised as follows. In Section 6.1, we introduce the main model ingredients and present a sample numerical realisation that shows how the procedure for the phenotypic switch works. In Section 6.2, we apply our approach to the representative case of a heterogeneous tumour aggregate evolving in an oxygen-deprived domain. In Section 6.3, we finally give some conclusive remarks and hints for further model developments.

The model described in this chapter and the results shown have been published in Chiari et al., 2022.

6.1 Proposed approach and representative simulation

We are interested in modelling the evolution of an aggregate of cells within a closed two-dimensional domain $D \subset \mathbb{R}^2$, whose dynamics are studied for the period $T = [0, t_F] \subset \mathbb{R}_0^+$, t being the time variable. The spatial domain D may reproduce, for instance, a planar section of an *in vivo* tissue or the surface of a *Petri dish*, usually employed in experimental studies.

The cells composing the system are here differentiated according to two determinants, as sketched in Fig. 6.1a:

- their *genotype*, by the use of a *discrete trait variable* u;
- their *phenotype*, by the use of different *mathematical representations*.

Our approach is indeed based on the assumption that there is not a deterministic and/or necessary relation between the genetic trait of a cell and its phenotype: the latter is, in fact, determined at the protein level, i.e., by effective gene transcription and expression levels, which are eventually affected by stochasticity and extracellular/environmental stimuli and conditions (by the so-called surrounding *ecology*).

The structuring variable u is set to assume a given number of values, say K, i.e., $u \in U = \{u_k\}_{k=1}^K$. In this respect, the generic state $u_{\hat{k}}$ defines the cell clone characterised by the $\hat{k}$-th genetic makeup, i.e., by the $\hat{k}$-th sequence of genes.

We then consider two alternative cell phenotypes, say "A" and "B", and associate each of them to a distinct mathematical descriptive instance, as proposed in Colombi et al., 2017; Scianna and Colombi, 2017. In particular, for a given cell variant with genotypic trait $u_{\hat{k}} \in U$, the individuals that show phenotype A have a *discrete* representation: they are reproduced with dimensionless points with concentrated unitary mass and identified by their actual position in space (see Fig. 6.1a). Such subgroup of agents can be indeed collected in the following set:

$$\boldsymbol{X}^{\mathrm{A}}_{u_{\hat{k}}}(t) = \left\{ \boldsymbol{x}_{1,u_{\hat{k}}}(t), \ldots, \boldsymbol{x}_{N^{\mathrm{A}}_{u_{\hat{k}}}(t),u_{\hat{k}}}(t) \right\} \tag{6.1}$$

with $\boldsymbol{x}_{i,u_{\hat{k}}}(t) \in D$, for $i = 1, ..., N^{\mathrm{A}}_{u_{\hat{k}}}(t)$, being $N^{\mathrm{A}}_{u_{\hat{k}}}(t)$ the number of cells with phenotype A and genotype $u_{\hat{k}}$ at time t. The overall amount of individuals with phenotype A within the entire aggregate can be, therefore, computed as

$$N^{\mathrm{A}}(t) = \sum_{k=1}^{K} N^{\mathrm{A}}_{u_k}(t) \tag{6.2}$$

The remaining part of the clone of cells with the $\hat{k}$-th genetic trait is instead characterised by phenotype B and *collectively* described by the number density function

$$a^{\mathrm{B}}(t, \boldsymbol{y}, u_{\hat{k}}) \colon T \times D \times U \mapsto \mathbb{R}^{+}_{0}$$

as shown in Fig. 6.1a. The local amount of individuals with phenotype B can be, therefore, evaluated as

$$\rho^{\mathrm{B}}(t, \boldsymbol{y}) = \sum_{k=1}^{K} a^{\mathrm{B}}(t, \boldsymbol{y}, u_k) \tag{6.3}$$

In this respect, $a^{\mathrm{B}}(t, \boldsymbol{y}, \cdot)$ can be interpreted as the local distribution of cells with phenotype B on the genotype space U. The overall number of agents with phenotype B actually present within the entire domain D can be then approximated by integrating ρ^{B} along the space variable and rounding the obtained value to the lower integer:

$$N^{\mathrm{B}}(t) = \left\lfloor \int_{D} \rho^{\mathrm{B}}(t, \boldsymbol{y}) \, \mathrm{d}\boldsymbol{y} \right\rfloor \tag{6.4}$$

The total number of cells composing the aggregate at any given time t is finally equal to $N(t) = N^{\mathrm{A}}(t) + N^{\mathrm{B}}(t)$.

Remark 6.1 *For the sake of completeness, we now give some comments on the above-proposed modelling framework:*

- *The association between the different cell genetic makeups and the corresponding values of the variable u is arbitrary.*
- *The association between a cell phenotype and the corresponding mathematical representation is instead suggested by biological considerations. For example, the discrete description adopted for phenotype A is particularly suitable for active cells, while the collective description adopted for phenotype B is more appropriate for quiescent cells. In the next section, the two phenotypes are associated respectively to* mesenchymal *and* epithelial *cells: in this way, we can track the individual directional movement of mesenchymal cells and, at the same time, keep the computational cost of the simulation low by adopting a continuous description for the epithelial mass.*

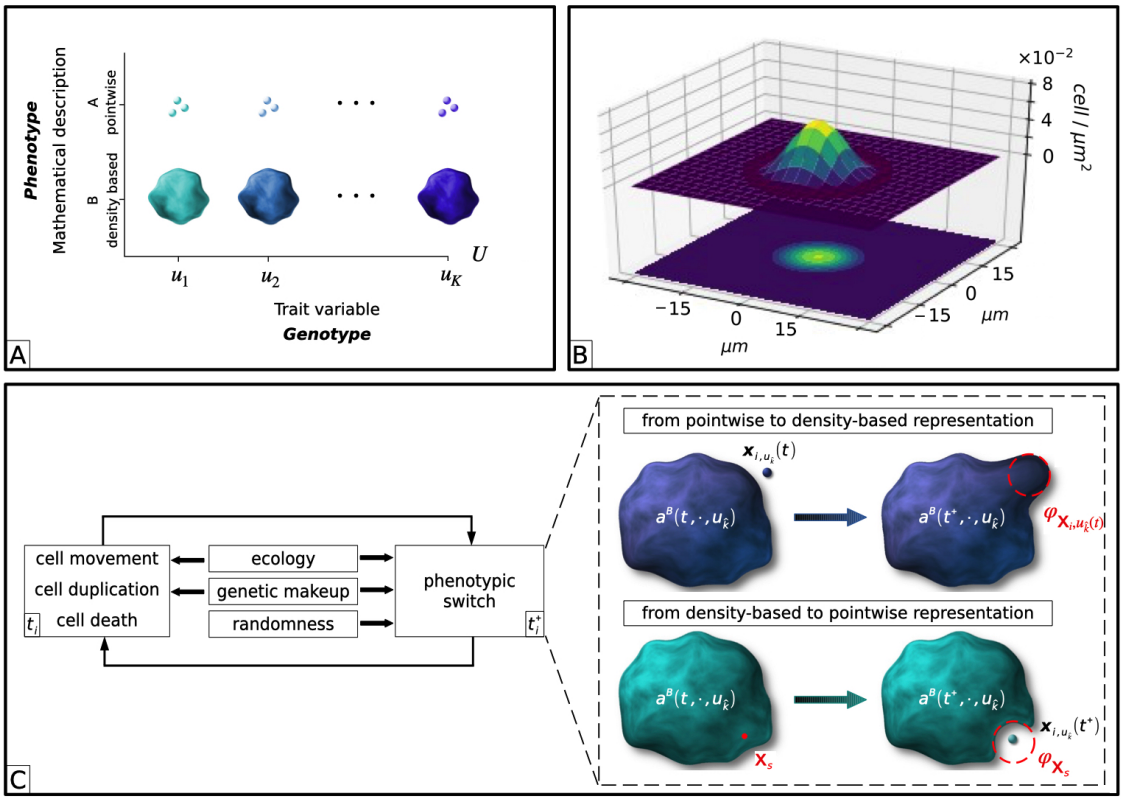

FIGURE 6.1: (a) In our modelling environment, each cell is differentiated for genotype, i.e., by the use of a discrete structuring variable $u \in U$, and for phenotype, i.e., by the use of a specific mathematical representation. In particular, we only consider two alternative individual phenotypes, which are set to correspond either to a pointwise or to a density-based descriptive instance. (b) For representative purposes, bi-dimensional and three-dimensional plots of the bubble function centred in $\boldsymbol{x} = (0,0)$, i.e., $\varphi_{(0,0)}$ (cf. Eq. (6.6)). We recall that the radius r of the round support of φ is constantly taken equal to 15 μm. (c) We here set that cell dynamics such as growth, migration, and phenotypic switches are affected both by individual genetic traits and by variations in environmental (i.e., ecological) conditions. Stochasticity plays a role as well. In particular, A-to-B phenotypic transition of the generic cell i with genotype $u_{\hat{k}}$ is implemented by the removal of the material point located in $x_{i,u_{\hat{k}}}$ and the simultaneous addition of the corresponding bubble function $\varphi_{x_{i,u_{\hat{k}}}}$ to the mass distribution $a^{\mathrm{B}}(\cdot,\cdot,u_{\hat{k}})$. Conversely, a B-to-A phenotypic switch, stimulated in the domain point x_{s} and involving the cell variant with genotype $u_{\hat{k}}$, amounts to the local creation of a new material point $x_{N^{\mathrm{A}}_{u_{\hat{k}}}(t)+1,u_{\hat{k}}}$ and in the simultaneous removal of the bubble function $\varphi_{x_{\mathrm{s}}}$ to the mass distribution $a^{\mathrm{B}}(\cdot,\cdot,u_{\hat{k}})$.

- *In principle, our approach could include more than two cell phenotypes. This would require the use of hybrid mathematical representations, i.e., able to account for a proper amount of microscopic granularity within a macroscopic/continuous description of the system of interest, which would be possible, for instance, by employing tools of Measure Theory (Colombi et al., 2014; Colombi et al., 2015).*

- *The proposed modelling environment is hybrid but not, so far, multiscale, in the sense that different mathematical objects (i.e., material points and number densities) are used together but represent biological elements at the same spatial scale, i.e., different types of cells.*

Modelling cell phenotypic plasticity In a wide range of biological phenomena, cells are able to change phenotype while maintaining their genetic makeup, i.e., to vary the expression level of one or more of their genes. To reproduce this phenomenon in our modelling framework, we need to set up a procedure to switch between the two cell

descriptive instances. It is indeed necessary to define a proper correspondence between the pointwise and the density-based representation of a single cell. In this respect, let us proceed as in Colombi et al., 2017; Scianna and Colombi, 2017 and introduce a function $\varphi_{\boldsymbol{x}}(\boldsymbol{y})\colon D \times D \mapsto \mathbb{R}_0^+$ such that:

$$\int_D \varphi_{\boldsymbol{x}}(\boldsymbol{y})\,\mathrm{d}\boldsymbol{y} = 1 \tag{6.5}$$

$\varphi_{\boldsymbol{x}}$ approximates the spatial distribution of a cell whose centre is located in $\boldsymbol{x} \in D$. In principle, there exist several possible options to explicit $\varphi_{\boldsymbol{x}}(\boldsymbol{y})$. However, in accordance with the already-cited works (Colombi et al., 2017; Scianna and Colombi, 2017), we hereafter use the following *bubble* function, which assumes a greater amount of cell mass around $\boldsymbol{x}$, as shown in Fig. 6.1b:

$$\varphi_{\boldsymbol{x}}(\boldsymbol{y}) = \begin{cases} \dfrac{4}{\pi r^8}(r^2 - |\boldsymbol{y}-\boldsymbol{x}|^2)^3 & \text{if } |\boldsymbol{y}-\boldsymbol{x}| \leq r \\ 0, & \text{otherwise} \end{cases} \tag{6.6}$$

In Eq. (6.6), $|\cdot|$ identifies the Euclidean norm while r is set to approximate a mean cell radius: hereafter, it will have a value of 15 μm.

Let us now assume that, at a certain time t, the i-th cell with phenotype A and genotype $u_{\hat{k}} \in U$ undergoes a transition to phenotype B. From a biological perspective, this may be the result of environmental stimuli (triggered by chemical signals or by intercellular communication) or of the fact that the individual i is able to maintain phenotype A only for a limited period of time (e.g., due to high metabolic costs). The proposed A-to-B phenotypic switch can be then implemented in our modelling framework by removing the material point located in $\boldsymbol{x}_{i,u_{\hat{k}}}(t)$ and by simultaneously adding the equivalent mass function $\varphi_{\boldsymbol{x}_{i,u_{\hat{k}}}(t)}$ to the density of the cell variant characterised by the same trait $u_{\hat{k}}$, as shown in Fig. 6.1c. In mathematical terms, we indeed get the following relations:

$$\begin{cases} \boldsymbol{X}^{\mathrm{A}}_{u_{\hat{k}}}(t^+) = \boldsymbol{X}^{\mathrm{A}}_{u_{\hat{k}}}(t) \setminus \{\boldsymbol{x}_{i,u_{\hat{k}}}(t)\} \\ \boldsymbol{X}^{\mathrm{A}}_{u_k}(t^+) = \boldsymbol{X}^{\mathrm{A}}_{u_k}(t), \quad \text{for all } k \neq \hat{k} \\ a^{\mathrm{B}}(t^+, \boldsymbol{y}, u_{\hat{k}}) = a^{\mathrm{B}}(t, \boldsymbol{y}, u_{\hat{k}}) + \varphi_{\boldsymbol{x}_{i,u_{\hat{k}}}(t)}(\boldsymbol{y}), \quad \text{for all } \boldsymbol{y} \in D \\ a^{\mathrm{B}}(t^+, \boldsymbol{y}, u_k) = a^{\mathrm{B}}(t, \boldsymbol{y}, u_k), \quad \text{for all } k \neq \hat{k};\ \text{ and }\ \boldsymbol{y} \in D \end{cases} \tag{6.7}$$

Finally, the remaining particles with phenotype A and genotype $u_{\hat{k}}$ are renumbered according to the rule

$$\boldsymbol{x}_{j,u_{\hat{k}}}(t^+) = \begin{cases} \boldsymbol{x}_{j,u_{\hat{k}}}(t), & \text{if } j < i \\ \boldsymbol{x}_{j-1,u_{\hat{k}}}(t), & \text{if } j > i \end{cases} \tag{6.8}$$

In Eqs. (6.7) and (6.8), as well as in the following, the notation t^+ is used to specify that, from a *numerical point of view*, phenotypic transitions are not simultaneously implemented with the other processes, e.g., cell movement, duplication, death, which occur at the same time instant (see also Colombi et al., 2017; Scianna and Colombi, 2017). The generalisation of the above procedure to more cells that actually switch from phenotype A to phenotype B, possibly with different genotypic traits, is straightforward.

Let us then conversely assume that, at time t, an environmental stimulus, which is in principle able to trigger a transition from phenotype B to phenotype A in individuals with the generic genotype $u_{\hat{k}} \in U$, is active in a given domain location, say $\boldsymbol{x}_{\mathrm{s}} \in D$. Such a switch can occur only if there is a sufficient density of the cell variant of interest to

have a localised agent placed in $\boldsymbol{x}_{\mathrm{s}}$. In mathematical terms, this amounts to satisfying the following local constraint:

$$a^{\mathrm{B}}(t, \boldsymbol{y}, u_{\hat{k}}) \geq \varphi_{\boldsymbol{x}_{\mathrm{s}}}(\boldsymbol{y}) \quad \text{for all } \boldsymbol{y} \in D \tag{6.9}$$

In this case, the cell phenotypic transition from B to A (and the corresponding representation switch) results from the removal of $\varphi_{\boldsymbol{x}_{\mathrm{s}}}$ from the distribution $a^{\mathrm{B}}(t, \cdot, u_{\hat{k}})$, accompanied by the addition of the corresponding new element to the set $\mathbf{X}^{\mathrm{A}}_{u_{\hat{k}}}$ (see Fig. 6.1c):

$$\begin{cases} \boldsymbol{X}^{\mathrm{A}}_{u_{\hat{k}}}(t^{+}) = \boldsymbol{X}^{\mathrm{A}}_{u_{\hat{k}}}(t) \cup \{\boldsymbol{x}_{N^{\mathrm{A}}_{u_{\hat{k}}}(t)+1, u_{\hat{k}}}(t) \equiv \boldsymbol{x}_{\mathrm{s}}\} \\ \boldsymbol{X}^{\mathrm{A}}_{u_k}(t^{+}) = \boldsymbol{X}^{\mathrm{A}}_{u_k}(t), \quad \text{for all } k \neq \hat{k} \\ a^{\mathrm{B}}(t^{+}, \boldsymbol{y}, u_{\hat{k}}) = a^{\mathrm{B}}(t, \boldsymbol{y}, u_{\hat{k}}) - \varphi_{\boldsymbol{x}_{\mathrm{s}}(t)}(\boldsymbol{y}), \quad \text{for all } \boldsymbol{y} \in D \\ a^{\mathrm{B}}(t^{+}, \boldsymbol{y}, u_k) = a^{\mathrm{B}}(t, \boldsymbol{y}, u_k), \quad \text{for all } k \neq \hat{k} \text{ and } \boldsymbol{y} \in D \end{cases} \tag{6.10}$$

Furthermore, the following rules are set:

- in the case of B-to-A phenotypic transitions involving the same cell clone, e.g., with genotype $u_{\hat{k}}$, and simultaneously stimulated in two distinct domain points $\boldsymbol{x}_{\mathrm{s}1}$ and $\boldsymbol{x}_{\mathrm{s}2}$ such that $\varphi_{\boldsymbol{x}_{\mathrm{s}1}}$ and $\varphi_{\boldsymbol{x}_{\mathrm{s}2}}$ overlap, two alternative options are accounted for: (i) if $a^{\mathrm{B}}(t, \boldsymbol{y}, u_{\hat{k}}) \geq \varphi_{\boldsymbol{x}_{\mathrm{s}1}}(\boldsymbol{y}) + \varphi_{\boldsymbol{x}_{\mathrm{s}2}}(\boldsymbol{y})$ for any $\boldsymbol{y} \in D$, then both behavioral switches occur; (ii) if, otherwise, $a^{\mathrm{B}}(t, \boldsymbol{y}, u_{\hat{k}}) \geq \varphi_{\boldsymbol{x}_{\mathrm{s}1}}(\boldsymbol{y}), \varphi_{\boldsymbol{x}_{\mathrm{s}2}}(\boldsymbol{y})$ but $a^{\mathrm{B}}(t, \boldsymbol{y}, u_{\hat{k}}) < \varphi_{\boldsymbol{x}_{\mathrm{s}1}}(\boldsymbol{y}) + \varphi_{\boldsymbol{x}_{\mathrm{s}2}}(\boldsymbol{y})$ for at least one domain point, then only one transition takes place, which is randomly established. The same rule is extended in the case of more than two phenotypic transitions with analogous characteristics;

- B-to-A phenotypic transitions are not allowed in any domain point effectively occupied by a pointwise agent (regardless of its genotype). Coherently, only one B-to-A phenotypic switch is allowed (and arbitrarily established) at the same time in the same domain point. These constraints are consistent with the observation that, in a wide range of phenomena, a cell that activates inhibits the surrounding individuals to undergo the same process. It is the case, for instance, of the tip cell selection and lateral inhibition mechanism controlled by the Delta-Notch pathways during physio-pathological angiogenesis;

- simultaneous B-to-A phenotypic switches occurring at far enough spatial regions are instead always permitted.

It is instead useful to remark that the above ones are rules that always contain a level of arbitrariness and can be, in principle, neglected and/or replaced by other assumptions.

Sample simulation Before including in the proposed modelling framework more realistic biological mechanisms and dynamics, let us propose and comment on a representative numerical realisation. It deals with a colony of cells which do not grow or move but only undergo arbitrarily selected phenotypic transitions. In more detail, in the spatial domain $D = [-150\ \mu\mathrm{m}, 150\ \mu\mathrm{m}]^2$, we place an aggregate whose component individuals can have three different genetic makeups, i.e., $U = \{u_1, u_2, u_3\}$, while showing the usual dichotomy in the phenotype, i.e., A and B. The initial system configuration is then given

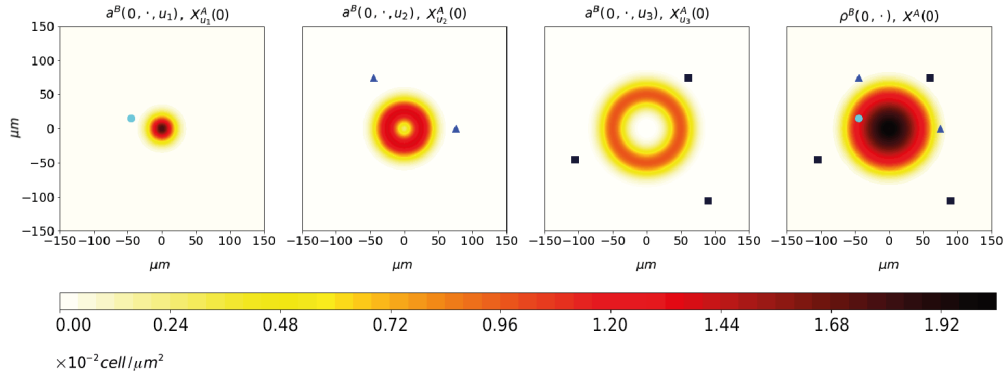

FIGURE 6.2: Initial condition of the representative simulation, as specified by Eq. (6.11). The subpopulation with phenotype B has a radial symmetry: in particular, the cell variant with genotype u_1 is mainly located at the bulk of the cluster, the cell variant with u_3 forms an external ring, whereas the cell variant with u_2 is distributed in the intermediate region. A group of individuals with phenotype A is then dispersed around and within the distribution of cells with phenotype B. In particular, we hereafter use light blue circles to indicate particles with phenotype A and genotype u_1, blue triangles to indicate particles with phenotype A and genotype u_2, and dark blue squares to indicate particles with phenotype A and genotype u_3. Such an initial cell configuration is maintained in the case of the model application proposed in Section 6.2.

by the following distribution of cells:

$$\begin{cases} \boldsymbol{X}^{\mathrm{A}}_{u_1}(0) = \{\, \boldsymbol{x}_{1,u_1} = (-45, 15) \,\} \\ \boldsymbol{X}^{\mathrm{A}}_{u_2}(0) = \{\, \boldsymbol{x}_{1,u_2} = (75, 0);\ \boldsymbol{x}_{2,u_2} = (-45, 75) \,\} \\ \boldsymbol{X}^{\mathrm{A}}_{u_3}(0) = \{\, \boldsymbol{x}_{1,u_3} = (60, 75);\ \boldsymbol{x}_{2,u_3} = (90, -105);\ \boldsymbol{x}_{3,u_3} = (-105, -45) \,\} \\ a^{\mathrm{B}}(0, \boldsymbol{y}, u_1) = 3.1\, m_\varphi \exp\left(-\dfrac{|\boldsymbol{y}|^2}{325}\right) \\ a^{\mathrm{B}}(0, \boldsymbol{y}, u_2) = 2.4\, m_\varphi \exp\left(-\dfrac{|\boldsymbol{y} - 25|^2}{325}\right) \\ a^{\mathrm{B}}(0, \boldsymbol{y}, u_3) = 1.7\, m_\varphi \exp\left(-\dfrac{|\boldsymbol{y} - 50|^2}{325}\right) \end{cases} \tag{6.11}$$

for all $\boldsymbol{y} \in D$, being $m_\varphi = 4/\pi r^8$ the maximum of the *bubble* function (cf. Eq. (6.6)), see Fig. 6.2. The overall number of cells at the onset of the simulation, which remains constant in time due to the absence of duplication/death mechanisms, amounts to:

$$\begin{aligned} N(0) &= N^{\mathrm{A}}(0) + N^{\mathrm{B}}(0) \\ &= [\boldsymbol{X}^{\mathrm{A}}_{u_1}(0)] + [\boldsymbol{X}^{\mathrm{A}}_{u_2}(0)] + [\boldsymbol{X}^{\mathrm{A}}_{u_3}(0)] + \left\lfloor \int_D \rho^{\mathrm{B}}(0, \boldsymbol{y})\, \mathrm{d}\boldsymbol{y} \right\rfloor \\ &= 6 + \left\lfloor \int_D \left(a^{\mathrm{B}}(0, \boldsymbol{y}, u_1) + a^{\mathrm{B}}(0, \boldsymbol{y}, u_2) + a^{\mathrm{B}}(0, \boldsymbol{y}, u_3) \right) \mathrm{d}\boldsymbol{y} \right\rfloor = 6 + 188 = 194, \end{aligned} \tag{6.12}$$

where $[Q]$ indicates the cardinality of a generic set Q.

At a given time t_1, an external input able to stimulate a switch from phenotype B to phenotype A for all cell clones, regardless of their genetic trait, activates in an arbitrary set of domain points, radially disposed along the main axies: $\boldsymbol{x}_{\mathrm{s}1} = (15, 0)$, $\boldsymbol{x}_{\mathrm{s}2} = (50, 0)$, $\boldsymbol{x}_{\mathrm{s}3} = (85, 0)$, $\boldsymbol{x}_{\mathrm{s}4} = (0, 15)$, $\boldsymbol{x}_{\mathrm{s}5} = (0, 50)$, $\boldsymbol{x}_{\mathrm{s}6} = (0, 85)$, $\boldsymbol{x}_{\mathrm{s}7} = (-15, 0)$, $\boldsymbol{x}_{\mathrm{s}8} = (-50, 0)$, $\boldsymbol{x}_{\mathrm{s}9} = (-85, 0)$, $\boldsymbol{x}_{\mathrm{s}10} = (0, -15)$, $\boldsymbol{x}_{\mathrm{s}11} = (0, -50)$, and $\boldsymbol{x}_{\mathrm{s}12} = (0, -85)$, see top panels in Fig. 6.3. In this respect:

- no transition takes place in $\boldsymbol{x}_{\mathrm{s}3}$, $\boldsymbol{x}_{\mathrm{s}6}$, $\boldsymbol{x}_{\mathrm{s}9}$, and $\boldsymbol{x}_{\mathrm{s}12}$ due to the lack of sufficient mass density of any cell genetic variant;

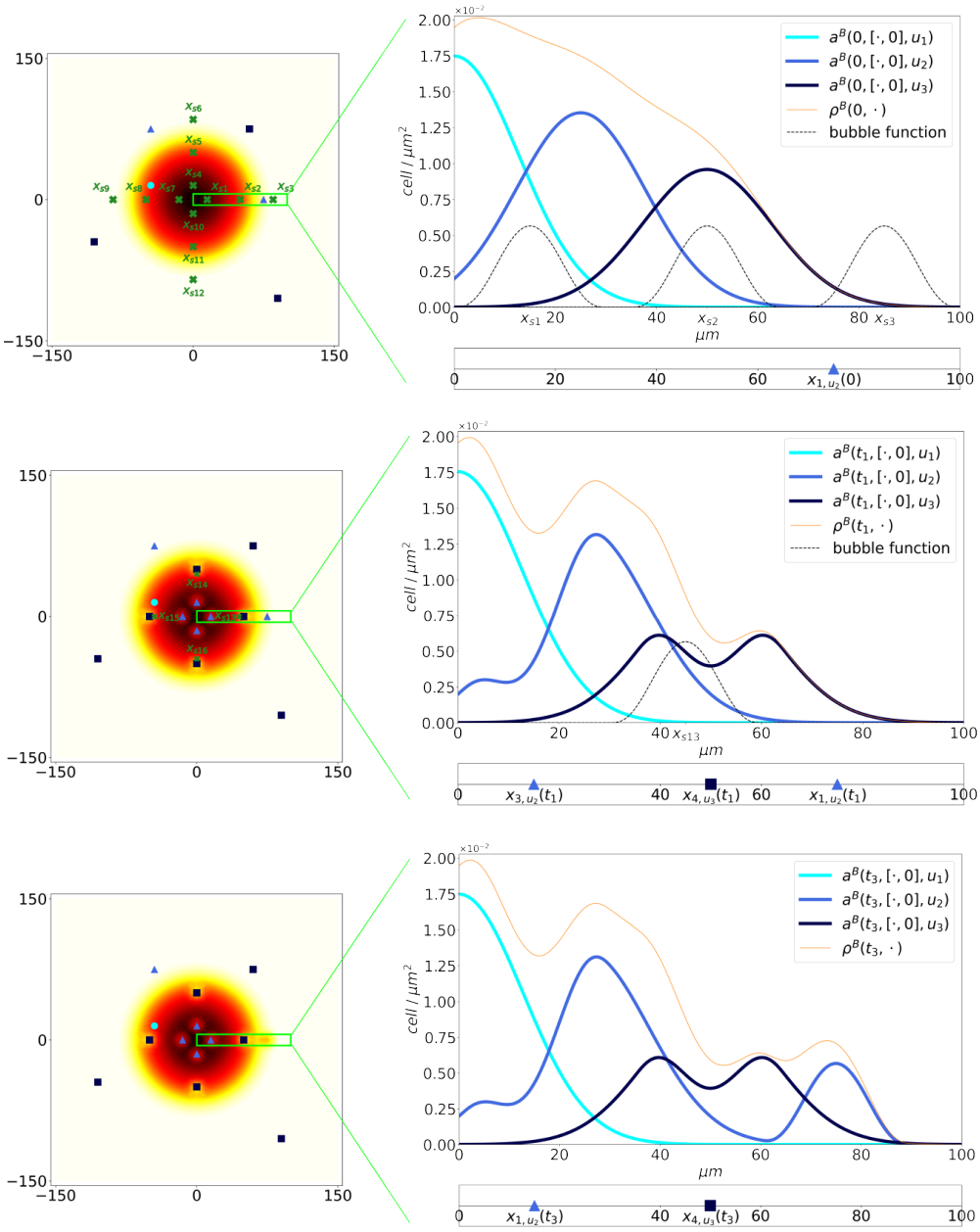

FIGURE 6.3: Sample simulation showing how phenotypic switches are implemented in the proposed modelling environment. In the left panels, we represent the evolution of the entire aggregate of cells: in particular, we plot both the overall density of the subpopulation with phenotype B, i.e., ρ^{B} (cf. Eq. (6.3)), and the set of particles with phenotype A. Within this subgroup, the light blue circles identify cells with genotype u_1, the blue triangles cells with genotype u_2, and the dark blue squares cells with genotype u_3. The right panels show the enlarged dynamics of a representative section of the domain.

- in $\boldsymbol{x}_{\mathrm{s2}}$, $\boldsymbol{x}_{\mathrm{s5}}$, $\boldsymbol{x}_{\mathrm{s8}}$, $\boldsymbol{x}_{\mathrm{s11}}$, only the subpopulation with genetic trait u_3 is able to undergo phenotypic switch, as $a^{\mathrm{B}}(0,\boldsymbol{y},u_3) \geq \varphi_{\boldsymbol{x}_{\mathrm{sj}}}(\boldsymbol{y})$ for all $\boldsymbol{y} \in D$ and sj $\in$ s2, s5, s8, s11, a condition that instead is not satisfied by the distributions of the other cell genotypes;

- in $\boldsymbol{x}_{\mathrm{s1}}$, $\boldsymbol{x}_{\mathrm{s4}}$, $\boldsymbol{x}_{\mathrm{s7}}$, $\boldsymbol{x}_{\mathrm{s10}}$, both the cell clone with genotype u_1 and the cell clone with genotype u_2 have in principle enough mass to undergo a single-cell switch from phenotype B to phenotype A (i.e., $a^{\mathrm{B}}(0,\boldsymbol{y},u_1), a^{\mathrm{B}}(0,\boldsymbol{y},u_2) \geq \varphi_{\boldsymbol{x}_{\mathrm{sj}}}(\boldsymbol{y})$ for all $\boldsymbol{y} \in D$ and sj $\in$ s1, s4, s7, s10). However, as previously commented, only a single B-to-A phenotypic switch is allowed to occur at a given time in a given domain location: in

this respect, we arbitrarily establish that in each of the four points, only the genetic variant u_2 is subjected to phenotypic conversion.

The above-described dynamics are schematically visualised, in the case of a representative domain section, in the top-right graph of Fig. 6.3. The updated system configuration then reads as

$$\begin{cases} \boldsymbol{X}^{\mathrm{A}}_{u_1}(t_1^+) = \boldsymbol{X}^{\mathrm{A}}_{u_1}(0) \\ \boldsymbol{X}^{\mathrm{A}}_{u_2}(t_1^+) = \boldsymbol{X}^{\mathrm{A}}_{u_2}(0) \cup \{\, \boldsymbol{x}_{3,u_2} \equiv \boldsymbol{x}_{\mathrm{s}1}; \boldsymbol{x}_{4,u_2} \equiv \boldsymbol{x}_{\mathrm{s}4}; \boldsymbol{x}_{5,u_2} \equiv \boldsymbol{x}_{\mathrm{s}7}; \boldsymbol{x}_{6,u_2} \equiv \boldsymbol{x}_{\mathrm{s}10} \,\} \\ \boldsymbol{X}^{\mathrm{A}}_{u_3}(t_1^+) = \boldsymbol{X}^{\mathrm{A}}_{u_3}(0) \cup \{\, \boldsymbol{x}_{4,u_3} \equiv \boldsymbol{x}_{\mathrm{s}2}; \boldsymbol{x}_{5,u_3} \equiv \boldsymbol{x}_{\mathrm{s}5}; \boldsymbol{x}_{6,u_3} \equiv \boldsymbol{x}_{\mathrm{s}8}; \boldsymbol{x}_{7,u_3} \equiv \boldsymbol{x}_{\mathrm{s}11} \,\} \\ a^{\mathrm{B}}(t_1^+, \boldsymbol{y}, u_1) = a^{\mathrm{B}}(0, \boldsymbol{y}, u_1) \\ a^{\mathrm{B}}(t_1^+, \boldsymbol{y}, u_2) = a^{\mathrm{B}}(0, \boldsymbol{y}, u_2) - \varphi_{\boldsymbol{x}_{\mathrm{s}1}}(\boldsymbol{y}) - \varphi_{\boldsymbol{x}_{\mathrm{s}4}}(\boldsymbol{y}) - \varphi_{\boldsymbol{x}_{\mathrm{s}7}}(\boldsymbol{y}) - \varphi_{\boldsymbol{x}_{\mathrm{s}10}}(\boldsymbol{y}) \\ a^{\mathrm{B}}(t_1^+, \boldsymbol{y}, u_3) = a^{\mathrm{B}}(0, \boldsymbol{y}, u_3) - \varphi_{\boldsymbol{x}_{\mathrm{s}2}}(\boldsymbol{y}) - \varphi_{\boldsymbol{x}_{\mathrm{s}5}}(\boldsymbol{y}) - \varphi_{\boldsymbol{x}_{\mathrm{s}8}}(\boldsymbol{y}) - \varphi_{\boldsymbol{x}_{\mathrm{s}11}}(\boldsymbol{y}) \end{cases} \tag{6.13}$$

for all $\boldsymbol{y} \in D$. We indeed have that $N(t_1^+) = N^{\mathrm{A}}(t_1^+) + N^{\mathrm{B}}(t_1^+) = 14 + 180 = 194 = N(0)$.

Successively, at t_2, an analogous local signal is present in the following set of points: $\boldsymbol{x}_{\mathrm{s}13} = (45, 0)$, $\boldsymbol{x}_{\mathrm{s}14} = (0, 45)$, $\boldsymbol{x}_{\mathrm{s}15} = (-45, 0)$, and $\boldsymbol{x}_{\mathrm{s}16} = (0, -45)$, see the central panels in Fig. 6.3. In all cases, no phenotypic switch actually occurs. In fact, no cell genetic variant has a sufficient amount of mass over the support of $\varphi_{\boldsymbol{x}_{\mathrm{sj}}}$ (with $j = 13, 14, 15, 16$) despite the overall mass of individuals with phenotype B, measured by ρ^{B}, would be in principle high enough. In this sense, the system does not vary with respect to (6.13).

We finally set that at time t_3, the cell $\boldsymbol{x}_{1,u_2}$, located in (75, 0) from the beginning of the observation time, is triggered to turn back to phenotype B, as shown in the bottom panels of Fig. 6.3. The pointwise particle is indeed replaced by the corresponding bubble function, which is added to the mass of the proper cell genetic variant as

$$\begin{cases} \boldsymbol{X}^{\mathrm{A}}_{u_1}(t_3^+) = \boldsymbol{X}^{\mathrm{A}}_{u_1}(t_2^+) = \boldsymbol{X}^{\mathrm{A}}_{u_1}(t_1^+) = \boldsymbol{X}^{\mathrm{A}}_{u_1}(0) \\ \boldsymbol{X}^{\mathrm{A}}_{u_2}(t_3^+) = \boldsymbol{X}^{\mathrm{A}}_{u_2}(t_2^+) \setminus \{\, \boldsymbol{x}_{1,u_2} \,\} = \boldsymbol{X}^{\mathrm{A}}_{u_2}(t_1^+) \setminus \{\, \boldsymbol{x}_{1,u_2} \,\} \\ \boldsymbol{X}^{\mathrm{A}}_{u_3}(t_3^+) = \boldsymbol{X}^{\mathrm{A}}_{u_3}(t_2^+) = \boldsymbol{X}^{\mathrm{A}}_{u_3}(t_1^+) \\ a^{\mathrm{B}}(t_3^+, \boldsymbol{y}, u_1) = a^{\mathrm{B}}(t_2^+, \boldsymbol{y}, u_1) = a^{\mathrm{B}}(t_1^+, \boldsymbol{y}, u_1) = a^{\mathrm{B}}(0, \boldsymbol{y}, u_1) \\ a^{\mathrm{B}}(t_3^+, \boldsymbol{y}, u_2) = a^{\mathrm{B}}(t_2^+, \boldsymbol{y}, u_2) + \varphi_{\boldsymbol{x}_{1,u_2}}(\boldsymbol{y}) = a^{\mathrm{B}}(t_1^+, \boldsymbol{y}, u_2) + \varphi_{\boldsymbol{x}_{1,u_2}}(\boldsymbol{y}) \\ a^{\mathrm{B}}(t_3^+, \boldsymbol{y}, u_3) = a^{\mathrm{B}}(t_2^+, \boldsymbol{y}, u_3) = a^{\mathrm{B}}(t_1^+, \boldsymbol{y}, u_3) \end{cases} \tag{6.14}$$

for all $\boldsymbol{y} \in D$, so that $N(t_3^+) = N^{\mathrm{A}}(t_3^+) + N^{\mathrm{B}}(t_3^+) = 13 + 181 = 194 = N(0)$. For the sake of the reader's convenience, we recall that the element belonging to the set $\boldsymbol{X}^{\mathrm{A}}_{u_2}$ have to be renumbered according to Eq. (6.8).

Remark 6.2 *As already commented in the introduction of the chapter and sketched in Fig. 6.1c, a cell is stimulated to undergo phenotypic plasticity by environmental signals, but the effective transition depends on its genetic makeup and on the intrinsic stochasticity of the mechanism. These aspects have not been accounted for so far, as all the proposed cell phenotypic switches have been set to actually take place (provided a sufficient cell mass in the case of B-to-A conversions). Such a model shortcoming is tackled in the next section, where more realistic rules underlying variations in cell phenotype will be given.*

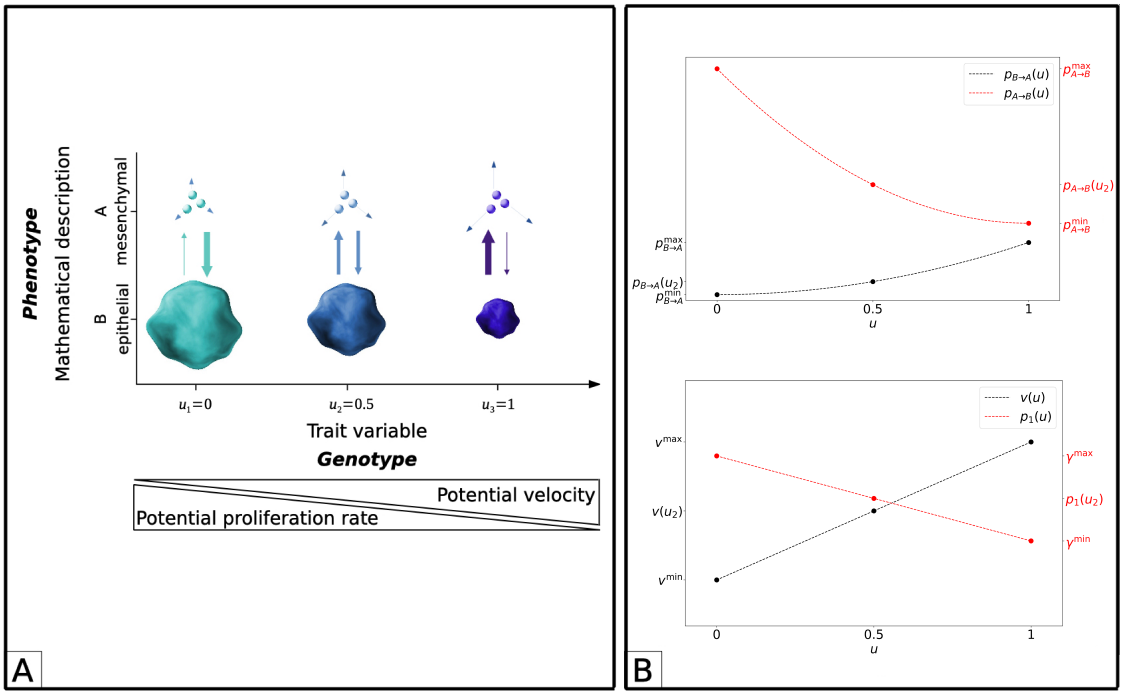

FIGURE 6.4: (a) In the proposed model application, the trait value u is set to qualitatively evaluate the cell motility/proliferation potential. In particular, the higher the value of u, the more a tumour individual is assigned a sequence of genes that, if expressed, enhances its migratory ability while dropping its duplication capacity. The phenotype A, and therefore the corresponding pointwise representation, is given to malignant cells with mesenchymal characteristics; the phenotype B, and the corresponding density-based representation, is instead assigned to tumour agents with epithelial hallmarks. The thickness of the vertical arrows gives a qualitative indication of the probability that a cell with a given genotype has to undergo one of the two phenotypic transitions. In particular, as also shown in the bottom graph of panel (b), cells with genotype $u = u_1 = 0$ more likely acquire (or maintain) an epithelial behaviour. In contrast, cells with genotype $u = u_3 = 1$ more likely acquire (or maintain) mesenchymal hallmarks. (b) Top plot: influence of the genetic trait of a cell on the probability of phenotypic conversions (see Eqs. (6.17) and (6.20)). Bottom plot: genotypic-dependent duplication rate of malignant epithelial cells (p_1, see Eq. (6.23)) and speed of mesenchymal individuals (v, see Eq. (6.27)).

6.2 Model application: early dynamics of an *in vitro* tumour aggregate

We then turn to apply the proposed model to tumour growth. In particular, we hereafter show how our approach can be used to reproduce selected aspects of the early dynamics of a malignant aggregate cultured *in vitro*.

6.2.1 Model description

In the context of our interest, the trait variable u is set to assume three values, i.e., $U = \{u_1 = 0; u_2 = 0.5; u_3 = 1\}$, each indicating a distinct sequence of genes. In this respect, the higher the value of u, the more the corresponding genotype is associated with cells that, in principle, have high migratory potential and low proliferation capacity, see Fig. 6.4a. The definition of the structuring variable u is indeed coherent with the "Go or Grow" (GoG) assumption (Gallaher et al., 2019), which finds support from both the experimental (Giese et al., 1996a; Giese et al., 1996b) and the theoretical literature (Schaller et al., 2012). Phenotype A, and therefore an individual pointwise representation, is then assigned to describe tumour cells with *mesenchymal* determinants (i.e., that show effectively high invasiveness and poor mitotic activity). Phenotype B, as long as a

collective density-based representation, is instead assigned to malignant individuals with *epithelial* hallmarks (i.e., low migratory ability but high duplication rates). Such modelling assumptions are sketched in the already-mentioned Fig. 6.4a.

Modelling epithelial-mesenchymal plasticity In agreement with the scheme shown in Fig. 6.1c, we assume that phenotypic transitions are:

- Stimulated by variations in environmental conditions, in particular in the availability of oxygen, whose local concentration is given by the field variable $O(t, \boldsymbol{y}) \colon T \times D \mapsto \mathbb{R}_0^+$. In this respect, hypoxia has been widely shown to boost phenotypic instability, acting as a stimulus of selective pressure that pushes tumour cells to shift towards more aggressive (mesenchymal) hallmarks (Kao et al., 2016). For instance, tumour cells displaying high levels of hypoxia-inducible factors, such as hypoxia-inducible factor 1 (HIF-1), have been demonstrated to overexpress genes relative to the migratory machinery and underexpress genes related to mitotic processes (see Barrak et al., 2020 and the references therein). In the case of a sufficient amount of resources, malignant individuals have been instead shown to maintain or recover a less invasive (epithelial) behaviour. In this respect, cells with low levels of HIF-1 have been shown to transcript mainly genes implicated in duplication activities (Barrak et al., 2020).
- Affected by the cell genetic makeup: for instance, a variant characterised by a sequence of genes mainly relative to the migratory machinery more likely maintains or acquires a mesenchymal behaviour (and *vice versa*) (Rocha et al., 2021).
- Subjected to randomness, which is a critical aspect in most biological phenomena.

In principle, transition probabilities have to be given as random variables defined on spatio-temporal continuous domains. However, in view of numerical realisations of the proposed model, we only account for their discretised counterpart. According to these considerations, the probability of a cell $\boldsymbol{x}_{i,u_{\hat{k}}}(t)$ with phenotype A and genotype $u_{\hat{k}} \in U$ to undergo phenotypic transition in an interval of time $(t - \Delta t, t] \subset T$, being Δt the size of the time grid (see below), is equal to:

$$P_{\mathrm{A}\to\mathrm{B}}(O(t, \boldsymbol{x}_{i,u_{\hat{k}}}(t)), u_{\hat{k}}) = q_{\mathrm{A}\to\mathrm{B}}(O(t, \boldsymbol{x}_{i,u_{\hat{k}}}(t)))\ p_{\mathrm{A}\to\mathrm{B}}(u_{\hat{k}}) \tag{6.15}$$

In Eq. (6.15), the first factor evaluates the environmental conditions experienced by the i-th individual, i.e.,

$$q_{\mathrm{A}\to\mathrm{B}}(O(t, \boldsymbol{x}_{i,u_{\hat{k}}}(t))) = H(O(t, \boldsymbol{x}_{i,u_{\hat{k}}}(t)) - O_M) \tag{6.16}$$

being

$$H(O(t, \boldsymbol{x}_{i,u_{\hat{k}}}(t)) - O_M) = \begin{cases} 1 & \text{if } O(t, \boldsymbol{x}_{i,u_{\hat{k}}}(t)) \geq O_M \\ 0 & \text{if } O(t, \boldsymbol{x}_{i,u_{\hat{k}}}(t)) < O_M \end{cases}$$

the Heaviside function and O_M the amount of molecular substance needed by tumour cells to remain in a normoxic condition., i.e., to avoid hypoxia. With Eq. (6.16), we are assuming that mesenchymal cells experiencing oxygen deprivation do not undergo phenotypic transitions. The second factor in Eq. (6.15) instead reads as:

$$p_{\mathrm{A}\to\mathrm{B}}(u_{\hat{k}}) = (p^{\max}_{\mathrm{A}\to\mathrm{B}} - p^{\min}_{\mathrm{A}\to\mathrm{B}})(1 - u_{\hat{k}})^2 + p^{\min}_{\mathrm{A}\to\mathrm{B}} \tag{6.17}$$

It indeed sets a quadratic dependence between the genetic makeup of the cell and its possibility to switch phenotype. In this respect, in the case of normoxic conditions,

mesenchymal individuals with genotype $u_1 = 0$ acquire epithelial hallmarks with a probability equal to $p^{\max}_{\mathrm{A}\to\mathrm{B}}$ whereas particles with genotype $u_3 = 1$ with a probability equal to $p^{\min}_{\mathrm{A}\to\mathrm{B}}$ where, according to the above-explained biological arguments, $p^{\min}_{\mathrm{A}\to\mathrm{B}} < p^{\max}_{\mathrm{A}\to\mathrm{B}}$, see Fig. 6.4b (top plot).

Conversely, considering the same time and space discretisation of the previous case, a cell clone with genotype $u_{\hat{k}}$ and phenotype B, i.e., whose distribution is given by the density $a^{\mathrm{B}}(t,\cdot,u_{\hat{k}})$, is set to acquire mesenchymal determinants at a certain point $\boldsymbol{x}_{\mathrm{s}} \in D$ of the discretised space and in an interval of time $(t-\Delta t, t] \subset T$ with a probability equal to

$$P_{\mathrm{B}\to\mathrm{A}}(O(t,\boldsymbol{x}_{\mathrm{s}}),u_{\hat{k}}) = q_{\mathrm{B}\to\mathrm{A}}(O(t,\boldsymbol{x}_{\mathrm{s}}))\; p_{\mathrm{B}\to\mathrm{A}}(u_{\hat{k}}) \tag{6.18}$$

where, recalling Eq. (6.16),

$$q_{\mathrm{B}\to\mathrm{A}}(O(t,\boldsymbol{x}_{\mathrm{s}})) = H(O_M - O(t,\boldsymbol{x}_{\mathrm{s}})) \tag{6.19}$$

The above formula implies that epithelial-to-mesenchymal transitions can only be triggered by hypoxic conditions and the probability that they effectively occur depends also in this case by the cell genotype:

$$p_{\mathrm{B}\to\mathrm{A}}(u_{\hat{k}}) = (p^{\max}_{\mathrm{B}\to\mathrm{A}} - p^{\min}_{\mathrm{B}\to\mathrm{A}})u^2_{\hat{k}} + p^{\min}_{\mathrm{B}\to\mathrm{A}} \tag{6.20}$$

where $p^{\max}_{\mathrm{B}\to\mathrm{A}}$ characterises the cell clone with trait $u_3 = 1$ and $p^{\min}_{\mathrm{B}\to\mathrm{A}}$ the cell variant with $u_1 = 0$, being $p^{\max}_{\mathrm{B}\to\mathrm{A}} > p^{\min}_{\mathrm{B}\to\mathrm{A}}$, as plotted in the top graph of Fig. 6.4b. Obviously, the B-to-A phenotypic transition actually takes place if the $u_{\hat{k}}$-th cell variant has enough mass over the support of $\varphi_{\boldsymbol{x}_{\mathrm{s}}}$.

Remark 6.3 *For the sake of completeness, we now give some comments on the above-proposed modelling framework:*

- *As we explain later, the sizes of the time and space discretisation steps affect the estimate of the parameters $p^{max}_{\mathrm{A}\to\mathrm{B}}$, $p^{max}_{\mathrm{A}\to\mathrm{B}}$, $p^{max}_{\mathrm{B}\to\mathrm{A}}$ and $p^{min}_{\mathrm{B}\to\mathrm{A}}$.*
- *Phenotypic transitions are actually employed according to the procedures explained in the previous section.*
- *In the case of simultaneously possible epithelial-to-mesenchymal switches occurring in the same domain point, it only takes place in the one involving the cell variant with the highest value of u.*
- *In Eqs. (6.17) and (6.20), we have assumed a quadratic relationship between the value of the structuring variable u and the transition probabilities. Different laws may, of course, be chosen; however, they have to maintain the same qualitative trends as those proposed here.*
- *More sophisticated functions may be set to describe the influence of oxygen on phenotypic variations. For instance, the probability of a cell acquiring mesenchymal determinants may increase upon decrements in the chemical concentration below the threshold O_M. One could also consider two different oxygen thresholds $O_{M1} < O_{M2}$ such that the phenotypic switch from A to B occurs for oxygen concentrations above O_{M1} and the phenotypic switch from B to A occurs for oxygen concentrations below O_{M2}.*

Cell dynamics Malignant cells with epithelial determinants are here assumed to proliferate and undergo random movement. The evolution of the density of the $u_{\hat{k}}$-th variant

with phenotype B can be indeed described by means of the following PIDE:

$$\partial_t a^{\mathrm{B}}(t, \boldsymbol{y}, u_{\hat{k}}) = \underbrace{D_{\mathrm{B}} \Delta a^{\mathrm{B}}(t, \boldsymbol{y}, u_{\hat{k}})}_{\text{diffusive movement}} + \underbrace{p(u_{\hat{k}}, \rho(t, \boldsymbol{y}))\, a^{\mathrm{B}}(t, \boldsymbol{y}, u_{\hat{k}})}_{\text{proliferation}} \tag{6.21}$$

where $\rho(t, \boldsymbol{y})$ accounts for the local tumour mass (see below Eqs. (6.25) and (6.26)). The diffusion term in Eq. (6.21), with constant coefficient $D_{\mathrm{B}} > 0$, models Brownian cell displacements. The reaction term instead expresses local variations in the mass of the $u_{\hat{k}}$-th epithelial cell variant. In particular, they are assumed to depend on (i) individual genetic trait and (ii) physical limitations determined by the available space. In this respect, p can be factorised as follows:

$$p(u_{\hat{k}}, \rho(t, \boldsymbol{y})) = p_1(u_{\hat{k}})\, p_2(\rho(t, \boldsymbol{y})) \tag{6.22}$$

The duplication law p_1 accounts for the fact that higher proliferation rates characterise cell variants with lower values of the trait variable u (which, as previously seen, are associated with a sequence of genes mainly implicated in the mitotic machinery). In this respect, to avoid overcomplications, we assign to p_1 a linear trend, see Fig. 6.4b (bottom plot):

$$p_1(u_{\hat{k}}) = (\gamma^{\max} - \gamma^{\min})(1 - u_{\hat{k}}) + \gamma^{\min} \tag{6.23}$$

being $\gamma^{\max}$ a maximal duplication rate, characteristic of cells with genotype $u = u_1 = 0$, and $\gamma^{\min}$ the corresponding minimal value, that is instead assigned to individuals with genotype $u = u_3 = 1$. The factor p_2 in Eq. (6.22) instead models the fact that the mitotic cycle is typically disrupted in overcompressed cells, although abnormal proliferation is a relevant characteristic of malignant masses. This phenomenon can be replicated by setting the following logistic law:

$$p_2(\rho(t, \boldsymbol{y})) = 1 - \frac{\rho(t, \boldsymbol{y})}{c} \tag{6.24}$$

where $c > 0$ is the carrying capacity, while

$$\rho(t, \boldsymbol{y}) = \rho^{\mathrm{A}}(t, \boldsymbol{y}) + \rho^{\mathrm{B}}(t, \boldsymbol{y}) \tag{6.25}$$

being ρ^{B} defined as in Eq. (6.3), and

$$\rho^{\mathrm{A}}(t, \boldsymbol{y}) = \sum_{k=1}^{3} \sum_{i=1}^{N_{u_k}^{\mathrm{A}}} \varphi_{\boldsymbol{x}_{i,u_k}(t)}(\boldsymbol{y}) \tag{6.26}$$

In Eq. (6.24), we consider that the available space is also reduced by the presence of mesenchymal individuals, whose influence on the overall mass distribution can be accounted for by the use of the corresponding set of bubble functions, as given in Eq. (6.26). Eq. (6.21) is then equipped by Neumann homogeneous boundary conditions on the spatial domain D, which are consistent with the fact that cells cannot physically cross the border of an experimental *Petri dish*.

The dynamics of tumour cells with mesenchymal determinants only include a directional movement towards domain regions with higher oxygen concentrations. In this respect, for the i-th individual with phenotype A and generic genotype $u_{\hat{k}}$, we set:

$$\frac{\mathrm{d}\boldsymbol{x}_{i,u_{\hat{k}}}}{\mathrm{d}t}(t) = \frac{\nabla O(t, \boldsymbol{x}_{i,u_{\hat{k}}}(t))}{|\nabla O(t, \boldsymbol{x}_{i,u_{\hat{k}}}(t))|}\, v(u_{\hat{k}}) \tag{6.27}$$

with $v(u_{\hat{k}}) = (v^{\max} - v^{\min})u_{\hat{k}} + v^{\min}$, see the bottom graph in Fig. 6.4b. In Eq. (6.27), cell speed and direction of movement are decoupled, given their distinct physical meaning. The former depends on the pattern of available resources, and the latter, quantified by the scalar functions $v\colon U \mapsto [v^{\min}, v^{\max}]$, is instead affected by individual genetic makeup. In this respect, recalling that higher values of u imply higher motile potential, $v^{\max}$ is the speed of cells with genotype $u = u_3 = 1$, whereas $v^{\min}$ of cells with genotype $u = u_1 = 0$. It is finally useful to underline that Eq. (6.27) is based on the *overdamped force-velocity assumption*: it establishes that, in extremely viscous regimes such as biological environments, the velocity of moving agents and not their acceleration is proportional to the sensed forces (see Scianna and Preziosi, 2012 and the references therein for a detailed comment). When a mesenchymal cancer cell reaches a point of the border of D, the component of its velocity locally normal to the boundary is arbitrarily set equal to zero.

Summing up, it is possible to conclude that, in this sample model application, genetic trait and ecological/environmental conditions affect not only the phenotypic transitions of the cancer cells but also their effective growth and migratory dynamics, as sketched in Fig. 6.1c.

Chemical dynamics We assume that oxygen diffuses within the domain and is consumed equally by all tumour individuals, regardless of their genotype and phenotype. Its kinetics can be therefore described by the following reaction-diffusion equation:

$$\partial_t O(t, \boldsymbol{y}) = \underbrace{D_O \Delta O(t, \boldsymbol{y})}_{\text{diffusion}} - \underbrace{\lambda_O \rho(t, \boldsymbol{y}) O(t, \boldsymbol{y})}_{\substack{\text{consumption by} \\ \text{tumour cells}}} - \underbrace{q_O O(t, \boldsymbol{y})}_{\text{decay}} \tag{6.28}$$

where D_O, λ_O, and q_O are constant coefficients that quantify chemical diffusion, consumption by malignant cells and natural decay, respectively, being ρ defined as in Eq. (6.25). Eq. (6.28) is finally completed with Dirichlet conditions along the entire domain boundary ∂D, i.e., $O(t, \partial D) = \overline{O}$, for all $t \in T$: we are indeed assuming a continuous and constant chemical supply. It is useful to remark that the inclusion of chemical dynamics gives our model a *multiscale* aspect, as it now deals with elements characteristic of both the cellular and the subcellular levels.

6.2.2 Details of numerical simulations

Numerical method For the spatial domain D, we have employed a triangular mesh with radial symmetry with respect to the centre point $(0, 0)$. The characteristic diameter of each grid element has been taken equal to $\Delta x = 5\,\mu$m. For the time domain T, we have used a uniform discretisation with a step equal to $\Delta t = 1$ h.

Eqs. (6.21) and (6.28), describing the dynamics of the continuous population and of the oxygen, have been solved employing a time-explicit Euler method coupled with a Galerkin finite-element technique. An explicit Euler method has also been employed for the system of ODEs describing the movement of pointwise cells (cf. Eq. (6.27)). At any discrete time-step, phenotypic switches are implemented (as explained in Section 6.1) just *after* the numerical solution of the above-cited equation for cell dynamics.

Considering B-to-A switches, the following algorithmic rules are implemented for each numerical node of the domain:

(i) The oxygen level is checked: if it is higher than O_M, then no phenotypic transition occurs and we pass to another domain point;

(ii) Otherwise, we check the mass of the cell subpopulation with $u = u_3 = 1$: if it satisfies condition (6.9), then a random number from the uniform distribution between

0 and 1 is drawn. If this number is lower than the value of the probability given in Eq. (6.18) and evaluated in the case of our interest, then the phenotypic transition occurs and we pass to another domain point (recall that a B-to-A phenotypic transition of a given subpopulation locally inhibits analogous processes involving other subpopulations);

(iii) Otherwise, the same evaluations described at point (ii) are performed for the other subpopulations in descending order with respect to u (to be coherent with the fact that cells with higher genotypic traits u are more likely to switch phenotype).

We keep into account that, when a B-to-A transition takes place at one point, it affects the possibility of transition at neighbouring points, as some of the continuous mass is removed. Thus, in order to avoid biases in the spatial location of B-to-A phenotypic switches, at every iteration, we randomise the order in which the points of the numerical lattice are visited.

We then turn on considering possible A-to-B transitions, which take place in areas with oxygen concentration above O_M with probability given by Eq. (6.15) (using the same drawing algorithm described above). We finally remark that the order in which cells with phenotype A are checked for possible transitions does not affect numerical outcomes, since A-to-B transitions are independent of each other.

All numerical computations have been performed in FeniCS (see Alnaes et al., 2015; Logg et al., 2012 and the references therein).

Parameters estimate As previously commented, the probabilities of phenotypic transitions introduced in Eqs. (6.15) and (6.18) are the discretised approximations of the corresponding continuous-in-time (and in-space) laws. In more detail, the coefficient $p^{\max}_{\mathrm{A}\to\mathrm{B}}$ ($p^{\min}_{\mathrm{A}\to\mathrm{B}}$, respectively) defines the probability that the i-th cell with genotype $u = u_1 = 0$ ($u = u_3 = 1$, respectively) undergoes phenotypic transition at a given time step, i.e., in the case of normoxic conditions. The estimation of these values is based on the average time that a cell with mesenchymal characteristics takes to reacquire epithelial hallmarks; in our model we assume that it ranges from $T^{\min}_{\mathrm{A}\to\mathrm{B}} = 50$ h to $T^{\max}_{\mathrm{A}\to\mathrm{B}} = 200$ h. Such quantities (poorly measured in the empirical literature, see Aiello et al., 2018 for one of the few contributions in this respect) have been fixed in order to have a reasonable number of phenotypic transitions in the period of observation. By recalling that our model is based on the assumption that cells with lower values of the trait variable are more likely to undergo A-to-B transitions, we can indeed set

$$p^{\max}_{\mathrm{A}\to\mathrm{B}} = \frac{\Delta t}{T^{\min}_{\mathrm{A}\to\mathrm{B}}} \qquad \text{and} \qquad p^{\min}_{\mathrm{A}\to\mathrm{B}} = \frac{\Delta t}{T^{\max}_{\mathrm{A}\to\mathrm{B}}}$$

so that $p^{\max}_{\mathrm{A}\to\mathrm{B}} = 2 \times 10^{-2}$, $p^{\min}_{\mathrm{A}\to\mathrm{B}} = 5 \times 10^{-3}$. The coefficients $p^{\max,\min}_{\mathrm{B}\to\mathrm{A}}$ instead give the probability that a single-cell-fraction of mass with phenotype B and centred in $\boldsymbol{x}_s$ changes phenotype at a given time step when falls in hypoxic conditions. A proper estimate can be obtained by taking into account three aspects: (i) epithelial cells experiencing oxygen deprivation are here assumed to acquire mesenchymal determinants in a time interval that ranges from $T^{\min}_{\mathrm{B}\to\mathrm{A}} = 8.8$ h to $T^{\max}_{\mathrm{B}\to\mathrm{A}} = 35.4$ h; (ii) in our modelling framework higher values of the genotypic variable imply more possibility to switch towards phenotype A; and (iii) a finer spatial grid requires a smaller transition probability for each node $\boldsymbol{x}_s$, otherwise a higher amount of possible nodes of the domain in principle could allow a higher number of transitions. The above considerations lead to

$$p^{\max}_{\mathrm{B}\to\mathrm{A}} \propto \Delta t, (T^{\min}_{\mathrm{B}\to\mathrm{A}})^{-1}, \Delta x^2 \qquad \text{and} \qquad p^{\min}_{\mathrm{B}\to\mathrm{A}} \propto \Delta t, (T^{\max}_{\mathrm{B}\to\mathrm{A}})^{-1}, \Delta x^2$$

Parameter	Description	Value [Units]	Reference
r	cell's radius	15 [μm]	Alberts et al., 2002
$p^{\min}_{A\to B}$	minimal A-to-B transition probability	5×10^{-3} [non dim.]	model estimate
$p^{\max}_{A\to B}$	maximal A-to-B transition probability	2×10^{-2} [non dim.]	model estimate
$p^{\min}_{B\to A}$	minimal B-to-A transition probability	10^{-3} [non dim.]	model estimate
$p^{\max}_{B\to A}$	maximal B-to-A transition probability	4×10^{-3} [non dim.]	model estimate
D_B	cells' diffusion coefficient (phenotype B)	1.29×10^3 [μm^2/h]	Martínez-González et al., 2012
$\gamma_{\min}$	minimal duplication rate (phenotype B)	$\ln(2)/48$ [h^{-1}]	Martínez-González et al., 2012
$\gamma_{\max}$	maximal duplication rate (phenotype B)	$\ln(2)/24$ [h^{-1}]	Martínez-González et al., 2012
c	tissue carrying capacity (phenotype B)	1.69 [cell/μm^2]	model estimate
$v^{\min}$	minimal speed (phenotype A)	2.5 [μm/h]	Gallaher et al., 2019
$v^{\max}$	maximal speed (phenotype A)	10 [μm/h]	Gallaher et al., 2019
O_M	hypoxic threshold	2.56×10^{-15} [μmol/μm^2]	Martínez-González et al., 2012
D_O	oxygen diffusion coefficient	3.60×10^6 [μm^2/h]	Martínez-González et al., 2012
λ_O	oxygen consumption rate	1.67×10^{-10} [μm^2/(cell $\cdot$ h)]	model estimate
q_O	oxygen physiological decay	3.60×10^{-4} [h^{-1}]	Cumsille et al., 2015

TABLE 6.1: Simulation parameter set. . The probabilities are non dimensional (abbreviated as "non dim.").

After preliminary simulations, we have fixed $p^{\max}_{B\to A} = 4 \times 10^{-3}$, and $p^{\min}_{B\to A} = 10^{-3}$; these values allow us to observe a reasonable rate of B-to-A phenotypic conversions.

The diffusion coefficient of epithelial cell movement, i.e., D_B, has been taken equal to $1.29 \times 10^3 \mu m^2/h$, as in Martínez-González et al., 2012. The coefficients $\gamma^{\min}$ and $\gamma^{\max}$ quantify the minimal and maximal mitotic rate of cells with phenotype B in the case of fully available space. The chosen values $\gamma^{\min} = \ln(2)/48\ h^{-1}$ and $\gamma^{\max} = \ln(2)/24\ h^{-1}$ fall within the range quantified for glioblastoma cell lines in either hypoxic or normoxic conditions, see again Martínez-González et al., 2012. The carrying capacity c has been set equal to 1.69 cell/μm^2, in order to maintain a quasi-monolayered cell configuration, in agreement with the bidimensional nature of experimental cultures.

Cells with phenotype A are allowed to move freely within the domain. In this respect, the maximal value of their speed $v^{\max}$, which characterises mesenchymal individuals with trait $u_3 = 1$ has been fixed to 10 μm/h, whereas the minimal threshold $v^{\min}$, which characterises mesenchymal individuals with trait $u_1 = 0$, is set to 2.5 μm/h. These parameters have been taken from Gallaher et al., 2019 and assure that the modulus of the overall cell velocity substantially falls within the range of the corresponding experimental counterparts evaluated for different malignancies.

The chemical threshold that leads to hypoxia, i.e., O_M, has been set to 2.56×10^{-15} μmol/μm^2, as it is done in Martínez-González et al., 2012. The diffusion coefficient of oxygen has been fixed to $D_O = 3.60 \times 10^6$ μm^2/h, and taken again from Martínez-González et al., 2012. The chemical consumption rate then amounts to $\lambda_O = 1.67 \times 10^{-10}$ μm^2/(cell $\cdot$ h): it has been empirically measured taking into account the proposed computational setup, in order to have a realistic time evolution of the molecular pattern. The oxygen decay coefficient has been fixed to $q_O = 3.60 \times 10^{-4}$ h^{-1}, according to Cumsille et al., 2015. The constant production of oxygen at the domain border, i.e., $\overline{O}$, has been set equal to 2.8×10^{-15} μmol/μm^2: for the reader's convenience, we remark that

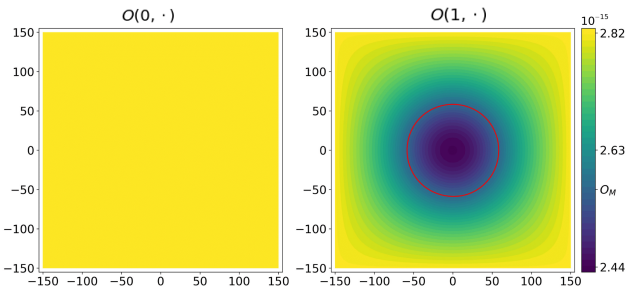

FIGURE 6.5: Representative time instants of the evolution of the oxygen density. At the onset of the numerical realisation, the oxygen is quasi-homogenously present within the entire domain with a level that is higher than the hypoxic threshold O_M (left panel). Subsequent oxygen consumption results in harsh conditions for malignant epithelial cells (right panel): some of them are then able to acquire mesenchymal hallmarks, as shown in Fig. 6.6. The red circle in the right panel encloses the area in which the oxygen density is lower than O_M.

this value is $1.1 \times O_M$. The final observation time t_F has been instead set equal to 35 h.

The employed parameter set is listed in Table 6.1.

6.2.3 Numerical results

The spatial domain D, as well as the initial configuration of the cell system, is exactly the same adopted in the representative simulation given in Section 6.1, specified by Eqs. (6.11) and (6.12), and represented in Fig 6.2. At the onset of the forthcoming numerical realisation, we indeed have a tumour aggregate with few mesenchymal cells (heterogenous for genotype) dispersed within and around a cluster of malignant epithelial individuals. In particular, the node of tumour cells with phenotype B has a radial distribution with respect to the centre of the domain, with the bulk mainly constituted by the cell variant with $u_1 = 0$ and the external region by the cell variant with $u_3 = 1$. The initial oxygen concentration is instead given by the stationary solution of Eq. (6.28), evaluated in the absence of cancer cells (i.e., in the case only of chemical diffusion and decay): given the low value of the decay rate q_O (see above and Table 6.1), it consists of a spatially quasi-homogeneous pattern with a chemical level approximately equal to $2.8 \times 10^{-15}\ \mu\text{mol}/\mu\text{m}^2$, as shown in the left panel of Fig. 6.5. The initial oxygen level indeed exceeds the hypoxic threshold O_M in the entire domain.

Oxygen consumption then starts to occur at the domain area occupied by the tumour aggregate, with the extent of local decrements obviously determined by the density of malignant individuals. The level of chemical at the inner part of the mass drops to the critical value O_M (see the area enclosed in the red circle in the right panel of Fig. 6.5) and an increasing number of epithelial tumour cells (characterised by negligible motility) experiences hypoxia. Some of them are then able to undergo phenotypic transition and acquire mesenchymal determinants, see Fig. 6.6. This group is mainly composed of individuals with a trait value $u_3 = 1$, which is associated with the sequence of genes that favours (from a probabilistic point of view) such a phenotypic switch.

The just-differentiated mesenchymal cells, as long as those already present at the onset of the simulation, crawl towards oxygenated domain regions: in particular, each of them moves with a speed dictated by its genetic trait, as shown by the length of the arrows attached to the "particles" in Fig. 6.6. The remaining fraction of epithelial individuals is instead not able to escape harsh environmental conditions: in the case of long-term hypoxia (e.g., long-lasting oxygen deprivation), their fate would be irreversible necrosis.

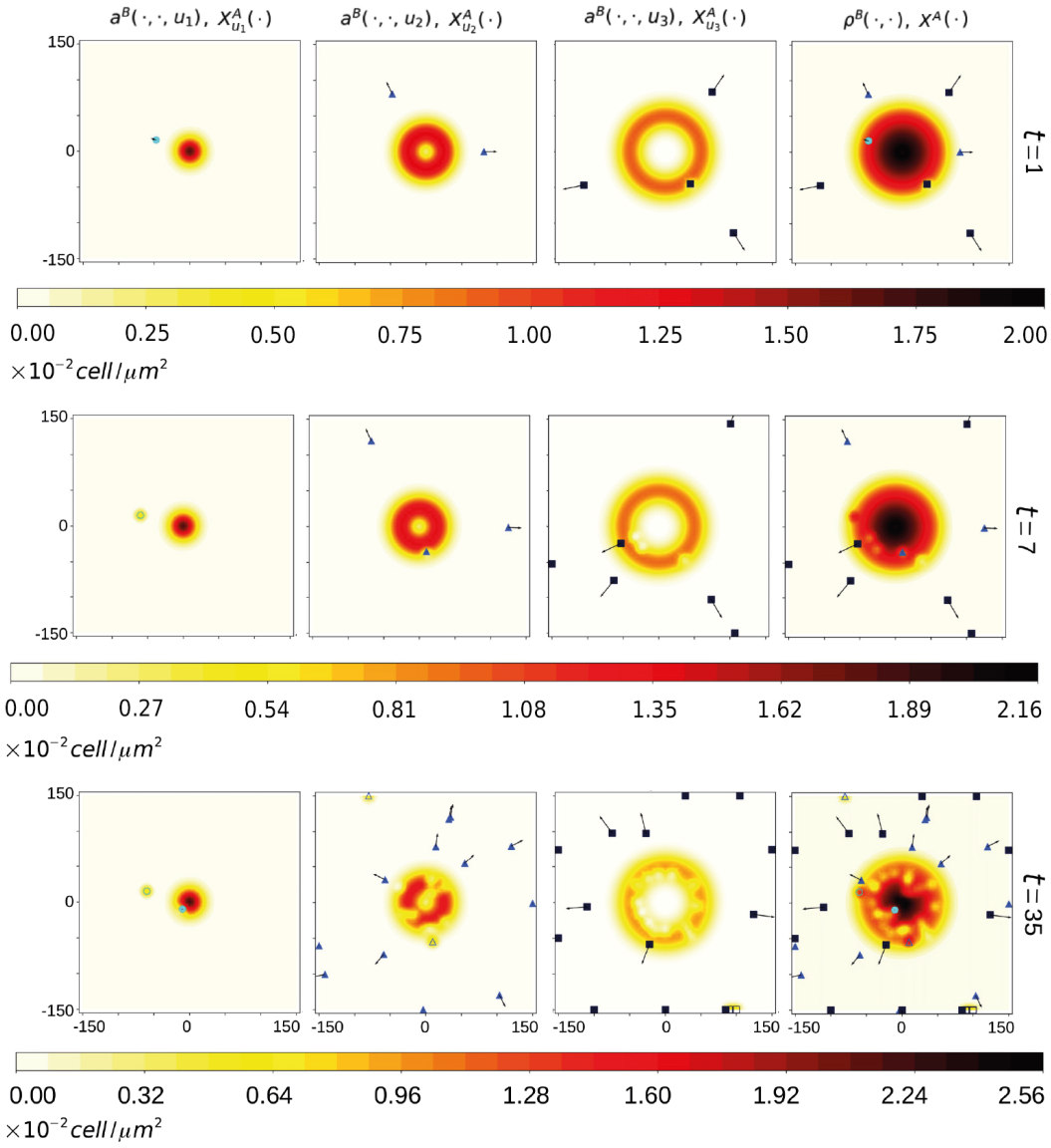

FIGURE 6.6: Representative time instants of the evolution of our virtual tumour aggregate. The initial condition of the cell system is exactly the same as in Section 6.1, see Fig. 6.2. The oxygen consumption by cancer cells results in environmental conditions that allow for EMT in the centre of the tumour (as shown in the right panel of Fig. 6.5). The cells that aquire mesenchymal hallmarks move towards domain regions with more availability of resources (see top and middle panels, i.e., those relative to $t = 1$ and 7 h). Arrived close to the border of our virtual *Petri dish*, few of them experience normoxia and recover epithelial determinants (see the bottom panels, i.e., those relative to $t = t_F = 35$ h). We remark that light blue circles identify mesenchymal cells with genotype u_1, blue triangles identify mesenchymal cells with genotype u_2, and dark blue squares identify mesenchymal cells with genotype u_3. The same *empty* geometric labels instead identify mesenchymal cell variants that have undergone the inverse, i.e., A-to-B, phenotypic transition. The arrow attached to each mesenchymal individual identifies its velocity: its length is qualitatively proportional to the individual genotype-dependent speed.

As the simulation proceeds, the domain region with a low chemical level enlarges; as a result, the above-described cell dynamics take place in more peripheral areas of the tumour aggregate and involve an increasing amount of epithelial mass. In particular, at the end of the observation time (i.e., at $t = t_F = 35$ hours), the cell configuration consists of a hypoxic cluster of epithelial tissue, mainly formed by individuals with a trait variable equal to $u_1 = 0$. It is surrounded by scattered mesenchymal cells, that have reached the external regions of the domain, i.e., those with higher oxygen availability. Interestingly, few of these agents have been able to undergo the inverse transition and reacquire epithelial hallmarks (see the bottom panels of Fig. 6.6). During the entire observation time, the fraction of malignant epithelial mass goes on proliferating (cf. the variations in the values of the colorbar in Fig. 6.6).

Our numerical results qualitatively agree with a wide range of experimental evidence, showing that malignant cells with different phenotypic properties occupy tumour regions characterised by different oxygen levels. For instance, glioblastoma spheroids cultured *in vitro* have their core mainly populated by cells with a proliferative activity higher than those located at the invasive edges (Abramovitch et al., 1995; Castro et al., 2003; Khaitan et al., 2006; Stein et al., 2007). Analogously, mesenchymal cancer stem cells have been found to be abundant near the tumour-stroma boundary (i.e., at the external region of the malignant mass) (Liu et al., 2013). Similar phenotypic spatial heterogeneity has been observed in malignant spheroids of ovarian (Burleson et al., 2006; Shield et al., 2009) or breast (Gatenby et al., 2007) carcinomas grown in spinner cultures.

Analogous growth of tumour masses, i.e., characterised by an inner region of poorly motile individuals unable to escape nutrient deprivation and by an external possibly scattered ring of aggressive cells, has also been predicted by a wide spectrum of theoretical models, see comprehensive books Cristini and Lowengrub, 2010; Preziosi, 2003 and the excellent reviews Araujo and McElwain, 2004; Bellomo et al., 2008; Byrne et al., 2006; Chaplain, 1996; Quaranta et al., 2005.

6.3 Conclusions and future perspectives

In this chapter, we have proposed a modelling framework where cells are distinguished in terms of genotype by a discrete structuring variable and in terms of phenotype by the assigned mathematical representation (i.e., pointwise or density-based). A procedure to consistently switch between the two descriptive instances, which is based on the definition and the use of a bubble function, has then allowed to account for phenotypic plasticity.

We have then presented a representative simulation to show how phenotypic transitions actually take place within our theoretical environment, which has been then applied to a more realistic scenario, i.e., the early evolution of a heterogeneous tumour aggregate hypothetically cultured *in vitro*. In particular, we have assumed that malignant cells can have one of three distinct genotypes and one of two alternatives, i.e., mesenchymal versus epithelial, behaviour. Phenotypic conversions have been set to depend on (i) oxygenation levels, (ii) intrinsic genotype, and (iii) randomness. The latter is the main novelty of this work with respect to Colombi et al., 2017; Scianna and Colombi, 2017 and allows to better characterise the time and position at which transitions take place: while in previous works all the transitions take place as soon as some conditions are satisfied and points are chosen arbitrarily, we here assume that both time and place of the transitions are chosen stochastically, so that the arbitrariness of the model is reduced. The resulting numerical realisation has captured the realistic emergence of a hypoxic core

within the tumour cluster with the consequent cell tendency to acquire a more aggressive and invasive (i.e., mesenchymal) phenotype.

Model improvements The proposed mathematical environment may be improved at least in two directions.

From a strict modelling perspective, it would be relevant to account for genetic alterations that may be induced by cell-cell communication and changes in environmental conditions but are usually determined by random mutations. This last aspect can be included in the proposed modelling environment by stochastic variations of the value of the trait variable u assigned to one or more pointwise individuals and/or to one or more portions of the cell mass with the density-based representation. Furthermore, one could consider a continuous trait u that takes values in a given interval (e.g., $[0, 1]$). This would amount to using a structuring variable to represent not only genetic heterogeneity (as in our model) but also epigenetic heterogeneity: each value of u, in fact, would represent the (normalised) expression of a gene or of a group of genes (or the level of one or more proteins). In this case, epigenetic variations in the cell population could be accounted for by including a diffusion term in the trait domain (see also Eq. (1.1))

From an application perspective, our model could be extended to reproduce the evolution of a malignant mass *in vivo*, i.e., to shed light on the effect of intratumoral heterogeneity and phenotypic plasticity on the invasiveness of the disease. In this respect, one may include in the picture the presence of both the pre-existing and the tumour-induced vasculature. As a natural extension of our model assumptions, we would, in fact, have to take into account that cancer cells in hypoxic conditions not only shift towards more aggressive phenotypes but also secrete proangiogenic factors that induce the formation of new blood vessels departing from existing ones (Plate et al., 1992). In addition, our model could be developed to incorporate a more comprehensive description of the metabolism of the different cell variants. However, in order to provide consistent results of such an *in vivo* scenario, model parametrisation should be better calibrated, for instance, by focusing on a specific tumour type and using proper sets of existing data.

Finally, the proposed modelling approach could be used to analyse the impact of immunotherapy and virotherapy on EMT. Indeed, the activation of the immune system is not restricted to the tumour area and immune cells could enhance the recognition of cancer cells that invade other healthy tissues. In this respect, this inclusion is a significant frontier.

7 Conclusions

In the past decades, oncolytic virotherapy has emerged as a promising targeted cancer therapy. Despite some interesting achievements and clinical progress, such as the celebrated cases of Adenovirus H101 for neck and head cancers or T-Vec for melanomas, the goal of routinely using viruses in a therapeutic setting is still elusive. There are still questions to be addressed to optimise viral delivery in oncolytic virotherapy and the balance between failure and success is very fragile. In this thesis, we developed several mathematical models to elucidate those dynamics and suggest approaches that could optimise the treatment, including the combination with other therapies. Each model was analysed using the most suitable techniques, including analytical and numerical methods.

We first developed agent-based and continuous models for the infection of tumour cells due to oncolytic viruses in the absence of an immune response, taking into account two alternative sets of rules governing cell movement (Chapter 2). Our results suggest that the inability of free virions to propagate in the tumour microenvironment combined with constraints of cellular movement may cause the failure of the therapy due to stochastic effects; the continuous model cannot reproduce such a scenario, hence it does not appear a good approximation for the underlying biological phenomena. On the other hand, our simulations of the model with unrestricted cell movement show partial tumour remission for parameter values within the biologically meaningful range. Notably, the excellent agreement between the agent-based and continuous models in this second case allows us to use our theoretical knowledge of the latter to better understand the outcome of the therapy in different situations and establish strategies and trends to help clinicians.

Building on this partial success, we then analysed the impact of the immune system on the second situation (Chapter 3) to determine whether eradication or long-term control of the tumour is attainable, at least in the absence of relevant physical constraints. We found that tumour eradication is indeed possible in a few situations. In general, any undirected immune response tends to decrease the effectiveness of the virotherapy; hence, immune boosting through immunotherapy may cause the complete failure of virotherapy if the therapies' time and location are not well calibrated. The appearance of wide oscillations may lead to disagreements between the agent-based and the continuum models.

We then focused on the effects of viral dynamics and cell heterogeneity on virotherapy (Chapter 4). Including a viral population that diffuses in the whole domain without significant obstacles results in a good treatment outcome in discrete and continuous mathematical models, irrespective of cell movement rules. This approach could be generalised to account for viral interactions with the tumour's microenvironment. On the other hand, when cancer heterogeneity is considered, virotherapy may significantly lose its efficacy due to the emergence of a subpopulation resistant to viral infection.

Building upon this last observation, we also considered environmental conditions as the source of epigenetic cancer heterogeneity and analysed the influence of hypoxia on oncolytic virotherapy (Chapter 5). The treatment outcome appears to depend significantly on the oxygen spatial configuration and the choice of the most suitable kind of virus may

Chapter	Most salient results
2 (diffusion)	Good quantitative agreement between discrete and continuum models with enough cells; good qualitative agreement even with less cells. Stochasticity does not play a key role; hence, the PDEs can be used to understand the outcome in different parameter regimes. Infected cells should not be killed too fast. The infection spreads in the whole tumour, but eradication appears unlikely.
2 (pressure)	A localised infection does not propagate. A widely spread infection keeps propagating in the continuum model, but fails to propagate in the whole tumor in the discrete model (even with higher cell numbers); hence, stochasticity should not be ignored. Constraints in cell motility may cause treatment failure; high motility of both cell populations improves the therapy.
3	In the continuum model, any immune response has the tendency to decrease the effectiveness of the virotherapy. In the agent-based model, oscillations may result in a complete failure of virotherapy because of stochastic events; on the other hand, an enhancement of the immune response after the infection is well-established could lead all the cancer cells close to extinction due to stochasticity. Multiple viral injections could keep the tumour under control.
4 (Sec. 4.1)	Spatial viral dynamics have a more substantial effect on the evolution of the system than cellular spatial dynamics. Pressure-driven movement shows a decrease of the invasion speed in case of lower cell densities, while undirected movement always shows the same invasion speed (and, in this respect, is less realistic).
4 (Sec. 4.2)	The emergence of a subpopulation resistant to viral infection may significantly hinder the success of the therapy. Formal asymptotic analysis predicts the equilibrium values in a spatially homogeneous scenario, approximating the behaviour at the centre of the tumour well.
5	Formal asymptotic analysis predicts the equilibrium values in a spatially homogeneous scenario, which provides significant information regarding the therapy outcome. Hypoxia may constitute a significant obstacle to the success of virotherapy. The effectiveness can be increased by selecting the most appropriate kind of virus based on the oxygenation of the tumour.
6	A hybrid modelling framework that distinguishes cells in terms of genotype by a discrete structuring variable and in terms of phenotype by the assigned mathematical representation allows us to reproduce hypoxia-driven EMT.

TABLE 7.1: Summary of the most salient results obtained in the thesis.

improve the efficacy. Our results highlight the high potential of oncolytic viruses to treat hypoxic tumours that are less sensitive to other therapies.

Finally, we focused on one of the most relevant effects of hypoxia on the tumour's dynamics in the absence of therapies, namely epithelial-to-mesenchymal transitions (Chapter 6). This required the development of a plasticity-oriented modelling framework, in which discrete structuring variables distinguish cells in terms of genotype and mathematical representation differentiate them in terms of phenotype. Numerical realisations reproduce the emergence of a hypoxic core within the tumour cluster that triggers EMT, resulting in invasive dynamics.

Table 7.1 summarises the most salient results obtained in the thesis. Each chapter of this thesis contains some conclusive remarks and research perspectives. We now discuss more general remarks and potential future directions.

7.1 Conclusive remarks

Cell movement and viral diffusion Several parts of the thesis are devoted to comparing undirected and pressure-driven movements, as summarised in Table 1.1. Undirected cell movement (corresponding to standard diffusion) is the most elementary approach, which does not consider any external influence: as a result, the invasion speed of a tumour mass in the surrounding environment is constant (irrespective of the height of the front) and a viral infection localised in the centre of the cancer faces no obstacle in spreading in the whole domain through cells' displacement; furthermore, the resulting system of reaction-diffusion equations has been extensively studied in the literature, allowing us to rely on some theoretical insights. All these features were extensively analysed in Chapter 2. The addition of viral diffusion in the model does not significantly affect the dynamics, as shown in Chapter 4.

On the other hand, pressure-driven movement (corresponding to nonlinear diffusion) relies on the assumption that a cell only moves because of the pressure exerted by the surrounding cells: as a result, the movement is directed towards less crowded areas and is more relevant for steep changes in the cell density. This approach is well-justified by biological evidence and can model the decreased invasion speed that results from lower cell densities. Furthermore, in the presence of pressure-driven movement, cells' displacement alone cannot spread viral infection: central infections remain localised and even wide infections may be stopped by stochastic events, as explained in Chapter 2. The situation significantly changes when viral particles are allowed to freely move around the tumour and cell-to-cell contact becomes less relevant for the infection: indeed, the results of Chapter 4 show that this infection is qualitatively similar to the case of undirected cell movement. We may conclude that pressure-driven movement allows us to describe both the situations of constrained and unconstrained cellular and viral movements, while such constraints cannot be modelled with undirected movement. The increased realism of pressure-driven movement comes at the cost of a lower degree of theoretical understanding of the models.

Overall, undirected movement (with or without viral diffusion) and pressure-driven movement without viral diffusion exhibit similar behaviour regarding the spread of the infection throughout a tumour. These considerations have guided us in choosing the most suitable expression for cell movement throughout the thesis. In Chapter 3 and Section 4.2, we aimed to analyse the impact of other kinds of obstacles to viral infection (namely, the interaction with the immune system and the emergence of resistant cancer cells) and undirected movement was a suitable modelling assumption to avoid additional complications. On the other hand, in Chapter 5, we developed a model that considers several biological aspects related to hypoxia with the goal of providing valuable insights for medical protocols: this justifies the use of a more realistic model, even though spatial constraints of the viral diffusion are not considered. Indeed, the choice of pressure-driven movement avoids the mixing of different cancer subpopulations due to spatial displacement and contributes to a better characterisation of the epigenetic traits selected by the dynamics; furthermore, the dependence of the invasion speed on the front height emphasises the different efficacy of virotherapy on the reduction of the tumour burden in different oxygen configurations.

Practical implications of the findings and limitations In this thesis, we restrict our attention to general mathematical models formulated in light of a few underlying principles, which, therefore, only capture the main dynamics. This approach allowed us to address specific biological questions and elucidate some important biological actions that govern them.

As explained in Chapter 1, the effectiveness of oncolytic virotherapy is significantly affected by interactions with the tumour microenvironment. The use of mathematical models allowed us to analyse several of these interactions separately and investigate ways to overcome most of these obstacles. In particular, our results suggest that virotherapy is intrinsically limited for tumours whose microenvironments constrain cell movement and viral diffusion; these spatial dynamics are not easy to modify in clinical settings. The excessive activation of the immune system constitutes another potential concern for the treatment, but a correct calibration of the immune response appears able to lead the cancer close to extinction. Virotherapy loses effectiveness significantly if tumour cells evolve to acquire some kind of resistance to the infection. The resistance is particularly relevant in the case of hypoxic tumours; nevertheless, using viral particles that specifically target hypoxic cells may completely overcome this obstacle. In general, virotherapy alone appears unable to eradicate a tumour and the combination with other therapies appears more promising.

In all the cases we analysed, the strategies we suggest require a good knowledge of the biological conditions of the tumour, which, however, in practice, might be challenging. Furthermore, although our models are amenable to a comprehensive mathematical study, we do not focus on a particular kind of tumour and the application of our results to specific biological situations is not straightforward: indeed, in experimental settings, several of the obstacles explained above are present at the same time and the result of their combination could not be trivial. On the other hand, our approach can still provide general conclusions and insights about the most relevant aspects of tumour development and virotherapy, as well as insights into the parameters' role in the dynamics and indications on how to adapt our results in more specific settings.

7.2 Research perspectives

Mathematical future development In most cases, reaction-diffusion equations are well understood from the mathematical point of view. On the other hand, cross-diffusion systems have been studied much less: even in the simplest case of Eq. (2.11), the well-posedness is not trivial and travelling waves are not fully characterised. As recalled above, the behaviours that emerge from the pressure-driven movement are particularly significant in view of the applications, motivating further mathematical analysis. Formal asymptotic techniques may be instrumental in elucidating some of these dynamics.

Similar considerations hold true also in presence of explicit viral dynamics: the case of cell undirected movement and unrestricted viral diffusion (see Eq. (4.2)) has already partially been analysed in the literature (Baabdulla and Hillen, 2024; Pooladvand et al., 2021), while the situation of cell pressure-driven movement and unrestricted viral diffusion (see Eq. (4.3)) is mostly unexplored. It is reasonable to expect this second case to give rise under appropriate conditions to behaviours similar to the ones associated with Eq. (2.11) and discussed in Chapter 2; yet, in the parameter range of our interest, we observe significant differences (see Chapter 4). A better understanding of these dynamics could be interesting not only from the mathematical point of view: indeed, it could elucidate some aspects of viral dynamics in the presence of spatial constraints.

Another important point involves the oscillations observed in spatial models. Our bifurcation analyses are only numerical and refer to nonspatial cases. Given the importance that oscillations may have in the context of oncolytic virotherapy, an improved theoretical understanding could be beneficial.

Optimisation of anti-tumour treatments Most of the models developed in the thesis could be helpful to determine the optimal treatment protocol in different situations, both in terms of treatment schedules (as in Jenner et al., 2018b; Sherlock and Coster, 2023) and viral injection locations (as in Jenner et al., 2020). This aspect appears particularly crucial in the combination of different cancer therapies. In particular, the combination of oncolytic virotherapy and immunotherapy is the most promising strategy, as discussed in Chapter 3 and well documented in the literature (Engeland et al., 2022). Another promising development involves the treatment of hypoxic tumours, as hypoxia-targeting viruses are among the few cancer treatments that do not lose their efficacy in such conditions. Our results in Chapter 5 suggest that virotherapy may select cancer subpopulations that are particularly sensitive to standard treatment (such as radiotherapy); hence, their combination could be particularly beneficial. The correct timing of the therapies is probably relevant and mathematical models could help to elucidate this aspect. Furthermore, the definition of tailored optimal control models may constitute a promising tool in this respect.

Model extensions All the models developed in this thesis neglect direct interactions with the surrounding extracellular matrix and healthy tissues. As a consequence, spatial constraints are only implicitly modelled. Nevertheless, a direct inclusion of these aspects is a particularly intriguing perspective. The importance of viral interactions with the extracellular matrix has already been extensively remarked. Another interesting aspect is the compression and displacement of the surrounding healthy tissues resulting from the tumour development, which may lead to severe clinical complications; these phenomena can be easily included in mechanical models (Ballatore et al., 2024).

When hypoxia is considered, it is clearly relevant to take into account the preexisting vasculature, as well as the tumour-induced vascularisation. These aspects acquire a particular importance in the context of oncolytic virotherapy due to their capability to target vascular endothelial cells and act similarly to antiangiogenic therapy. Blood vessels also play an essential role in spreading cancer cells across the body, potentially leading to metastasis formation. Tumour cell migration was only partially explored in Chapter 6 and studying the effects of therapies would be beneficial. In particular, both virotherapy and immunotherapy could potentially target cancer cells that invade other healthy tissues.

Data availability and model validity Spatial dynamics of oncolytic virotherapy have seldom been experimentally studied. This lack of data motivated our modelling approach, which builds upon a few underlying principles to answer general biological questions. However, more empirical validation of the models would strengthen our results' robustness. Furthermore, there are several interesting aspects that we were not able to address due to the lack of significant biological data: for example, it would be very interesting to understand how the tumour microenvironment affects viral diffusion, improving the insights obtained in Chapter 2; only a few models have already taken it into account (Pooladvand and Kim, 2022) and additional experimental evidence is needed to find a suitable mathematical description of the interactions between viral particles and the physical obstacles of the tumour microenvironment.

In principle, experiments *in vitro* could reproduce the settings we considered in several models in the thesis by analysing one aspect at a time. In this respect, our models could, in principle, guide the development of future experiments. The situation *in vivo* is more complicated: for example, spatial obstacles to viral diffusion could not be easily overcome.

Developing decision tools that can guide the definition of patient-specific cancer treatments based on clinical data is among the main goals of mathematical oncology. Although it is clearly impossible to model all the complex aspects of cancer evolution, this thesis's results may contribute to the process of developing such personalised treatment by highlighting the aspects that affect the outcome more significantly.

Ringraziamenti

Ringrazio in primo luogo i Professori Marcello Delitala e Federico Frascoli per essere stati i miei relatori e per avermi seguito e consigliato durante tutto il dottorato. Grazie a Marcello per avermi per primo introdotto nel mondo della ricerca, per l'accoglienza a Torino, per la sua guida nella definizione degli obiettivi e per avermi insegnato a rimodularli quando necessario, portandomi a concludere il dottorato con molte più idee di quelle che verosimilmente avrei potuto sviluppare; e anche per le cene con gli altri membri del *Delitala's Lab* (accompagnate da vino come richiesto dagli standard piemontesi). E grazie a Federico per aver sempre facilitato per quanto possibile le infinite procedure burocratiche (che hanno coinvolto istitutzioni di entrambi gli emisferi durante una pandemia), per l'accoglienza a Melbourne, per aver sempre valorizzato le interazioni con i biologi, per le correzioni della tesi a tempo di record (con il fuso orario che per una volta giocava a nostro favore); e anche per le pizze a Melbourne e per i preziosi consigli sul cibo italiano in Australia, fondamentali per combattere la nostalgia.

Thanks to Dr. Adrianne Jenner for welcoming in Brisbane in the most beautiful campus I have ever been to and finding the way to develop a research project together despite her little time in that period. Grazie al Prof. Marco Scianna per aver accompagnato Giulia e me nei primi passi della stesura del primo articolo, da cui ho potuto trarre molti insegnamenti per lo sviluppo della ricerca successivo.

Ringrazio la Dott.ssa Giulia Chiari per aver condiviso con me numerosi momenti del dottorato, spalmati su tre continenti in entrambi gli emisferi; per avermi mostrato fin dai primi momenti la sua passione per la ricerca, che tuttora continua a motivarla nonostante le contingenze; e per aver trovato con me un certo equilibrio, andando oltre le discussioni e i disaccordi.

A livello più personale, ci tengo a ringraziare tutte le persone che in questi anni hanno contribuito a farmi sentire a casa nonostante tutti gli sballottamenti, a Torino e perfino a Melbourne, e quelle che mi hanno ricordato che Roma e l'Argentario saranno sempre casa mia. Non è facile trovare un ordine, per cui procedo in ordine geografico (da sud a nord).

Ringrazio i compagni di "ufficio" (o, più propriamente, di vagabondaggio tra posti di lavoro) di Melbourne Edoardo e Riccardo, raggiunti di tanto in tanto da Carlo. Grazie a Edoardo per i numerosi consigli di programmazione e soprattutto per aver offerto a tutti la sua pizza. Grazie a Riccardo e Carlo per le gite nei weekend e per tutti i momenti spensierati che hanno accompato il soggiorno australiano. Thanks to Theodora for helping to bring some Mediterranean culture even so far away from Europe.

Grazie a Federico per essere sempre disponibile per una pizzocherata organizzata all'ultimo e per il costante ascolto e supporto per qualsiasi questione emersa negli ultimi circa 15 anni. Grazie a tutti i componenti di *Vera Myk* Nasbi, Fricco, Gabbo, Sasmi e Pip per le grigliate e per le serate romane. Grazie a Pedullà (londinese ormai da un po', ma continua a contare in quota romana) per il reciproco supporto nella stesura di lettere motivazionale e nel dirimere questioni accademiche di qualsiasi tipo. Grazie ad

Alessandra, celebre fan di falafel, per condividermi i racconti della sua vita anche da Strasburgo.

Grazie a Marco per essere ancora in grado di inventarsi con me regole di nuovi giochi dopo 23 anni e per avermi introdotto al mondo delle immersioni. Grazie a Petru, che da qualche anno riesce ad esprimere al meglio la sua milanesità prima latente, e alla promessa sposa Lucia per aver condiviso con me questa prima fase di immersioni. E grazie anche agli altri *Krapfen* Felix, Sara e Jack per i momenti di mare (ormai purtroppo non così frequenti) che ci riportano indietro all'adolescenza. Grazie a Lorenzo Sorrentini per essere il mio medico di fiducia anche a distanza.

Piccola parentesi Camaldolese per ringraziare Giacomo e Gabriella, senza i quali la stesura di questa tesi sarebbe stata accompagnata da molto meno stress; e anche per il costante impegno al dialogo, che ci ha permesso di creare qualcosa che va decisamente controcorrente rispetto al mondo che ci circonda. Ringrazio anche Maddalena, che ultimamente mi insegue in giro per l'Europa, regalandomi sempre momenti piacevoli.

Grazie a Chiara e Simone per l'accoglienza a Torino e per avermi fornito una vita sociale anche extrauniversitaria. L'ultima serie di ringraziamenti va ai colleghi di dottorato *dismini*, che più di tutti mi hanno accompagnato in questi anni: sarebbe bello poter dire di non sapere come avrei fatto senza di voi; invece lo so bene, non è stato piacevole. Procedendo sempre in ordine sud-nord (più o meno), grazie a Stefano per l'organizzazione dei seminari dottorandi e di altri eventi fondamentali per la vita accademica (come la cena di Natale e il Secret Santa), oltre che per aver cercato di insegnarci il bridge e l'armocromia; a Giuseppe per avermi fornito la colonna sonora dell 'ultimo anno di dottorato (che sto ascoltando in questo momento); a Federico per aver egregiamente gestito le questioni amministrative e di cucina in veste di rappresentante, oltre ad averci reso parte dei misteriosi eventi legati alla sua casa; a Lorenzo, per la precisione con cui dispone le pantofole da farci indossare all'ingresso di casa sua; a Davide, per l'organizzazione delle dismoteche e per l'aroma di tartufo; a Elena, che ha introdotto l'acroyoga al DISMA, per essere sempre presente nel momento del bisogno; agli sposi Martina e Vittorio per farci mantenere la fiducia che al mondo esista ancora qualcosa di bello; a Sara, per avermi fornito una prospettiva accademica da un punto di vista più avanzato; a Martina Fraia per l'accoglienza sulla sdraio del suo ufficio nei momenti di abbiocco post-pranzo; ad Alessandro Baldi per il taglio della mela in ottavi in modalità zen, che resta la cosa più rilassante mai successa al DISMA; a Elisa, che mi ha attaccato la dipendenza da cioccolato fondente post caffè; ad Anderson, per i provvidenziali massaggi; a Pica, che ci ha spiegato che per arrivare a casa sua "piji 'a Salaria p'annà a Rieti" e ha portato un po' di Roma anche a Torino; a Juan, per aver contribuito a rendere il fresbee sport dismico; ad Andrea Pastore, perpetuo dottorando del mese, per l'aiuto nei fiori di zucca vincitori di Voucherchef; ad Alessandro Giammarini, per i tensori del sesto ordine e per la romanità che non riesce proprio ad esternare; a Roberta, regina degli aperitivi del mercoledì e spacciatrice di olio (spero anche oltremanica); ad Alexia, che forse sta imparando che può sopravvivere a un weekend fuori Cuneo. Infine, ringrazio Francesca per avermi sopportato nei momenti in cui ero io il primo a non sopportarmi e per aver continuato a credere in me, riuscendo un pochetto perfino a convincermi.

Bibliography

Abbas, Z. and S. Rehman (2018). "An overview of cancer treatment modalities". In: *Neoplasm* 1, pp. 139–57. DOI: 10.5772/intechopen.76558 (cit. on p. 5).

Abramovitch, R., G. Meir, and M. Neeman (1995). "Neovascularization induced growth of implanted C6 glioma multicellular spheroids: Magnetic-resonance microimaging". In: *Cancer Research* 55.9, pp. 1956–1962 (cit. on p. 155).

Aiello, N. M., R. Maddipati, R. J. Norgard, D. Balli, J. Li, S. Yuan, T. Yamazoe, T. Black, A. Sahmoud, E. E. Furth, D. Bar-Sagi, and B. Z. Stanger (2018). "EMT subtype influences epithelial plasticity and mode of cell migration". In: *Developmental Cell* 45, pp. 681–695. DOI: 10.1016/j.devcel.2018.05.027 (cit. on p. 151).

Aktipis, C. A., A. M. Boddy, R. A. Gatenby, J. S. Brown, and C. C. Maley (2013). "Life history trade-offs in cancer evolution". In: *Nature Reviews Cancer* 13.12, pp. 883–892. DOI: 10.1038/nrc3606 (cit. on p. 4).

Al-Hajj, M., M. S. Wicha, A. Benito-Hernandez, S. J. Morrison, and M. F. Clarke (2003). "Prospective identification of tumorigenic breast cancer cells". In: *Proceedings of the National Academy of Sciences* 100.7, pp. 3983–3988. DOI: 10.1073/pnas.0530291100 (cit. on p. 3).

Alberts, B., A. Johnson, and J. Lewis (2002). *Molecular biology of the cell. 4th edition*. Garland Science (cit. on p. 152).

Alfaro, M., J. Coville, and G. Raoul (2013). "Travelling waves in a nonlocal reaction-diffusion equation as a model for a population structured by a space variable and a phenotypic trait". In: *Communications in Partial Differential Equations* 38.12, pp. 2126–2154. DOI: 10.1080/03605302.2013.828069 (cit. on p. 13).

Almeida, L., C. Audebert, E. Leschiera, and T. Lorenzi (2022). "A hybrid discrete–continuum modelling approach to explore the impact of T-cell infiltration on anti-tumour immune response". In: *Bulletin of Mathematical Biology* 84.141. DOI: 10.1007/s11538-022-01095-3 (cit. on pp. 17, 20, 21, 29, 30, 61, 62, 64, 65, 70, 73, 74, 76, 88).

— (2023). "Discrete and continuum models for the coevolutionary dynamics between CD8+ cytotoxic T lymphocytes and tumour cells". In: *Mathematical Medicine and Biology: A Journal of the IMA* 40.2, pp. 141–174. DOI: 10.1093/imammb/dqac017 (cit. on pp. 20, 21, 29, 30).

Almeida, L., P. Bagnerini, G. Fabrini, B. D. Hughes, and T. Lorenzi (2019). "Evolution of cancer cell populations under cytotoxic therapy and treatment optimisation: Insight from a phenotype-structured model". In: *ESAIM: Mathematical Modelling and Numerical Analysis* 53.4, pp. 1157–1190. DOI: 10.1051/m2an/2019010 (cit. on p. 24).

Almeida, L., P.-A. Bliman, G. Nadin, B. Perthame, and N. Vauchelet (2021). "Final size and convergence rate for an epidemic in heterogeneous populations". In: *Mathematical Models and Methods in Applied Sciences* 31.5, pp. 1021–1051. DOI: 10.1142/S0218202521500251 (cit. on p. 18).

Almuallem, N., D. Trucu, and R. Eftimie (2021). "Oncolytic viral therapies and the delicate balance between virus-macrophage-tumour interactions: A mathematical approach".

In: *Mathematical Biosciences and Engineering* 18.1, pp. 764–799. DOI: 10.3934/MBE.2021041 (cit. on p. 21).
Alnaes, M. S., J. Blechta, J. Hake, A. Johansson, B. Kehlet, A. Logg, A. Richardson, J. Ring, M. E. Rognes, and G. N. Wells (2015). "The FEniCS Project Version 1.5". In: *Archive of Numerical Software* 3.100, pp. 9–23 (cit. on p. 151).
Alzahrani, T., R. Eftimie, and D. Trucu (2019). "Multiscale modelling of cancer response to oncolytic viral therapy". In: *Mathematical Biosciences* 310, pp. 76–95. DOI: 10.1016/j.mbs.2018.12.018 (cit. on p. 17).
Anderson, A. R. A., A. M. Weaver, P. T. Cummings, and V. Quaranta (2006). "Tumor morphology and phenotypic evolution driven by selective pressure from the microenvironment". In: *Cell* 127.5, pp. 905–915. DOI: 10.1016/j.cell.2006.09.042 (cit. on pp. 12, 17).
Araujo, R. P. and D. L. S. McElwain (2004). "A history of the study of solid tumour growth: The contribution of mathematical modelling". In: *Bulletin of Mathematical Biology* 66, pp. 1039–1091. DOI: 10.1016/s0092-8240(03)00126-5 (cit. on pp. 1, 155).
Ardaševa, A., A. R. A. Anderson, R. A. Gatenby, H. M. Byrne, P. K. Maini, and T. Lorenzi (2020a). "Comparative study between discrete and continuum models for the evolution of competing phenotype-structured cell populations in dynamical environments". In: *Physical Review E* 102.4, p. 042404. DOI: 10.1103/PhysRevE.102.042404 (cit. on pp. 23, 111).
Ardaševa, A., R. A. Gatenby, A. R. A. Anderson, H. M. Byrne, P. K. Maini, and T. Lorenzi (2020b). "Evolutionary dynamics of competing phenotype-structured populations in periodically fluctuating environments". In: *Journal of Mathematical Biology* 80.3, pp. 775–807. DOI: 10.1007/s00285-019-01441-5 (cit. on p. 23).
Ardaševa, A., R. A. Gatenby, A. R. A. Anderson, H. M. Byrne, P. K. Maini, and T. Lorenzi (2020c). "A mathematical dissection of the adaptation of cell populations to fluctuating oxygen levels". In: *Bulletin of Mathematical Biology* 82.6, pp. 1–24. DOI: 10.1007/s11538-020-00754-7 (cit. on pp. 23, 111).
Aronson, D. G. (1980). "Density-dependent interaction–diffusion systems". In: *Dynamics and Modelling of Reactive Systems*. Ed. by W. E. Stewart, W. H. Ray, and C. C. Conley. Academic Press, pp. 161–176. DOI: 10.1016/B978-0-12-669550-2.50010-5 (cit. on pp. 16, 39, 117, 123).
Astanin, S. and L. Preziosi (2008). "Multiphase models of tumour growth". In: *Selected topics in cancer modeling*. Springer, pp. 1–31. DOI: 10.1016/j.jtbi.2009.01.034 (cit. on p. 22).
Atsou, K., F. Anjuère, V. M. Braud, and T. Goudon (2020). "A size and space structured model describing interactions of tumor cells with immune cells reveals cancer persistent equilibrium states in tumorigenesis". In: *Journal of Theoretical Biology* 490, p. 110163. DOI: https://doi.org/10.1016/j.jtbi.2020.110163 (cit. on pp. 20, 74).
Baabdulla, A. A. and T. Hillen (2024). "Oscillations in a spatial oncolytic virus model". In: *Bulletin of Mathematical Biology* 86.8. DOI: 10.1007/s11538-024-01322-z (cit. on pp. 17, 61, 97, 160).
Bajzer, Ž., T. Carr, K. Josić, S. J. Russell, and D. Dingli (2008). "Modeling of cancer virotherapy with recombinant measles viruses". In: *Journal of Theoretical Biology* 252.1, pp. 109–122. DOI: 10.1016/j.jtbi.2008.01.016 (cit. on p. 16).
Ballatore, F., G. Lucci, and C. Giverso (2024). "Modelling and simulation of anisotropic growth in brain tumours through poroelasticity: A study of ventricular compression and therapeutic protocols". In: *Computational Mechanics*. DOI: 10.1007/s00466-024-02471-7 (cit. on p. 161).
Barbarossa, M. V. and G. Röst (2015). "Immuno-epidemiology of a population structured by immune status: a mathematical study of waning immunity and immune system

boosting". In: *Journal of Mathematical Biology* 71.6–7, pp. 1737–1770. DOI: 10.1007/s00285-015-0880-5 (cit. on p. 18).
Barles, G., L. Evans, and P. Sougandis (1990). "Wavefront propagation for reaction-diffusion systems of PDE". In: *Duke Mathematical Journal* 61.3, pp. 835–858. DOI: 10.1215/S0012-7094-90-06132-0 (cit. on p. 103).
Barrak, H. N., A. K. Maitham, and Y. A. Luqmani (2020). "Hypoxic environment may enhance migration/penetration of endocrine resistant MCF7-derived breast cancer cells through monolayers of other non-invasive cancer cells in vitro". In: *Scientific Reports* 10.1, pp. 1–14. DOI: 10.1038/s41598-020-58055-x (cit. on pp. 22, 147).
Bellomo, N., N. K. Li, and P. K. Maini (2008). "On the foundations of cancer modelling: Selected topics, speculations, and perspectives". In: *Mathematical Models and Methods in Applied Sciences* 18.04, pp. 593–646. DOI: 10.1142/s0218202508002796 (cit. on p. 155).
Benzekry, S., C. Lamont, A. Beheshti, A. Tracz, J. M. L. Ebos, L. Hlatky, and P. Hahnfeldt (2014). "Classical mathematical models for description and prediction of experimental tumor growth". In: *PLoS Computational Biology* 10.8, pp. 1–19. DOI: 10.1371/journal.pcbi.1003800 (cit. on p. 14).
Berezovskaya, F. S., A. S. Novozhilov, and G. P. Karev (2007). "Population models with singular equilibrium". In: *Mathematical Biosciences* 208.1, pp. 270–299. DOI: 10.1016/j.mbs.2006.10.006 (cit. on p. 14).
Bernardi, E., L. Pareschi, G. Toscani, and M. Zanella (2022). "Effects of vaccination efficacy on wealth distribution in kinetic epidemic models". In: *Entropy* 24.2. DOI: 10.3390/e24020216 (cit. on p. 18).
Bessemoulin-Chatard, M. and F. Filbet (2012). "A finite volume scheme for nonlinear degenerate parabolic equations". In: *SIAM Journal on Scientific Computing* 34.5, pp. B559–B583. DOI: 10.1137/110853807 (cit. on p. 121).
Bhatt, D. K., R. Chammas, and T. Daemen (2021). "Resistance mechanisms influencing oncolytic virotherapy, a systematic analysis". In: *Vaccines* 9.10. DOI: 10.3390/vaccines9101166 (cit. on p. 99).
Bhatt, D. K., T. Janzen, T. Daemen, and F. J. Weissing (2022). "Modelling the spatial dynamics of oncolytic virotherapy in the presence of virus-resistant tumour cells". In: *PLOS Computational Biology* 18.12. Ed. by P. K. Maini, pp. 1–21. DOI: 10.1371/journal.pcbi.1010076 (cit. on p. 18).
Binz, E. and U. M. Lauer (2015). "Chemovirotherapy: Combining chemotherapeutic treatment with oncolytic virotherapy". In: *Oncolytic virotherapy*, pp. 39–48. DOI: 10.2147/OV.S54780 (cit. on p. 7).
Blanchette, P. and J. G. Teodoro (2023). "A renaissance for oncolytic adenoviruses?" In: *Viruses* 15.2. DOI: 10.3390/v15020358 (cit. on p. 5).
Boareto, M., M. K. Jolly, A. Goldman, P. M., S. A. Mani, S. Sengupta, B.-J. Eshel, L. Herbert, and N. O. Jose' (2016). "Notch-Jagged signalling can give rise to clusters of cells exhibiting a hybrid epithelial/mesenchymal phenotype". In: *Journal of the Royal Society Interface* 13.118, pp. 1–11. DOI: 10.1098/rsif.2015.1106 (cit. on p. 137).
Boddy, A. M., W. Huang, and A. Aktipis (2018). "Life history trade-offs in tumors". In: *Current pathobiology reports* 6.4, pp. 201–207. DOI: 10.1007%2Fs40139-018-0188-4 (cit. on p. 4).
Boemo, M. A. and H. M. Byrne (2019). "Mathematical modelling of a hypoxia-regulated oncolytic virus delivered by tumour-associated macrophages". In: *Journal of Theoretical Biology* 461, pp. 102–116. DOI: 10.1016/j.jtbi.2018.10.044 (cit. on p. 24).
Bottger, K., H. Hatzikirou, A. Chauviere, and A. Deutsch (2012). "Investigation of the migration/proliferation dichotomy and its impact on avascular glioma invasion". In:

Mathematical Modelling Natural Phenomena 7.1, pp. 105–135. DOI: 10.1051/mmnp/20127106 (cit. on p. 11).

Bubba, F., T. Lorenzi, and F. R. Macfarlane (2020a). "From a discrete model of chemotaxis with volume-filling to a generalized Patlak–Keller–Segel model". In: *Proceedings of the Royal Society A: Mathematical, Physical and Engineering Sciences*, p. 20190871. DOI: 10.1098/rspa.2019.0871 (cit. on pp. 17, 61, 64, 65, 76).

Bubba, F., B. Perthame, C. Pouchol, and M. Schmidtchen (2020b). "Hele–Shaw limit for a system of two reaction-(cross-)diffusion equations for living tissues". In: *Archive for Rational Mechanics and Analysis* 236.2, pp. 735–766. DOI: 10.1007/s00205-019-01479-1 (cit. on pp. 15, 27).

Burleson, K. M., M. P. Boente, S. E. Parmabuccian, and A. P. Skubitz (2006). "Disaggregation and invasion of ovarian carcinoma ascites spheroids". In: *Journal of Translational Medicine* 4.6, pp. 1–16. DOI: 10.1186/1479-5876-4-6 (cit. on p. 155).

Byrne, H. M., T. Alarcon, M. R. Owen, S. D. Webb, and P. K. Maini (2006). "Modelling aspects of cancer dynamics: A review". In: *Philosophical Transactions of the Royal Society A: Mathematical, Physical and Engineering Sciences* 364.1843, pp. 1563–1578. DOI: 10.1098/rsta.2006.1786 (cit. on pp. 1, 155).

Byrne, H. and D. Drasdo (2009). "Individual-based and continuum models of growing cell populations: A comparison". In: *Journal of Mathematical Biology* 58.4-5, pp. 657–687. DOI: 10.1007/s00285-008-0212-0 (cit. on pp. 15, 35).

Byrne, H. M. (2010). "Dissecting cancer through mathematics: From the cell to the animal model". In: *Nature Reviews Cancer* 10.3, pp. 221–230. DOI: 10.1038/nrc2808 (cit. on p. 1).

Capasso, V. and D. Morale (2009). "Asymptotic behavior of a system of stochastic particles subject to nonlocal interactions". In: *Stochastic Analysis and Applications* 27.3, pp. 574–603. DOI: 10.1080/07362990902844421 (cit. on p. 11).

Carrillo, J. A., M. Fornasier, G. Toscani, and F. Vecil (2010). "Particle, kinetic, and hydrodynamic models of swarming". In: *Mathematical Modeling of Collective Behavior in Socio-Economic and Life Sciences, Modeling and Simulation in Science, Engineering and Technology*. Ed. by G. Naldi, L. Pareschi, and G. Toscani. Birkäuser, pp. 297–336. DOI: 10.1007/978-0-8176-4946-3_12 (cit. on p. 11).

Carrillo, J., S. Fagioli, F. Santambrogio, and M. Schmidtchen (2018). "Splitting schemes and segregation in reaction cross-diffusion systems". In: *SIAM Journal on Mathematical Analysis* 50.5, pp. 5695–5718. DOI: 10.1137/17M1158379 (cit. on pp. 15, 27).

Carrillo, J. A., A. Chertock, and Y. Huang (2015). "A finite-volume method for nonlinear nonlocal equations with a gradient flow structure". In: *Communications in computational physics* 17.1, pp. 233–258. DOI: 10.4208/cicp.160214.010814a (cit. on p. 121).

Castro, M. A. A., F. Klamt, V. A. Grieneisen, I. Grivicich, and J. C. F. Moreira (2003). "Gompertzian growth pattern correlated with phenotypic organization of colon carcinoma, malignant glioma and non-small cell lung carcinoma cell line". In: *Cell Proliferation* 36.2, pp. 65–73. DOI: 10.1046/j.1365-2184.2003.00259.x (cit. on p. 155).

Celora, G. L., H. M. Byrne, and P. Kevrekidis (2023). "Spatio-temporal modelling of phenotypic heterogeneity in tumour tissues and its impact on radiotherapy treatment". In: *Journal of Theoretical Biology* 556, p. 111248. DOI: 10.1016/j.jtbi.2022.111248 (cit. on p. 24).

Celora, G. L., H. M. Byrne, C. E. Zois, and P. Kevrekidis (2021). "Phenotypic variation modulates the growth dynamics and response to radiotherapy of solid tumours under normoxia and hypoxia". In: *Journal of Theoretical Biology* 527, p. 110792. DOI: 10.1016/j.jtbi.2021.110792 (cit. on pp. 24, 105, 106, 118, 119, 135).

Champagnat, N. and S. Méléard (2007). "Invasion and adaptive evolution for individual-based spatially structured populations". In: *Journal of Mathematical Biology* 55.2, pp. 147–188. DOI: 10.1007/s00285-007-0072-z (cit. on pp. 11, 30).

Chaplain, M. A. (1996). "Avascular growth, angiogenesis and vascular growth in solid tumours: The mathematical modelling of the stages of tumour development". In: *Mathematical and Computer Modelling* 23.6, pp. 47–87. DOI: 10.1016/0895-7177(96)00019-2 (cit. on p. 155).

Chaplain, M. A. J., T. Lorenzi, and F. R. Macfarlane (2020). "Bridging the gap between individual-based and continuum models of growing cell populations". In: *Journal of Mathematical Biology* 80.1-2, pp. 343–371. DOI: 10.1007/s00285-019-01391-y (cit. on pp. 11, 28, 30).

Chaplin, D. D. (2010). "Overview of the immune response". In: *Journal of Allergy and Clinical Immunology* 125.2, pp. S3–S23. DOI: 10.1016/j.jaci.2009.12.980 (cit. on p. 8).

Charteris, N. and E. Khain (2014). "Modeling chemotaxis of adhesive cells: Stochastic lattice approach and continuum description". In: *New Journal of Physics* 16, p. 025002. DOI: 10.1088/1367-2630/16/2/025002 (cit. on pp. 17, 61).

Chatzopoulos, K., V. Kotoula, K. Manoussou, K. Markou, K. Vlachtsis, N. Angouridakis, A. Nikolaou, M. Vassilakopoulou, A. Psyrri, and G. Fountzilas (2020). "Tumor infiltrating lymphocytes and CD8+ T cell subsets as prognostic markers in patients with surgically treated laryngeal squamous cell carcinoma". In: *Head and Neck Pathology* 14.3, pp. 689–700. DOI: 10.1007/s12105-019-01101-6 (cit. on p. 75).

Chen, Y., T. DeWeese, J. Dilley, Y. Zhang, Y. Li, N. Ramesh, J. Lee, R. Pennathur-Das, J. Radzyminski, J. Wypych, et al. (2001). "CV706, a prostate cancer-specific adenovirus variant, in combination with radiotherapy produces synergistic antitumor efficacy without increasing toxicity". In: *Cancer Research* 61.14, pp. 5453–5460 (cit. on pp. 42, 43, 91, 120).

Chiari, G., M. E. Delitala, D. Morselli, and M. Scianna (2022). "A hybrid modeling environment to describe aggregates of cells heterogeneous for genotype and behavior with possible phenotypic transitions". In: *International Journal of Non-Linear Mechanics* 144, p. 104063. DOI: 10.1016/j.ijnonlinmec.2022.104063 (cit. on pp. 26, 138).

Chiari, G., G. Fiandaca, and M. E. Delitala (2023a). "Hypoxia-related radiotherapy resistance in tumors: treatment efficacy investigation in an eco-evolutionary perspective". In: *Frontiers in Applied Mathematics and Statistics* 9. DOI: 10.3389/fams.2023.1193191 (cit. on pp. 24, 135).

— (2023b). "Hypoxia-resistance heterogeneity in tumours: the impact of geometrical characterization of environmental niches and evolutionary trade-offs. A mathematical approach". In: *Mathematical Modelling of Natural Phenomena* 18, p. 18. DOI: 10.1051/mmnp/2023023 (cit. on pp. 23, 111, 119).

Chisholm, R. H., T. Lorenzi, L. Desvillettes, and B. D. Hughes (2016). "Evolutionary dynamics of phenotype-structured populations: from individual-level mechanisms to population-level consequences". In: *Zeitschrift fur Angewandte Mathematik und Physik* 67.4. DOI: 10.1007/s00033-016-0690-7 (cit. on p. 13).

Chisholm, R. H., T. Lorenzi, A. Lorz, A. K. Larsen, L. N. d. Almeida, A. Escargueil, and J. Clairambault (2015). "Emergence of drug tolerance in cancer cell populations: An evolutionary outcome of selection, nongenetic instability, and stress-induced adaptation". In: *Cancer Research* 75.6, pp. 930–939. DOI: 10.1158/0008-5472.can-14-2103 (cit. on p. 24).

Christophe, C., S. Mller, M. Rodrigues, A.-E. Petit, P. Cattiaux, L. Dupré, S. Gadat, and S. Valitutti (2015). "A biased competition theory of cytotoxic T lymphocyte interaction

with tumor nodules". In: *PLOS ONE* 10.3, pp. 1–23. DOI: 10.1371/journal.pone.0120053 (cit. on p. 20).
Collins, A. T., P. A. Berry, C. Hyde, M. J. Stower, and N. J. Maitland (2005). "Prospective identification of tumorigenic prostate cancer stem cells". In: *Cancer Research* 65.23, pp. 10946–10951. DOI: 10.1158/0008-5472.can-05-2018 (cit. on p. 3).
Colombi, A., M. Scianna, and L. Preziosi (2015). "A measure-theoretic model for cell migration and aggregation". In: *Mathematical Modelling of Natural Phenomena* 10.1, pp. 4–35. DOI: 10.1051/mmnp/201510101 (cit. on p. 140).
— (2017). "Coherent modelling switch between pointwise and distributed representations of cell aggregates". In: *Journal of mathematical biology* 74.4, pp. 783–808. DOI: 10.1007/s00285-016-1042-0 (cit. on pp. 12, 137, 139, 141, 155).
Colombi, A., M. Scianna, and A. Tosin (2014). "Differentiated cell behaviour: a multiscale approach using measure theory". In: *Journal of Mathematical Biology* 71.5, pp. 1049–1079. DOI: 10.1007/s00285-014-0846-z (cit. on p. 140).
Cooper, A. K. and P. S. Kim (2014). "A cellular automata and a partial differential equation model of tumor–immune dynamics and chemotaxis". In: *Mathematical models of tumor-immune system dynamics*. Springer, pp. 21–46. DOI: https://doi.org/10.1007/978-1-4939-1793-8_2 (cit. on pp. 17, 20, 62, 73, 74).
Cristini, V. and J. Lowengrub (2010). *Multiscale modeling of cancer: An integrated experimental and mathematical modeling approach*. Cambridge University Press (cit. on p. 155).
Crivelli, J. J., J. Földes, P. S. Kim, and J. R. Wares (2012). "A mathematical model for cell cycle-specific cancer virotherapy". In: *Journal of Biological Dynamics* 6.SUPPL. 1, pp. 104–120. DOI: 10.1080/17513758.2011.613486 (cit. on p. 18).
Cumsille, P., A. Coronel, C. Conca, C. Quiñinao, and C. Escudero (2015). "Proposal of a hybrid approach for tumor progression and tumor-induced angiogenesis". In: *Theoretical Biology and Medical Modelling* 12.13, pp. 1–22. DOI: 10.1186/s12976-015-0009-y (cit. on p. 152).
Darvin, P., S. M. Toor, V. Sasidharan Nair, and E. Elkord (2018). "Immune checkpoint inhibitors: Recent progress and potential biomarkers". In: *Experimental & Molecular Medicine* 50.12, pp. 1–11. DOI: 10.1038/s12276-018-0191-1 (cit. on p. 9).
de Araujo, A. L., A. C. Fassoni, K. F. Madalena, and L. F. Salvino (2024). "Analysis and simulation of an integro-differential Lotka–Volterra model with variable reproduction rates and optimal control". In: *Communications in Nonlinear Science and Numerical Simulation* 134, p. 108000. DOI: https://doi.org/10.1016/j.cnsns.2024.108000 (cit. on p. 18).
Delitala, M. and T. Lorenzi (2013a). "Evolutionary branching patterns in predator-prey structured populations". In: *Discrete and Continuous Dynamical Systems - Series B* 18.9, pp. 2267–2282. DOI: 10.3934/dcdsb.2013.18.2267 (cit. on p. 18).
— (2013b). "Recognition and learning in a mathematical model for immune response against cancer". In: *Discrete and Continuous Dynamical Systems - Series B* 18.4, pp. 891–914. DOI: 10.3934/dcdsb.2013.18.891 (cit. on p. 20).
Diekmann, O. (1978). "Thresholds and travelling waves for the geographical spread of infection". In: *Journal of Mathematical Biology* 6.2, pp. 109–130. DOI: 10.1007/BF02450783 (cit. on p. 18).
Diekmann, O., P.-E. Jabin, S. Mischler, and B. Perthame (2005). "The dynamics of adaptation: An illuminating example and a Hamilton-Jacobi approach". In: *Theoretical Population Biology* 67.4, pp. 257–271. DOI: 10.1016/j.tpb.2004.12.003 (cit. on pp. 13, 103).

Ding, C., Z. Wang, and Q. Zhang (2022). "Age-structure model for oncolytic virotherapy". In: *International Journal of Biomathematics* 15.01, p. 2150091. DOI: 10.1142/S1793524521500911 (cit. on p. 18).

Dobson, A. and M. Meagher (1996). "The population dynamics of brucellosis in the yellowstone national park". In: *Ecology* 77.4, pp. 1026–1036. DOI: 10.2307/2265573 (cit. on p. 14).

d'Onofrio, A. (2005). "A general framework for modeling tumor-immune system competition and immunotherapy: Mathematical analysis and biomedical inferences". In: *Physica D: Nonlinear Phenomena* 208.3–4, pp. 220–235. DOI: 10.1016/j.physd.2005.06.032 (cit. on p. 19).

Drasdo, D. (2005). "Coarse graining in simulated cell populations". In: *Advanced Complex Systems* 8.2-3, pp. 319–363. DOI: 10.1142/s0219525905000440 (cit. on p. 11).

Dunbar, S. R. (1984). "Traveling wave solutions of diffusive Lotka–Volterra equations: a heteroclinic connection in $\mathbb{R}^4$". In: *Transactions of the American Mathematical Society*, pp. 557–594. DOI: 10.1090/S0002-9947-1984-0760975-3 (cit. on pp. 15, 27, 35, 39).

Dunn, G. P., A. T. Bruce, H. Ikeda, L. J. Old, and R. D. Schreiber (2002). "Cancer immunoediting: From immunosurveillance to tumor escape". In: *Nature Immunology* 3.11, pp. 991–998. DOI: 10.1038/ni1102-991 (cit. on p. 8).

Eftimie, R. and G. Eftimie (2018). "Tumour-associated macrophages and oncolytic virotherapies: A mathematical investigation into a complex dynamics". In: *Letters in Biomathematics* 5.sup1, pp. S6–S35. DOI: 10.1080/23737867.2018.1430518 (cit. on p. 21).

Eftimie, R., C. MacNamara, J. Dushoff, J. Bramson, and D. Earn (2016). "Bifurcations and chaotic dynamics in a tumour-immune-virus system". In: *Mathematical Modelling of Natural Phenomena* 11.5, pp. 65–85. DOI: 10.1051/mmnp/201611505 (cit. on pp. 21, 61).

Eftimie, R., J. L. Bramson, and D. J. Earn (2011a). "Interactions between the immune system and cancer: A brief review of non-spatial mathematical models". In: *Bulletin of Mathematical Biology* 73.1, pp. 2–32. DOI: 10.1007/s11538-010-9526-3 (cit. on pp. 20, 61).

Eftimie, R., J. Dushoff, B. W. Bridle, J. L. Bramson, and D. J. D. Earn (2011b). "Multistability and multi-instability phenomena in a mathematical model of tumor-immune-virus interactions". In: *Bulletin of Mathematical Biology* 73.12, pp. 2932–2961. DOI: 10.1007/s11538-011-9653-5 (cit. on p. 21).

Eissa, I., I. Bustos-Villalobos, T. Ichinose, S. Matsumura, Y. Naoe, N. Miyajima, D. Morimoto, N. Mukoyama, W. Zhiwen, M. Tanaka, H. Hasegawa, S. Sumigama, B. Aleksic, Y. Kodera, and H. Kasuya (2018). "The current status and future prospects of oncolytic viruses in clinical trials against melanoma, glioma, pancreatic, and breast cancers". In: *Cancers* 10.10. DOI: 10.3390/cancers10100356 (cit. on p. 48).

Enderling, H. and O. Wolkenhauer (2021). "Are all models wrong?" In: *Computational and Systems Oncology* 1.1, p. e1008. DOI: 10.1002/cso2.1008 (cit. on p. 1).

Engeland, C. E., J. P. Heidbuechel, R. P. Araujo, and A. L. Jenner (2022). "Improving immunovirotherapies: The intersection of mathematical modelling and experiments". In: *ImmunoInformatics* 6, p. 100011. DOI: 10.1016/j.immuno.2022.100011 (cit. on pp. 1, 7, 60, 161).

Evans, L. C. and P. E. Souganidis (1989). "A PDE approach to geometric optics for certain semilinear parabolic equations". In: *Indiana University Mathematics Journal* 38.1, pp. 141–172 (cit. on p. 103).

Fesnak, A. D., C. H. June, and B. L. Levine (2016). "Engineered T cells: The promise and challenges of cancer immunotherapy". In: *Nature Reviews Cancer* 16.9, pp. 566–581. DOI: 10.1038/nrc.2016.97 (cit. on p. 9).

Fiandaca, G., M. Delitala, and T. Lorenzi (2021). "A mathematical study of the influence of hypoxia and acidity on the evolutionary dynamics of cancer". In: *Bulletin of mathematical biology* 83.83, pp. 1–29. DOI: 10.1007/s11538-021-00914-3 (cit. on pp. 23, 111).

Fiandaca, G., S. Bernardi, M. Scianna, and M. E. Delitala (2022). "A phenotype-structured model to reproduce the avascular growth of a tumor and its interaction with the surrounding environment". In: *Journal of Theoretical Biology* 535, p. 110980. DOI: https://doi.org/10.1016/j.jtbi.2021.110980 (cit. on p. 13).

Filley, A. C. and M. Dey (2017). "Immune system, friend or foe of oncolytic virotherapy?" In: *Frontiers in Oncology* 7. DOI: 10.3389/fonc.2017.00106 (cit. on pp. 6, 87).

Fisher, R. A. (1937). "The wave of advance of advantageous genes". In: *Annals of Eugenics* 7.4, pp. 355–369 (cit. on p. 37).

Fleming, W. H. and P. E. Souganidis (1986). "PDE-viscosity solution approach to some problems of large deviations". In: *Annali della Scuola Normale Superiore di Pisa – Classe di Scienze* 13, pp. 171–192 (cit. on p. 103).

Fountzilas, C., S. Patel, and D. Mahalingam (2017). "Review: Oncolytic virotherapy, updates and future directions". In: *Oncotarget* 8.60, pp. 102617–102639. DOI: 10.18632/oncotarget.18309 (cit. on p. 5).

Friedman, A. and X. Lai (2018). "Combination therapy for cancer with oncolytic virus and checkpoint inhibitor: A mathematical model". In: *PloS one* 13.2, pp. 1–21. DOI: 10.1371/journal.pone.0192449 (cit. on p. 22).

Friedman, A. and Y. Tao (2003). "Analysis of a model of a virus that replicates selectively in tumor cells". In: *Journal of Mathematical Biology* 47.5, pp. 391–423. DOI: 10.1007/s00285-003-0199-5 (cit. on pp. 17, 22).

Friedman, A., J. P. Tian, G. Fulci, E. A. Chiocca, and J. Wang (2006). "Glioma virotherapy: Effects of innate immune suppression and increased viral replication capacity". In: *Cancer Research* 66.4, pp. 2314–2319. DOI: 10.1158/0008-5472.CAN-05-2661 (cit. on pp. 17, 22, 41, 42, 73, 91, 92, 118–120).

Gallaher, J. A., J. S. Brown, and A. R. A. Anderson (2019). "The impact of proliferation-migration tradeoffs on phenotypic evolution in cancer". In: *Scientific Reports* 9.2425, pp. 1–10. DOI: 10.1038/s41598-019-39636-x (cit. on pp. 24, 146, 152).

Galon, J. and D. Bruni (2019). "Approaches to treat immune hot, altered and cold tumours with combination immunotherapies". In: *Nature Reviews Drug Discovery* 18.3, pp. 197–218. DOI: 10.1038/s41573-018-0007-y (cit. on pp. 8, 61, 64, 78).

Ganly, I., V. Mautner, and A. Balmain (2000). "Productive replication of human adenoviruses in mouse epidermal cells". In: *Journal of Virology* 74.6, pp. 2895–2899. DOI: 10.1128/JVI.74.6.2895-2899.2000 (cit. on pp. 41, 91, 106, 118, 119).

Gao, L., Y. Tan, J. Yang, and C. Xiang (2022). "Dynamic analysis of an age structure model for oncolytic virus therapy". In: *Mathematical Biosciences and Engineering* 20.2, pp. 3301–3323. DOI: 10.3934/mbe.2023155 (cit. on p. 18).

Gao, Y., Q. Zhou, Z. Matharu, Y. Liu, T. Kwa, and A. Revzin (2014). "A mathematical method for extracting cell secretion rate from affinity biosensors continuously monitoring cell activity". In: *Biomicrofluidics* 8.2, p. 021501. DOI: 10.1063/1.4874216 (cit. on pp. 73, 74).

Garber, K. (2006). "China Approves World's First Oncolytic Virus Therapy For Cancer Treatment". In: *JNCI: Journal of the National Cancer Institute* 98.5, pp. 298–300. DOI: 10.1093/jnci/djj111 (cit. on p. 6).

Gatenby, R. A., K. Smallbone, P. K. Maini, F. Rose, J. Averill, R. B. Nagle, L. Worrall, and R. J. Gillies (2007). "Cellular adaptations to hypoxia and acidosis during somatic evolution of breast cancer". In: *British Journal of Cancer* 97.5, pp. 646–653. DOI: 10.1038%2Fsj.bjc.6603922 (cit. on pp. 23, 155).

Gatenby, R. A. and J. S. Brown (2020). "Integrating evolutionary dynamics into cancer therapy". In: *Nature Reviews Clinical Oncology* 17.11, pp. 675–686. DOI: 10.1038/s41571-020-0411-1 (cit. on p. 5).

Giese, A., L. Kluwe, M. E. Berens, and M. Westphal (1996a). "Migration of human glioma cells on myelin". In: *Neurosurgery* 38.4, pp. 755–764. DOI: 10.1097/00006123-199604000-00026 (cit. on p. 146).

Giese, A., M. A. Loo, N. Tran, D. Haskett, S. W. Coons, and M. E. Berens (1996b). "Dichotomy of astrocytoma migration and proliferation". In: *Int. J. Cancer* 67.2, pp. 275–282. DOI: 10.1002/(sici)1097-0215(19960717)67:2<275::aid-ijc20>3.3.co;2-y (cit. on p. 146).

Giverso, C., T. Lorenzi, and L. Preziosi (2022). "Effective interface conditions for continuum mechanical models describing the invasion of multiple cell populations through thin membranes". In: *Applied Mathematics Letters* 125.107708, pp. 1–9. DOI: 10.1016/j.aml.2021.107708 (cit. on p. 12).

Graw, F. and A. S. Perelson (2016). "Modeling viral spread". In: *Annual Review of Virology* 3, pp. 555–572. DOI: 10.1146/annurev-virology-110615-042249 (cit. on p. 6).

Grimes, D. R., C. Kelly, K. Bloch, and M. Partridge (2014). "A method for estimating the oxygen consumption rate in multicellular tumour spheroids". In: *Journal of The Royal Society Interface* 11.92, p. 20131124. DOI: 10.1098/rsif.2013.1124 (cit. on pp. 118, 120).

Gross, G. and Z. Eshhar (2016). "Therapeutic potential of T cell chimeric antigen receptors (CARs) in cancer treatment: Counteracting off-tumor toxicities for safe CAR T cell therapy". In: *Annual Review of Pharmacology and Toxicology* 56.1, pp. 59–83. DOI: 10.1146/annurev-pharmtox-010814-124844 (cit. on p. 9).

Gwiazda, P., B. Perthame, and A. Świerczewska-Gwiazda (2019). "A two-species hyperbolic-parabolic model of tissue growth". In: *Communications in Partial Differential Equations* 44.12, pp. 1605–1618. DOI: 10.1080/03605302.2019.1650064 (cit. on pp. 15, 27, 35).

Hamis, S., G. G. Powathil, and M. A. Chaplain (2019). "Blackboard to bedside: A mathematical modeling bottom-up approach toward personalized cancer treatments". In: *JCO Clinical Cancer Informatics* 3, pp. 1–11. DOI: 10.1200/cci.18.00068 (cit. on p. 24).

Hanahan, D. (2022). "Hallmarks of cancer: New dimensions". In: *Cancer discovery* 12.1, pp. 31–46. DOI: 10.1158/2159-8290.CD-21-1059 (cit. on pp. 1–4).

Hanahan, D. and R. A. Weinberg (2000). "The hallmarks of cancer". In: *Cell* 100.1, pp. 57–70. DOI: 10.1016/S0092-8674(00)81683-9 (cit. on pp. 1, 2, 4).

— (2011). "Hallmarks of cancer: The next generation". In: *Cell* 144.5, pp. 646–674. DOI: 10.1016/j.cell.2011.02.013 (cit. on pp. 1, 2, 4, 5).

Hao, W., E. D. Crouser, and A. Friedman (2014). "Mathematical model of sarcoidosis". In: *Proceedings of the National Academy of Sciences* 111.45, pp. 16065–16070. DOI: https://doi.org/10.1073/pnas.1417789111 (cit. on pp. 73, 74).

Hausser, J. and U. Alon (2020). "Tumour heterogeneity and the evolutionary trade-offs of cancer". In: *Nature Reviews Cancer* 20.4, pp. 247–257. DOI: 10.1038/s41568-020-0241-6 (cit. on p. 4).

He, J., F. Munir, D. Ragoonanan, W. Zaky, S. J. Khazal, P. Tewari, J. Fueyo, C. Gomez-Manzano, and H. Jiang (2023). "Combining CAR T cell therapy and oncolytic virotherapy for pediatric solid tumors: A promising option". In: *Immuno* 3.1, pp. 37–56. DOI: 10.3390/immuno3010004 (cit. on pp. 83, 88).

Hemminki, O., J. Dos Santos, and A. Hemminki (2020). "Oncolytic viruses for cancer immunotherapy". In: *Journal of Hematology and Oncology* 13.1. DOI: 10.1186/s13045-020-00922-1 (cit. on pp. 48, 60).

Hill, C. and R. Carlisle (2019). "Achieving systemic delivery of oncolytic viruses". In: *Expert Opinion on Drug Delivery* 16.6, pp. 607–620. DOI: 10.1080/17425247.2019.1617269 (cit. on p. 6).
Hillen, T. and K. Painter (2009). "A user's guide to PDE models for chemotaxis". In: *Journal of Mathematical Biology* 58.1–2, pp. 183–217. DOI: 10.1007/s00285-008-0201-3 (cit. on pp. 20, 88).
Hillen, T. and A. Swan (2016). "The diffusion limit of transport equations in biology". In: *Lecture Notes in Mathematics* 2167, pp. 73–129. DOI: 10.1007/978-3-319-42679-2_2 (cit. on p. 74).
Holt, R. D. and M. Roy (2007). "Predation can increase the prevalence of infectious disease". In: *American Naturalist* 169.5, pp. 690–699. DOI: 10.1086/513188 (cit. on p. 14).
Holzel, M., A. Bovier, and T. Tuting (2012). "Plasticity of tumour and immune cells: A source of heterogeneity and a cause for therapy resistance?" In: *Nature Reviews Cancer* 13.5, pp. 365–376. DOI: 10.1038/nrc3498 (cit. on p. 137).
Ilina, O. and P. Friedl (2009). "Mechanisms of collective cell migration at a glance". In: *Journal of Cell Science* 122.18, pp. 3203–3208. DOI: 10.1242/jcs.036525 (cit. on p. 137).
Iwai, Y., M. Ishida, Y. Tanaka, T. Okazaki, T. Honjo, and N. Minato (2002). "Involvement of PD-L1 on tumor cells in the escape from host immune system and tumor immunotherapy by PD-L1 blockade". In: *Proceedings of the National Academy of Sciences of the United States of America* 99.19, pp. 12293–12297. DOI: 10.1073/pnas.192461099 (cit. on p. 61).
Jacqueline, C., P. A. Biro, C. Beckmann, A. P. Moller, F. Renaud, G. Sorci, A. Tasiemski, B. Ujvari, and F. Thomas (2017). "Cancer: A disease at the crossroads of trade-offs". In: *Evolutionary Applications* 10.3, pp. 215–225. DOI: 10.1111/eva.12444 (cit. on p. 4).
Jarrett, A. M., E. A. Lima, D. A. Hormuth, M. T. McKenna, X. Feng, D. A. Ekrut, A. C. M. Resende, A. Brock, and T. E. Yankeelov (2018). "Mathematical models of tumor cell proliferation: A review of the literature". In: *Expert Review of Anticancer Therapy* 18.12, pp. 1271–1286. DOI: 10.1080/14737140.2018.1527689 (cit. on p. 14).
Jenner, A., C.-O. Yun, A. Yoon, P. S. Kim, and A. C. Coster (2018a). "Modelling heterogeneity in viral-tumour dynamics: The effects of gene-attenuation on viral characteristics". In: *Journal of Theoretical Biology* 454, pp. 41–52. DOI: 10.1016/j.jtbi.2018.05.030 (cit. on p. 18).
Jenner, A. L., F. Frascoli, A. C. Coster, and P. S. Kim (2020). "Enhancing oncolytic virotherapy: Observations from a Voronoi cell-based model". In: *Journal of Theoretical Biology* 485. DOI: 10.1016/j.jtbi.2019.110052 (cit. on pp. 17, 37, 161).
Jenner, A. L., P. S. Kim, and F. Frascoli (2019). "Oncolytic virotherapy for tumours following a Gompertz growth law". In: *Journal of Theoretical Biology* 480, pp. 129–140. DOI: 10.1016/j.jtbi.2019.08.002 (cit. on pp. 17, 37, 61).
Jenner, A. L., M. Smalley, D. Goldman, W. F. Goins, C. S. Cobbs, R. B. Puchalski, E. A. Chiocca, S. Lawler, P. Macklin, A. Goldman, and M. Craig (2022). "Agent-based computational modeling of glioblastoma predicts that stromal density is central to oncolytic virus efficacy". In: *iScience* 25.6, p. 104395. DOI: 10.1016/j.isci.2022.104395 (cit. on pp. 22, 74).
Jenner, A. L., C.-O. Yun, P. S. Kim, and A. C. F. Coster (2018b). "Mathematical modelling of the interaction between cancer cells and an oncolytic virus: Insights into the effects of treatment protocols". In: *Bulletin of Mathematical Biology* 80.6, pp. 1615–1629. DOI: 10.1007/s11538-018-0424-4 (cit. on pp. 16, 37, 161).
Jenner, A., A. Coster, P. Kim, and F. Frascoli (2018c). "Treating cancerous cells with viruses: Insights from a minimal model for oncolytic virotherapy". In: *Letters in Biomathematics* 5.sup1, S117–S136. DOI: 10.1080/23737867.2018.1440977 (cit. on pp. 17, 37, 48, 61).

Jin, K.-T., W.-L. Du, Y.-Y. Liu, H.-R. Lan, J.-X. Si, and X.-Z. Mou (2021). "Oncolytic virotherapy in solid tumors: The challenges and achievements". In: *Cancers* 13.4, pp. 1–28. DOI: 10.3390/cancers13040588 (cit. on pp. 5–7, 75).

Johnston, S. T., M. J. Simpson, and R. E. Baker (2015). "Modelling the movement of interacting cell populations: A moment dynamics approach". In: *Journal of Theoretical Biology* 370, pp. 81–92. DOI: 10.1016/j.jtbi.2015.01.025 (cit. on pp. 11, 30).

Johnston, S. T., M. J. Simpson, and E. J. Crampin (2020). "Predicting population extinction in lattice-based birth-death-movement models". In: *Proceedings of the Royal Society A: Mathematical, Physical and Engineering Sciences* 476.2238, p. 20200089. DOI: 10.1098/rspa.2020.0089 (cit. on p. 55).

Kalia, M. and S. Jameel (2011). "Virus entry paradigms". In: *Amino Acids* 41.5, pp. 1147–1157. DOI: 10.1007/s00726-009-0363-3 (cit. on p. 6).

Kao, S.-H., K.-J. Wu, and W.-H. Lee (2016). "Hypoxia, epithelial-mesenchymal transition, and TET-mediated epigenetic changes". In: *Journal of Clinical Medicine* 5.2, pp. 24–38. DOI: 10.3390/jcm5020024 (cit. on pp. 22, 147).

Karev, G. P., A. S. Novozhilov, and E. V. Koonin (2006). "Mathematical modeling of tumor therapy with oncolytic viruses: Effects of parametric heterogeneity on cell dynamics". In: *Biology Direct* 1. DOI: 10.1186/1745-6150-1-30 (cit. on p. 18).

Kather, J. N., J. Poleszczuk, M. Suarez-Carmona, J. Krisam, P. Charoentong, N. A. Valous, C.-A. Weis, L. Tavernar, F. Leiss, E. Herpel, F. Klupp, A. Ulrich, M. Schneider, A. Marx, D. Jäger, and N. Halama (2017). "In silico modeling of immunotherapy and stroma-targeting therapies in human colorectal cancer". In: *Cancer Research* 77.22, pp. 6442–6452. DOI: 10.1158/0008-5472.can-17-2006 (cit. on p. 20).

Ke, L. D., Y.-X. Shi, S.-A. Im, X. Chen, and W. A. Yung (2000). "The relevance of cell proliferation, vascular endothelial growth factor, and basic fibroblast growth factor production to angiogenesis and tumorigenicity in human glioma cell lines". In: *Clinical Cancer Research* 6.6, pp. 2562–2572 (cit. on pp. 41, 73, 91, 106, 118, 119).

Keeling, M., H. Wilson, and S. Pacala (2002). "Deterministic limits to stochastic spatial models of natural enemies". In: *American Naturalist* 159.1, pp. 57–80. DOI: 10.1086/324119 (cit. on p. 16).

Kelly, E. and S. Russell (2007). "History of oncolytic viruses: Genesis to genetic engineering". In: *Molecular Therapy* 15.4, pp. 651–659. DOI: 10.1038/sj.mt.6300108 (cit. on p. 5).

Kermack, W. O. and A. G. McKendrick (1927). "A contribution to the mathematical theory of epidemics". In: *Proceedings of the royal society of london. Series A, Containing papers of a mathematical and physical character* 115.772, pp. 700–721 (cit. on pp. 14, 18).

Khaitan, D., S. Chandna, M. B. Arya, and D. B. S. (2006). "Establishment and characterization of multicellular spheroids from a human glioma cell line: Implications for tumor therapy". In: *J. Transl. Med.* 4.12, pp. 1–13. DOI: 10.1186/1479-5876-4-12 (cit. on p. 155).

Khalil, A. A. and P. Friedl (2010). "Determinants of leader cells in collective cell migration". In: *Integrative Biology* 2.11-12, pp. 568–574. DOI: 10.1039/c0ib00052c (cit. on p. 137).

Kim, J.-H., Y.-S. Lee, H. Kim, J.-H. Huang, A.-R. Yoon, and C.-O. Yun (2006). "Relaxin expression from tumor-targeting adenoviruses and its intratumoral spread, apoptosis induction, and efficacy". In: *Journal of the National Cancer Institute* 98.20, pp. 1482–1493. DOI: 10.1093/jnci/djj397 (cit. on pp. 41, 43, 73, 91, 92, 106, 118, 119, 124).

Kim, Y., H. G. Lee, N. Dmitrieva, J. Kim, B. Kaur, and A. Friedman (2014). "Choindroitinase ABC I-mediated enhancement of oncolytic virus spread and anti tumor efficacy: A mathematical model". In: *PloS one* 9.7, pp. 1–19. DOI: 10.1371/journal.pone.0102499 (cit. on pp. 17, 60).

Kim, Y., J. Y. Yoo, T. J. Lee, J. Liu, J. Yu, M. A. Caligiuri, B. Kaur, and A. Friedman (2018). "Complex role of NK cells in regulation of oncolytic virus–bortezomib therapy". In: *Proceedings of the National Academy of Sciences of the United States of America* 115.19, pp. 4927–4932. DOI: 10.1073/pnas.1715295115 (cit. on p. 22).

Knútsdóttir, H., E. Pálsson, and L. Edelstein-Keshet (2014). "Mathematical model of macrophage-facilitated breast cancer cells invasion". In: *Journal of Theoretical Biology* 357, pp. 184–199. DOI: 10.1016/j.jtbi.2014.04.031 (cit. on p. 20).

Kolmogorov, A. N., I. G. Petrovskii, and N. S. Piskunov (1937). "Étude de l'équation de la diffusion avec croissance de la quantité de matière et son application à un problème biologique". In: *Moscow University Mathematics Bulletin, Sec. A* 1, pp. 1–26 (cit. on p. 37).

Komarova, N. L. and D. Wodarz (2010). "ODE models for oncolytic virus dynamics". In: *Journal of Theoretical Biology* 263.4, pp. 530–543. DOI: 10.1016/j.jtbi.2010.01.009 (cit. on pp. 14, 29).

Krabbe, T., J. Marek, T. Groll, K. Steiger, R. M. Schmid, A. M. Krackhardt, and J. Altomonte (2021). "Adoptive T cell therapy is complemented by oncolytic virotherapy with fusogenic VSV-NDV in combination treatment of murine melanoma". In: *Cancers* 13.5, pp. 1–18. DOI: 10.3390/cancers13051044 (cit. on p. 88).

Kumar, A., J. H. Kim, P. Ranjan, M. G. Metcalfe, W. Cao, M. Mishina, S. Gangappa, Z. Guo, E. S. Boyden, S. Zaki, I. York, A. García-Sastre, M. Shaw, and S. Sambhara (2017). "Influenza virus exploits tunneling nanotubes for cell-to-cell spread". In: *Scientific Reports* 7. DOI: 10.1038/srep40360 (cit. on p. 6).

Kuznetsov, M., J. Clairambault, and V. Volpert (2021). "Improving cancer treatments via dynamical biophysical models". In: *Physics of Life Reviews* 39, pp. 1–48. DOI: 10.1016/j.plrev.2021.10.001 (cit. on p. 1).

Kuznetsov, M. and A. Kolobov (2020). "Optimization of dose fractionation for radiotherapy of a solid tumor with account of oxygen effect and proliferative heterogeneity". In: *Mathematics* 8.8, p. 1204. DOI: 10.3390/math8081204 (cit. on p. 24).

Laland, K., B. Matthews, and M. W. Feldman (2016). "An introduction to niche construction theory". In: *Evolutionary ecology* 30.2, pp. 191–202. DOI: 10.1007/s10682-016-9821-z (cit. on p. 3).

Lawler, S. E., M.-C. Speranza, C.-F. Cho, and E. A. Chiocca (2017). "Oncolytic viruses in cancer treatment: A review". In: *JAMA Oncology* 3.6, pp. 841–849. DOI: 10.1001/jamaoncol.2016.2064 (cit. on pp. 5, 6, 48).

Lee, T., A. L. Jenner, P. S. Kim, and J. Lee (2020). "Application of control theory in a delayed-infection and immune-evading oncolytic virotherapy". In: *Mathematical Biosciences and Engineering* 17.3, pp. 2361–2383. DOI: 10.3934/mbe.2020126 (cit. on p. 18).

Leschiera, E., T. Lorenzi, S. Shen, L. Almeida, and C. Audebert (2022). "A mathematical model to study the impact of intra-tumour heterogeneity on anti-tumour CD8+ T cell immune response". In: *Journal of Theoretical Biology* 538, p. 111028. DOI: 10.1016/j.jtbi.2022.111028 (cit. on p. 20).

LeVeque, R. J. (2007). *Finite difference methods for ordinary and partial differential equations: Steady-state and time-dependent problems*. SIAM (cit. on pp. 44, 76).

Lewin, T. D., P. K. Maini, E. G. Moros, H. Enderling, and H. M. Byrne (2018). "The evolution of tumour composition during fractionated radiotherapy: Implications for outcome". In: *Bulletin of Mathematical Biology* 80.5, pp. 1207–1235. DOI: 10.1007/s11538-018-0391-9 (cit. on p. 24).

Lewis, M. (2000). "Spread rate for a nonlinear stochastic invasion". In: *Journal of Mathematical Biology* 41.5, pp. 430–454. DOI: 10.1007/s002850000022 (cit. on p. 60).

Lewis, M. and S. Pacala (2000). "Modeling and analysis of stochastic invasion processes". In: *Journal of Mathematical Biology* 41.5, pp. 387–429. DOI: 10.1007/s002850000050 (cit. on p. 60).

Li, L. (2015). "Patch invasion in a spatial epidemic model". In: *Applied Mathematics and Computation* 258, pp. 342–349. DOI: 10.1016/j.amc.2015.02.006 (cit. on pp. 15, 60).

Liu, S., Y. Cong, D. Wang, Y. Sun, L. Deng, Y. Liu, R. Martin-Trevino, L. Shang, S. P. McDermott, M. D. Landis, S. Hong, A. Adams, R. D'Angelo, C. Ginestier, E. Charafe-Jauffret, S. G. Clouthier, D. Birnbaum, W. S. T., M. Zhan, J. C. Chang, and M. S. Wicha (2013). "Breast cancer stem cells transition between epithelial and mesenchymal states reflective of their normal counterparts". In: *Stem Cell Reports* 2.1, pp. 78–91. DOI: 10.1016/j.stemcr.2013.11.009 (cit. on pp. 137, 155).

Lodish, H., A. Berk, C. A. Kaiser, C. Kaiser, M. Krieger, M. P. Scott, A. Bretscher, H. Ploegh, P. Matsudaira, et al. (2008). *Molecular cell biology*. Macmillan (cit. on pp. 41, 42, 73, 91, 118, 119).

Logg, A., K.-A. Mardal, and G. N. Wells (2012). *Automated solution of differential equations by the finite element method*. Springer (cit. on p. 151).

Lorenzi, T., B. Perthame, and X. Ruan (2021a). "Invasion fronts and adaptive dynamics in a model for the growth of cell populations with heterogeneous mobility". In: *European Journal of Applied Mathematics*, pp. 766–783. DOI: 10.1017/S0956792521000218 (cit. on pp. 13, 103).

Lorenzi, T., C. Venkataraman, A. Lorz, and M. A. J. Chaplain (2018). "The role of spatial variations of abiotic factors in mediating intratumour phenotypic heterogeneity". In: *Journal of Theoretical Biology* 451, pp. 101–110. DOI: 10.1016/j.jtbi.2018.05.002 (cit. on pp. 23, 24, 104).

Lorenzi, T., R. H. Chisholm, M. Melensi, A. Lorz, and M. Delitala (2015). "Mathematical model reveals how regulating the three phases of T-cell response could counteract immune evasion". In: *Immunology* 146.2, pp. 271–280. DOI: 10.1111/imm.12500 (cit. on p. 20).

Lorenzi, T., A. Lorz, and B. Perthame (2017). "On interfaces between cell populations with different mobilities". In: *Kinetic and Related Models* 10.1, pp. 299–311. DOI: 10.3934/krm.2017012 (cit. on pp. 15, 27).

Lorenzi, T., P. J. Murray, and M. Ptashnyk (2020). "From individual-based mechanical models of multicellular systems to free-boundary problems". In: *Interfaces and Free Boundaries* 22.2, pp. 205–244. DOI: 10.4171/IFB/439 (cit. on pp. 11, 30).

Lorenzi, T. and K. J. Painter (2022). "Trade-offs between chemotaxis and proliferation shape the phenotypic structuring of invading waves". In: *International Journal of Non-Linear Mechanics* 139, p. 103885. DOI: 10.1016/j.ijnonlinmec.2021.103885 (cit. on p. 103).

Lorenzi, T., K. J. Painter, and C. Villa (2024a). "Phenotype structuring in collective cell migration:a tutorial of mathematical models and methods". Preprint. DOI: 10.48550/arXiv.2410.13629 (cit. on p. 13).

Lorenzi, T., E. Paparelli, and A. Tosin (2024b). "Modelling coevolutionary dynamics in heterogeneous SI epidemiological systems across scales". In: *Communications in Mathematical Sciences* 22.8, pp. 2131–2165. DOI: 10.4310/cms.240918045626 (cit. on p. 18).

Lorenzi, T. and C. Pouchol (2020). "Asymptotic analysis of selection-mutation models in the presence of multiple fitness peaks". In: *Nonlinearity* 33.11, pp. 5791–5816. DOI: 10.1088/1361-6544/ab9bad (cit. on p. 13).

Lorenzi, T., A. Pugliese, M. Sensi, and A. Zardini (2021b). "Evolutionary dynamics in an SI epidemic model with phenotype-structured susceptible compartment". In: *Journal*

of Mathematical Biology 83.6-7. DOI: 10.1007/s00285-021-01703-1 (cit. on pp. 18, 19, 99, 102, 108, 135).

Lorz, A., T. Lorenzi, J. Clairambault, A. Escargueil, and B. Perthame (2015). "Modeling the effects of space structure and combination therapies on phenotypic heterogeneity and drug resistance in solid tumors". In: *Bulletin of mathematical biology* 77.1, pp. 1–22. DOI: 10.1007/s11538-014-0046-4 (cit. on p. 24).

Lorz, A., S. Mirrahimi, and B. Perthame (2011). "Dirac mass dynamics in multidimensional nonlocal parabolic equations". In: *Communications in Partial Differential Equations* 36.6, pp. 1071–1098. DOI: 10.1080/03605302.2010.538784 (cit. on pp. 13, 103).

Lotka, A. J. (1926). "Elements of physical biology". In: *Science Progress in the Twentieth Century (1919-1933)* 21.82, pp. 341–343 (cit. on p. 14).

Macfarlane, F. R., T. Lorenzi, and M. A. J. Chaplain (2018). "Modelling the immune response to cancer: An individual-based approach accounting for the difference in movement between inactive and activated T cells". In: *Bulletin of Mathematical Biology* 80.6, pp. 1539–1562. DOI: 10.1007/s11538-018-0412-8 (cit. on p. 20).

Macfarlane, F. R., X. Ruan, and T. Lorenzi (2022). "Individual-based and continuum models of phenotypically heterogeneous growing cell populations". In: *AIMS Bioengineering* 9.1, pp. 68–92. DOI: 10.3934/bioeng.2022007 (cit. on pp. 11, 28, 30, 55).

Macfarlane, F., M. Chaplain, and T. Lorenzi (2019). "A stochastic individual-based model to explore the role of spatial interactions and antigen recognition in the immune response against solid tumours". In: *Journal of Theoretical Biology* 480, pp. 43–55. DOI: 10.1016/j.jtbi.2019.07.019 (cit. on p. 20).

Mahasa, K. J., R. Ouifki, A. Eladdadi, and L. de Pillis (2022). "A combination therapy of oncolytic viruses and chimeric antigen receptor T cells: A mathematical model proof-of-concept". In: *Mathematical Biosciences and Engineering* 19.5, pp. 4429–4457. DOI: 10.3934/mbe.2022205 (cit. on p. 21).

Mallet, D. and L. De Pillis (2006). "A cellular automata model of tumor–immune system interactions". In: *Journal of Theoretical Biology* 239.3, pp. 334–350. DOI: 10.1016/j.jtbi.2005.08.002 (cit. on p. 20).

Martin, N. T. and J. C. Bell (2018). "Oncolytic virus combination therapy: Killing one bird with two stones". In: *Molecular Therapy* 26.6, pp. 1414–1422. DOI: 10.1016/j.ymthe.2018.04.001 (cit. on p. 7).

Martínez-González, A., G. F. Calvo, L. A. Pérez Romasanta, and V. Pérez-García (2012). "Hypoxic cell waves around necrotic cores in glioblastoma: a biomathematical model and its therapeutic implications". In: *Bulletin of Mathematical Biology* 74.12, pp. 2875–2896. DOI: 10.1007/s11538-012-9786-1 (cit. on pp. 22, 118, 119, 152).

Marusyk, A., V. Almendro, and K. Polyak (2012). "Intra-tumour heterogeneity: A looking glass for cancer?" In: *Nature Reviews Cancer* 12, pp. 323–334. DOI: 10.1038/nrc3261 (cit. on p. 2).

Matzavinos, A., M. A. Chaplain, and V. A. Kuznetsov (2004). "Mathematical modelling of the spatio-temporal response of cytotoxic T-lymphocytes to a solid tumour". In: *Mathematical Medicine and Biology* 21.1, pp. 1–34. DOI: https://doi.org/10.1093/imammb/21.1.1 (cit. on pp. 20, 73, 74).

McCallum, H., N. Barlow, and J. Hone (2001). "How should pathogen transmission be modelled?" In: *Trends in Ecology and Evolution* 16.6, pp. 295–300. DOI: 10.1016/S0169-5347(01)02144-9 (cit. on p. 14).

McKeown, S. R. (2014). "Defining normoxia, physoxia and hypoxia in tumours-implications for treatment response". In: *The British Journal of Radiology* 87.1035, p. 20130676. DOI: 10.1259/bjr.20130676 (cit. on pp. 118, 120).

Mirrahimi, S. and B. Perthame (2015). "Asymptotic analysis of a selection model with space". In: *Journal de Mathématiques Pures et Appliquées* 104.6, pp. 1108–1118. DOI: 10.1016/j.matpur.2015.07.006 (cit. on pp. 13, 104).

Mok, W., T. Stylianopoulos, Y. Boucher, and R. K. Jain (2009). "Mathematical modeling of herpes simplex virus distribution in solid tumors: Implications for cancer gene therapy". In: *Clinical Cancer Research* 15.7, pp. 2352–2360. DOI: 10.1158/1078-0432.CCR-08-2082 (cit. on pp. 42, 91, 118, 120).

Morozov, A., S. Petrovskii, and B.-L. Li (2006). "Spatiotemporal complexity of patchy invasion in a predator-prey system with the Allee effect." In: *Journal of Theoretical Biology* 238.1, pp. 18–35. DOI: 10.1016/j.jtbi.2005.05.021 (cit. on pp. 15, 60).

Morselli, D., G. Chiari, F. Frascoli, and M. E. Delitala (2024a). "A phenotype-structured mathematical model for the influence of hypoxia on virotherapy". Preprint. DOI: 10.48550/arXiv.2411.02413 (cit. on pp. 26, 110, 114, 120, 124, 125, 127, 129, 132).

Morselli, D., M. E. Delitala, and F. Frascoli (2023). "Agent-based and continuum models for spatial dynamics of infection by oncolytic viruses". In: *Bulletin of Mathematical Biology* 85.10. DOI: 10.1007/s11538-023-01192-x (cit. on pp. 25, 27, 44, 46, 51, 56).

Morselli, D., M. E. Delitala, A. L. Jenner, and F. Frascoli (2024b). "A hybrid discrete-continuum modelling approach for the interactions of the immune system with oncolytic viral infections". Preprint. DOI: 10.48550/arXiv.2404.06459 (cit. on pp. 25, 62, 75, 78, 80, 82, 84, 86).

Mueller-Klieser, W. and R. Sutherland (1984). "Oxygen consumption and oxygen diffusion properties of multicellular spheroids from two different cell lines". In: *Advances in Experimental Medicine and Biology* 180, pp. 311–321. DOI: 10.1007/978-1-4684-4895-5_30 (cit. on pp. 118, 120).

Murray, J. D. (2003). *Mathematical biology: II: spatial models and biomedical applications*. Vol. 18. Interdisciplinary Applied Mathematics. Springer New York. DOI: 10.1007/b98869 (cit. on p. 39).

Murray, J. D. (2002). *Mathematical biology: I. An introduction*. Springer New York. DOI: 10.1007/b98868 (cit. on p. 40).

Najm, F., M. Ahmed, R. Yafia, M. Aziz Alaoui, and L. Boukrim (2023). "Hopf bifurcation and normal form in a delayed oncolytic model". In: *International Journal of Biomathematics*. DOI: 10.1142/S1793524523501115 (cit. on p. 18).

Newman, W. I. (1980). "Some exact solutions to a non-linear diffusion problem in population genetics and combustion". In: *Journal of Theoretical Biology* 85.2, pp. 325–334. DOI: 10.1016/0022-5193(80)90024-7 (cit. on pp. 39, 117, 123).

Nieto, M. A., R. Y.-J. Huang, R. A. Jackson, and J. P. Thiery (2016). "EMT: 2016". In: *Cell* 166.1, pp. 21–45. DOI: 10.1016/j.cell.2016.06.028 (cit. on p. 4).

Novozhilov, A. S. (2008). "On the spread of epidemics in a closed heterogeneous population". In: *Mathematical biosciences* 215.2, pp. 177–185. DOI: https://doi.org/10.1016/j.mbs.2008.07.010 (cit. on p. 18).

Novozhilov, A. S., F. S. Berezovskaya, E. V. Koonin, and G. P. Karev (2006). "Mathematical modeling of tumor therapy with oncolytic viruses: Regimes with complete tumor elimination within the framework of deterministic models". In: *Biology Direct* 1.1, pp. 1–18. DOI: 10.1186/1745-6150-1-6 (cit. on pp. 14, 29).

Nowell, P. C. (1976). "The clonal evolution of tumor cell populations". In: *Science* 194.4260, pp. 23–28 (cit. on pp. 1, 2).

O'Brien, C. A., A. Pollett, S. Gallinger, and J. E. Dick (2007). "A human colon cancer cell capable of initiating tumour growth in immunodeficient mice". In: *Nature* 445.7123, pp. 106–110. DOI: 10.1038/nature05372 (cit. on p. 3).

O'Donnell, J. S., M. W. L. Teng, and M. J. Smyth (2018). "Cancer immunoediting and resistance to T cell-based immunotherapy". In: *Nature Reviews Clinical Oncology* 16.3, pp. 151–167. DOI: 10.1038/s41571-018-0142-8 (cit. on pp. 9, 83).
Oey, H. and E. Whitelaw (2014). "On the meaning of the word 'epimutation'". In: *Trends in Genetics* 30.12, pp. 519–520. DOI: 10.1016/j.tig.2014.08.005 (cit. on p. 4).
Othmer, H. G. and T. Hillen (2002). "The diffusion limit of transport equations II: Chemotaxis equations". In: *SIAM Journal on Applied Mathematics* 62.4, pp. 1222–1250. DOI: 10.1137/S0036139900382772 (cit. on p. 74).
Ottolino-Perry, K., J.-S. Diallo, B. D. Lichty, J. C. Bell, and J. Andrea McCart (2010). "Intelligent design: Combination therapy with oncolytic viruses". In: *Molecular Therapy* 18.2, pp. 251 –263. DOI: 10.1038/mt.2009.283 (cit. on p. 7).
Owen, M. R. and J. A. Sherratt (1997). "Pattern formation and spatiotemporal irregularity in a model for macrophage-tumour interactions". In: *Journal of Theoretical Biology* 189.1, pp. 63–80. DOI: 10.1006/jtbi.1997.0494 (cit. on p. 20).
Painter, K. J. (2019). "Mathematical models for chemotaxis and their applications in self-organisation phenomena". In: *Journal of Theoretical Biology* 481, pp. 162–182. DOI: 10.1016/j.jtbi.2018.06.019 (cit. on pp. 20, 61, 70).
Paiva, L. R., C. Binny, S. C. Ferreira Jr, and M. L. Martins (2009). "A multiscale mathematical model for oncolytic virotherapy". In: *Cancer Research* 69.3, pp. 1205–1211. DOI: 10.1158/0008-5472.CAN-08-2173 (cit. on p. 17).
Palumbo, A., N. d. O. M. Da Costa, M. H. Bonamino, L. F. R. Pinto, and L. E. Nasciutti (2015). "Genetic instability in the tumor microenvironment: A new look at an old neighbor". In: *Molecular cancer* 14.1, pp. 1–15. DOI: 10.1186/s12943-015-0409-y (cit. on p. 3).
Pansy, K., B. Uhl, J. Krstic, M. Szmyra, K. Fechter, A. Santiso, L. Thüminger, H. Greinix, J. Kargl, K. Prochazka, J. Feichtinger, and A. J. Deutsch (2021). "Immune regulatory processes of the tumor microenvironment under malignant conditions". In: *International Journal of Molecular Sciences* 22.24. DOI: 10.3390/ijms222413311 (cit. on p. 8).
Penington, C. J., B. D. Hughes, and K. A. Landman (2011). "Building macroscale models from microscale probabilistic models: A general probabilistic approach for nonlinear diffusion and multispecies phenomena". In: *Physical Review E - Statistical, Nonlinear, and Soft Matter Physics* 84.4. DOI: 10.1103/PhysRevE.84.041120 (cit. on pp. 11, 30).
Perthame, B. (2006). *Transport equations in biology*. Springer Science & Business Media (cit. on pp. 13, 103, 104).
Perthame, B. and G. Barles (2008). "Dirac concentrations in Lotka-Volterra parabolic PDEs". In: *Indiana University Mathematics Journal* 57.7, pp. 3275–3301. DOI: 10.1512/iumj.2008.57.3398 (cit. on pp. 13, 103, 104).
Perthame, B., F. Quirós, and J. L. Vázquez (2014). "The Hele–Shaw asymptotics for mechanical models of tumor growth". In: *Archive for Rational Mechanics and Analysis* 212.1, pp. 93–127. DOI: 10.1007/s00205-013-0704-y (cit. on pp. 28, 35).
Petrovskii, S. V., H. Malchow, F. M. Hilker, and E. Venturino (2005). "Patterns of patchy spread in deterministic and stochastic models of biological invasion and biological control". In: *Biological Invasions* 7.5, pp. 771–793. DOI: 10.1007/s10530-005-5217-7 (cit. on pp. 15, 60).
Petrovskii, S. V., A. Y. Morozov, and E. Venturino (2002). "Allee effect makes possible patchy invasion in a predator-prey system". In: *Ecology Letters* 5.3, pp. 345–352. DOI: 10.1046/j.1461-0248.2002.00324.x (cit. on pp. 15, 60).
Pittman, R. N. (2011). "Regulation of tissue oxygenation". In: *Colloquium Series on Integrated Systems Physiology: From Molecule to Function* 3.3, pp. 1–100. DOI: 10.4199/c00029ed1v01y201103isp017 (cit. on pp. 118, 120).

Plate, K. H., G. Breier, H. A. Weich, and W. Risau (1992). "Vascular endothelial growth factor is a potential tumour angiogenesis factor in human gliomas in vivo". In: *Nature* 359.6398, pp. 845–848. DOI: 10.1038/359845a0 (cit. on p. 156).

Pooladvand, P. and P. S. Kim (2022). "Modelling oncolytic virus diffusion in collagen-dense tumours". In: *Frontiers in Systems Biology* 2.903512. DOI: 10.3389/fsysb.2022.903512 (cit. on pp. 17, 108, 161).

Pooladvand, P., C.-O. Yun, A.-R. Yoon, P. S. Kim, and F. Frascoli (2021). "The role of viral infectivity in oncolytic virotherapy outcomes: A mathematical study". In: *Mathematical Biosciences* 334, p. 108520. DOI: 10.1016/j.mbs.2020.108520 (cit. on pp. 16, 17, 35, 37, 41, 61, 91, 92, 160).

Pouchol, C., J. Clairambault, A. Lorz, and E. Trélat (2018). "Asymptotic analysis and optimal control of an integro-differential system modelling healthy and cancer cells exposed to chemotherapy". In: *Journal de Mathématiques Pures et Appliquées* 116, pp. 268–308. DOI: 10.1016/j.matpur.2017.10.007 (cit. on p. 24).

Preziosi, L. (2003). *Cancer modelling and simulation*. CRC Press (cit. on p. 155).

Quaranta, V., A. M. Weaver, P. T. Cummings, and A. R. A. Anderson (2005). "Mathematical modeling of cancer: The future of prognosis and treatment". In: *Clinica Chimica Acta* 357.2, pp. 173–179 (cit. on p. 155).

Rajalakshmi, M. and M. Ghosh (2022). "Hopf-bifurcation analysis of a delayed model for the treatment of cancer using virotherapy". In: *Kyungpook Mathematical Journal* 62.1, pp. 119–132. DOI: 10.5666/KMJ.2022.62.1.119 (cit. on p. 18).

Ramaj, T. and X. Zou (2023). "On the treatment of melanoma: a mathematical model of oncolytic virotherapy". In: *Mathematical Biosciences* 365. DOI: 10.1016/j.mbs.2023.109073 (cit. on p. 24).

Rioja, V. L. de, N. Isern, and J. Fort (2016). "A mathematical approach to virus therapy of glioblastomas". In: *Biology Direct* 11.1. DOI: 10.1186/s13062-015-0100-7 (cit. on p. 18).

Rocha, H. L., I. Godet, F. Kurtoglu, J. Metzcar, K. Konstantinopoulos, S. Bhoyar, D. M. Gilkes, and P. Macklin (2021). "A persistent invasive phenotype in post-hypoxic tumor cells is revealed by fate mapping and computational modeling". In: *Science* 24.9, pp. 1–22. DOI: 10.1016/j.isci.2021.102935 (cit. on pp. 23, 147).

Roy, M. and R. D. Holt (2008). "Effects of predation on host-pathogen dynamics in SIR models". In: *Theoretical Population Biology* 73.3, pp. 319–331. DOI: 10.1016/j.tpb.2007.12.008 (cit. on p. 14).

Ruan, K., G. Song, and G. Ouyang (2009). "Role of hypoxia in the hallmarks of human cancer". In: *Journal of Cellular Biochemistry* 107.6, pp. 1053–1062. DOI: 10.1002/jcb.22214 (cit. on p. 3).

Russell, L. and K.-W. Peng (2018). "The emerging role of oncolytic virus therapy against cancer". In: *Chinese Clinical Oncology* 7.2. DOI: 10.21037/cco.2018.04.04 (cit. on pp. 5, 43).

Sadri, M., A. Najafi, A. Rahimi, N. Behranvand, M. Hossein Kazemi, H. Khorramdelazad, and R. Falak (2023). "Hypoxia effects on oncolytic virotherapy in cancer: Friend or foe?" In: *International Immunopharmacology* 122, p. 110470. DOI: 10.1016/j.intimp.2023.110470 (cit. on pp. 7, 109, 132).

Santry, L. A., J. P. van Vloten, J. P. Knapp, K. Matuszewska, T. M. McAusland, J. A. Minott, R. C. Mould, A. A. Stegelmeier, P. P. Major, S. K. Wootton, J. J. Petrik, and B. W. Bridle (2020). "Tumour vasculature: Friend or foe of oncolytic viruses?" In: *Cytokine & Growth Factor Reviews* 56, pp. 69–82. DOI: 10.1016/j.cytogfr.2020.07.007 (cit. on p. 7).

Schaller, S. M., A. Deutsch, H. Hatzikirou, and D. Basanta (2012). "'Go or grow': the key to the emergence of invasion in tumour progression?" In: *Mathematical Medicine and Biology* 29.1, pp. 49–65. DOI: 10.1093/imammb/dqq011 (cit. on p. 146).
Scianna, M. and A. Colombi (2017). "A coherent modeling procedure to describe cell activation in biological systems". In: *Communications in Applied and Industrial Mathematics* 8.1, pp. 1–22. DOI: 10.1515/caim-2017-0001 (cit. on pp. 12, 137, 139, 141, 155).
Scianna, M. and L. Preziosi (2012). "Multiscale developments of cellular Potts models". In: *Multiscale Modeling & Simulation* 10.2, pp. 342–382. DOI: 10.1137/100812951 (cit. on pp. 12, 150).
Servedio, M. R., Y. Brandvain, S. Dhole, C. L. Fitzpatrick, E. E. Goldberg, C. A. Stern, J. Van Cleve, and D. J. Yeh (2014). "Not just a theory–The utility of mathematical models in evolutionary biology". In: *PLoS Biology* 12.12, pp. 1–5. DOI: 10.1371/journal.pbio.1002017 (cit. on p. 1).
Shalhout, S. Z., D. M. Miller, K. S. Emerick, and H. L. Kaufman (2023). "Therapy with oncolytic viruses: progress and challenges". In: *Nature Reviews Clinical Oncology* 20.3, pp. 160–177. DOI: 10.1038/s41571-022-00719-w (cit. on p. 6).
Sheng Guo, Z. (2011). "The impact of hypoxia on oncolytic virotherapy". In: *Virus Adaptation and Treatment* 3.1, pp. 71–82. DOI: 10.2147/VAAT.S17832 (cit. on pp. 7, 109, 111, 132, 134).
Sherlock, B. D. and A. C. Coster (2023). "Oncolytic virus treatment of human breast cancer cells: Modelling therapy efficacy". In: *Journal of Theoretical Biology* 560, p. 111394. DOI: 10.1016/j.jtbi.2022.111394 (cit. on p. 161).
Shi, T., X. Song, Y. Wang, F. Liu, and J. Wei (2020). "Combining Oncolytic Viruses With Cancer Immunotherapy: Establishing a New Generation of Cancer Treatment". In: *Frontiers in Immunology* 11. DOI: 10.3389/fimmu.2020.00683 (cit. on pp. 6, 10, 61, 88).
Shield, K., M. L. Ackland, N. Ahnmed, and G. E. Rice (2009). "Multicellular spheroids in ovarian cancer metastases: Biology and pathology". In: *Gynecologic Oncology* 113.1, pp. 143–148. DOI: 10.1016/j.ygyno.2008.11.032 (cit. on p. 155).
Singh, S. K., C. Hawkins, I. D. Clarke, J. A. Squire, J. Bayani, T. Hide, R. M. Henkelman, M. D. Cusimano, and P. B. Dirks (2004). "Identification of human brain tumour initiating cells". In: *Nature* 432.7015, pp. 396–401. DOI: 10.1038/nature03128 (cit. on p. 3).
Singh, T. and S. Banerjee (2020). "Spatiotemporal dynamics of immunogenic tumors". In: *International Journal of Biomathematics* 13.5, p. 2050044. DOI: 10.1142/S1793524520500448 (cit. on p. 20).
Slaney, C. Y., P. Wang, P. K. Darcy, and M. H. Kershaw (2018). "CARs versus BiTEs: A comparison between T cell–redirection strategies for cancer treatment". In: *Cancer Discovery* 8.8, pp. 924–934. DOI: 10.1158/2159-8290.cd-18-0297 (cit. on p. 9).
Sonugür, F. G. and H. Akbulut (2019). "The role of tumor microenvironment in genomic instability of malignant tumors". In: *Frontiers in genetics* 10, p. 1063 (cit. on p. 3).
Stace, R. E., T. Stiehl, M. A. Chaplain, A. Marciniak-Czochra, and T. Lorenzi (2020). "Discrete and continuum phenotype-structured models for the evolution of cancer cell populations under chemotherapy". In: *Mathematical Modelling of Natural Phenomena* 15. Ed. by F. Hubert, p. 14. DOI: 10.1051/mmnp/2019027 (cit. on p. 24).
Stein, A. M., T. Demuth, D. Mobley, M. Berens, and L. M. Sander (2007). "A mathematical model of glioblastoma tumor spheroid invasion in a three-dimensional in vitro experiment". In: *Biophysical Journal* 92.1, pp. 356–365. DOI: 10.1529/biophysj.106.093468 (cit. on p. 155).
Storey, K. M. and T. L. Jackson (2021). "An agent-based model of combination oncolytic viral therapy and anti-PD-1 immunotherapy reveals the importance of spatial location

when treating glioblastoma". In: *Cancers* 13.21. DOI: 10.3390/cancers13215314 (cit. on p. 22).
Storey, K. M., S. E. Lawler, and T. L. Jackson (2020). "Modeling oncolytic viral therapy, immune checkpoint inhibition, and the complex dynamics of innate andaAdaptive immunity in glioblastoma treatment". In: *Frontiers in Physiology* 11. DOI: 10.3389/fphys.2020.00151 (cit. on p. 21).
Surendran, A., A. L. Jenner, E. Karimi, B. Fiset, D. F. Quail, L. A. Walsh, and M. Craig (2023). "Agent-cased modelling reveals the role of the tumor microenvironment on the short-term success of combination temozolomide/immune checkpoint blockade to treat glioblastoma". In: *Journal of Pharmacology and Experimental Therapeutics* 387.1, pp. 66–77. DOI: 10.1124/jpet.122.001571 (cit. on p. 22).
Textor, J., A. Peixoto, S. E. Henrickson, M. Sinn, U. H. Von Andrian, and J. Westermann (2011). "Defining the quantitative limits of intravital two-photon lymphocyte tracking". In: *Proceedings of the National Academy of Sciences of the United States of America* 108.30, pp. 12401–12406. DOI: 10.1073/pnas.1102288108 (cit. on p. 74).
Touchefeu, Y., P. Franken, and K. Harrington (2012). "Radiovirotherapy: Principles and prospects in oncology". In: *Current Pharmaceutical Design* 18.22, pp. 3313–3320. DOI: 10.2174/1381612811209023313 (cit. on p. 7).
Vaghi, C., A. Rodallec, R. Fanciullino, J. Ciccolini, J. P. Mochel, M. Mastri, C. Poignard, J. M. Ebos, and S. Benzekry (2020). "Population modeling of tumor growth curves and the reduced Gompertz model improve prediction of the age of experimental tumors". In: *PLoS Computational Biology* 16.2, pp. 1–24. DOI: 10.1371/journal.pcbi.1007178 (cit. on p. 14).
Van Saarloos, W. (2003). "Front propagation into unstable states". In: *Physics Reports* 386.2-6, pp. 29–222. DOI: 10.1016/j.physrep.2003.08.001 (cit. on p. 37).
Veliov, V. M. and A. Widder (2016). "Aggregation and asymptotic analysis of an SI-epidemic model for heterogeneous populations". In: *Mathematical Medicine and Biology: a journal of the IMA* 33.3, pp. 295–318. DOI: https://doi.org/10.1093/imammb/dqv018 (cit. on p. 18).
Villa, C., M. A. J. Chaplain, and T. Lorenzi (2021a). "Modeling the emergence of phenotypic heterogeneity in vascularized tumors". In: *SIAM Journal on Applied Mathematics* 81.2, pp. 434–453. DOI: 10.1137/19m1293971 (cit. on pp. 22, 23, 103, 111).
Villa, C., M. A. Chaplain, and T. Lorenzi (2021b). "Evolutionary dynamics in vascularised tumours under chemotherapy: Mathematical modelling, asymptotic analysis and numerical simulations". In: *Vietnam Journal of Mathematics* 49.1, pp. 143–167. DOI: 10.1007/s10013-020-00445-9 (cit. on p. 24).
Vithanage, G., H.-C. Wei, and S. R.-J. Jang (2023). "The role of tumor activation and inhibition with saturation effects in a mathematical model of tumor and immune system interactions undergoing oncolytic viral therapy". In: *Mathematical Methods in the Applied Sciences* 46.9, pp. 10787–10813. DOI: 10.1002/mma.9152 (cit. on p. 21).
Volterra, V. (1937). "Principes de biologie mathématique". In: *Acta Biotheoretica* 3.1, pp. 1–36. DOI: 10.1007/bf01556501 (cit. on p. 14).
Wagner, B. A., S. Venkataraman, and G. R. Buettner (2011). "The rate of oxygen utilization by cells". In: *Free Radical Biology and Medicine* 51.3, pp. 700–712. DOI: 10.1016/j.freeradbiomed.2011.05.024 (cit. on pp. 118, 120).
Wang, X. and I. Rivière (2016). "Clinical manufacturing of CAR T cells: Foundation of a promising therapy". In: *Molecular Therapy - Oncolytics* 3, p. 16015. DOI: 10.1038/mto.2016.15 (cit. on p. 9).
Wang, Y., J. P. Tian, and J. Wei (2013). "Lytic cycle: A defining process in oncolytic virotherapy". In: *Applied Mathematical Modelling* 37.8, pp. 5962–5978. DOI: 10.1016/j.apm.2012.12.004 (cit. on p. 18).

Wang, Z., Z. Guo, and H. Smith (2019). "A mathematical model of oncolytic virotherapy with time delay". In: *Mathematical Biosciences and Engineering* 16.4, pp. 1836–1860. DOI: 10.3934/mbe.2019089 (cit. on p. 18).

Weerasinghe, H. N., P. M. Burrage, K. Burrage, and D. V. Nicolau (2019). "Mathematical models of cancer cell plasticity". In: *Journal of Oncology* 2019, pp. 1–14. DOI: 10.1155/2019/2403483 (cit. on p. 11).

Williams, C. K., J. L. Li, M. Murga, A. L. Harris, and G. Tosato (2006). "Upregulation of the Notch ligand delta-like inhibits VEGF induced endothelial cell function". In: *Blood* 107.3, pp. 931–939. DOI: 10.1182/blood-2005-03-1000 (cit. on p. 137).

Wilson, W., A. Deroos, and E. McCauley (1993). "Spatial instabilities within the diffusive Lotka-Volterra system: Individual-based simulation results". In: *Theoretical Population Biology* 43.1, pp. 91–127. DOI: 10.1006/tpbi.1993.1005 (cit. on p. 16).

Wing, A., C. A. Fajardo, A. D. Posey, C. Shaw, T. Da, R. M. Young, R. Alemany, C. H. June, and S. Guedan (2018). "Improving CART-cell therapy of solid tumors with oncolytic virus–driven production of a bispecific T-cell engager". In: *Cancer Immunology Research* 6.5, pp. 605–616. DOI: 10.1158/2326-6066.CIR-17-0314 (cit. on p. 88).

Wise, S. M., J. S. Lowengrub, H. B. Frieboes, and V. Cristini (2008). "Three-dimensional multispecies nonlinear tumor growth – I Model and numerical method". In: *Journal of Theoretical Biology* 253.3, pp. 524–543. DOI: 10.1016/j.jtbi.2008.03.027 (cit. on p. 12).

Wodarz, D. (2001). "Viruses as antitumor weapons: Defining conditions for tumor remission". In: *Cancer Research* 61.8, pp. 3501–3507 (cit. on p. 21).

Wodarz, D., C. N. Chan, B. Trinité, N. L. Komarova, and D. N. Levy (2014). "On the laws of virus spread through cell populations". In: *Journal of Virology* 88.22, pp. 13240–13248. DOI: 10.1128/JVI.02096-14 (cit. on p. 15).

Wodarz, D., A. Hofacre, J. W. Lau, Z. Sun, H. Fan, and N. L. Komarova (2012). "Complex spatial dynamics of oncolytic viruses in vitro: Mathematical and experimental approaches". In: *PLoS Computational Biology* 8.6, pp. 1–15. DOI: 10.1371/journal.pcbi.1002547 (cit. on pp. 16, 46, 60).

Wojton, J. and B. Kaur (2010). "Impact of tumor microenvironment on oncolytic viral therapy". In: *Cytokine and Growth Factor Reviews* 21.2-3, pp. 127–134. DOI: 10.1016/j.cytogfr.2010.02.014 (cit. on pp. 6, 7, 15).

Workenhe, S. T., G. Simmons, J. G. Pol, B. D. Lichty, W. P. Halford, and K. L. Mossman (2014). "Immunogenic HSV-mediated oncolysis shapes the antitumor immune response and contributes to therapeutic efficacy". In: *Molecular Therapy* 22.1, pp. 123–131. DOI: 10.1038/mt.2013.238 (cit. on pp. 42, 91, 120).

Wu, J. T., H. M. Byrne, D. H. Kirn, and L. M. Wein (2001). "Modeling and analysis of a virus that replicates selectively in tumor cells". In: *Bulletin of Mathematical Biology* 63.4, pp. 731–768. DOI: 10.1006/bulm.2001.0245 (cit. on pp. 17, 22).

Wu, J. T., D. H. Kirn, and L. M. Wein (2004). "Analysis of a three-way race between tumor growth, a replication-competent virus and an immune response". In: *Bulletin of Mathematical Biology* 66.4, pp. 605–625. DOI: 10.1016/j.bulm.2003.08.016 (cit. on p. 22).

Yasuda, K., T. Nirei, E. Sunami, H. Nagawa, and J. Kitayama (2011). "Density of CD4(+) and CD8(+) T lymphocytes in biopsy samples can be a predictor of pathological response to chemoradiotherapy (CRT) for rectal cancer". In: *Radiation Oncology* 6.1. DOI: 10.1186/1748-717X-6-49 (cit. on p. 75).

Zhuang, Y., K. Liu, Q. He, X. Gu, C. Jiang, and J. Wu (2023). "Hypoxia signaling in cancer: Implications for therapeutic interventions". In: *MedComm* 4, p. 110470. DOI: 10.1002/mco2.203 (cit. on pp. 22, 109, 132).